

PhD Dissertation

Modal Analysis And Design Of Antennas For Biomedical Applications

Universitat Politècnica de València - Departamento de
Comunicaciones

Université du Québec en Outaouais - Département d'Informatique
et d'Ingénierie

Author

Ferdaous Abderrazak

Advisors

Prof. Dr. Eva Antonino Daviu
Prof. Larbi Talbi

Gatineau, May 11, 2025

"If you want to live a happy life, tie it to a goal, not to people or things."

— Albert Einstein

"To Ali, Lilia, and Abdallah..."

Agradecimientos

Elegí expresar mi gratitud en español, un idioma hermoso que he llegado a amar profundamente. Este amor por el idioma proviene de mi profunda admiración por la cultura y por las personas que le dan vida. Soy alguien que puede decir con certeza que este doctorado ha cambiado mi vida, no solo la mía, sino también la vida de tres pequeñas almas que emprendieron un viaje con su madre a través de continentes. Esta aventura ha sido una experiencia increíblemente larga y agotadora, llena de risas, alegría y felicidad, pero también de luchas, lágrimas y numerosas crisis emocionales. Llevaré conmigo tanto la felicidad como la tristeza, porque los momentos felices seguirán motivándome, mientras que los momentos difíciles me recordarán siempre que hay cosas en este mundo por las que vale la pena sacrificarse. A la niña pequeña que vino de un pequeño pueblo tunecino con tradiciones profundamente arraigadas, le diría: ERES VALIOSA. Esta tesis, aunque lleve mi nombre, debería incluir el de muchas personas que la han hecho posible.

A mis hijos Ali, Lilia y Abdallah, por vuestros besos, abrazos y hermosas palabras; sois mi única motivación, y solo escuchar “mamá” cuando llego a casa, incluso en mis momentos más oscuros, siempre le da vida a mi alma. Viajar conmigo a España y Canadá ha moldeado vuestras personalidades y, sin duda, os ha convertido en algunas de las mejores versiones de vosotros mismos. Pero nunca olvidéis de dónde venís: aunque crezcáis, recordad siempre que en algún lugar de este mundo, un país llamado Túnez fue nuestro comienzo. Espero que siempre sigáis siendo humildes y agradecidos.

A mi hermano, Anas, por ser mi primer apoyo. Por el cariño y la atención que percibo que mis hijos experimentan. Por ser nuestro refugio seguro siempre que lo necesitamos.

A mis padres por amarme y sentir orgullo de quien soy. Por enseñarme idiomas, a pesar de que los detestaba cuando era niño. Por recordarme siempre que soy capaz de todo, que llevo dentro el poder de alcanzar todo lo que desee.

A Sheick, por ser la esencia de quien eres. Por ofrecerme una visión renovada de la vida y mostrarme que incluso los retos más complejos pueden ser enfrentados con una actitud más serena. Por enseñarme que lo único que necesito es la persona adecuada a mi lado.

A la noble alma de mi abuela Roukaya, por su amor incondicional, por enseñarme el valor de la responsabilidad, la paciencia y la capacidad de apreciar lo sencillo. A la mujer que sacrificó su vida trabajando la tierra para sustentar a su familia, y a la que siempre me alentó a seguir el camino del estudio.

A Eva, por revelarme una nueva perspectiva de lo que significa ser profesora. Por escucharme con atención y comprender las dificultades por las que he transitado. Por ser siempre un faro de ejemplo para sus alumnos, por su carácter abierto y su profunda capacidad para empatizar con los demás. Por acogerme en España en mi primer día y por permanecer a mi lado hasta este momento.

A Miguel Ferrando, por brindarme esta oportunidad, sin la cual este doctorado nunca habría sido posible. Por la dedicación y el amor con los que cultiva la ciencia. A Jaima, por ser la mejor compañía durante mi doctorado. Por animarme y ofrecerme su opinión siempre que la necesitaba. Por todos los momentos y eventos maravillosos que compartimos, y especialmente por las profundas conversaciones que contribuyeron enormemente a hacerme más consciente y más maduro. A Dani, por ser el científico sereno, por su tiempo, por su ayuda y por compartir sus recursos. Por introducirme a la hermosa cultura española y a sus exquisitos sabores.

Por gente maravillosa que he podido conocer en el APL. A Miguel Ferrando Rocher, por ser simplemente auténtico consigo mismo. A Marta, por la madre cariñosa que es. A María, por la mujer decidida y fuerte que representa. A Kaouding, Damián y Adrián, por reavivar el espíritu del laboratorio.

Mi experiencia en la Université du Québec en Outaouais fue tan distinta que dio vida a una nueva versión de mí misma: responsable, realista y capaz de enfrentar mis problemas. A Larbi Talbi, por enseñarme a confiar en mí misma y por ayudarme a descubrir la versión más fuerte de mi ser. A la rectora, Murielle Laberge, por estar a mi lado y brindarme su apoyo en todas las dificultades. A la decana de investigación, Stéphanie Demers, a la mujer dispuesta a generar cambios. Y a la trabajadora social, Valérie Buval, por escucharme y tratar de ayudarme en mis momentos más difíciles.

Por último me gustaría agradecer a "los amigos del camino", a quienes defino como las personas que conocí durante mi doctorado, cuya presencia en mi vida tuvo un impacto enorme. Este doctorado es una dedicación para todas las madres solteras, que se encuentran pensando cómo gestionar los costos de un nuevo mes. Siempre recuerda: Mujer es Poder.



Abstract

The current wireless communication landscape is defined by the progressive deployment of Wireless Power Transfer (WPT) systems, which have set high standards for efficiency, practicality, and safety in areas where traditional wired power transmission faces challenges or poses hazardous technical problems. The last deployment of WPT has taken place in implantable medical devices (IMDs) because of its ability to provide a continuous, reliable power supply without the need for invasive procedures. While the most common form of wireless power delivery in these devices is low-frequency inductive coupling ($f < 10$ MHz), recent experimental results and modeling have shown that optimal Power Transfer Efficiency (PTE) occurs in the UHF band (300 MHz – 3 GHz). As a matter of fact, several aspects of architectures, hardware designs and implementations of RF-based WPT systems for IMDs have been explored. Although, they demonstrated considerable PTE when the transmitting (TX) and receiving (Rx) antennas are perfectly aligned, the slightest misalignment leads to significant drop in efficiency, causing a sharp decline in energy transfer. This thesis focuses on the design and analysis of novel WPT systems for biomedical applications, introducing, for the first time, the use of Characteristic Modes Analysis (CMA) based methodologies, with the goal of enhancing the resilience and tolerance of these systems to misalignments.

In RF-based WPT systems for IMDs, a guideline for analysis and fabrication is employed, focusing on interactions near resonance to optimize energy transfer, efficiency, and impedance matching. However, misalignments or environmental variations can disrupt these ideal conditions, leading to significant efficiency loss. These factors highlight the need for a deeper physical understanding of the complex interactions, particularly at non-resonant frequencies. The CMA becomes particularly pertinent in this context, as it provides a deeper physical insight into how minor misalignments or fluctuations in the operating environment disrupt optimal resonant condition and alter the modal behavior of the system. A novel CMA is introduced, analyzing the modal behavior of various system architectures, including single-transmitter, dual-transmitter, strongly coupled magnetic resonance, and near-field plates WPT systems, to provide physical insight into the topic.

Resumen

El actual panorama de las comunicaciones inalámbricas está definido por el despliegue progresivo de sistemas de Transferencia de Energía Inalámbrica (WPT, que han establecido altos estándares de eficiencia, practicidad y seguridad en áreas donde la transmisión de energía mediante cables tradicionales enfrenta desafíos o plantea problemas técnicos peligrosos. El último despliegue de WPT ha tenido lugar en dispositivos médicos implantables (IMD) debido a su capacidad para proporcionar un suministro continuo y fiable de energía sin necesidad de procedimientos invasivos. Si bien la forma más común de entrega de energía inalámbrica en estos dispositivos es el acoplamiento inductivo de baja frecuencia ($f < 10$ MHz), resultados experimentales recientes y modelos han mostrado que la eficiencia óptima de transferencia de energía (PTE) ocurre en la banda UHF (300 MHz – 3 GHz). De hecho, se han explorado varios aspectos de arquitecturas, diseños de hardware e implementaciones de sistemas WPT basados en RF para IMDs. Aunque demostraron una considerable PTE cuando las antenas transmisora (TX) y receptora (Rx) están perfectamente alineadas, la más mínima desalineación provoca una caída significativa en la eficiencia, lo que causa una fuerte disminución en la transferencia de energía. Esta tesis se centra en el diseño y análisis de nuevos sistemas WPT para aplicaciones biomédicas, introduciendo, por primera vez, el uso de metodologías basadas en el Análisis de Modos Característicos (CMA, por sus siglas en inglés), con el objetivo de mejorar la resiliencia y tolerancia de estos sistemas ante desalineaciones.

En los sistemas WPT basados en RF para IMDs, se emplea una guía para el análisis y la fabricación, centrada en las interacciones cercanas a la resonancia para optimizar la transferencia de energía, la eficiencia y el ajuste de impedancia. Sin embargo, las desalineaciones o variaciones ambientales pueden interrumpir estas condiciones ideales, lo que lleva a una pérdida significativa de eficiencia. Estos factores destacan la necesidad de una comprensión física más profunda de las interacciones complejas, particularmente a frecuencias no resonantes. El CMA se vuelve particularmente pertinente en este contexto, ya que proporciona una comprensión física más profunda de cómo las pequeñas desalineaciones o fluctuaciones en el entorno operativo interrumpen la condición resonante óptima y

alteran el comportamiento modal del sistema. Se introduce un novedoso CMA, que analiza el comportamiento modal de diversas arquitecturas de sistemas, incluyendo sistemas de un solo transmisor, doble transmisor, resonancia magnética fuertemente acoplada y sistemas WPT de placas de campo cercano, para proporcionar una visión física sobre este tema.

Résumé

L'environnement technologique actuel des communications sans fil est marqué par l'essor continu des systèmes de transfert d'énergie sans fil (Wireless Power Transfer, WPT), qui s'imposent comme une solution performante, sécurisée et pratique dans des contextes où la transmission filaire présente des limitations fonctionnelles ou des risques techniques. L'intégration récente du WPT dans les dispositifs médicaux implantables (IMD) illustre pleinement ce potentiel, en permettant une alimentation électrique fiable et continue, sans recours à des procédures invasives.

Traditionnellement, le transfert d'énergie dans les IMD repose sur le couplage inductif à basse fréquence ($f < 10$ MHz). Toutefois, des travaux récents, combinant modélisation électromagnétique et validation expérimentale, ont mis en évidence que le rendement de transfert d'énergie (Power Transfer Efficiency, PTE) peut être significativement amélioré dans la bande UHF (300 MHz – 3 GHz). Plusieurs contributions ont ainsi porté sur l'optimisation des architectures, la conception des dispositifs émetteurs/récepteurs et la mise en œuvre de systèmes WPT à base de radiofréquences. Néanmoins, bien que des performances élevées soient atteintes sous condition d'alignement optimal entre les antennes de transmission (Tx) et de réception (Rx), un désalignement même minime provoque une chute marquée du rendement, limitant considérablement l'efficacité du système. Cette thèse propose une approche innovante pour la conception et l'analyse de systèmes WPT adaptés aux contraintes des applications biomédicales. Elle introduit, pour la première fois, l'utilisation de méthodologies fondées sur l'analyse des modes caractéristiques (Characteristic Mode Analysis, CMA) dans le but d'améliorer la robustesse et la tolérance des systèmes WPT aux désalignements mécaniques ou environnementaux.

Dans les systèmes WPT à base de RF pour les IMD, l'optimisation repose généralement sur une exploitation du comportement proche de la résonance afin de maximiser le transfert d'énergie, l'efficacité globale et l'adaptation d'impédance. Toutefois, des écarts par rapport à cette condition idéale, induits par des variations d'alignement ou des perturbations environnementales, peuvent détériorer drastiquement les performances du système. Dans ce contexte, l'approche

CMA offre un cadre analytique pertinent pour comprendre, à un niveau modal, l'impact physique de ces perturbations sur le comportement électromagnétique du système, en particulier dans les régimes non résonants.

La thèse propose une nouvelle application de l'analyse modale pour caractériser le comportement électromagnétique de différentes architectures WPT, incluant les configurations à simple émetteur, à double émetteur, les systèmes à résonance magnétique fortement couplée (CSCMR), ainsi que les dispositifs à plaques de champ proche (Near-Field Plates). L'objectif est de fournir une compréhension physique approfondie de la dynamique modale afin d'identifier, contrôler et exciter sélectivement les modes les plus favorables au transfert d'énergie dans un contexte biomédical contraint.

Resum

El context actual de les comunicacions sense fil està definit pel desplegament progressiu dels sistemes de Transferència d'Energia Sense Fil (WPT), que han establert altes normes d'eficiència, practicitat i seguretat en àrees on la transmissió d'energia mitjançant cables tradicionals s'enfronta a reptes o planteja problemes tècnics perillosos. El darrer desplegament de WPT ha tingut lloc en dispositius mèdics implantables (IMD) a causa de la seva capacitat per proporcionar una alimentació contínua i fiable sense la necessitat de procediments invasius.

Tot i que la forma més comuna de transferència d'energia sense fil en aquests dispositius és el acoblament inductiu de baixa freqüència ($f < 10$ MHz), resultats experimentals recents i models han demostrat que l'eficiència òptima de transferència d'energia (PTE) es produeix en la banda UHF (300 MHz – 3 GHz). De fet, s'han explorat diversos aspectes d'arquitectures, dissenys de maquinari i implementacions dels sistemes WPT basats en RF per a IMD. Encara que van demostrar una PTE considerable quan les antenes emissora (TX) i receptora (Rx) estan perfectament alineades, la més mínima desalineació provoca una caiguda important de l'eficiència, causant una forta disminució en la transferència d'energia. Aquesta tesi es centra en el disseny i l'anàlisi de nous sistemes WPT per a aplicacions biomèdiques, introduint, per primera vegada, l'ús de metodologies basades en l'Anàlisi dels Modes Característics (CMA), amb l'objectiu de millorar la resiliència i la tolerància d'aquests sistemes davant desalineacions.

En els sistemes WPT basats en RF per a IMD, s'utilitza una guia per a l'anàlisi i la fabricació, centrant-se en les interaccions properes a la ressonància per a optimitzar la transferència d'energia, l'eficiència i l'adaptació d'impedància. No obstant això, les desalineacions o variacions ambientals poden interrompre aquestes condicions ideals, provocant una pèrdua significativa d'eficiència. Aquests factors destaquen la necessitat d'una comprensió física més profunda de les interaccions complexes, especialment a freqüències no ressonants. El CMA esdevé especialment pertinent en aquest context, ja que proporciona una comprensió física més profunda de com petits desalineaments o fluctuacions en l'entorn d'exploració interrompen la condició ressonant òptima i alteren el comportament

modal del sistema. Es presenta un nou CMA, que analitza el comportament modal de diverses arquitectures de sistemes, incloent-hi sistemes d'un sol emissor, doble emissor, ressonància magnètica fortament acoblada i sistemes WPT de plaques de camp proper, per a proporcionar una visió física sobre aquest tema.

Table of contents

1	Introduction	1
1.1	Motivation and Context	8
1.2	Objectives	9
1.3	Methodology	10
1.4	Thesis Structure	11
2	Characteristic Modes Analysis (CMA)	13
2.1	Introduction	13
2.2	Mathematical Foundations of the TCM	13
2.2.1	Characteristic Currents	15
2.2.2	Characteristic Fields and Patterns	15
2.2.3	Characteristic Modes Computation	16
2.2.4	Modal Solutions	18
2.3	Physical Interpretation of Modal Analysis	19
2.3.1	Modal Significance	22
2.3.2	Characteristic Angle	24
2.4	Excitation of Characteristic Modes	25
2.5	Review on the CMA Applications for Coupling	27
3	CMA for Misalignment in WPT System	47
3.1	Guidelines For Coupling Numerical Analysis for WPT System Using CMA	47
3.2	Mathematical Formulation of The Coupling of CMA for WPT Systems	50
3.3	CMA Analysis of Mis. in WPT System	52
3.3.1	Lateral Mis. Along The X-axis	53
3.3.2	Lateral Mis. Along The Y-axis	56
3.3.3	Azimuthal Mis.	59
3.3.4	Rotational Mis. of The Excitation Port Placed on The TX Loop	62

TABLE OF CONTENTS

3.3.5	Rotational Mis. of The RX loop	64
3.4	Main observations: CMA of the proposed WPT system	64
4	Validation of CMA for Misalignment in WPT System	69
4.1	Experimental Setup and Validation Methodology	69
4.2	Measurement of The Lateral Mis. Along The X-axis	71
4.3	Measurement of The Lateral Mis. Along The Y-axis	73
4.4	Measurement of The Azimuthal Mis.	74
4.5	Measurement of The Rotational Mis. of The Excitation Port Placed on The Tx Loop	76
4.6	Measurement of The Rotational Mis. of The Rx Loop	77
4.7	Key Findings from Experimental Measurements	79
5	Comparison Between Different WPT Systems	81
5.1	Description of the Proposed WPT Configurations	81
5.1.1	Topologies Based on Loop WPT Systems	82
5.1.2	Topologies Based on Near-Field Plates WPT Systems	83
5.2	Frequency Selection in the Proposed WPT Systems	84
5.3	Comparison Between The Loop Based WPT Systems	85
5.3.1	Comparison Based on CMA Between The Loop Based WPT Systems	85
5.3.2	A Performance Comparison Between The Loop Based WPT Systems	91
5.4	Comparison Between The Near-Field Plates WPT Systems	95
5.4.1	CMA of Near-Field Plates WPT System	96
5.4.2	Comparison Between Conventional and NFP WPT Sys- tems	99
5.4.3	Effect of NFPs Position Between the Tx and Rx on the PTE of the system	102
6	Dual Tx WPT System for Enhanced Lateral Misalignment Tol- erance	105
6.1	Proposed Methodology	105
6.1.1	The Structure of The Proposed Dual Tx MCR-WPT Sys- tem	107
6.2	Decoupling Techniques	109
6.2.1	Decoupling Using Simulation Outcomes	110
6.2.2	Decoupling Using Electromagnetic Theory	111
6.3	Decoupling Tx1 and Tx2: Simulations and Measurements	113
6.3.1	Simulations of The Magnetic NF Plots and The Sparam- eters	114

TABLE OF CONTENTS

6.3.2	Measurements: Optimal Configuration of The Decoupled Tx Loops	115
6.4	Measurements and Validation of the Dual Tx WPT System . .	117
6.4.1	The Conventionnal Wikelson Power Divider	117
6.4.2	Experimental Validation of The System	119
7	Selective Excitation Technique for WPT in Biomedical Devices Using CMA	125
7.1	SCMR and CSCMR Systems	126
7.1.1	Design Features of SCMR Systems	126
7.1.2	Limitations of SCMR Systems	128
7.1.3	CSCMR Systems	129
7.1.4	CSCMR Systems For Biomedical Application	130
7.1.5	Limitations of the Existing Analysis of CSCMR Systems	133
7.2	CMA Analysis of the Tx Unit and the CSCMR System Before Adding Capacitive Loading	134
7.2.1	CMA of The Tx	134
7.2.2	CMA of The CSCMR System	135
7.3	Discrimination of The Unfunctionnal Modes Using Selective Excitation Technique	139
7.3.1	Selective Excitation Technique Using CMA	140
7.4	Comparison between SCMR and CSCMR Systems based on CMA	141
7.5	The Final Performance of the CSCMR system	144
8	Conclusion	147
8.1	Further work	151
A	Technical Results	153
A.1	JCR Indexed journals	153
A.2	International Conferences	153
A.3	National Conferences	155
A.4	Stays In Other Institutions	155
A.5	Fellowships	155
A.6	Awards	155
A.7	International Seminars	155
A.8	Professional Achievements	156
	References	157

TABLE OF CONTENTS

Chapter 1

Introduction

In the last decade, the rapid evolution of biomedical technologies has spurred significant advancements in the design and implementation of medical devices, enabling continuous monitoring, targeted treatment, and improved quality of life for patients [1]. The surge has led to the development of numerous complex diagnostic tools and monitoring devices, such as implantable medical devices (IMDs) and wearable medical devices (WMDs) [2].

Recent studies and industry projections for the global medical implants market indicate a significant growth in demand for various types of implants in different medical specialties, including orthopedic spinal [3], [4], neurostimulator [5], cardiovascular [6], and ophthalmic [7] implants. However, the development of healthcare-embedded systems presents clear challenges [8]. First, predicting or detecting the lead connection of an on-board battery after implantation is difficult. Moreover, regular changes of implanted batteries to prolong the lifespan of the system present potential risks to patients [9]. Among the most notable power sources previously used for IMDs are electrochemical sources, such as lithium-ion batteries [10]. These batteries consume a substantial portion of the internal space within the device, increase local temperatures, and contribute to the overall bulk of WIMDs, which is in contrast to the ongoing trend of miniaturization within modern healthcare systems. As a prominent solution to these issues, Wireless Power Transfer (WPT) technology has been widely proposed and researched over the past decade [8–10].

Near Field WPT for Biomedical Applications

WPT offers a promising solution by ensuring the rechargeability of implantable devices without the need for bulky batteries; Hence, allowing for reasonable device sizes. In addition, it eliminates the need for battery replacement surgeries,

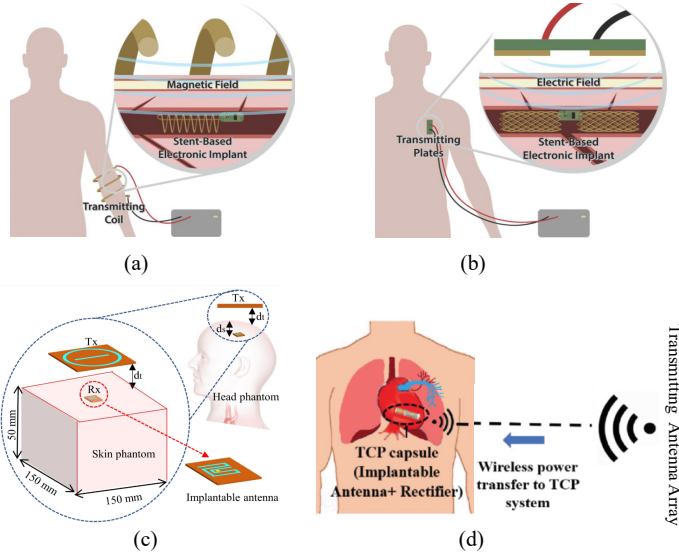


Figure 1.1: EM radiation based WPT for IMDS: (a) Inductive NF [11], (b) Capacitive NF [11], (c) Mid-field [12], (d) Far-field [13].

significantly reducing associated risks. WPT is a technology that is being explored as a potential solution for powering IMDs through Electromagnetic (EM) radiations [8]. WPT systems are broadly categorized into Near-Field (NF) magnetic [14–16], NF capacitive [11, 17, 18], mid-field, and Far-Field (FF) [19–21] radiation coupling (see Fig. 1.1). Their main distinctions are based on the transmission distance between the transmitter (Tx) and the receiver (Rx), as well as the operating frequency of the IMD. Yet, due to the complexity of human tissue, radiation coupling can lead to time- and frequency-selective fading, which presents challenges for both antenna and system design.

Indeed, the human body exhibits significant absorption of EM radiation, particularly in the frequency range of 100 MHz to 10 GHz, which results in substantial power losses. Consequently, to compensate for these losses, higher power levels are often required, which increase the specific absorption rate (SAR) values [22]. Given the stringent safety regulations in medical applications, the power received from radiation-based coupling methods must be kept below 1 mW to stay within acceptable safety limits. Taking into consideration these challenges, NF magnetic coupling blooms as the solution to fulfill the requirements for IMDs:

-
- A stable and uniform magnetic flux, resulting from the close proximity of the transmitting (Tx) and receiving (Rx) coils, which plays a crucial role in achieving high Power Transfer Efficiency (PTE) [8]
 - Similar behavior to free space is observed due to the human body's non-magnetic properties ($\mu_r = 1$), supporting stable and efficient power transfer [22]
 - Lower SAR with reduced energy absorption in lossy dielectric mediums, including water, underground environments, and biological tissues [23,24]
 - A relatively short distance between the Tx and Rx coils, as the power rapidly attenuates with increased distance, necessitating tight alignment tolerances

Despite its advantages, NF coupling presents limitations, including the rapid attenuation of transmitted power with increasing distance and the necessity for precise alignment between the Tx and Rx. In particular, multiple research works have advanced the design of NF WPT for IMDs at frequencies such as 5–10 MHz [25], 13.56 MHz [26], 39.86 MHz [27], 403 MHz [28], 430 MHz [29], and 434 MHz [30]. Due to sensitivity, misalignment, small coupling coefficients, and a low quality factor (Q) of the coils, these systems typically exhibit a low PTE of approximately $\leq 47\%$ [31]. On the other hand, FF WPT for IMDs, which use rectennas to convert RF energy into DC power, have been investigated at frequencies like 1.96 GHz [32], 2.45 GHz [33], 3.7 GHz [34], and 0.915/2.4/5.8 GHz [35]. FF systems have shown less sensitivity to misalignment over longer distances; however, they suffer from a much lower PTE of around $\leq 1\%$, compared to NF systems [36]. As a result, NF WPT is commonly utilized to power IMDs, with inductive coupling being the most prevalent method due to its high overall transmission efficiency.

Antenna Design

In 1899, Nikola Tesla conducted pioneering experiments in WPT, devoting his efforts to developing schemes for transferring power wirelessly using high-power electromagnetic waves [37]. Despite his groundbreaking efforts, the results were marked by limited success and reproducibility, as typical embodiments (e.g., Tesla coils) generated undesirably large electric fields.

In the past decade, interest in wireless power has reemerged, driven by the increasing use of autonomous electronic devices such as laptops, smartphones, robots, etc. [38, 39]. Although radiative transfer via lasers or highly directional antennas is perfectly suitable for transferring information, it poses several difficulties for WPT. The PTE is very low if the radiation is omnidirectional, and unidirectional radiation requires an uninterrupted line of sight and

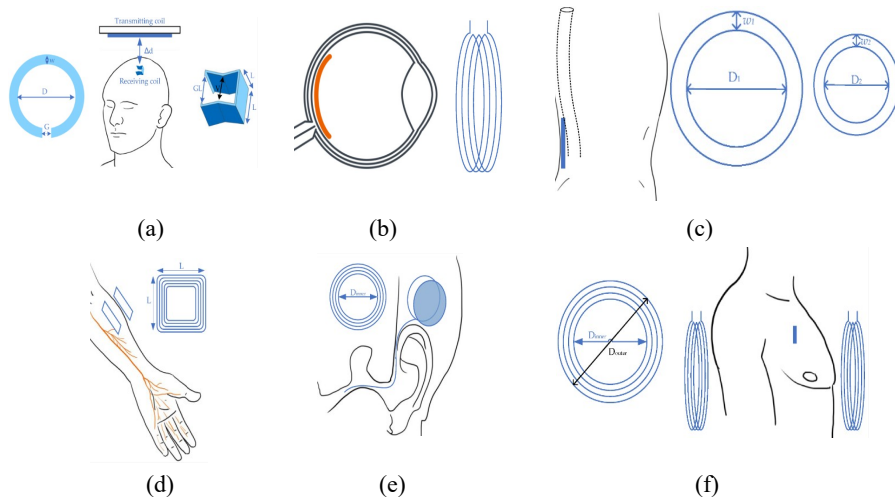


Figure 1.2: Examples of coil-based WPT systems for biomedical applications [8]: (a) Deep brain stimulator, (b) Retinal neurostimulator, (c) Spinal for a Cochlear implant system, (f) Heart pacemaker.

sophisticated tracking mechanisms, particularly in scenarios involving mobile objects [40].

In 2007, an MIT research team developed an innovative system that utilizes strongly coupled magnetic resonances, significantly extending the magnetic induction power transfer range [41]. The setup included two identical single-loop copper coils, positioned in the Tx and Rx units, with a radius of 25 cm. The Tx coil generated a magnetic field at a resonant frequency of 9.9 MHz, enabling energy transfer up to eight times the coil radius while maintaining 40% efficiency over distances greater than two meters. The pioneering concept of "WiTricity" marks a significant breakthrough in WPT technology, utilizing strongly coupled magnetic resonance and loop coil architectures to enhance PTE and range. Unlike conventional methods such as simple induction, microwaves, or air-ionization, this technology relies on strong coupling between electromagnetic resonant entities for efficient energy transmission. Both Tx and Rx, equipped with magnetic loop antennas, are precisely tuned to the same frequency. The proposed system primarily uses magnetic fields for coupling, with electric fields confined within device capacitors, ensuring greater safety compared to electric-field-based resonant energy transfer mechanisms [42].

Since then, research has continued to explore magnetic coupling through loop antennas. In 2015, [43] provided a comprehensive overview of wireless power transmission, while [44] examined its typologies and potential to re-

duce transmission losses. Subsequent studies have addressed key challenges, including efficiency limitations 2019 [45], multiresonator systems, and lateral misalignment in multitransmitter configurations [46]. More recent advances have focused on inductive loop coupling, with extensive research dedicated to developing prototypes of resonant magnetic coupling, particularly for biomedical applications [8], [47]. In this context, IMDs and WMDs have employed Inductive Power Transfer (IPT) and Magnetic Resonant Coupling (MRC) techniques for wireless power transfer, with both approaches relying on coil-based systems (see Fig. 1.2). Therefore, the computation and analysis of magnetic NF coupling between circular wire coils remains a critical research topic, given its importance in various technological and scientific fields [48].

Misalignment Sensitivity of WPT

Although inductive power transfer (IPT) and magnetic resonance coupling (MRC) systems are the most widely used methods for biomedical WPT, their loop-based structures are sensitive to misalignment [49–51]. In particular, PTE is significantly affected by variations in magnetic coupling between the Tx and Rx coils [52]. These variations occur when the Rx coil is not perfectly aligned with the Tx coil or when an unexpected misalignment occurs. The misalignment scenarios between the Tx-Rx coils are broadly classified as lateral [53], angular [54], and longitudinal [55]. Lateral misalignment refers to the displacement of the coplanar Rx coil relative to the Tx coil, whereas angular misalignment refers to the rotation of the Rx coil from its intended orientation. The longitudinal misalignment concerns the variation in the transfer distance between the Tx-Rx coils. Among these, lateral misalignment is the most prominent in many WPT applications [56].

Several studies have put efforts to mitigate the misalignment problem in wireless biomedical electric-driven devices, where misalignment issues are even more critical because of the complex and dynamic nature of the human body [57] (see Fig. 1.3). Traditional solutions, such as sensing coils combined with mechanically movable robots, have been explored to correct misalignment in WPT systems; however, their high maintenance demands, susceptibility to damage, and lack of precision make them unsuitable for biomedical applications [58]. Similarly, hybrid compensation networks, despite improving PTE in certain scenarios, introduce excessive complexity, increase power losses, and pose safety concerns due to potential tissue heating, making them impractical for biomedical use [59]. While metamaterials offer an alternative approach to enhancing WPT performance, their inherently bulky structure limits their feasibility for biomedical implants, where miniaturization is crucial [60]. In contrast, more efficient approaches, such as the deployment of multi-coil inductive links [61] and the incorporation of ferrite cores [62], have demonstrated

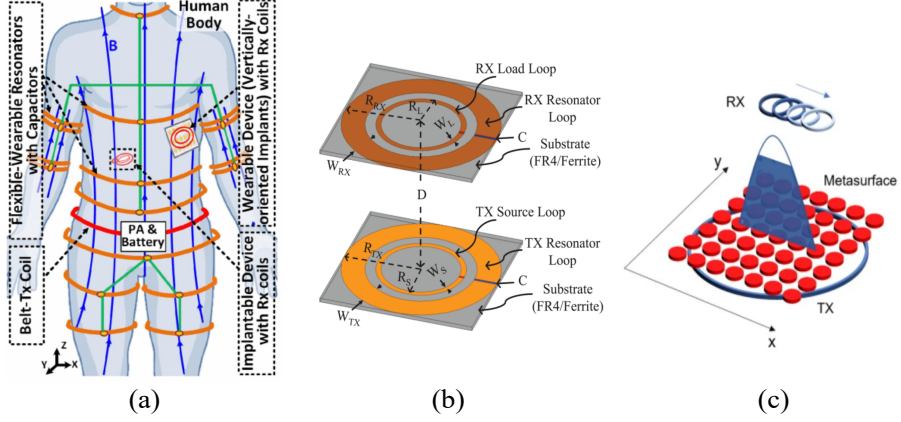


Figure 1.3: Misalignment Solutions in WPT for Biomedical Systems: (a) Multi-coil inductive links [61], (b) Incorporation of ferrite cores [62], (c) Positioning of a metasurface between the Tx and Rx loops [60].

significant advantages in addressing misalignment challenges. However, achieving precise alignment between the Tx and Rx loops remains crucial for proper performance of the system.

Within this framework, numerous studies have been carried out to analyze and develop models for NF magnetic coupling in IPT and MRC systems. Their main objective consists of enhancing the PTE of WPT systems by understanding the influence of critical parameters, such as antenna size, separation distance, and misalignment, on the effectiveness of the system. The proposed techniques include circuit-based analysis [63] and the use of mathematical equations in analytical modeling [56]. However, to ensure their accuracy in addressing the specific challenges of WPT systems, these coupling analysis methods aim to align with experimental measurements. Therefore, hybrid modeling, which combines experimental data with coupling analysis, offers greater precision in assessing the efficiency and effectiveness of WPT systems in practical applications. This PhD will provide characteristic modes analysis to elucidate the physical phenomena underlying various misalignment scenarios, rigorously validated through experimental measurements.

Characteristic Modes Analysis

Characteristic Modes Analysis (CMA) is employed throughout the thesis to harness the physical insights obtained from investigating the inherent resonances of the analyzed structures. This methodology not only simplifies the design process but also provides a clear visual framework for understanding the

radiation mechanisms of antennas throughout their operating bands. Following this overview, Chapter 2 offers a comprehensive exploration of the Theory of Characteristic Modes (TCM).

Based on the method of moments and employing Rao Wilton Glisson basis functions, the TCM was initially proposed and formulated by Garbacz [64] and later refined by Harrington and Mautz in the seventies [65, 66]. Initially utilized in antenna geometry synthesis and scattering, TCM remained a niche topic and has largely been overlooked by the antenna community. However, its potential for simplifying antenna design was revitalized in 2007 (see Fig. 1.4(a)) when the Antennas and Propagation Lab (APL) at the Universitat Politècnica de València published an article [67] introducing the theory for hot topic applications such as the excitation of mobile phone chassis modes.

In Fig. 1.4, the cumulative count of IEEE publications based on CMA is presented, showing a significant increase since 2007, surpassing the count recorded in the years following its initial discovery. This exponential growth highlights the increasing adoption of CMA in antenna design during the last decade, demonstrating its usefulness in providing physical insight into radiating performance and offering a systematic approach to developing antennas with specific radiation characteristics. The deployment of modal solutions into electromagnetic software has further contributed to this rise, reinforcing CMA's role in advancing antenna design methodologies.

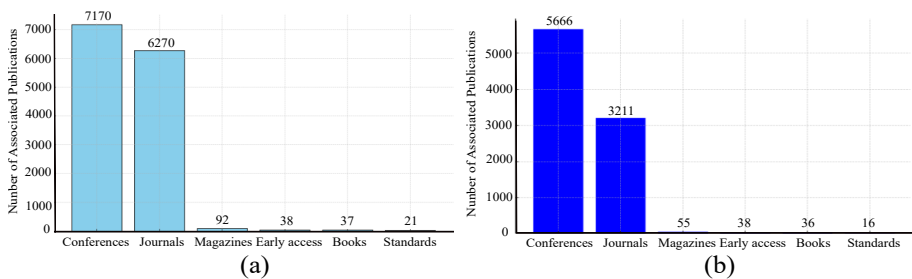


Figure 1.4: Number of publications related to characteristic modes published in IEEE: (a) Since 2007, (b) Since their formulation in 1971.

From a technical perspective, designing and modeling antennas with arbitrary geometries necessitates the use of electromagnetic simulation software due to the absence of analytical solutions. These antenna models must be discretized and solved using numerical methods, where factors such as operating frequency, complexity, and desired accuracy influence the required mesh resolution; hence, finer meshing increases simulation time.

Notably, the integration of antennas into platforms with diverse geometries poses a significant challenge for designers, as multiple operating principles in-

interact within the same resonating structure. This complexity results in an increased number of simulations, given the uncertainty regarding the optimal placement and excitation method. The TCM is based on solving an eigenvalue problem for a given conductive or dielectric body, yielding a set of real current modes known as Characteristic Modes (CM) or eigenmodes. CM offer a solution by providing critical insights into the natural resonances of any platform, as well as the appropriate location and type of feeding required for resonance tuning and excitation. Consequently, A key advantage of TCM over traditional design methods is its ability to provide a clear physical understanding of the radiation phenomena that contribute to antenna performance. This insight enables a more efficient design and optimization process while reducing computational demands.

CMs allow the decomposition of the total current on the surface of a conducting body into a set of orthogonal functions which can be numerically computed for any arbitrary structure. These modes offer valuable information for antenna design by providing a physical interpretation of radiation performance. In particular, CMs are calculated independently of any excitation, relying solely on the size and shape of the analyzed body. This excitation-independent nature is particularly useful for initial analyzing surface currents, facilitating the optimal selection of excitation type and location to achieve the desired radiation characteristics.

The design process of an antenna using CMA consists of two main steps. First, the antenna's geometry is optimized to align the modal resonance with the desired frequency. In the second step, the feeding mechanism is refined to effectively excite the targeted modes. The number of modes that can be excited provides an estimation of the achievable bandwidth. In summary, CMA offer a structured approach to antenna design, providing a controlled methodology that enhances understanding by offering a graphical representation of the antenna's operating principles.

1.1 Motivation and Context

This Ph.D. thesis was developed within the framework of a cotutelle agreement between the Universitat Politècnica de València (UPV - València, Spain) and the Université du Québec en Outaouais (UQO - Gatineau, Canada) and was conducted at the Antennas and Propagation Lab (APL) of UPV. Additionally, it was supported by the Mobility Grant for Ph.D. Students with CoTutelle from the Universitat Politècnica de València.

In addition, this research initiative was launched at the Antennas and Propagation Lab (APL), which has a longstanding tradition in designing and studying antennas using CMA, having published numerous high-impact journals that

have attracted significant attention. As pioneers in applying CMA to modern antenna design [67], APL reintroduced the Theory of Characteristic Modes (TCM) to the antenna community. In recent years, TCM has been extended to various applications, including small antennas [68], vehicle-mounted antennas [69], MIMO antennas [70], and wideband antennas [71]. This extensive application of TCM, coupled with the demand for efficient solutions in wireless biomedical devices, underpins the decision to dedicate this thesis to the analysis and design of biomedical WPT systems using CMA.

Furthermore, the APL group is actively involved in national and international projects focused on the design and integration of antennas for IoT, LTE/5G, and satellite communications applications. This project served as a valuable introduction to the limitations of WPT systems and the key challenges associated with their integration into biomedical applications. Additionally, as part of this thesis, an internship was conducted at the Institut National de la Recherche Scientifique (INRS) in Montreal, Canada, providing an opportunity to collaborate with highly experienced scientists. Given these factors, this thesis begins with an analysis of traditional WPT systems using CMA and concludes with the proposal of novel approaches to optimize WPT systems for biomedical applications.

The expertise gained throughout this thesis, encompassing fundamental electromagnetic theory, as well as analysis, design, and measurement of antennas facilitated the acquisition of multiple university lecturer positions in Canada, teaching courses related to these specialized fields.

1.2 Objectives

This thesis pursues two global objectives. The first is to utilize CMA to provide deeper insight into the near-field magnetic coupling analysis between loop antennas, as the next generation of IMDs is expected to incorporate closed-loop systems integrating sensors, actuators, and algorithms to facilitate their interaction [72]. This is particularly relevant given the complications associated with wires commonly used in deep brain stimulation devices, pacemakers, and implantable cardioverter-defibrillators. These wires can lead to infections or introduce noise in recordings due to movement artifacts, highlighting the need for alternative WPT solutions to enhance the reliability and safety of biomedical implants.

The second objective is to analyze both existing and innovative WPT biomedical systems, focusing on their behavior around resonance to achieve optimal performance. Traditionally, the efficiency of these antenna systems is assessed solely through S_{21} parameters, without a deeper physical interpretation. In this thesis, a CMA based analysis will be conducted to provide

CHAPTER 1. INTRODUCTION

a comprehensive explanation of optimal magnetic field intensity across various proposed systems, offering deeper insights into their efficiency and design optimization.

The following specific objectives have been defined:

1. Develop a comprehensive reference for future research on CMA and WPT systems for IMDs, focusing on enhancing NF magnetic coupling between coils, leveraging the deeper penetration and increased safety of magnetic fields over electric fields for improved WPT biomedical devices.
2. Conduct a generalized modal coupling framework based on CMA and Coupled Mode Theory (CMT) to enhance antenna performance and extend their application across diverse wireless communication systems, including IoT devices employing loop and coil antennas.
3. Analyze the designed antennas by evaluating the effects of various configurations, sizes, and frequency bands on WPT system performance, investigating electromagnetic interactions through parametric evaluations, including separation distance, overlap, misalignments, and angular sensitivities using the TCM, for improved PTE in biomedical applications.
4. Optimize the antenna system's resonance behavior for peak performance by tuning specific CMs to configurate the coupling at desired frequencies, with validation through measurements conducted in a clean laboratory at UPV.
5. Analyze with CMA the impact of different transmitters configurations, proposing new WPT link designs and configurations to enhance magnetic coupling and the PTE while minimizing efficiency losses due to misalignment.
6. Develop a novel selective excitation technique based on CMA to enhance PTE in biomedical applications.

1.3 Methodology

The **first phase** of the thesis includes a comprehensive bibliographic review, which will be conducted extensively during the documentation and state-of-the-art phase and will become more focused as the research progresses. The review of scientific literature will primarily rely on indexed databases such as Web of Science (WoS), with a particular emphasis on IEEE Xplore, which specializes in antennas and microwaves. To complement this continuous information intake, active participation in national and international conferences related to the research topic is planned. Additionally, specialized courses relevant to the study

were delivered by experienced professors at the Escuela Técnica Superior de Ingeniería de Telecomunicación (UPV) and the European School of Antennas (ESoA).

The **second phase** of the thesis focuses on the analysis of WPT systems using CMA in free space. This phase involves examining prevalent WPT systems commonly employed in both industry and research, utilizing CMA to gain deeper insights into their performance. Various parametric investigations will be conducted, including misalignment scenarios resulting from typical device or user movements, to thoroughly assess the impact on modal coupling. Additionally, the study will involve post-processing the interactions and modal coupling effects between multiple radiating structures using the Coupled Characteristic Modes Theory (CCMT). Special attention will be given to analyze the influence of antenna size, particularly the effect of increasing loop width on coupling efficiency.

The **third phase** of the thesis is based on enhancing Power Transfer Efficiency (PTE) and evaluating the magnetic field distribution through a comparative analysis of various configurations, including both proposed designs and those documented in existing literature. This phase involves a detailed comparison between manufactured Strongly Coupled Magnetic Resonance (SCMR) and Conventional SCMR (CSCMR) systems, utilizing CMA to assess their efficiency. By leveraging CMA, this analysis aims to provide deeper insight into the electromagnetic mechanisms responsible for their superior performance and broad applicability across diverse research fields.

The **fourth phase** is dedicated to validating the findings obtained through CMA via practical measurements. This phase involves experimental verification of the theoretical analyses conducted throughout the study. Additionally, a final optimized design will be presented, integrating the insights gained from previous phases to propose an innovative RF solution for WPT applications, enhancing efficiency and applicability in real-world scenarios. The Antennas and Propagation Laboratory (APL) of the Institute of Telecommunications and Multimedia Applications (iTEAM) has provided the equipment to perform this process.

Throughout the thesis, the most relevant results disseminated to the scientific community through articles in journals and congresses related to the research topic, underscoring their novelty and impact in the field.

1.4 Thesis Structure

The thesis is divided as follows:

CHAPTER 1. INTRODUCTION

Chapter 1 introduces the core topics of the thesis, along with a detailed overview of its main objectives, methodology, motivation, and contextual framework.

Chapter 2 details the mathematical formulation of the Theory of Characteristic Modes and enumerates the key parameters employed in CMA. Specific parameters are illustrated using a loop antenna, which serves as the primary component in both IPT and MRC WPT systems, thereby offering additional physical insight into WPT.

Chapter 3 conducts a novel CMA-based methodology for a comprehensive investigation of NF magnetic coupling in an MCR-WPT system through the lens of TCM, governed by Coupled Mode Theory (CMT). This chapter explores various misalignment scenarios, revealing significant modal interactions responsible for coupling and frequency shifts.

Chapter 4 sets the groundwork for comparing simulation and measurement results of CMA for the various misalignment scenarios proposed in the previous chapter. This comprehensive comparison validates the effectiveness of CMA in providing critical insights into the performance of WPT systems, and its relevance for practical applications.

Chapter 5 leverages the effectiveness of CMA, as established in the preceding chapters, to enhance PTE through a comparative analysis of various configurations for biomedical applications. This study examines both innovative designs and established configurations from the literature, including dual Tx topologies, and NF plates.

Chapter 6 proposes an axial misalignment-tolerant solution for biomedical WPT systems by deploying a dual Tx configuration that employs a conventional Wilkinson Power Divider (WPD). The novelty of this approach lies in its elimination of the need for an additional power source, utilizing near-field (NF) focusing concepts.

Chapter 7 Chapter 3 explores the design and analysis of SCMR and CSCMR systems, emphasizing their physical interpretation through the TCM. The optimized performance of the CSCMR system is demonstrated by selectively exciting specific modes that enhance efficiency. This chapter also investigates selective excitation techniques to analyze and improve NF magnetic coupling.

Chapter 8 outlines the principal conclusions of the thesis.

Chapter 2

Characteristic Modes Analysis (CMA)

2.1 Introduction

Characteristic Modes Analysis (CMA) is a powerful tool for examining and visualizing the radiation performance of metallic structures. This chapter introduces the mathematical framework of the Theory of Characteristic Modes (TCM), which underscores the application of CMA throughout this thesis. In addition, a review of key CMA applications in antenna coupling in recent decades is provided, offering a comprehensive state-of-the-art perspective that lays the foundation for the research presented in the following chapters.

2.2 Mathematical Foundations of the TCM

By diagonalizing the scattering matrix, Garbacz introduced Characteristic Modes (CMs) [64], demonstrating that the resulting modal currents are real and that the tangential modal electric field maintains a constant phase over the body's surface. Subsequently, Harrington [65] introduced a refined formulation by diagonalizing the operator that relates the current to the tangential electric field on a body. He proposed a weighted eigenvalue equation to obtain the same modes introduced by Garbacz in a more accessible manner.

Figure 2.1 features a typical scenario in the computation of characteristic modes with an arbitrarily shaped perfect electric conductor (PEC) defined by the surface S and an incident electric field E^i . The formulation of the Theory of Characteristic Modes for conducting bodies originates from the operator

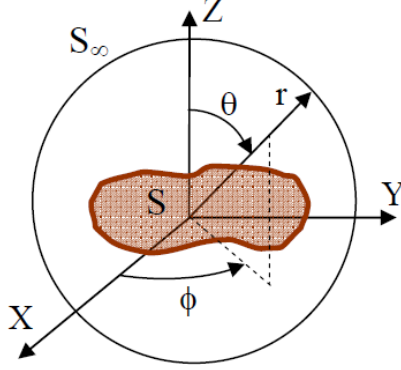


Figure 2.1: Typical Scenario for the computation of characteristic modes, and system coordinates.

equation (2.1), which relates the current J on the surface S and the tangential component of an electric incident field E^i .

$$[L(J) - E^i]_{tan} = 0 \quad (2.1)$$

where the subscript *tan* denotes tangential components on S . The linear operator L is defined as follows:

$$L(J) = jwA(J) + \nabla\Phi(J) \quad (2.2)$$

$$A(J) = \mu \iint_S J(r')\psi(r, r')ds' \quad (2.3)$$

$$\Phi(J) = -\frac{1}{jw\epsilon} \iint_S \nabla' J(r')\psi(r, r')ds' \quad (2.4)$$

$$\psi(r, r') = \frac{e^{-jk|r-r'|}}{4\pi|r-r'|} \quad (2.5)$$

where r' represents a source point, r a field point, k the wavenumber, ϵ the permittivity, and μ the permeability of the free space.

The term $-L(J)$ can be physically interpreted as the electric intensity at any point in the space produced by the current J on the surface S . This implies that the operator L in 2.1 has impedance dimensions and can thus be redefined using the following notation:

$$Z(J) = [L(J)]_{tan} \quad (2.6)$$

where the Z operator is complex and defined in [65] as:

$$Z(J) = R(J) + jX(J) \quad (2.7)$$

2.2.1 Characteristic Currents

Following the approach developed in [65], characteristic current modes emerge as the eigenfunctions of a weighted eigenvalue equation:

$$X(\vec{J}_n) = \lambda_n R(\vec{J}_n) \quad (2.8)$$

where X and R are, respectively, the imaginary and real parts of the impedance operator Z , λ_n stand for the eigenvalues, and \vec{J}_n present the eigenfunctions (also called eigencurrents or characteristic currents). Based on the reciprocity theorem, the operator Z is a linear symmetric operator; hence, its hermitian parts (X and R) will be real symmetric operators. From this, λ_n and \vec{J}_n must be real and satisfy orthogonality relationships.

According to [65], upon the normalization of each radiating eigencurrent ($\langle J_n^*, RJ_n \rangle = 1$), they fulfill the orthogonality relationships, which can be summarized as:

$$\langle J_m, RJ_n \rangle = \langle J_m^*, RJ_n \rangle = \delta_{mn} \quad (2.9)$$

$$\langle J_m, XJ_n \rangle = \langle J_m^*, XJ_n \rangle = \lambda_n \delta_{mn} \quad (2.10)$$

$$\langle J_m, ZJ_n \rangle = \langle J_m^*, ZJ_n \rangle = (1 + j\lambda_n) \delta_{mn} \quad (2.11)$$

where δ_{mn} is the Kronecker delta (1 if $m = n$, and 0 if $m \neq n$).

2.2.2 Characteristic Fields and Patterns

The eigencurrents J_n produce electric E_n and magnetic H_n fields known as eigenfields or characteristic fields. By applying the complex Poynting theorem, the orthogonality relationship for the characteristic fields is derived from that of the characteristic currents:

$$\begin{aligned} P(J_m, J_n) &= \langle J_m^*, ZJ_n \rangle = \langle J_m^*, RJ_n \rangle + j \langle J_m^*, XJ_n \rangle \\ &= \iint_{S'} \vec{E}_n \times \vec{H}_n^* ds + jw \iiint_{\tau'} (\mu \vec{H}_m \cdot \vec{H}_n^* - \varepsilon \vec{E}_m \cdot \vec{E}_n^*) d\tau \quad (2.12) \\ &= (1 + j\lambda_n) \delta_{mn} \end{aligned}$$

CHAPTER 2. CHARACTERISTIC MODES ANALYSIS (CMA)

Drawing analogy with Fig.2.1, if the surface S is of finite extent and S' is chosen as the radiation sphere S_∞ , it can be demonstrated:

$$\frac{1}{\eta} \oint\!\!\!\oint_{S_\infty} \vec{E}_n \cdot \vec{E}_m^* ds = \delta_{mn} \quad (2.13)$$

Then, characteristic electric fields form an orthonormal set, in the Hilbert space of all square-integrable vector functions on S_∞ . The magnetic field can also be expressed using 2.13:

$$\eta \oint\!\!\!\oint_{S_\infty} \vec{H}_n \cdot \vec{H}_m^* ds = \delta_{mn} \quad (2.14)$$

Finally, the orthogonality relationship including both the electric and magnetic field could be expressed as:

$$w \iiint_{\tau'} (\mu \vec{H}_n \cdot \vec{H}_m^* - \varepsilon \vec{E}_n \cdot \vec{E}_m^*) d\tau = \lambda_n \delta_{mn} \quad (2.15)$$

where the integration extends over all space. In particular, for $m = n$, 2.15 states that λ_n is $2w$ times the total stored magnetic energy minus the total stored electric energy. This result assumes normalization ($\langle J_n^*, RJ_n \rangle = 1$).

2.2.3 Characteristic Modes Computation

The Theory of Characteristic Modes (TCM) for conducting bodies was initially introduced by Garbacz [64] and later refined by Harrington and Mautz [65]. Early computational approaches, such as Turpin's method [73], were limited to wire objects or bodies with simple symmetries, producing only a few modes due to computational constraints. Later, Harrington pioneered the use of a numerical method called Method of Moments (MoM) to address these difficulties [66], allowing the calculation of characteristic modes for arbitrarily shaped conductors.

For the calculation of Characteristic Modes, the generalized impedance matrix is obtained using the Method of Moments (MoM) with Rao-Wilton-Glisson (RWG) edge elements. In practice, equation (2.8) is approximated by the Galerkin formulation, resulting in a matrix eigenvalue equation:

$$[X]\vec{J}_n = \lambda_n [R]\vec{J}_n \quad (2.16)$$

where $[R]$ and $[X]$ are, respectively, the real and imaginary components of the generalized impedance matrix defined as $[Z] = [R + jX]$.

The Maxwell equations with the boundary conditions are combined to compute the generalized impedance matrix to derive the Electric Field Integral

2.2 Mathematical Foundations of the TCM

Equation (EFIE). This later provides the surface currents induced by an incident electric field on a conducting body surface S . An alternative formulation frequently employed in computational electromagnetics is the Mixed Potential Integral Equation (MPIE), which represents a specialized form of the EFIE. The EFIE establishes a relationship between surface currents, the vector potential, and the gradient of the scalar potential. To efficiently model unknown currents on planar structures, Rao-Wilton-Glisson (RWG) edge elements are commonly used as basis functions, offering a convenient approach that aligns with EFIE formulations and facilitates the discretization of triangular patch structures.

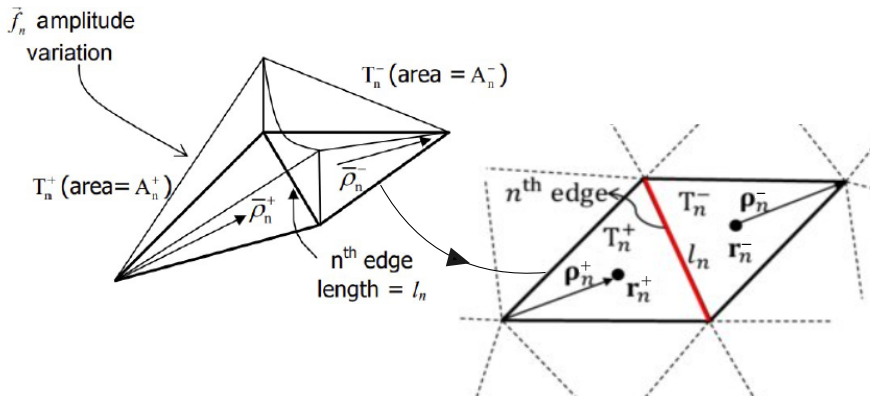


Figure 2.2: RWG basis function description and its divergence for a given common edge (red) of two triangular elements.

The surface S of a conducting object can be effectively approximated using an appropriate triangular patch mesh. Each pair of triangles sharing a common edge defines an RWG edge element with a length l_n , illustrated by the red edge in Fig. 2.2. The basis function is associated with an edge and two adjacent triangular elements, denoted as T_n^+ and T_n^- with corresponding areas A_n^+ and A_n^- . As illustrated in Fig. 2.2, the plus or minus sign designation of the triangles follows the reference current direction along the n^{th} edge, which is assumed to flow from T_n^+ to T_n^- . Therefore, a position vector $\vec{\rho}_n^+$ is defined to represent the points within T_n^+ , originating from the free (non-contiguous) corner of the edge. Similarly, the vector $\vec{\rho}_n^-$ is also defined for T_n^- , but it is oriented towards its respective free corner. The RWG vector basis function associated with the n^{th} edge is defined as:

$$f_n(\vec{r}) = \begin{cases} \frac{l_n}{2A_n^+} \rho_n^+ & , \vec{r} \text{ in } T_n^+ \\ \frac{l_n}{2A_n^-} \rho_n^- & , \vec{r} \text{ in } T_n^- \\ 0 & , \text{ outside} \end{cases}$$

Therefore, the total current on the surface S can be approximated by the superposition of contributions from all interior edge elements:

$$\vec{J}_n = \sum_{n=1}^N I_n \vec{f}_n \quad (2.17)$$

where N is the number of total interior edges and I_n is the unknown coefficient, calculated with the classical moment equations.

2.2.4 Modal Solutions

The orthogonal properties of characteristic modes on the body's surface enables the decomposition of the total current J as a superposition of independent currents, each corresponding to a distinct characteristic mode. Characteristic modes thus serve as a basis for expanding the unknown total current J on a conducting body. The contribution of each mode J_n to the total current J is governed by the coefficient α_n and their computation is given by:

$$J = \sum_n \alpha_n J_n \quad (2.18)$$

The expression of the total current can be formulated into various forms by substituting 2.19 into 2.1, by using the modes orthogonality properties:

$$J = \sum_n \frac{\langle J_n, E^i \rangle}{1 + j\lambda_n} J_n = \sum_n \frac{V_n^i}{1 + j\lambda_n} J_n \quad (2.19)$$

where V_n^i is the modal excitation coefficient, which indicates the excitation of a specific mode based on the feeding configuration.

The equation 2.19 illustrates the dependence of the total current J and each eigenvalue λ_n of the n^{th} mode. Eigenvalues analysis is pivotal in the Theory of Characteristic Modes, as it offers insights into the resonance frequency and the radiation behavior and performance of the associated modes.

To provide a clear physical interpretation of characteristic modes in the context of this Ph.D. research, which focuses on the analysis of wireless biomedical systems, a metallic circular wire (see Fig.2.3) with a diameter (D) of 23.18 cm ($\simeq 0.3\lambda$) using a metal wire with a thickness (w) of 0.14 cm has been analyzed by computing the first nine characteristic modes. A loop with a single term is considered because, from an electromagnetic perspective, as the number of

2.3 Physical Interpretation of Modal Analysis

turns in a coil increases, the interaction between each turn and its neighboring turns creates a multifaceted coupling phenomenon that results in an increased count of higher order modes. This modal behavior encompasses intricate resonant frequencies and field distributions. Consequently, the analysis of these coupling modes becomes increasingly complex and involved.

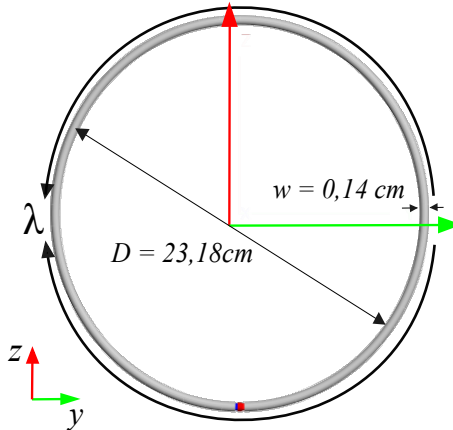


Figure 2.3: Analyzed loop antenna with a diameter (D) of 23.18 cm ($\simeq 0.3\lambda$) using a metal wire with a thickness (w) of 0.14 cm.

The following section reviews the parameters derived from the eigenvalues, offering physical insight into the radiation performance of the analyzed modes.

2.3 Physical Interpretation of Modal Analysis

The corresponding modes J_n of the proposed loop are depicted in Fig.2.4, and the different current distributions of the natural resonances of a single-loop antenna can be observed. Accurate analysis and interpretation of these eigenvalues is crucial for understanding the frequency-dependent radiation performance of the associated modes.

The relation between eigenvalues and the radiation power of modes is expressed in equation 2.12. It can be deduced that while the radiated power is normalized to the unit, the reactive power depends on the magnitude of the eigenvalues. Consequently, the eigenvalues convey essential information about the resonance of each mode. The eigenvalues λ_n , defined in 2.8, span from $-\infty$ to $+\infty$ and can be grouped into three categories of values: negative, null, or positive. In particular, the sign of the eigenvalues defines whether the mode contributes to storing magnetic energy ($\lambda_n > 0$ inductive behavior) or whether

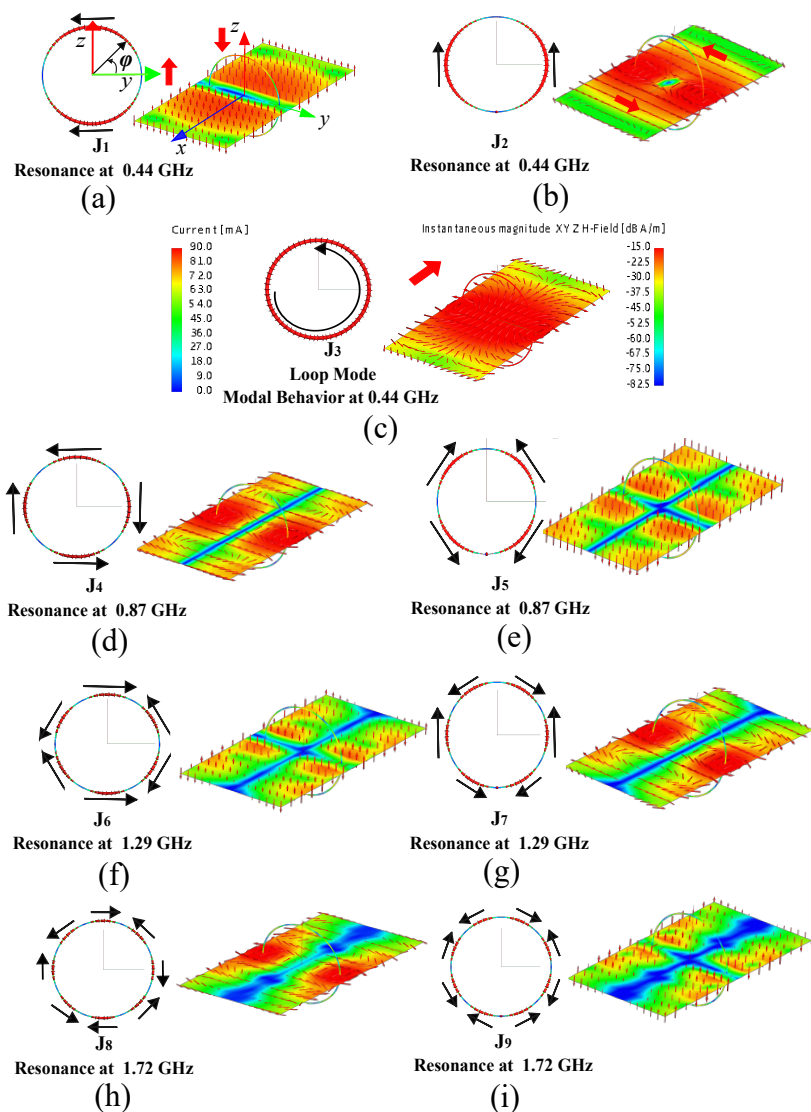


Figure 2.4: Eigen currents and their associated magnetic NF distributions in XY-plane for the first nine characteristic modes of the loop with a diameter (D) of 23.18 cm ($\approx 0.3\lambda$) using a metal wire with a thickness (w) of 0.14 cm: (a) J_1 ; (b) J_2 ; (c) J_3 ; (d) J_4 ; (e) J_5 ; (f) J_6 ; (g) J_7 ; (h) J_8 ; (i) J_9 .

2.3 Physical Interpretation of Modal Analysis

it contributes to storing electric energy ($\lambda_n < 0$ capacitive behavior). However, when λ_n is equal to 0, the associated mode J_n is considered at resonance since the reactive power is also 0. It is desired to excite the modes close to their resonances, since they radiate more efficiently.

To better interpret the eigenvalues, the reference design of the wire loop (Fig. 2.3) proposed in the previous section is used, and its eigenvalues are represented in Fig. 2.5 within the frequency range of 0.35 GHz to 2 GHz. It can be observed the inductive behavior (positive eigenvalue values) that the first resonant modes present before resonance. After resonance ($\lambda_n = 0$), all the modes remain inductive with low positive eigenvalues close to 0, which can be interpreted as a potential wide bandwidth performance that a metallic loop can exhibit if appropriately excited. This persistent inductive behavior of the various characteristic modes stems from the fact that a circular wire loop behaves akin to an inductor. As alternating current passes through the loop, it generates a time-varying magnetic field, resulting in the storage of magnetic energy.

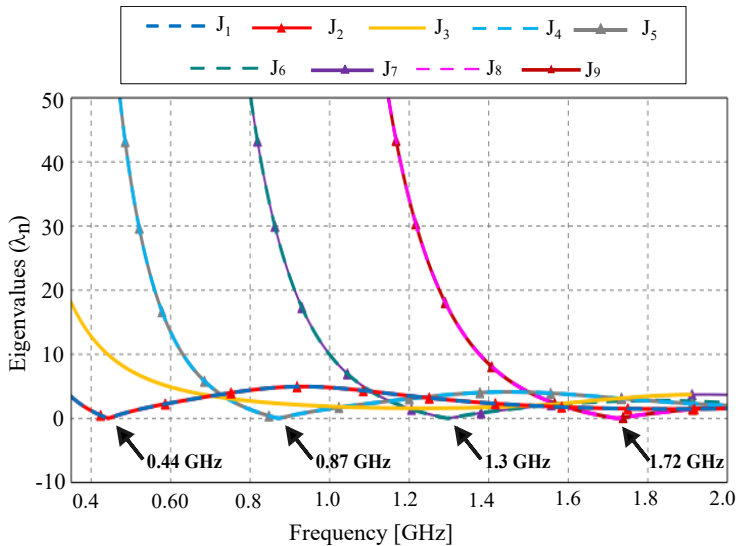


Figure 2.5: Eigenvalues of the first nine modes of the loop with a diameter (D) of 23.18 cm ($\simeq 0.3\lambda$) using a metal wire with a thickness (w) of 0.14 cm.

Furthermore, the results reveal the presence of four sets of degenerated modes, which are consecutively resonating. Each set comprises two resonating modes with identical resonance frequencies. The first pair resonates at 0.44 GHz, the second pair at 0.87 GHz, the third pair at 1.3 GHz, and the fourth pair at 1.72 GHz. For the sake of clarity, Fig.2.4 presents the eigen currents and their

associated magnetic NF distributions in XY-plane for the different modes, with degenerated modes consolidated into a single row. The eigencurrent patterns associated with the eigenvalues indicate that the observed degenerated modes have the same current distribution with a 90° phase difference. Each increase in the order of the mode set leads to an escalation in the number of current nulls placed along the perimeter of the loop. For instance, J_1 features two nulls distributed at $\phi = 0^\circ$ and $\phi = 180^\circ$, while J_8 comprises eight nulls positioned at $\phi = 30^\circ, 60^\circ, 120^\circ, 150^\circ, 210^\circ, 240^\circ, 300^\circ,$ and 330° . In contrast to the preceding modes, the only mode whose current distribution forms a continuous loop with no nulls is the third mode, J_3 , which is characterized as a non-resonant mode.

2.3.1 Modal Significance

Since eigenvalues reveal information regarding the resonance and behavior of the modes in a specific margin of frequency, various parameters derived from them have been introduced in the literature. These alternative figures of merit, such as modal significance, enhance the analysis of eigenvalues by providing additional insights. Consequently, most research on CMA includes information on eigenvalues with alternative parameters, such as modal significance.

The modal significance (MS_n) is derived from the modal expansion of the current detailed in 2.18, which is reversely dependent on the eigenvalues. By excluding the modal excitation coefficient and the modal current, the focus is placed solely on the term that includes the eigenvalues:

$$MS_n = \left| \frac{1}{1 + j\lambda_n} \right| \quad (2.20)$$

Mathematically, the MS_n defined in 2.20 varies between 0 and 1, reaching its maximum when the mode is at resonance. It represents the normalized amplitude of the current modes and depends solely on the geometry of the analyzed structure, independent of any excitation.

Fig. 2.6 represents the modal significance of the first nine modes of the wire loop illustrated in Fig. 2.3. Characteristic modes reach a peak value of one at resonance; and the closer they remain to this peak across the frequency range, the broader the potential bandwidth for each mode will be.

At the resonance ($MS_n=1$) and nearby frequencies, a figure of merit for the radiating bandwidth of a mode, denoted BW_n , can be defined by examining the modal significance. In this context, the BW_n corresponds to the frequency range where the radiated power is greater than half of the power radiated at the mode resonance. The half power of the power radiated at the mode resonance is expressed as a reduction of $\sqrt{2}$:

2.3 Physical Interpretation of Modal Analysis

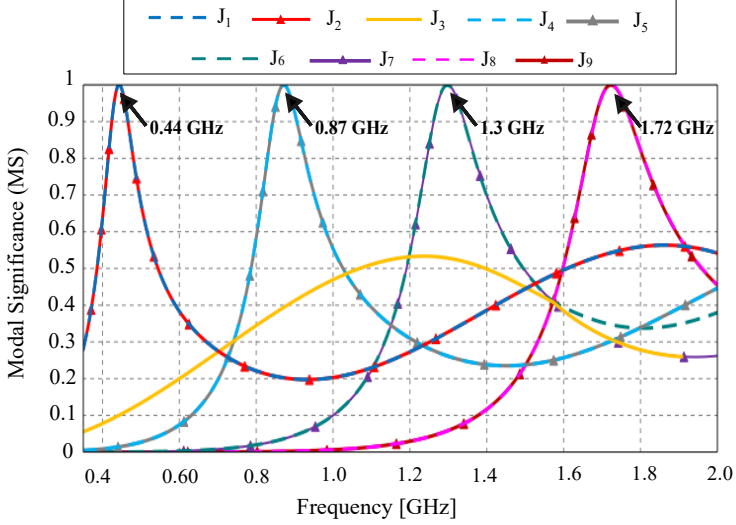


Figure 2.6: Modal Significance of the first nine modes of the loop with a diameter (D) of 23.18 cm ($\simeq 0.3\lambda$) using a metal wire with a thickness (w) of 0.14 cm.

$$MS_{HP_n} = \left| \frac{1}{1 + j\lambda_n} \right| = \left| \frac{1}{\sqrt{2}} \right| = 0.707 \quad (2.21)$$

Using the threshold condition given in 2.21 ($MS_n=0.707$), the maximum and minimum frequency of the frequency bandwidth of each mode can be identified. Thus, the radiation bandwidth is calculated as follows:

$$BW_n = \frac{f_{max} - f_{min}}{f_{res}} \quad (2.22)$$

Another parameter employed in modal analysis, derived from the radiation bandwidth, is the modal quality factor $Q_{rad,n}$:

$$Q_{rad,n} = \frac{1}{BW_n} \quad (2.23)$$

The modal quality factor $Q_{rad,n}$ is the reciprocal of the mode's radiation bandwidth BW_n . Hence, a higher quality factor corresponds to a narrower modal bandwidth (i.e., a sharper resonance), whereas a lower quality factor leads to a broader bandwidth (i.e., a less selective resonance). The $Q_{rad,n}$ measures how narrow each mode's resonance is.

2.3.2 Characteristic Angle

The Characteristic angle (α_n) is another widely employed parameter in modal analysis, offering an intuitive way to interpret the eigenvalues as shown in Fig. 2.7. It represents the phase difference between the characteristic current J_n and the associated characteristic field E_n , and it is calculated as follows:

$$\alpha_n = 180^\circ - \tan^{-1}(\lambda_n) \quad (2.24)$$

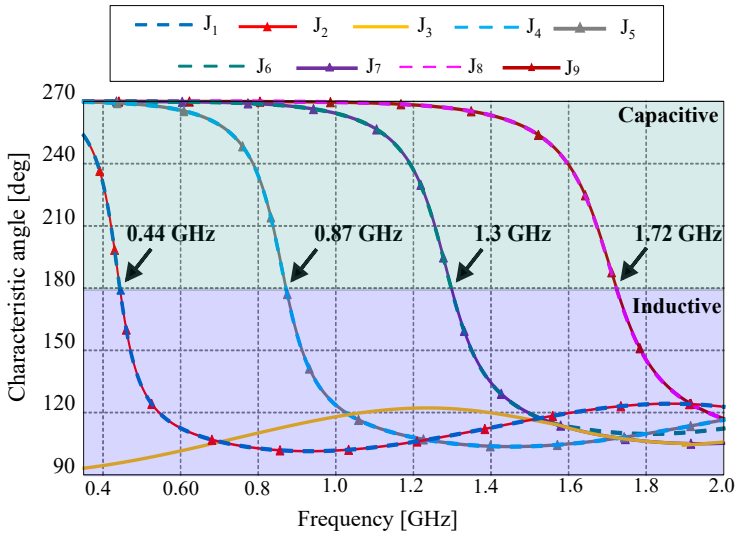


Figure 2.7: Characteristic Angle of the first nine modes of the loop with a diameter (D) of 23.18 cm ($\simeq 0.3\lambda$) using a metal wire with a thickness (w) of 0.14 cm.

Based on 2.24, it can be inferred that at resonance ($\lambda_n=0$), the corresponding characteristic angle α_n is equal to 180° . When the characteristic angle is less than 180° , the system exhibits inductive behavior, storing magnetic energy, with the stored energy increasing as the angle approaches 90° . Conversely, when the characteristic angle exceeds 180° , the system demonstrates capacitive behavior, storing electric energy, which becomes more significant as the angle nears 270° .

To determine the radiating bandwidth using 2.22 based on the half-radiated power at resonance (the values of MS_n equal to 0.707), the corresponding eigenvalues are $\lambda_n=1$ and $\lambda_n=-1$. Alternatively, the radiating bandwidth can be calculated from the frequencies associated with these characteristic angle values

for each mode in 2.24. Specifically, it can be computed using the frequencies obtained at $\alpha_n = 135^\circ$ and $\alpha_n = 225^\circ$ values for each mode.

2.4 Excitation of Characteristic Modes

In the previous section, all of the parameters introduced were independent of excitation and served to highlight the different excitation possibilities of the analyzed structure, enabling the selection of the appropriate feeding based on the desired characteristics or application. In this section, additional parameters are introduced to identify the excited modes and evaluate their contribution to the total radiated power based on the applied feeding method.

To evaluate the contribution of each mode to the input bandwidth, the input admittance, the input admittance Y_{in} is analyzed. For this calculation, the excitation is set to 1V, making the input impedance equivalent to the total current $J(P)$ measured at the feeding point P , and it is derived as follows:

$$Y_{in} = \frac{J(P)}{1V} = \sum_n \frac{V_n^i}{1 + j\lambda_n} J_n \quad (2.25)$$

The input impedance can also be expressed as the sum of modal admittances:

$$Y_{in} = \sum_n Y_n = \sum_n G_n + jB_n \quad (2.26)$$

Generally, the modal weighting coefficient (MWC) α_n and the modal radiated power are the parameters used to evaluate the contribution to each characteristic mode's power.

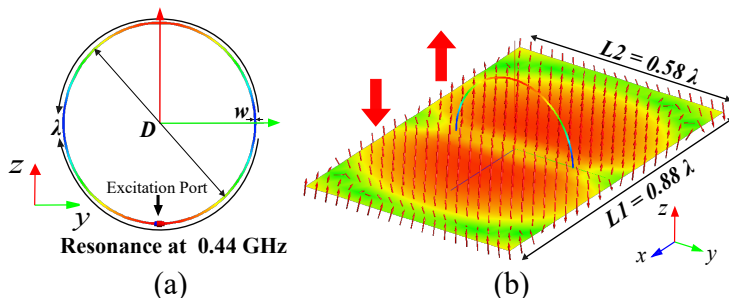


Figure 2.8: Description of the proposed single loop antenna configuration at its resonant frequency: (a) The loop geometry with its current distribution. (b) Associated magnetic NF distribution in x-y plane.

CHAPTER 2. CHARACTERISTIC MODES ANALYSIS (CMA)

A comparison between the characteristic modes of the unexcited loop, as shown in Fig. 2.4, and those of the excited loop, depicted in Fig. 2.9(b), reveals the excitation effect on characteristic modes.

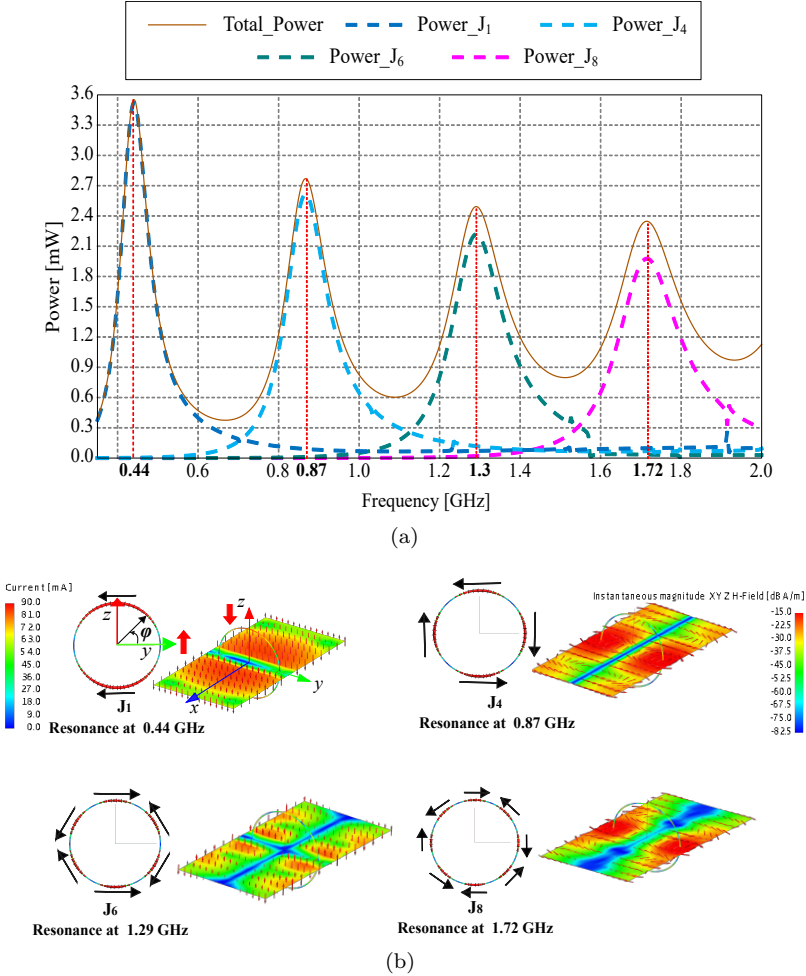


Figure 2.9: a) 150x100 metallic square plate with an ICE and a CCE and, b) Current distributions of the first six characteristic modes of the rectangular plate.

This excitation notably highlights the prominence of mode J_1 , which can act as the dominant mode in this case. It exhibits characteristics similar to those of the wire loop near its resonance, including the current distribution

2.5 Review on the CMA Applications for Coupling

and magnetic field patterns at the resonance frequency of 0.44 GHz. Additionally, it has the greatest contribution to the total radiated power. Other modes contribute to the total power at different frequencies; however, as the mode order increases, the total system power decreases, along with the intensity of the current distribution and the magnetic near-field density. The excitation results in the presence of antenna modes, characterized by the symmetry of their current distributions (J_4 , J_6 , and J_8), while other modes observed in the previous section (J_2 , J_3 , J_5 , J_9) are absent or exhibit only minimal contributions.

Other selective excitation methods can be governed by the theory of characteristic modes to excite specific modes according to the requirements of the antenna system. Capacitive coupling elements (CCEs) and inductive coupling elements (ICEs) serve as alternative excitation methods, CCEs, whether resonant or non-resonant, are positioned near the platform to induce a capacitive effect and must be placed where the characteristic mode exhibits a current minimum. Conversely, ICEs, also resonant or non-resonant, couple inductively via a magnetic field and must be positioned where the characteristic mode exhibits a current maximum. In the subsequent chapters, this technique will be explored for the first time in the context of Wireless Power Transmission, demonstrating its potential for optimizing coupling and power transfer efficiency.

2.5 Review on the CMA Applications for Coupling

The evolution of the Theory of Characteristic Modes (TCM), also known as Mode-Matching Technique, has evolved over years, unveiling contributions from numerous research works. The theory was initially developed to provide analysis for conducting objects [64,66], and was later extended to include dielectric and magnetic ones [74,75]. Previously, the CMA was applied primarily to a single radiator; therefore, an extension is necessary to analyze mutual coupling between radiators. The journal article by A. Yee and R. Garbacz, published in 1973 [76], was a pioneering work in applying CMA to analyze the coupling of multiple thin-wire antennas. In particular, this paper highlights that characteristic modes can also serve as a basis set for expanding the self- and mutual-admittances of transverse delta gaps positioned arbitrarily along a perfectly conducting thin-wire structure. Using this approach, particularly simple quadratic expressions are derived for these admittances in terms of the characteristic currents of the structure. The resulting bilinear form is significantly simpler than those obtained using other basis sets.

A typical obstacle, consisting of two disjoint wires, as shown in Fig. 2.10, was used to illustrate this concept. In this case, s_i , s_j , and s_k represented respectively the positions of the i_{th} , j_{th} , and k_{th} gaps relative to a chosen

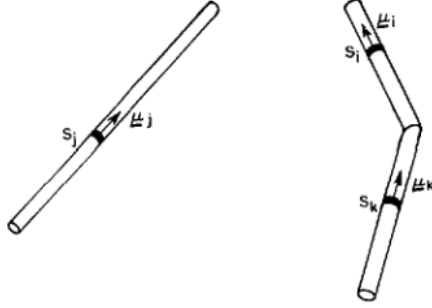


Figure 2.10: The proposed geometry of antenna array of arbitrarily located elements in [76].

reference, while u_i , u_j , and u_k are unit vectors normal to the planes of the gaps. This approach resulted in a bilinear form for admittance, significantly simplifying the expressions compared to those obtained using other basis sets:

$$Y_{jk} \approx \sum_{n=1}^{\infty} a_n [I_n(s_j)][I_n(s_k)] \quad (2.27)$$

where $I_n(s_j)$ and $I_n(s_k)$ are the n th values of the characteristic current at the positions of the j th and k th gaps, and the a_n are a set of complex characteristic values within the surface of the proposed thin wires:

$$a_n = |\cos \alpha_n| e^{i\alpha_n} \quad (2.28)$$

where α_n is the phase angle between I_n and their corresponding E_n , and that satisfies $\frac{\pi}{2} < \alpha_n < \frac{3\pi}{2}$.

The article presented two examples of gaps in two different wire structures to validate the proposed approach based on self and mutual admittances for analyzing the coupling. The first example consists of two parallel half-wave dipoles, spaced by a distance d and excited in their center gaps, as shown in Fig.2.11(a). The second example features a wire structure composed of two circular coaxial loops, each with a circumference of one wavelength and separated by a distance c , as illustrated in Fig.2.11(b). This proposed formulation has both theoretical and practical significance. Once the characteristic currents and eigenvalues are determined for a given wire structure at a specific frequency, the admittances for any number of arbitrarily placed gaps can be readily computed. This approach offers valuable applications in small array design and analysis, provides a systematic method for decoupling gaps in a

2.5 Review on the CMA Applications for Coupling

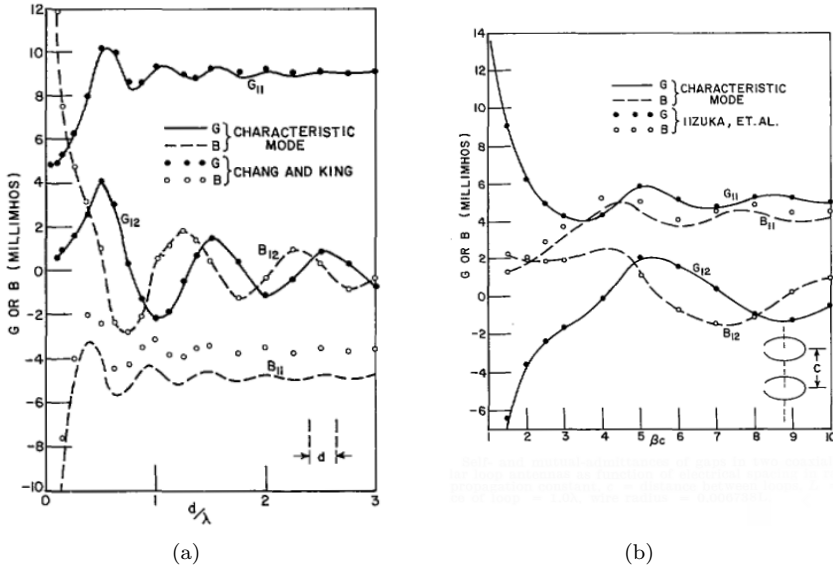


Figure 2.11: Self and mutual admittances of : (a) Center gaps parallel non-staggered array of two half-wave antennas with a wire radius of 0.007022λ as a function of electrical spacing d/λ , (b) Maps in two coaxial identical circular loop antennas with a wire radius of 0.006738λ as a function of electrical spacing in radians βc , where βc is the propagation constant. [76]

selected mode to achieve pattern control, and may contribute to optimizing array configurations. Therefore, CMA has been applied over the last decade for coupling analysis to optimize antenna design and gain physical understanding in a wide range of applications.

Since triangular surface meshes offer a more general approach for modeling arbitrarily shaped objects compared to the thin wire approximation used in previous work, Qi Wu, Wei Su, Zhi Li, and Donglin Su [77] proposed a novel solution to reduce out-of-band antenna coupling. Their approach extends the method presented in [76] by incorporating Rao–Wilton–Glisson (RWG) basis functions [78]. The functional and un-functional modes of the antenna system were characterized to enable the suppression of certain non-functional modes through the implementation of inductive loadings. The optimal loading positions were determined based on eigencurrent distributions, while the appropriate loading values were derived through an analysis of the Modal Mutual Admittance (MMA). Two case studies were presented to illustrate the proposed

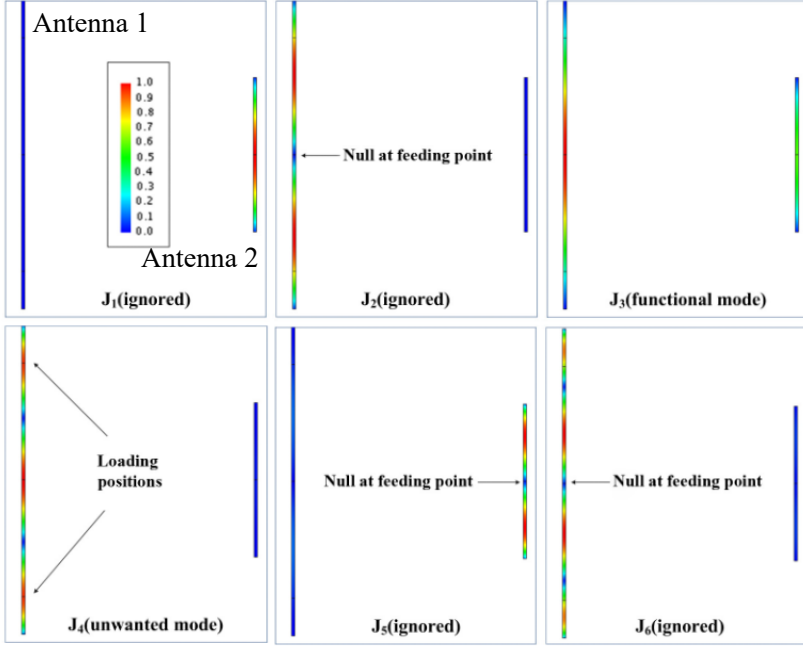


Figure 2.12: Eigencurrent Magnitudes (A/m) of the first proposed antenna system at $f_2 = 280$ MHz. [77]

design methodology, and a comparative analysis with existing approaches was conducted to assess its effectiveness.

The first example involves two center-fed dipole antennas, where the first antenna resonates at $f_1 = 140$ MHz and the second at $f_2 = 280$ MHz. Fig.2.12 classifies the modes based on their current distributions and identifies optimal inductive loading positions to mitigate the coupling at f_2 . The inductive loadings are strategically positioned at the locations of maximum magnitude of the unwanted mode J_4 , corresponding to approximately one-fourth of the antenna length, to effectively enhance isolation at its resonance frequency. This approach reduces out-of-band mutual coupling by an average of 10 dB around f_2 , with a minor impedance bandwidth reduction of 3 MHz as illustrated in Fig.2.13(a). Simulated radiation patterns show negligible variation, indicating that in-band performance is largely preserved as shown in Fig.2.13(b).

In the second example, antenna 1 is replaced with a broadband bowtie antenna composed of two equilateral triangles. The center frequency of the bowtie antenna remains the same as in the first example, $f_1 = 140$ MHz.

2.5 Review on the CMA Applications for Coupling

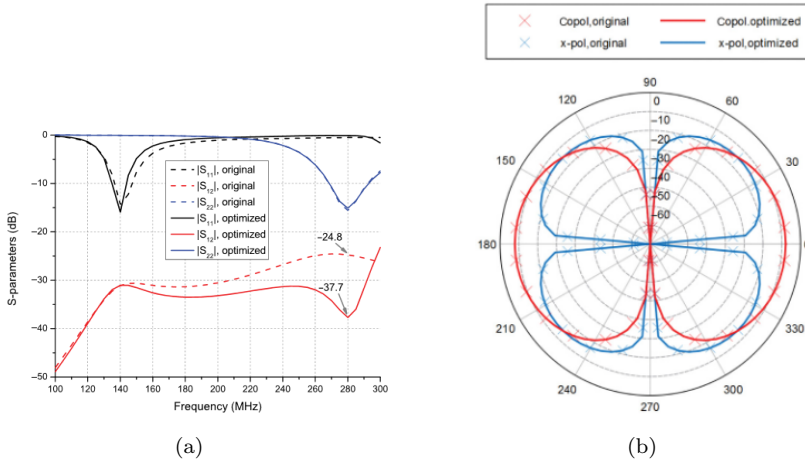


Figure 2.13: (a) S-parameters of the original and optimized antenna systems, (b) E-plane radiation patterns of antenna 1 at $f_2 = 140$ MHz. [77]

Besides, Antenna 2 remains unchanged, and the distance between the feeding points of both antennas is maintained. The first six-order eigencurrents of the antenna system at $f_2 = 280$ MHz are presented in Fig. 8, where J_4 , J_5 , and J_6 contribute minimally to the mutual admittance, and are therefore disregarded in the final design. However, J_2 is identified as the functional mode of antenna 1, while mode J_3 is the non-functional mode. The selected loading positions, shown in Fig.2.14(a), correspond to regions where the unwanted mode, J_3 , exhibits a higher surface current density than mode J_2 .

One challenge encountered in the placement of inductive loadings is that the surface current naturally follows the path of least impedance. When inductive loadings are positioned directly at the selected locations in Fig.2.14(a), the surface current may bypass them, reducing their effectiveness. Therefore, to address this issue, a modification is introduced, as illustrated in Fig.2.14(b), where a rectangular section is removed from each bowtie arm, leaving only small edge regions for the placement of inductive loadings in the simulation. This approach ensures that the surface current is forced to pass through the loadings, ensuring effective mode control.

To validate the proposed methodology based on the TCM, two prototypes were fabricated and measured. Initially, the prototype without inductive loading, shown in Fig.2.15(a), was analyzed, demonstrating a reasonable correlation between the measured and simulated results. However, the measured resonant frequency of the dipole antenna was approximately 50 MHz lower than an-

CHAPTER 2. CHARACTERISTIC MODES ANALYSIS (CMA)

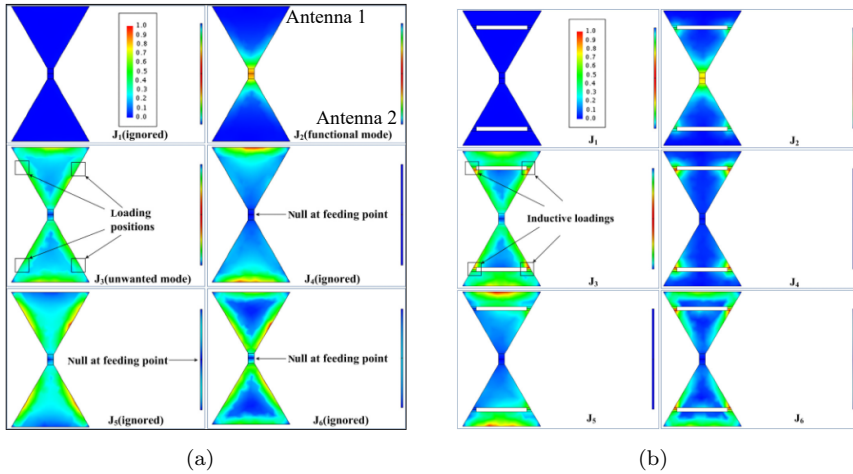


Figure 2.14: Eigencurrents (magnitude in A/m) of the antenna system : (a) of the original structure at f_2 , (b) of the modified structure at f_2 . [77]

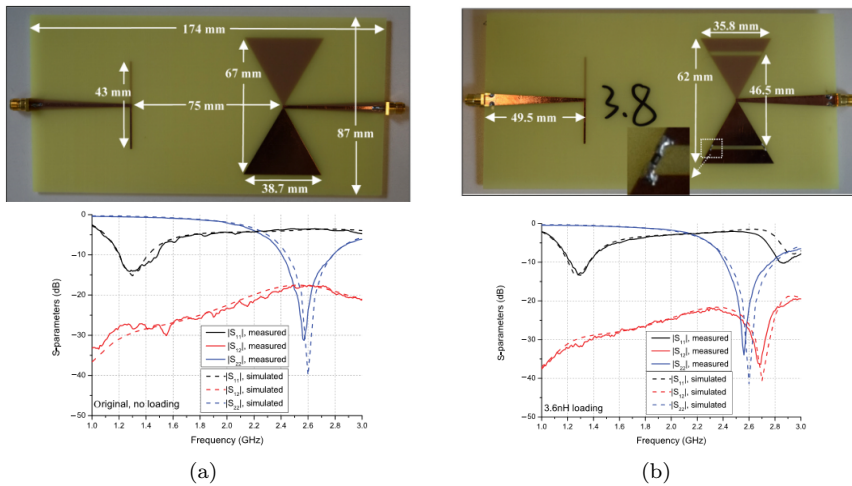


Figure 2.15: (a) Original prototype with corresponding simulated and measured results, (b) The optimised prototype integrating a 3.8 nH chip inductor with corresponding simulated and measured results. [77]

anticipated, likely due to deviations in the actual relative permittivity of the

2.5 Review on the CMA Applications for Coupling

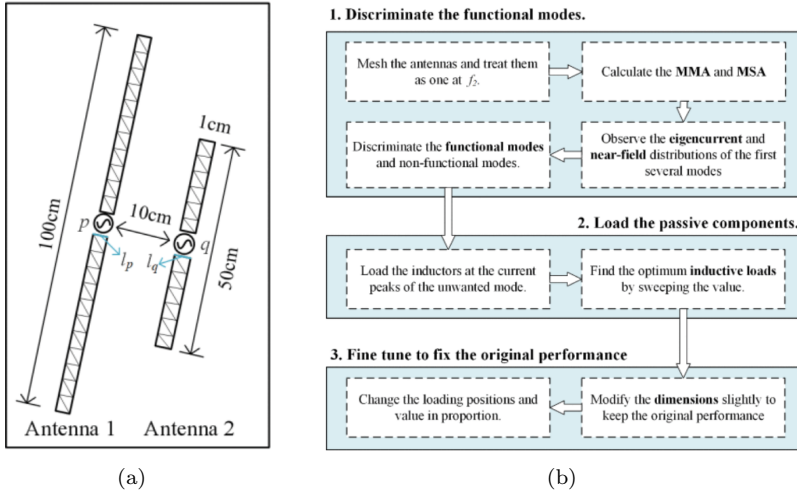


Figure 2.16: (a) Original system consisting of two center-fed dipole antennas with different lengths, (b) Modified procedure for CMA of antenna mutual coupling in the NF. [79]

FR-4 laminate used in fabrication, as the simulation assumed a value of 4.4. In contrast, the optimized prototypes, integrating a 3.8 nH chip inductor, exhibited a strong agreement between simulated and measured results below 2.0 GHz, as illustrated in Fig.2.15(b). The proposed method effectively addresses both scenarios but requires distinct approaches. In the lower frequency band, the platform is incorporated into the analysis, allowing for the suppression of specific associated modes.

Building on the previous study using inductive loads, where mutual coupling across both lower and higher frequency bands remained an open research question, Peiyu Liang and Qi Wu [79] propose a novel approach focused on the NF interaction for general two antenna system. It is essential to highlight that CMA has been extensively utilized in the context of far-field coupling, where its application is well-established within the scientific community. This prominence stems from its ability to characterize antenna radiation behavior, which is commonly assessed based on radiation patterns, directivity, and gain. However, with the advancement of emerging technologies such as Radio Frequency Identification (RFID), Near Field Communication (NFC), 5G, and Wireless Power Transfer (WPT), the analysis and integration of antennas within the same device remain a complex challenge. In particular, near-field (NF) coupling plays a crucial role in system performance, with its reduction or enhancement depend-

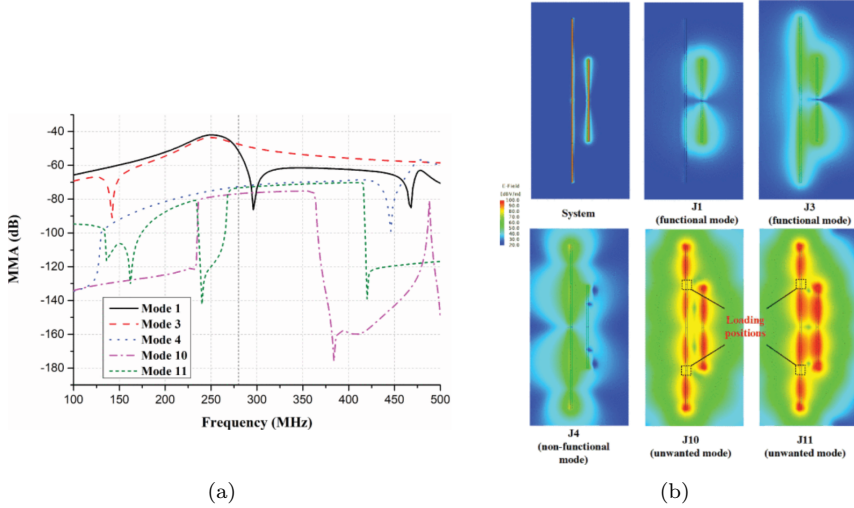


Figure 2.17: (a) Computed MMA curves of the remaining modes, (b) Modal NF distributions of the antenna system at 280 MHz. [79]

ing on the specific application requirements. Recently, Characteristic Modes (CMs) have been increasingly employed to provide a deeper theoretical understanding of NF antenna coupling, enabling quantitative analysis, improving antenna design methodologies, and contributing to system-level optimization. Unlike FF mutual coupling, where dominant modes are typically sufficient for analysis, the NF scenario requires consideration of higher-order modes. To address this, modal near-field distributions are proposed as a framework for identifying and characterizing these interactions, providing a clear guideline for applying the theory to general antenna structures. The study examines a two-antenna system, illustrated in Fig.2.16(a), which can be analyzed as a single radiating structure. Based on the analysis proposed in [77], a modified procedure is introduced to apply CMA to antenna mutual coupling in the NF, as illustrated in Fig.2.16(b). This paper focuses on the out-of-band mutual coupling scenario, where antenna 1 resonates at f_1 (lower frequency) and antenna 2 at f_2 (higher frequency).

The modified CMA procedure, illustrated in Fig.2.16(b), is implemented by first computing the Modal Significance (MSA) and Modal Mutual Admittance (MMA) for the first twelve modes over a frequency range of 100 to 500 MHz. The number of computed modes is doubled compared to the FF study [77], as higher-order modes play a crucial role in the NF region. Modes $J_2, J_5, J_6, J_7, J_8, J_9,$ and J_{12} are disregarded due to their relatively low Modal Significance

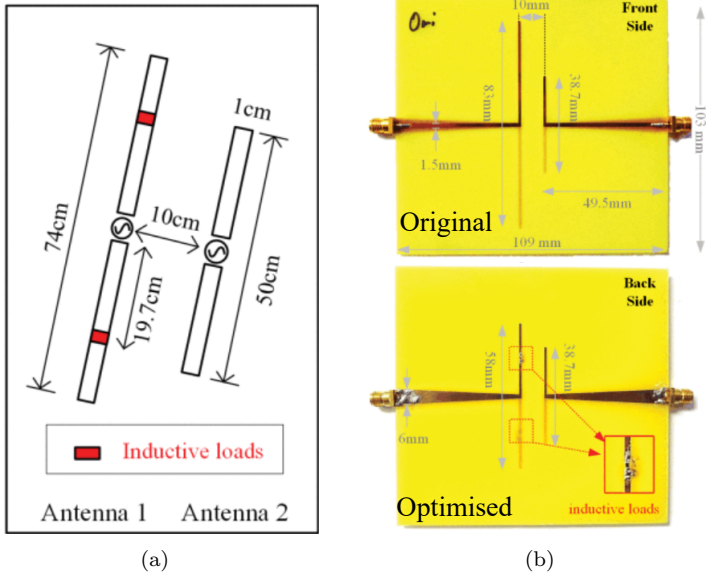


Figure 2.18: (a) Optimized analyzed structure with inductive loads, (b) The fabricated prototypes with a 1:10 scale. [79]

(MSA). However, modes J_1 , J_3 , J_4 , J_{10} , and J_{11} are identified as potential functional modes, as they exhibit higher Modal Mutual Admittance (MMA), as illustrated in Fig.2.17(a). While the MMA curves of these modes fluctuate with frequency, they all demonstrate significant values around $f_2 = 280$ MHz. Subsequently, the modal near-field distributions of these modes are computed at f_2 and presented in Fig.2.17(b). The results indicate that the NF distributions of J_{10} and J_{11} exhibit high density near antenna 2, significantly contributing to NF mutual coupling. Based on these observations, they are identified as unwanted modes that require suppression.

Following the placement of the optimal loadings in the proposed design and adjusting the dimensions of the structure to align with the required frequency range, as shown in Fig.2.18(a), experimental validation was performed using 1:10 scale prototypes of the original and optimized antenna systems.

Figure 2.18(a) illustrates the dimensional modifications of the two-antenna system to account for the influence of the dielectric substrate and achieve the desired resonant frequencies of $f_1 = 1,4$ GHz and $f_2 = 2,8$ GHz. It compares the original and optimized prototypes, highlighting changes in the length of antenna 1 from 83 mm to 58 mm, while antenna 2 remains at 38.7 mm. Both prototypes maintain a dipole width of 1 mm and a spacing of 10 mm. Additionally, the

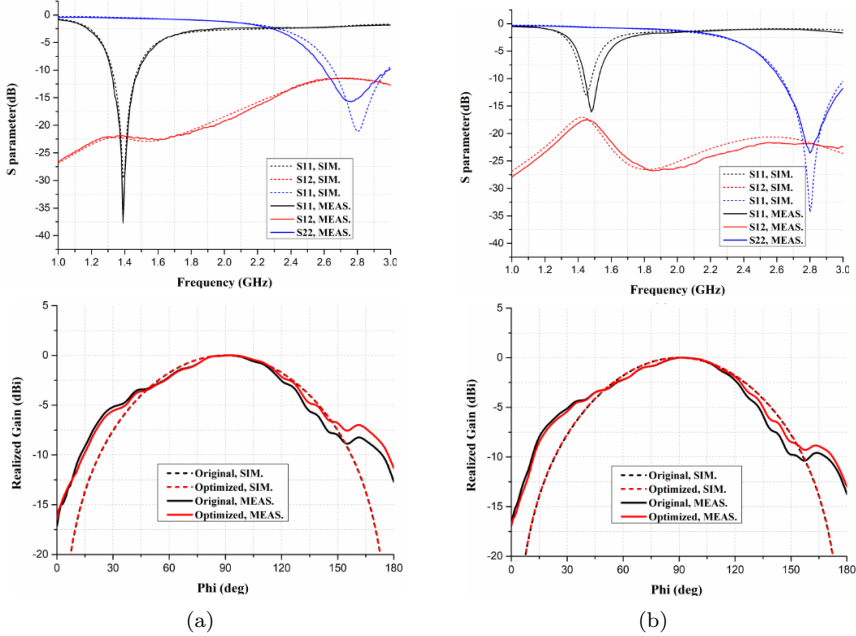


Figure 2.19: (a) Optimized analyzed structure with inductive loads, (b) The fabricated prototypes with a 1:10 scale. [79]

figure depicts the placement of inductive loads at ± 15.5 mm and the integration of two 16 nH chip inductors on antenna 1.

For the original prototype (Fig. 2.19(a)), the measured and simulated results closely match, with a slight deviation at 2.8 GHz, likely due to discrepancies in the permittivity and loss tangent of the FR-4 substrate. In addition, the E-plane radiation patterns also align well with simulations, with minor discrepancies at wider angles attributed to scattering from the measurement setup. The received signal levels remain consistent across the tested frequencies, confirming stable performance.

For the optimized prototype (Fig. 2.19(b)), the introduction of 16 nH inductors effectively reduces out-of-band mutual coupling by approximately 10 dB. However, a 40 MHz shift in the resonant frequency of antenna 1 is observed, likely due to inductance tolerances. Additionally, the radiation patterns follow similar trends as the original design but exhibit a lower received signal level at 1.4 GHz due to the frequency shift. At 1.5 GHz, both prototypes perform similarly, indicating that the inductors introduce minimal parasitic loss to the antenna gain.

2.5 Review on the CMA Applications for Coupling

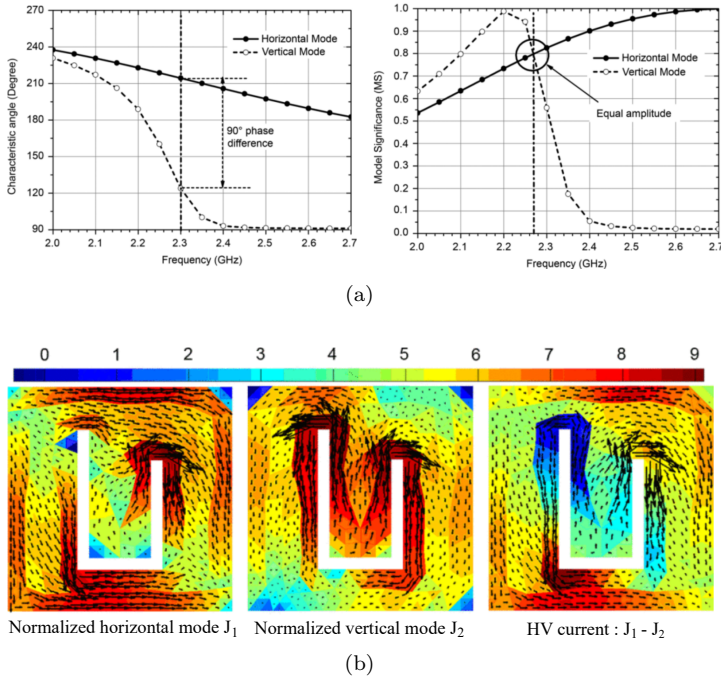


Figure 2.20: The U-slot antenna: (a) Characteristic angle and modal significance of the horizontal and vertical modes, (b) Related current distributions. [80]

In this study, NF mutual coupling in a general two-antenna system is analyzed using CMA. A comprehensive framework is developed by integrating modal admittance, near-field distributions, and eigencurrent analysis to systematically identify and distinguish functional from non-functional modes. Experimental validation, conducted through fabricated dipole prototypes, demonstrates a mutual coupling reduction exceeding 10 dB.

While previous studies primarily utilize modal excitation techniques for unwanted mode suppression, alternative approaches have been proposed in the literature for more complex structures, such as U-shaped slots and U-slot patches. Previously, various methods had introduced different strategies based on CMA [80–88]. For instance, in [80], Yikai Chen and Chao-Fu Wang applied CMA to enhance the performance of Circularly Polarized (CP) microstrip antennas, specifically U-slot and E-shaped patch antennas. The analysis focuses on understanding the underlying physics through characteristic angles and modal significance of both structures as depicted in Fig. 2.20(a)

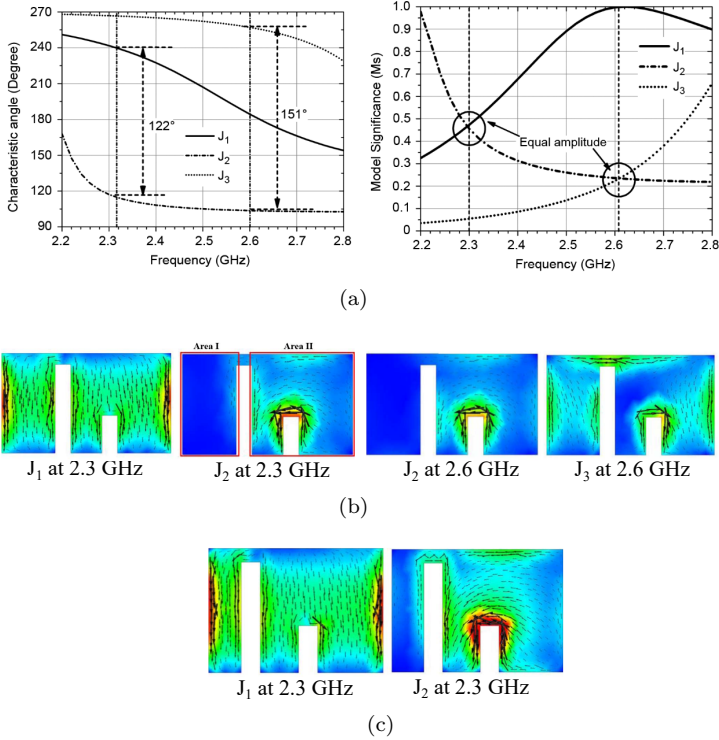


Figure 2.21: The E-shaped patch antenna: (a) Characteristic angle and modal significance of the horizontal and vertical modes, (b) Related current distributions, (c) Characteristic current distribution of the size-reduced E-shaped patch antenna at 2.3 GHz. [80]

and Fig. 2.21(a), enabling optimized designs with improved Axial Ratio (AR) and reduced cross-polarization without added complexity.

Notably, by optimizing the probe feed position, the U-slot patch antenna achieves superior axial ratio (AR) performance through an offset-fed design. Similarly, the E-shaped patch antenna benefits from removing redundant sections, which lowers cross-polarization and results in a more compact configuration. Experimental validation using fabricated prototypes confirms the effectiveness of CMA-based optimization, with the modified designs exhibiting improved radiation characteristics. Unlike conventional CP antenna designs that rely on parameter sweeps or optimization algorithms, this approach offers a more physics-driven methodology, providing deeper insight into mode behavior and enhancing overall antenna efficiency.

2.5 Review on the CMA Applications for Coupling

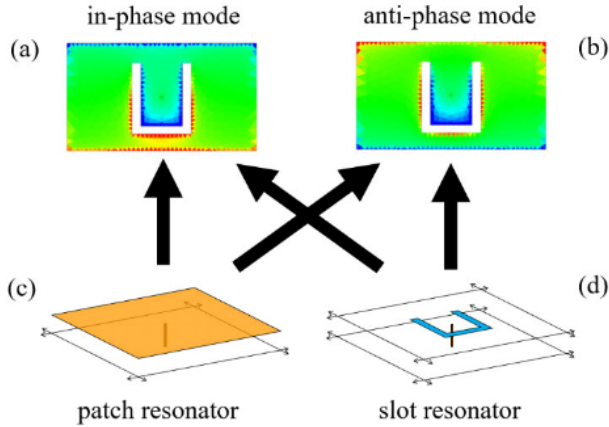


Figure 2.22: The proposed geometry of antenna array of arbitrarily located elements in [88].

However, the methodology proposed in [80] has limited applicability as it focuses on circularly polarized U-slot patches, failing to address the design challenges and performance optimization of wideband, linearly polarized U-slot patches. Although previous studies have explored CMA applications for various U-slot configurations, significant gaps remain in their applicability to practical antenna design. Studies [81–83] primarily focused on CMA mode tracking algorithms for U-shaped slots in ground planes or plates, which are not true patch antennas, limiting their relevance. Similarly, [84] applied CMA to a U-slot patch without a feed probe, providing no design guidelines or fundamental operational insights. While [85] introduced a third empirical design methodology for U-slot patches, it lacked deeper theoretical analysis. Besides, [86] and [87] examined probe location effects and slot shape optimization but failed to address the initial design process or provide a fundamental understanding of U-slot patch operation.

Therefore, John J. Borchardt and Tyler C. Lapointe [88] have introduced a significant advancement in U-slot patch antenna design by developing a novel analytical framework that combines the TCM with the Coupled Mode Theory (CMT) to provide a deeper theoretical foundation and a systematic design methodology. Unlike previous studies that primarily relied on empirical techniques, this research directly derives the design process from fundamental operational principles, extending earlier findings [89,90] that suggested the two resonances of the U-slot patch are linked to CMT, as illustrated in Fig. 2.22.

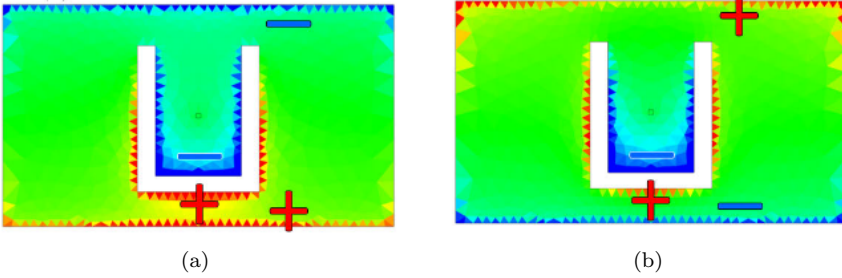


Figure 2.23: The normalized charge distributions of : (a) Mode 1, (b) Mode 3. [88]

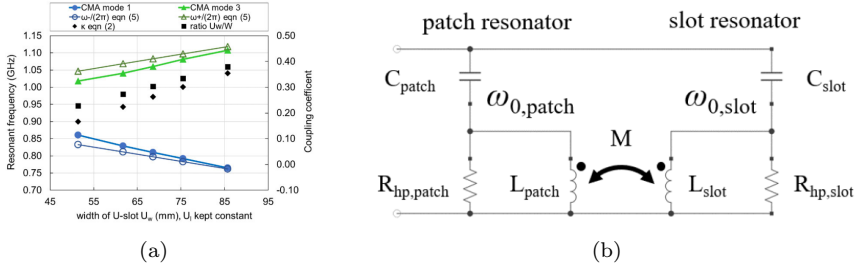


Figure 2.24: (a) Effect of U-Slot Width on Coupling Coefficient and Resonant Frequency Splitting of the CMs, (b) Circuit Model of Uncoupled Patch and Slot Resonators with Explicit Mutual Inductive Coupling. [88]

The key contributions of this work include demonstrating that the classic U-slot patch operates under the Couple Mode Theory (CMT) principles, offering a systematic explanation of its dual-resonance characteristics. In particular, the presence of in-phase and anti-phase charge distributions, as illustrated in Fig. 2.23(a) and 2.23(b), provided direct evidence of mode coupling. The CMT effectively quantified the observed frequency splitting in CMA, as shown in Fig. 2.24(a) and the PTFE design example, further validating its applicability. Moreover, the success of a CMT-based circuit model, explicitly depicting the coupling between two resonators (2.24(b)), reinforced the theoretical framework. Building on these insights, a CMT-driven design methodology was introduced, offering a systematic approach to optimizing U-slot patch antennas based on fundamental operational principles.

While previous studies on antenna coupling using CMA have primarily focused on mitigating coupling, particularly in reducing out-of-band coupling

2.5 Review on the CMA Applications for Coupling

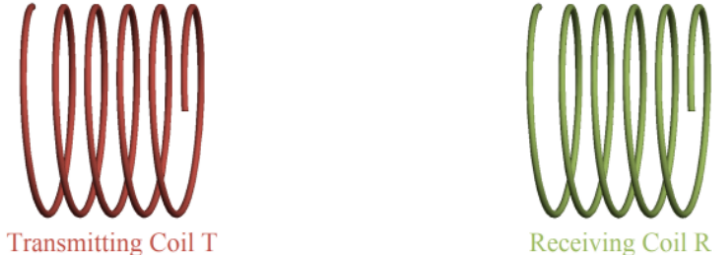


Figure 2.25: A WPT system consisting of a metallic transmitting coil (T) and a metallic receiving coil (R), as reported in [41]. Both coils have a radius of 30 cm, a height of 20 cm, and 5.25 turns. [91]

and mutual coupling, due to the need for integrating multiple antenna elements within a single structure, the exploration of NF coupling for the purpose of enhancing interaction between antennas remains a relatively novel research area [91–93]. This emerging field presents significant opportunities for optimizing antenna performance in applications where controlled NF coupling can be leveraged to improve energy transfer, signal integrity, and overall system efficiency.

Ren-Zun Lian and Xing-Yue Guo highlighted the necessity of a systematic modal analysis approach to facilitate both theoretical understanding and practical design in wireless power transfer (WPT) systems [91]. The primary objective of the authors was to develop a rigorous, frequency-independent, and geometry-independent modal analysis method for WPT systems. A systematic modal analysis approach plays a crucial role in facilitating both theoretical analysis and engineering design in power transfer applications. Various modal analysis methods have been explored, including coupled-mode theory [41], [94, 95], classical circuit theory [96], and other circuit-based approaches [97]. However, these methods predominantly rely on circuit models, which introduce approximations due to their dependence on scalar voltage, scalar current, modal analysis framework remains a key challenge in magnetic-resonance-based WPT, requiring new theoretical formulations to extend the applicability of modal analysis beyond traditional circuit-based methods.

This study proposed by [91] extends the conventional characteristic mode theory (CMT), traditionally used for scattering systems, to a novel formulation tailored for transferring systems. It begins by exploring the physical principles governing the transfer mechanism of the transferring system shown in Fig. 2.25. The analyzed WPT system consists of a metallic transmitting coil (T) and a metallic receiving coil (R). The proposed theory is validated through modal analysis applied to a classical transferring system, confirming its accuracy and

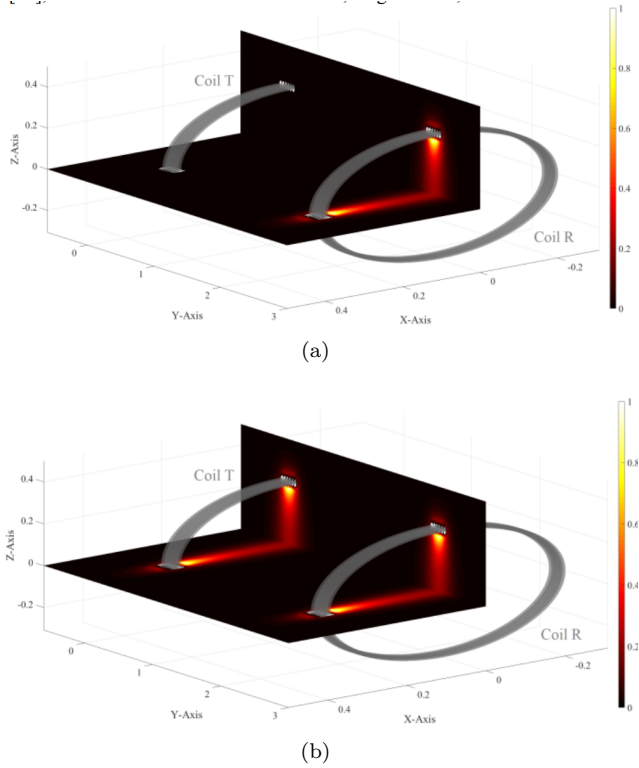


Figure 2.26: The time-averaged magnetic energy density distribution of: (a) The desired transferring mode in [91], (b) The resonant CM calculated from the conventional scattering modal analysis in previous study [93].

applicability through the development of rigorous mathematical formulations that establish the transferring modal framework. Unlike previous research that attempted to extend conventional Characteristic Mode Theory to transferring systems without success [93], this study establishes a generalized transferring framework based on CMA that effectively addresses these limitations. As illustrated in Fig. 2.26(a), the proposed approach yields a resonant CM that significantly enhances WPT by optimizing energy transfer from the transmitting coil T to the receiving coil R. In contrast, the method presented in previous research fails to achieve optimum performance, as the energy is not completely transferred from the transmitter to the receiver, as evidenced in Fig. 2.26(b).

The Wireless Energy Propagation Coupled Mode Theory was applied to analyze the wireless power transfer system, revealing key factors influencing

2.5 Review on the CMA Applications for Coupling

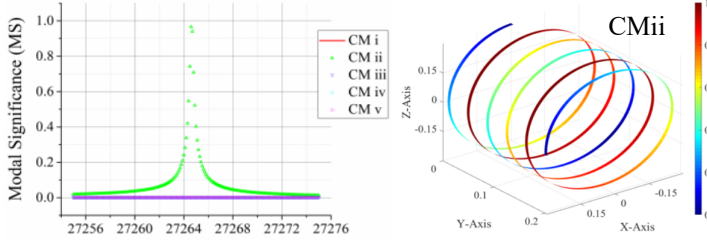


Figure 2.27: The MS of the first 5 CMs of the one-coil scattering system at the frequency band from 27.255 to 27.275 MHz, and the modal current magnitude distribution of the resonant mode CMii at 27.2646 MHz. [91]

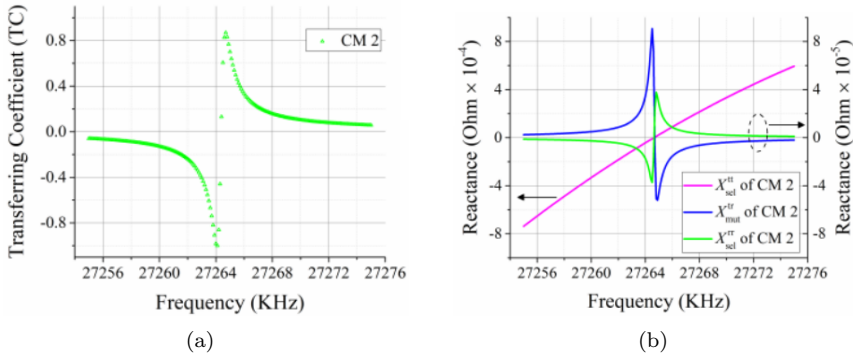


Figure 2.28: (a) The transferring coefficient, and (b) The reactance curves associated with the CM2 of the two-coils transferring system in frequency band from 27.255 to 27.275 MHz. [91]

transfer efficiency, particularly the relationship between scattering resonance and co-resonance frequencies. The modal significance curves of a single-coil scattering system exhibit resonance characteristics similar to those observed in two-coil transferring systems, reinforcing the connection between co-resonance wireless power transfer and conventional scattering phenomena.

As illustrated in Fig. 2.27, the presence of higher-order scattering-resonance frequency 27.2646 MHz further supports this relationship. This later is confirmed by the transfer coefficient and reactance curves in Fig. 2.28, which validate the co-resonance behavior of a two-coil system at 27.2646 MHz. The corresponding magnetic energy distribution provided by exciting this specific mode is presented Fig. 2.26(a).

CHAPTER 2. CHARACTERISTIC MODES ANALYSIS (CMA)

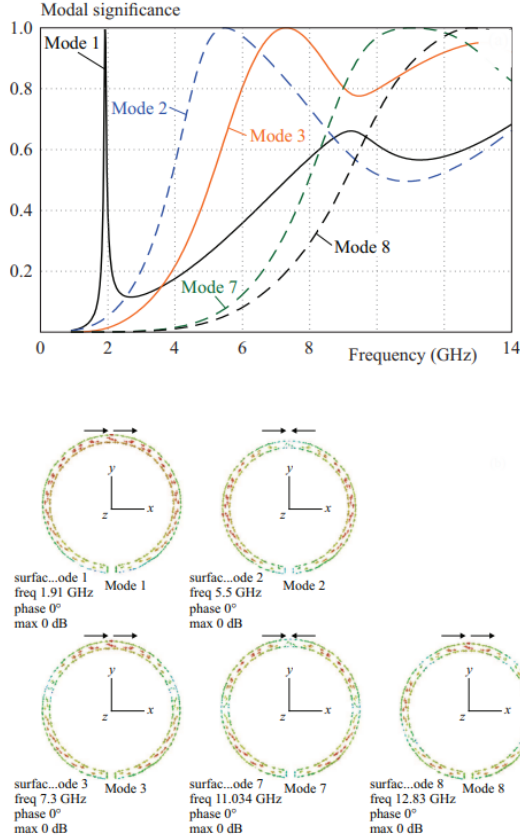


Figure 2.29: The modal significance of a single SRR with the corresponding current distributions of the related CMs at their resonance frequencies. [92]

The study in [91] requires extensive computational effort due to the development of a novel formulation tailored for transferring systems, referred to as transferring Characteristic Mode Theory (CMT). Unlike conventional Characteristic Mode Theory, which is widely available in electromagnetic simulation software for analyzing scattering systems, this approach necessitates a distinct mathematical framework. An alternative method proposed by Akaa Agbaeze Eteng [92] provides a more simplified and detailed CMA to investigate modal interactions in coupled split-ring resonators (SRRs). It explores how feed impedance and rotational orientation influence the excited resonant modes, affecting both power transfer levels and operating frequencies. The

2.5 Review on the CMA Applications for Coupling

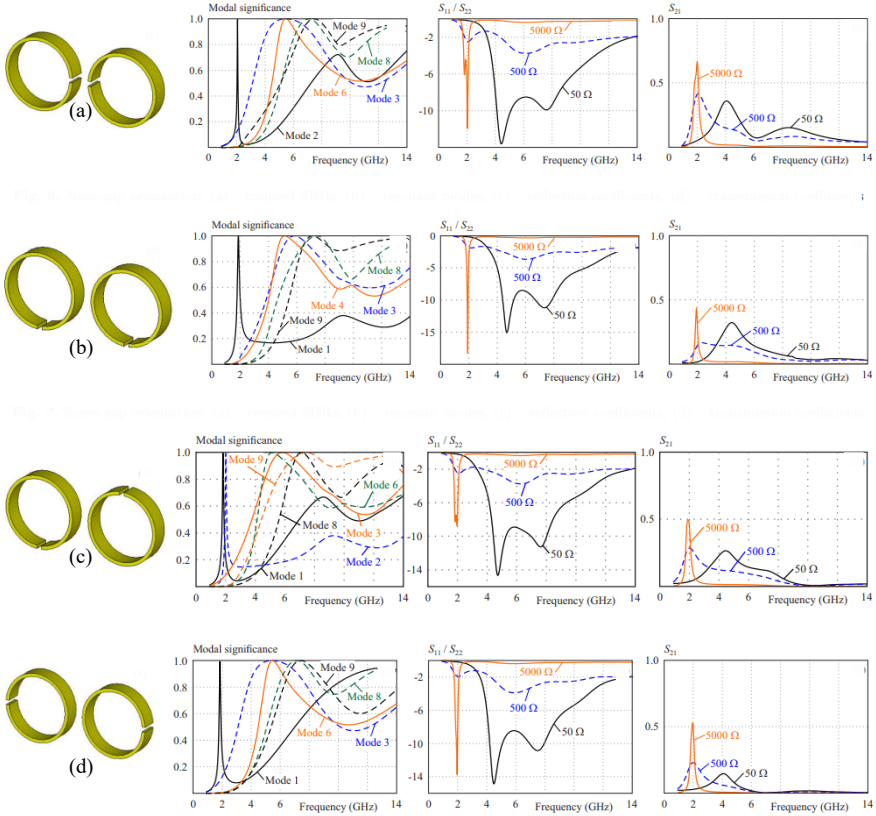


Figure 2.30: Modal significance, reflection coefficients, and transmission coefficients of the SRRs with : (a) Near-gap orientation, (b) Same-gap orientation, (c) Opposite-gap orientation, (d) Far-gap orientation. [92]

study highlights the importance of these parameters in optimizing SRR-based magneto-inductive waveguides and WPT systems.

Initially, CMA is applied to investigate the electromagnetic behavior of a single ring resonator, as illustrated in Fig. 2.29. Subsequently, a parametric study is conducted to analyze the coupling mechanisms in coplanar and parallel split-ring resonators (SRRs). For both configuration, the edge-coupled orientation is systematically varied, and a comprehensive modal analysis is performed alongside S-parameter simulations for different study cases. This approach enables a direct comparison between the system's behavior near its resonance and the dominant characteristic modes associated with each configuration.

CHAPTER 2. CHARACTERISTIC MODES ANALYSIS (CMA)

For instance, Fig. 2.30 illustrates the resonant CMs in a coplanar pair of edge-coupled split-ring resonators (SRRs) placed 5 mm apart. A narrowband resonant mode at 1.9 GHz is consistently observed, regardless of rotational orientation, while additional resonances appear between 4 and 8 GHz. Reflection coefficient results confirm minima at 1.9 GHz and within the 4 to 8 GHz range, aligning with the observed transmission characteristics. The feed impedance plays a crucial role in determining which modes contribute to high transmission coefficients. Depending on impedance levels, transmission peaks occur at 1.9 GHz or 4.5 GHz. Higher impedances are required to excite mode 1 and mode 2 in Fig. 2.30(c), leading to a higher transmission coefficient at 1.9 GHz. In contrast, the 4.5 GHz transmission peak exhibits a broader bandwidth but lower transmission levels due to the contribution of multiple overlapping modes at lower feed impedance.

Among the four edge-coupled orientations, the highest transmission coefficient of 0.67 is achieved using the near-gap orientation with a $5 k\Omega$ feed impedance. Notably, low reflection coefficients at individual SRRs do not always result in high transmission coefficients, as illustrated in Fig. 2.30 (b) and (c). A key finding is that the split-gap in SRRs introduces a lower-frequency characteristic mode, absent in conventional ring resonators. This mode, excitable through high feed impedance, enables narrowband, high-efficiency power transfer. Additionally, frequency splitting in the transmission coefficient is linked to two closely resonating characteristic modes, where eliminating one mode suppresses the split.

The application of CMA for coupling analysis is a relatively new research area. While previous studies have provided detailed theoretical analyses, they often lack experimental validation through measurements [91,92].

This chapter presents a comprehensive study of the mathematical formulation of the TCM, establishing the necessary foundation for understanding the subsequent chapters. Additionally, it reviews the key applications of CMA for coupling between antennas over the past decades and the current state of the art. The next chapter will focus on applying CMA for misalignment in WPT system.

Chapter 3

CMA for Misalignment in WPT System

This chapter evaluates the impact of misalignment in Magnetically Coupled Resonant Wireless Power Transfer (MCR-WPT) systems. It focuses on a configuration of two identical loops designed to support applications such as biomedical implants, Qi wireless charging, and wearable technologies. The study investigates typical misalignments between transmitting (Tx) and receiving (Rx) loops caused by user or device movement. Simulation results and post processing outcomes will be compared to the measurements in the next chapter to demonstrate, for the first time, a direct correlation between dominant mode behavior and power transfer efficiency (PTE), confirming the practical relevance of CMA in real-world WPT systems. By establishing a clear CMA-based methodology governed by the Coupled Mode Theory for coupling analysis, this chapter provides a solid reference for researchers aiming to advance the integration of CMA into WPT system design.

3.1 Guidelines For Coupling Numerical Analysis for WPT System Using CMA

Pioneering investigations have delved into analyzing, optimizing, and evaluating WPT antenna systems using various approaches, such as Equivalent Circuit Analysis (ECA) [98], Analytical Modeling (AM) [99], Numerical Methods (NM) [100], and Experimental Testing [101]. These methods have been employed across the literature for broad coupling analysis in diverse applications. Characteristic Modes Analysis (CMA) provides distinct insights into antenna coupling by offering a deeper understanding of the underlying electromagnetic

CHAPTER 3. CMA FOR MISALIGNMENT IN WPT SYSTEM

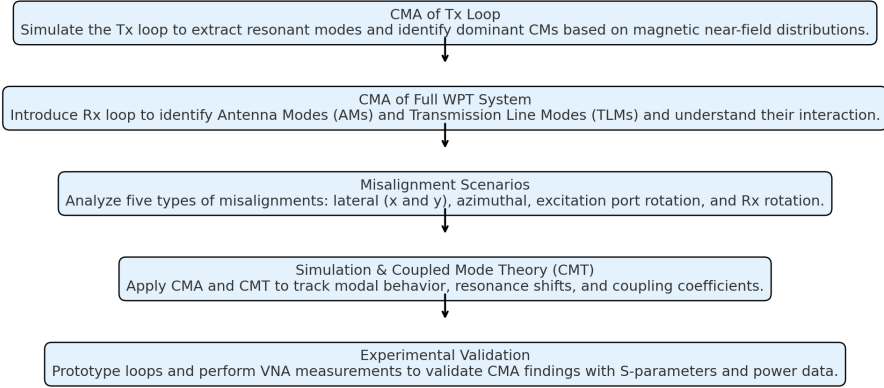


Figure 3.1: Guidelines for the proposed CMA-based numerical coupling analysis in wireless power transfer systems.

behavior and integrating well with existing techniques. A key strength of CMA lies in its ability to offer a rigorous, frequency-independent, and geometry-independent modal analysis framework for WPT systems, addressing one of the field’s most critical challenges.

In the context of WPT, CMA enables the decomposition of a complex system into its constituent modes, each representing a distinct pattern of energy distribution. This modal perspective offers significant advantages in understanding system behavior and assessing how various factors influence the coupling characteristics between antennas in WPT applications.

Achieving analytical results that align with measurements in antenna design offers several benefits, including cost and time efficiency, design optimization prior to prototyping, and confidence in performance. Analytical validation ensures that the antenna meets real-world performance expectations and specifications. However, existing studies on WPT using CMA have remained purely theoretical [80, 91, 92, 102–106], with no experimental validation. To address this gap, this work analyzes coupling behavior using CMA for both a single loop and a system of two identical loops, representing the Tx and Rx coils. To validate the practical relevance of CMA, the system’s resonant behavior is compared with the predictions provided by the modal analysis. To conduct an effective coupling analysis for WPT systems using CM, the methodology and key steps followed in this study can be outlined as follows:

1. Modeling the Transmitting Loop (Tx): The Tx loop is designed and simulated using the electromagnetic software FEKO, considering system-

3.1 Guidelines For Coupling Numerical Analysis for WPT System Using CMA

specific parameters such as frequency range, material properties, excitation source, geometry, physical constraints, and boundary conditions. Magnetic NF distributions are analyzed to identify modes with high magnetic field density near the Tx loop, as exciting these modes significantly enhances coupling and improves Power Transfer Efficiency (PTE).

2. Modeling the Full Antenna System: The complete WPT system, comprising two identical loops (Tx and Rx), is simulated under similar setup conditions. Various misalignment scenarios, reflecting realistic user or device movements are introduced to assess their impact on coupling and to evaluate system performance in practical applications
3. Solving the Eigenvalue Problem: To obtain the CMs and their associated frequencies, the eigenvalue problem related to the proposed system should be solved. Detailed mathematical and physical background behind those computations are going to be conducted.
4. Analyzing and Visualizing Modal Properties: The analysis of the obtained CMs and the visualization of the properties, such as the resonant frequencies, the electromagnetic field patterns, and the current distributions, is important for gaining insights into the coupling behavior within the structure. Moreover, emphasis will be placed on highlighting the contribution of the dominant CM to the overall power of the system with respect to each specific configuration. Mostly further post processing analysis within the simulation package or using additional software tools can take place to enable the conversion of the CMs into formats compatible with other theories, tools or techniques. Thus, more information facilitating their integration into more detailed and comprehensive study of the coupling scenario can be addressed. For instance, in this investigation, the CMT is conducted using MATLAB by extracting the resonant frequencies data of the different resonant CMs from FEKO.
5. Experimental Validation via VNA Measurements: By connecting the MCR-WPT system to a Vector Network analyzer (VNA), the accuracy and reliability of CMA is performed by comparing simulation and post processing results to experimental measurements. When assessing antenna coupling, the measurement of scattering parameters serves to gauge the transmitted power from the Tx to the Rx units.

These steps are also summarized visually in Fig. 3.1 to provide a clear overview of the entire process.

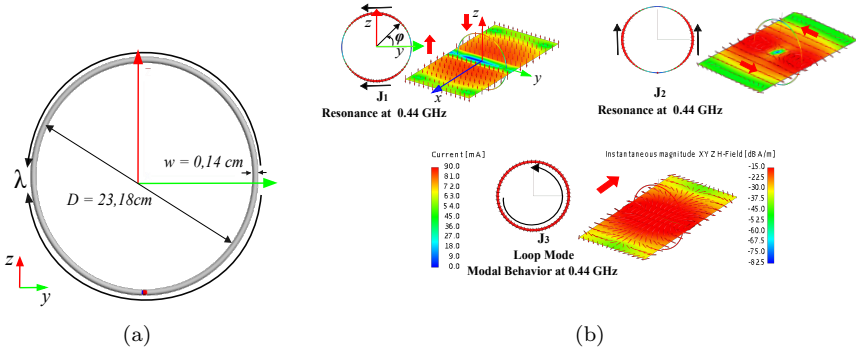


Figure 3.2: (a) Geometry and dimensions of the single loop antenna, (b) The lower order CMs. [76]

3.2 Mathematical Formulation of The Coupling of CMA for WPT Systems

The CMA of a single-turn transmitting loop antenna is performed over the 350 MHz to 2 GHz range to better understand the coupling behavior when a second loop is introduced. A loop is chosen over a multi-turn coil as shown in Fig. 3.2(a) because, electromagnetically, increasing the number of turns leads to complex inter-turn coupling, resulting in additional higher-order modes with intricate resonant frequencies and field distributions [107, 108]. Therefore, this study focuses on the CMA of a simplified MCR-WPT system using a single turn loop to minimize complexity. The Tx and Rx loops are identical and they have a diameter (D) of 23.18 cm (approximately 0.3λ) and are made of metal wire with a thickness (w) of 0.14 cm.

Building upon the CMA results of the single loop antenna presented in Chapter 2, the key outcomes will serve as a foundation for the analysis of the MCR-WPT system. In particular, special attention is given to the advantageous features of the lower-order modes in Fig. Fig. 3.2(b). In particular, the eigencurrents and their corresponding magnetic NF distributions in the XY-plane indicate that lower order modes exhibit more favorable characteristics than higher-order ones. Consequently, selectively exciting these modes can be advantageous when introducing the Rx loop, particularly in regions where the Tx loop produces a strong and stable magnetic NF density.

In the context of CMA, introducing a second loop in close proximity to the Tx loop leads to a classification of the characteristic currents \vec{J}_n into two distinct categories [102]. The first includes modes where the current distribution is identical and flows in the same direction on both loops, which are referred

3.2 Mathematical Formulation of The Coupling of CMA for WPT Systems

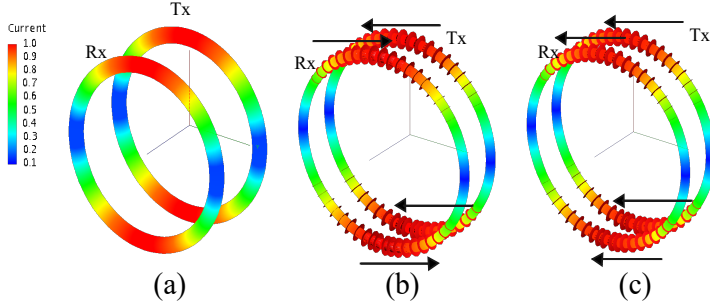


Figure 3.3: (a) Normalized current distribution of the MSC-WPT system near resonance; (b) Corresponding Transmission Line Mode (TLM) configuration; (c) Corresponding Antenna Mode (AM) configuration.

to as Antenna Modes (AM). Such modes typically exhibit a smooth variation in the characteristic angle CA_n near their resonance frequency. In contrast, when the currents on the two loops are of equal magnitude but flow in opposite directions, the resulting modes are known as Transmission Line Modes (TLM), which generally show a sharp variation in CA_n around resonance. CMA thus facilitates the identification of multiple CM pairs, each comprising an AM and its corresponding TLM. Fig. 3.3 illustrates the configuration of a TLM through the current distribution on two parallel loops.

This analysis will examine the variation in coupling between two loops under different misalignment scenarios, using a detailed physical interpretation of the fields and CMs. Leveraging Coupled Mode Theory (CMT), key parameters such as energy exchange, coupling coefficients, frequency shifts, and the influence of each AM on its corresponding TLM are analyzed at various separation distances. This analysis is based on the resonance frequency equation of coupled CMs, as presented in [88, 102, 109, 110]:

$$\omega = \frac{\omega_1 + \omega_2}{2} \pm \sqrt{\left(\frac{\omega_1 - \omega_2}{2}\right)^2 + |k_{1\leftrightarrow 2}|^2} \quad (3.1)$$

where ω_1 and ω_2 are respectively the resonance frequencies of the AM and its TLM, and $k_{1\leftrightarrow 2}$ is the coupling coefficient between these two CMs. Hence, a distinctive representation of the normalized coupling coefficient between the AM and its corresponding TLM, derived from (3.1), might be illustrated as:

$$k_{1\leftrightarrow 2} = k_{TLM\leftrightarrow AM} = \frac{|\omega_{AM}^2 - \omega_{TLM}^2|}{\omega_{AM}^2 + \omega_{TLM}^2} \quad (3.2)$$

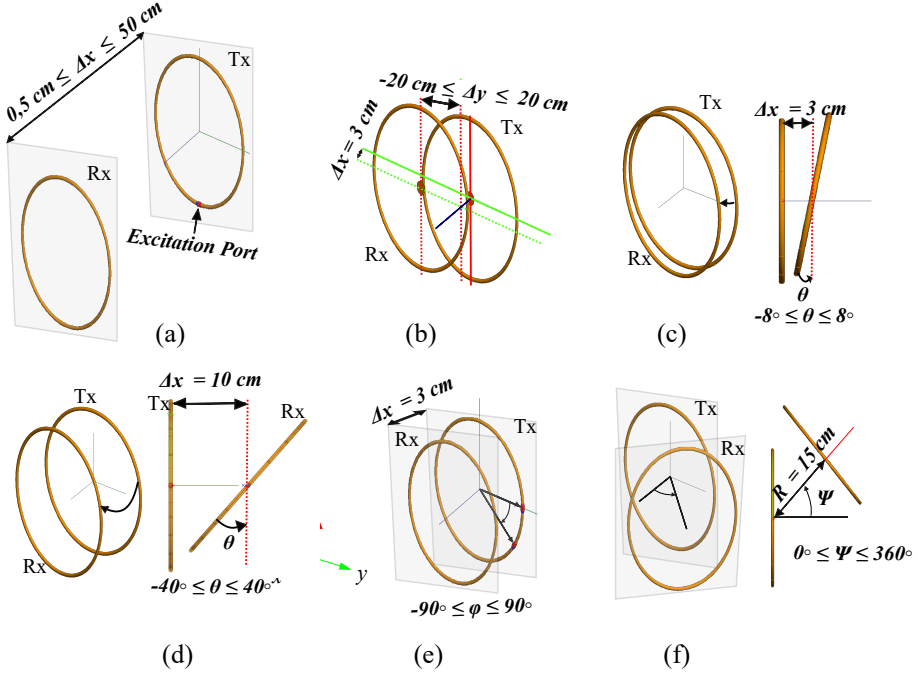


Figure 3.4: Illustration of the six misalignment scenarios analyzed: (a) Lateral misalignment along the x-axis; (b) Lateral misalignment along both x- and y-axes; (c) Azimuthal misalignment with $\Delta x = 3$ cm; (d) Azimuthal misalignment with $\Delta x = 10$ cm; (e) Rotational misalignment of the excitation port on the Tx loop; (f) Rotational misalignment of the Rx loop.

3.3 CMA Analysis of Mis. in WPT System

The variation in coupling between the Tx and Rx loops under different misalignment scenarios is investigated, as illustrated in Fig.3.4 and organized according to the sequence presented in Table3.1. In the MCR-WPT system, the Tx loop is excited by a voltage source, as shown in Fig.3.4(a), while the Rx loop includes a load port at the same angular position for measuring the received power. Using the FEKO simulation tool, the power level at the Tx source port is precisely controlled, and a constant input power of 330 mW is applied across all scenarios. The power received at the Rx load port is then recorded, taking into account the contributions of the different CMs. To accommodate the diverse eigen current configurations, the notation $J_j^{(i)}$ is used, where the subscript j denotes the mode order and the superscript i refers to the specific

3.3 CMA Analysis of Mis. in WPT System

Table 3.1: Specification of the misalignments considered under analysis.

Type of misalignment	Rx center position relative to Tx	Azimuthal angle	Tx port rotation angle	Rx center rotation angle
(1) Lateral along x-axis	$0.5 \text{ cm} \leq \Delta x \leq 50 \text{ cm}$	$\theta = 0^\circ$	$\varphi = 0^\circ$	$\Psi = 0^\circ$
(2) Lateral along y-axis	$\Delta x = 3 \text{ cm};$ $ \Delta y \leq 20 \text{ cm}$	$\theta = 0^\circ$	$\varphi = 0^\circ$	$\Psi = 0^\circ$
(3) Azimuthal	$\Delta x_1 = 3 \text{ cm};$ $\Delta x_2 = 10 \text{ cm}$	$-8^\circ \leq \theta_1 \leq 8^\circ;$ $-40^\circ \leq \theta_2 \leq 40^\circ$	$\varphi = 0^\circ$	$\Psi = 0^\circ$
(4) Rotation of Tx excitation port	$\Delta x = 3 \text{ cm}$	$\theta = 0^\circ$	$0^\circ \leq \varphi \leq 180^\circ$	$\Psi = 0^\circ$
(5) Rotation of the Rx	$R = 15 \text{ cm}$	$\theta = 0^\circ$	$\varphi = 0^\circ$	$0^\circ \leq \Psi \leq 360^\circ$

misalignment case, as detailed in Table 3.1. For example, $J_2^{(1)}$ identifies the second CM corresponding to the first misalignment scenario along the x-axis.

3.3.1 Lateral Mis. Along The X-axis

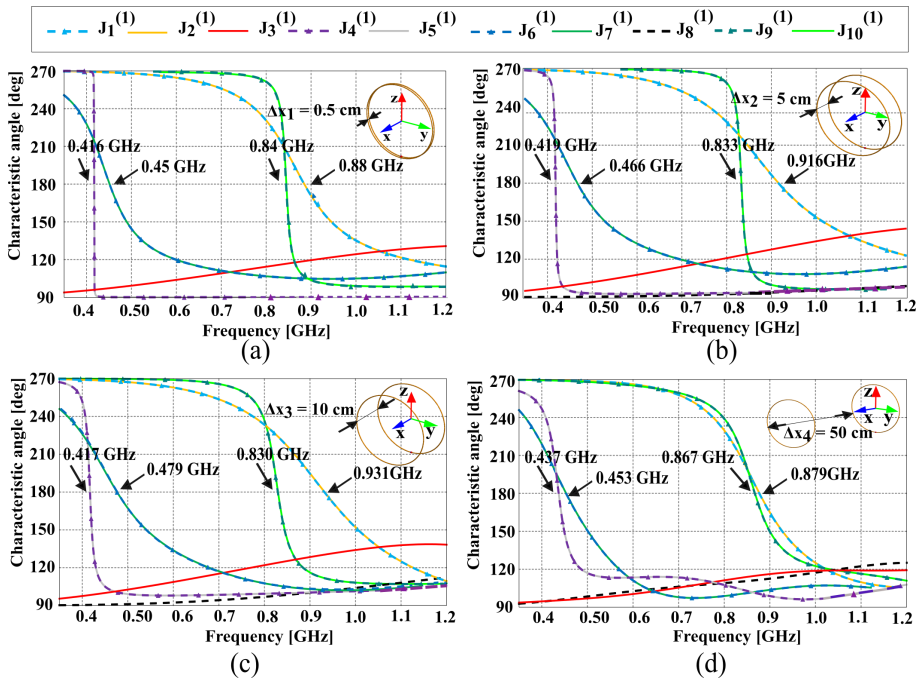


Figure 3.5: The impact of increasing the lateral mis. along the x-axis on the CA_n of the antenna system at: (a) $\Delta x_1 = 0.5 \text{ cm}$; (b) $\Delta x_2 = 5 \text{ cm}$; (c) $\Delta x_3 = 10 \text{ cm}$; (d) $\Delta x_4 = 50 \text{ cm}$.

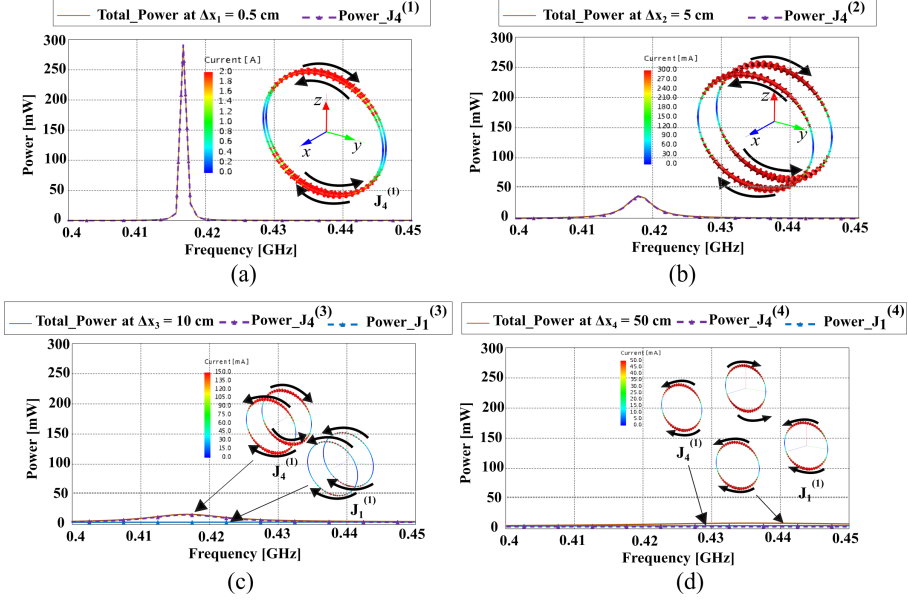


Figure 3.6: The impact of increasing lateral mis. along the x-axis on the total system power, the contribution of the dominant CMs, and their current distributions near resonance for: (a) $\Delta x_1 = 0.5$ cm; (b) $\Delta x_2 = 5$ cm; (c) $\Delta x_3 = 10$ cm; (d) $\Delta x_4 = 50$ cm.

In the first scenario described in Table 3.1 and illustrated in Fig. 3.4(a), the inter-antenna separation along the x-axis is analyzed across four discrete values ranging from 0.5 cm to 50 cm, approximately 0.007λ to 0.7λ . This range spans both the NF and FF zones, including distances beyond $\lambda/2$.

To examine how the characteristic modes (CMs) evolve with increasing lateral misalignment, Fig.3.5 presents the simulated CA_n results, obtained using FEKO, over a frequency range from 0.35 to 1.2 GHz. The figure reveals two main groups of resonant modes, each containing two subsets of degenerate CMs. Each subset comprises a pair of AMs and a pair of TLMs, each with distinct resonant frequencies. For example, Fig.3.5(a) highlights the first group of modes, consisting of a degenerate TLM pair ($J_4^{(1)}$ and $J_5^{(1)}$) and an AM pair ($J_1^{(1)}$ and $J_2^{(1)}$). The resonant frequencies of each degenerate CM set are also indicated in the figure.

It is of utmost significance to establish a clear delineation between the AM and TLM when addressing the interaction between two antennas. In this particular context, the AM mode refers to the CM in which the current configura-

3.3 CMA Analysis of Mis. in WPT System

Table 3.2: The shift of the f_{res} of $J_1^{(1)}$ and $J_4^{(1)}$ as a function of Δx .

Δx (cm)	f_{res} of $J_1^{(1)} : \omega_{AM}$ (GHz)	f_{res} of $J_4^{(1)} : \omega_{TLM}$ (GHz)
0.14λ	0.479	0.417
0.7λ	0.453	0.437
2λ	0.449	0.435
3λ	0.445	0.439
4λ	0.441	0.441
4.5λ	0.441	0.441

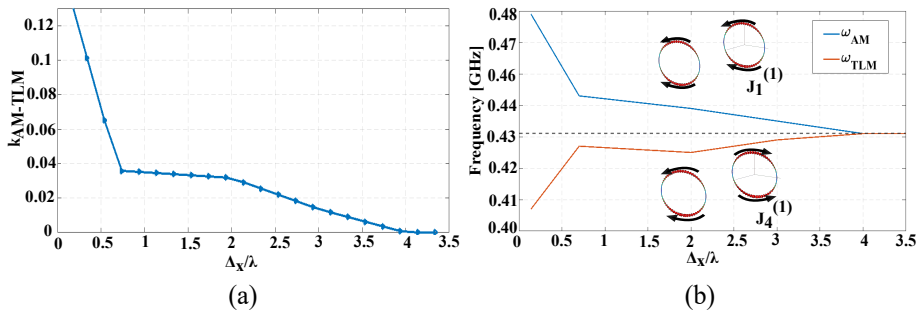


Figure 3.7: Modal intercoupling analysis when the lateral misalignment lies between $\Delta_x = 0.14\lambda$ and $\Delta_x = 3.5\lambda$: a) Normalized coupling coefficient between $J_1^{(1)}$ and $J_4^{(1)}$; b) The resonance frequency of $J_1^{(1)}$ and $J_4^{(1)}$.

tion and flow exhibit precisely identical characteristics in both loops. The TLM mode is characterized by the presence of opposite current directions in the two loops while maintaining the same current distribution as shown in Fig. 3.3.

As the separation distance between the loops progressively increases, a noticeable frequency shift is observed, as shown in Fig.3.5(b) and Fig.3.5(c). When the antennas are placed at a larger distance from each other, as presented in Fig. 3.5(d), the modes within each group tend to converge toward nearly identical resonant frequencies.

To determine which modes contribute most significantly to the system's power, Fig.3.6 displays the total received power along with the individual contributions of the dominant characteristic modes at various separation distances. At shorter distances, the system's power is primarily influenced by TLM $J_4^{(1)}$. However, as the distance between the loops increases, the AM $J_1^{(1)}$ begins to play a more prominent role. This shift, as illustrated in Fig.3.6(d), leads to a

noticeable reduction in the total received power. Notably, these findings are consistent with those reported in [111], confirming that $J_4^{(1)}$ is the dominant power-contributing mode at close range. To compute the normalized intercoupling between $J_1^{(1)}$ and $J_4^{(1)}$ using Eq.3.2, Table3.2 presents the variation in the resonant frequencies of the TLM and its associated AM as a function of Δx . Fig.3.7(a) illustrates the evolution of the coupling coefficient $k_{J_1^{(1)} \leftrightarrow J_4^{(1)}}$ with increasing lateral misalignment, while Fig.3.7(b) shows the corresponding resonant frequency shifts. The results indicate that the overall antenna coupling is strongly influenced by the intercoupling between the dominant TLM $J_4^{(1)}$ and its associated AM $J_1^{(1)}$. As the separation distance increases, the frequency shift between the two modes becomes more pronounced, and they gradually converge toward the same resonance frequency (f_{res}), marked by the dotted line in Fig. 3.7(b). This frequency corresponds to the f_{res} of J_1 , previously identified as the dominant mode of the isolated loop antenna. At this stage, the behavior of each loop becomes entirely decoupled from the other.

3.3.2 Lateral Mis. Along The Y-axis

The second scenario of misalignment, presented in Table 3.1 and illustrated in Fig. 3.4(b), consists of placing the Rx coil at a fixed distance of 3 cm (0.04λ) from the Tx coil along the x-axis, while varying the lateral offset along the y-axis (Δy). The choice of this specific Y-axis separation is motivated by practical design constraints associated with the Qi wireless charging standard and typical use cases in wearable and implantable device applications, where the effective power transfer range is intentionally constrained, usually limited to a few millimeters or centimeters, to ensure alignment and maximize efficiency.

The results of the CMA are presented in Fig.3.8 and Fig.3.9, with the frequency range constrained between 0.35 GHz and 0.6 GHz. This specific range was selected due to the dominant influence of lower-order characteristic modes, which have shown to be more effective in capturing the coupling behavior between the coils. The initial configuration, illustrated in Fig. 3.8(a), corresponds to a perfectly aligned Tx and Rx pair, where the characteristic angle responses (CA_n) reveal two distinct sets of degenerate modes, each centered around different resonant frequencies.

To investigate the effect of this misalignment, the Rx loop is progressively displaced along the y-axis in symmetric steps, ranging from -68 cm to $+68$ cm (i.e., $\pm\lambda$). Due to the geometric symmetry of the system, these mirrored configurations yield identical modal responses. This symmetry is evident in Fig.3.8(b) and Fig.3.8(c), which display the characteristic angles for Rx positions at $+5$ cm and -5 cm, respectively. Besides, as shown in Fig. 3.9, TLM $J_4^{(2)}$ emerges as the dominant mode proximate to the resonance of the sys-

3.3 CMA Analysis of Mis. in WPT System

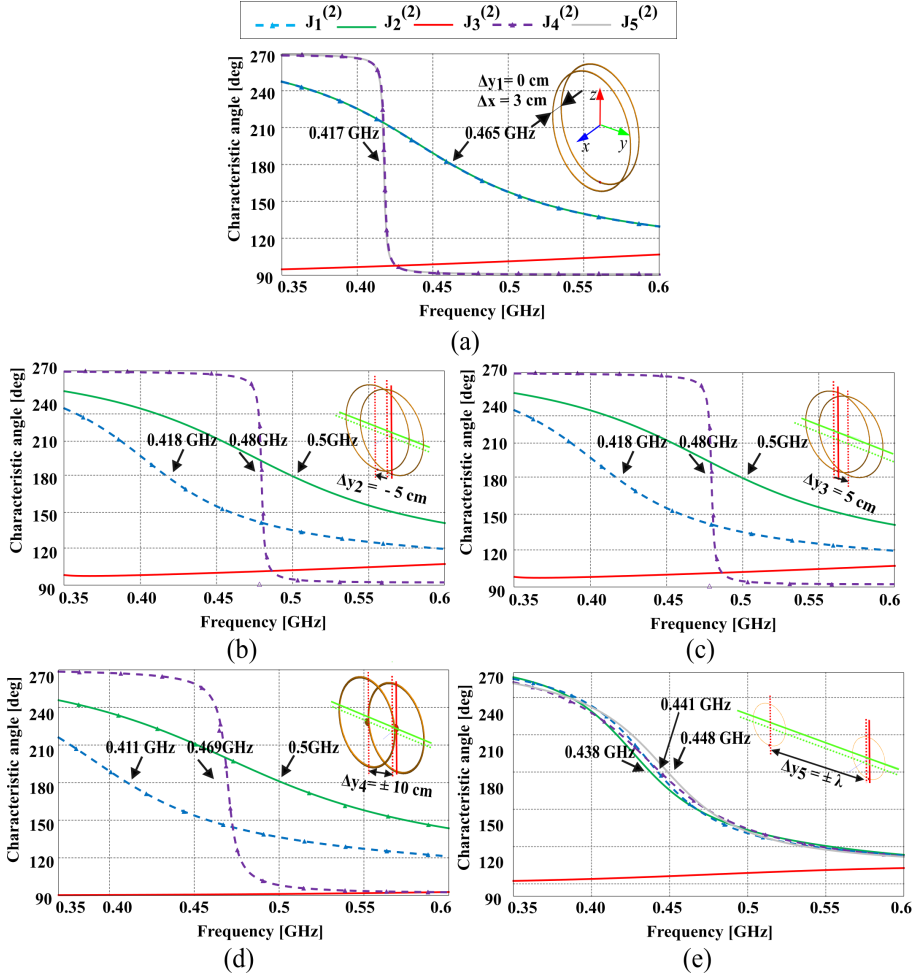


Figure 3.8: The impact of increasing the lateral mis. along the y -axis on the CA_n of the antenna system at: (a) $\Delta y_1 = 0$ cm; (b) $\Delta y_2 = +5$ cm. (c) $\Delta y_3 = -5$ cm; (d) $\Delta y_4 = \pm 10$ cm; (e) $\Delta y_5 = \pm \lambda$.

tem in both configurations. Thus, the broader overlap distances, illustrated in Fig. 3.8(d) and Fig. 3.8(e), correspond to symmetric positions of Δy , which are ± 10 cm ($\pm 0.14\lambda$) and $\pm \lambda$.

A comparison between the CMA results shown in Fig. 3.8(a) and Fig. 3.8(b) reveals that a small incremental displacement of just 5 cm (0.07λ) along the y -axis leads to a noticeable dispersion of the characteristic modes and a significant

CHAPTER 3. CMA FOR MISALIGNMENT IN WPT SYSTEM

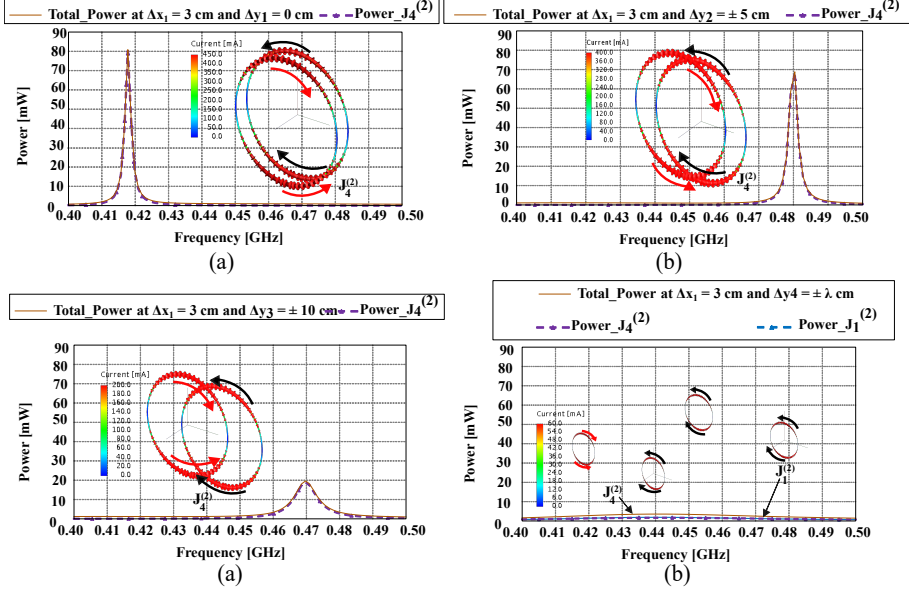


Figure 3.9: The impact of increasing lateral mis. along the y-axis on the total system power, the contribution of the dominant CMs, and their current distributions near resonance for: (a) $\Delta y_1 = 0$ cm; (b) $\Delta y_2 = \pm 5$ cm; (c) $\Delta y_3 = \pm 10$ cm; (d) $\Delta y_4 = 63$ cm ($\pm \lambda$).

shift in their resonance frequencies. This sensitivity to misalignment is further confirmed by the power simulations in Fig.3.9(a) and Fig.3.9(b), which clearly demonstrate that even a minor displacement results in a substantial reduction in the system's transmitted power.

Moreover, the observed frequency shift in the system's resonance aligns with the variation in the dominant TLM, as indicated by the close correspondence between the resonance peaks of the total transmitted power and the relevant characteristic modes. At larger separation distances, where coupling between the Tx and Rx units becomes negligible, as illustrated in Fig.3.9(e), the TLMs and AMs converge to the same resonance frequency. This decoupled state is also evident in the modal response of AM $J_1^{(2)}$, shown in Fig.3.9(c), which highlights the lack of interaction between the transmitting and receiving elements.

To provide a clearer understanding of the previously discussed frequency shifts and modal coupling behavior, Table 3.3 presents the variation in the resonant frequencies of the TLM and its associated AM as a function of Δx . These values are used to compute the normalized intercoupling coefficient between modes $J_1^{(1)}$ and $J_4^{(1)}$ using Eq.3.2. The corresponding coupling behavior

3.3 CMA Analysis of Mis. in WPT System

Table 3.3: The shift of the f_{res} of $J_1^{(2)}$ and $J_4^{(2)}$ as a function of Δy .

Δy (cm)	f_{res} of $J_1^{(2)}$: ω_{AM} (GHz)	f_{res} of $J_4^{(2)}$: ω_{TLM} (GHz)
0	0.465	0.417
$\pm 0.07\lambda$	0.418	0.448
$\pm 0.14\lambda$	0.411	0.469
$\pm \lambda$	0.441	0.441

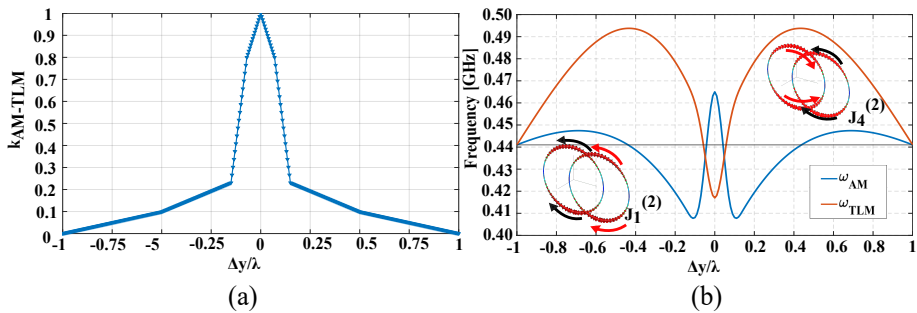


Figure 3.10: Modal intercoupling analysis when the lateral misalignment along the y-axis: (a) Normalized coupling coefficient between $J_1^{(2)}$ and $J_4^{(2)}$ for Δy between -2λ and 2λ , b) The resonant frequency of $J_1^{(2)}$ and $J_4^{(2)}$ for Δy ranging from $-\lambda$ and λ .

between the dominant TLM and its associated AM is illustrated in Fig.3.10. For the calculation of the coupling coefficient $k_{J_1^{(2)} \leftrightarrow J_4^{(2)}}$, the central configuration shown in Fig.3.9(a), which is characterized by negligible displacement along the y-axis, is identified as the optimal case, yielding the maximum power transfer. This configuration is therefore considered the reference point representing the system's optimal coupling condition. Coupling coefficients for other misaligned positions are determined relative to this baseline and are also illustrated in Fig.3.9. As shown, increasing the overlap between the coils leads to a significant enhancement in the coupling strength between AM $J_1^{(2)}$ and its corresponding TLM $J_4^{(2)}$.

3.3.3 Azimuthal Mis.

Azimuthal misalignment, denoted by the angle θ , refers to the angular deviation between the azimuthal orientations of the two loop antennas, as illustrated in Fig.3.4(c) and Fig.3.4(d). In practical applications, this type of misalignment

CHAPTER 3. CMA FOR MISALIGNMENT IN WPT SYSTEM

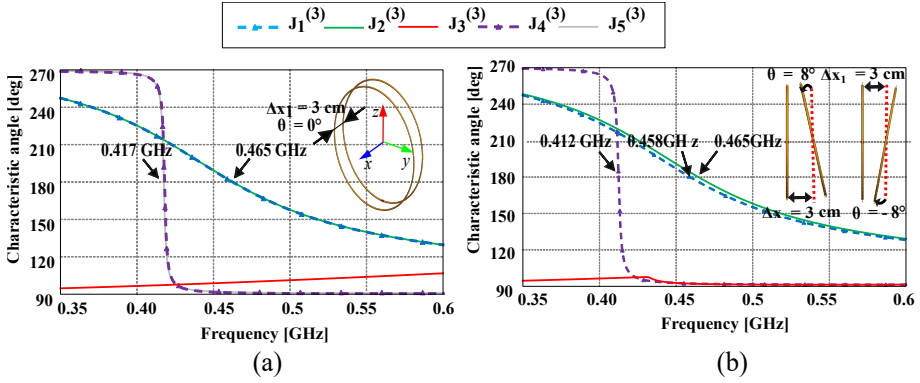


Figure 3.11: of the azimuthal misalignment at $\Delta x_1 = 3$ cm on the CA_n of the antenna system at: (a) $\theta = 0^\circ$; (b) $\theta = \pm 8^\circ$.

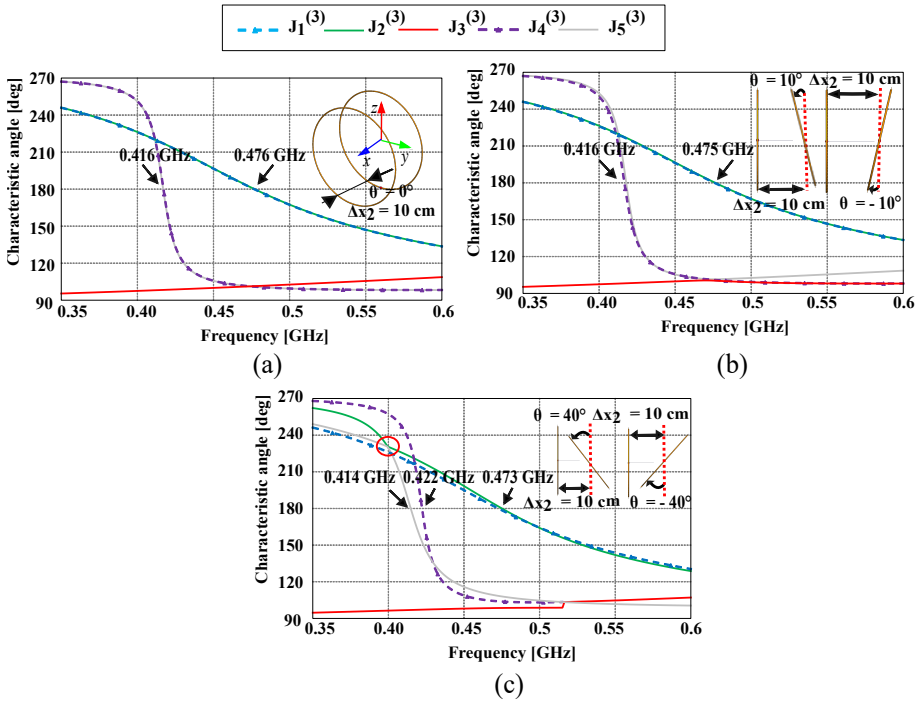


Figure 3.12: The impact of the azimuthal misalignment at $\Delta x_2 = 10$ cm on the CA_n of the antenna system at: (a) $\theta = 0^\circ$. (b) $\theta = \pm 10^\circ$. (c) $\theta = \pm 40^\circ$.

3.3 CMA Analysis of Mis. in WPT System

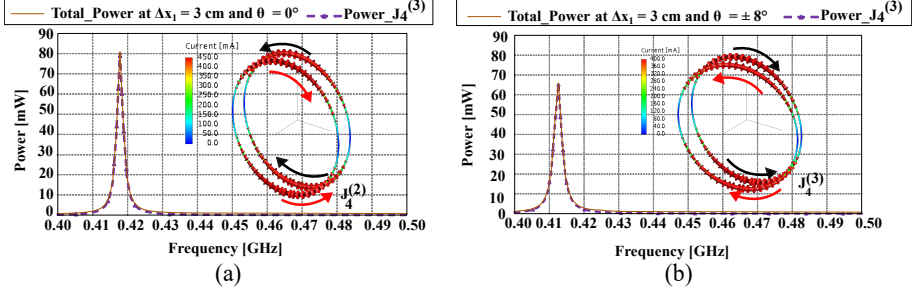


Figure 3.13: The impact of the azimuthal misalignment at $\Delta x_1 = 3$ cm on the total system power, the contribution of the dominant CMs, and their current distributions near resonance for: (a) $\theta = 0^\circ$. (b) $\theta = \pm 8^\circ$.

typically results from a non-parallel alignment of the Rx loop with respect to the Tx loop. In this study, azimuthal misalignment is examined under two distinct spatial configurations, given that the close proximity of the loops imposes limitations on the range of permissible angular orientations. In the first configuration, the Rx loop is positioned 3 cm away from the Tx loop along the x-axis, allowing for symmetric azimuthal deviations ranging from -8° to $+8^\circ$. In the second configuration, the lateral separation is increased to 10 cm (0.14λ), permitting a broader range of azimuthal rotations between -40° and $+40^\circ$. The CMA for both scenarios is carried out concurrently within the same section to enable a comprehensive assessment of the combined effects of angular deviation and lateral displacement on the coupling behavior.

As illustrated in Fig.3.11(b) and Fig.3.12(b), a minor azimuthal misalignment of the Rx loop, when $\theta =$ is equal to $\pm 8^\circ$ and $\pm 10^\circ$, has a negligible effect on the modal behavior when compared to the characteristic angles (CA_n) of the initial aligned configurations shown in Fig.3.12(a) and Fig.3.12(a). However, when the azimuthal deviation increases to $\pm 40^\circ$, as seen in Fig.3.12(c), the CA_n become more dispersed, indicating a more pronounced impact of misalignment on the modal structure.

A similar trend is observed in the power response plots in Fig.3.13 and Fig. 3.14, where small azimuthal deviations result in only a slight reduction in total transmitted power. Notably, the TLM $J_4^{(3)}$ consistently dominates and contributes most significantly to the system's power transfer across all configurations.

In summary of the interactions observed under azimuthal misalignment, and given the minimal influence detected at short separation distances, Fig. 3.15 clearly illustrates the resonance frequency shifts and modal coupling behavior of both the TLM $J_4^{(3)}$ and the AM $J_1^{(3)}$. This analysis corresponds to the

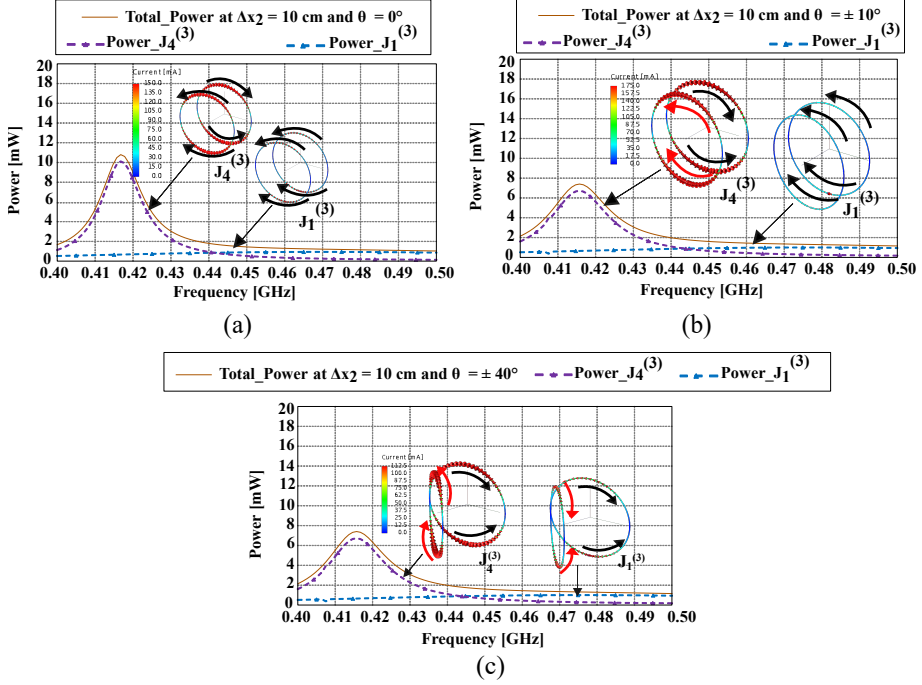


Figure 3.14: The impact of the azimuthal misalignment at $\Delta x_2 = 10$ cm on the total system power, the contribution of the dominant CMs, and their current distributions near resonance for: (a) $\theta = 0^\circ$; (b) $\theta = \pm 10^\circ$; (c) $\theta = \pm 40^\circ$.

configuration where the Rx loop is placed at Δx_2 , and its orientation spans a wide range of azimuthal angles, culminating in a fully perpendicular alignment between the two coils. Overall, the results confirm that azimuthal misalignment induces a less significant impact on the system's coupling behavior when compared to lateral displacement scenarios.

3.3.4 Rotational Mis. of The Excitation Port Placed on The TX Loop

As detailed in Table 3.1 and illustrated in Fig.3.4(e), this misalignment scenario involves a strictly parallel alignment of the Tx and Rx coils with a fixed separation distance of 3 cm (0.04λ). However, unlike previous configurations, the source excitation on the Tx loop is subjected to various angular rotations. This configuration simulates a realistic situation in which a device is placed

3.3 CMA Analysis of Mis. in WPT System

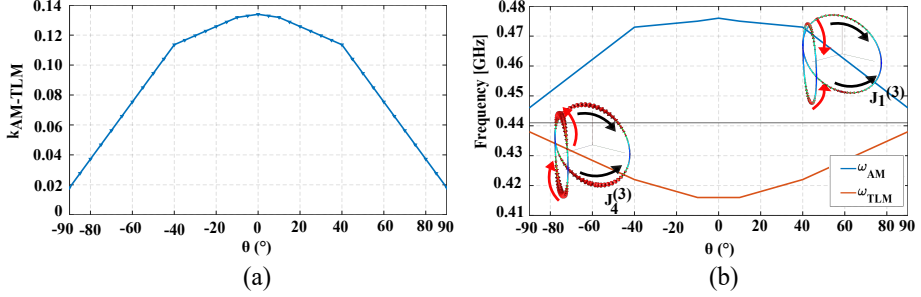


Figure 3.15: Modal intercoupling analysis when azimuthal misalignment at $\Delta x_2 = 10$ cm for θ between -90° and $+90^\circ$: (a) Normalized coupling between $J_1^{(3)}$ and $J_4^{(3)}$; (b) The resonance frequency of $J_1^{(3)}$ and $J_4^{(3)}$.

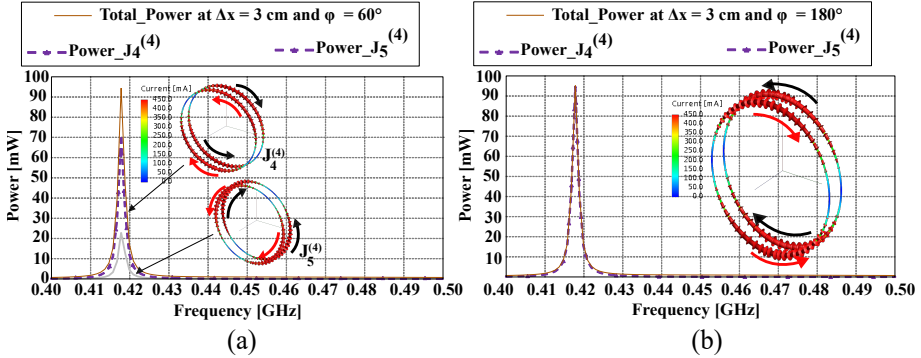


Figure 3.16: Modal intercoupling analysis when azimuthal misalignment at $\Delta x_2 = 10$ cm for θ between -90° and $+90^\circ$: (a) Normalized coupling between $J_1^{(3)}$ and $J_4^{(3)}$; (b) The resonance frequency of $J_1^{(3)}$ and $J_4^{(3)}$.

arbitrarily on a wireless charger, resulting in proper coil alignment, while the excitation and load ports remain misaligned due to the orientation of the device, the excitation port on the Tx loop is not parallel to the load port on the Rx loop, as illustrated in Fig.3.4(e).

The CMA results shown in Fig.3.16 reveal that even substantial rotations of the excitation port have negligible influence on the system's modal behavior. The resonant frequencies of the characteristic modes remain largely unaffected. This observation aligns with the theoretical foundation of CMA, wherein characteristic modes are inherently independent of excitation conditions. Conse-

quently, the characteristic angles (CA_n) remain consistent with those presented in Fig.3.8(a).

Furthermore, as shown in Fig. 3.16, the rotational misalignment of the Tx port has minimal impact on the total received power, which remains consistently within the range of 90 to 100 mW. This stability can be attributed to the rotational symmetry of the current distribution associated with the loop's CMs. Notably, the TLM $J_4^{(4)}$ and its degenerate counterpart $J_5^{(4)}$ contribute dominantly to the overall system power. The relative contribution of these two modes varies with the excitation port's orientation, while no significant presence of an Antenna Mode (AM) is observed in the power response. This absence of AM participation explains the lack of decoupling effects between the coils in contrast to the previously analyzed misalignment scenarios.

3.3.5 Rotational Mis. of The RX loop

This final scenario (described in Table 3.1 and illustrated in Fig. 3.4(f)) elucidates the CMA of the coupling within a WPT system, where the Rx coil executes rotational motion at specific distance around the Tx coil. This entails a stationary position for the Tx, while the Rx engages in circular rotation with a constant radius, thereby delineating a circular trajectory, as shown in Fig. 3.4(f). To enable this rotational movement, the radius of the circle R is set to 15 cm (0.21λ), which leads to a substantial power loss. Therefore, an assessment of various positions of the Rx coil will be conducted relative to the initial configuration, where both the Tx and Rx antennas are perfectly aligned in parallel, as described in Fig. 3.17. During the course of these analyses, it was observed that the CMA and power radiation exhibit three distinct variations with respect to the rotation angle, as shown in Fig. 3.17 and Fig. 3.18. As observed in Fig. 3.18, the system attains its peak power levels during the initial and the final positions, denoted by ψ equal to 0° and 180° . As the rotation angle ψ increases within the range of 0° to $\pm 90^\circ$, the power of the system and the current intensity of the dominant mode $J_4^{(5)}$ decrease enormously by reaching a null value.

3.4 Main observations: CMA of the proposed WPT system

The central objective of integrating Coupled Mode Theory (CMT) into Characteristic Mode Analysis (CMA) in this study is to highlight the strong relationship between modal intercoupling patterns and power variation. In this chapter, CMA was employed using characteristic angles (CA_n) to identify the resonant modes and their corresponding frequencies. Additionally, power dis-

3.4 Main observations: CMA of the proposed WPT system

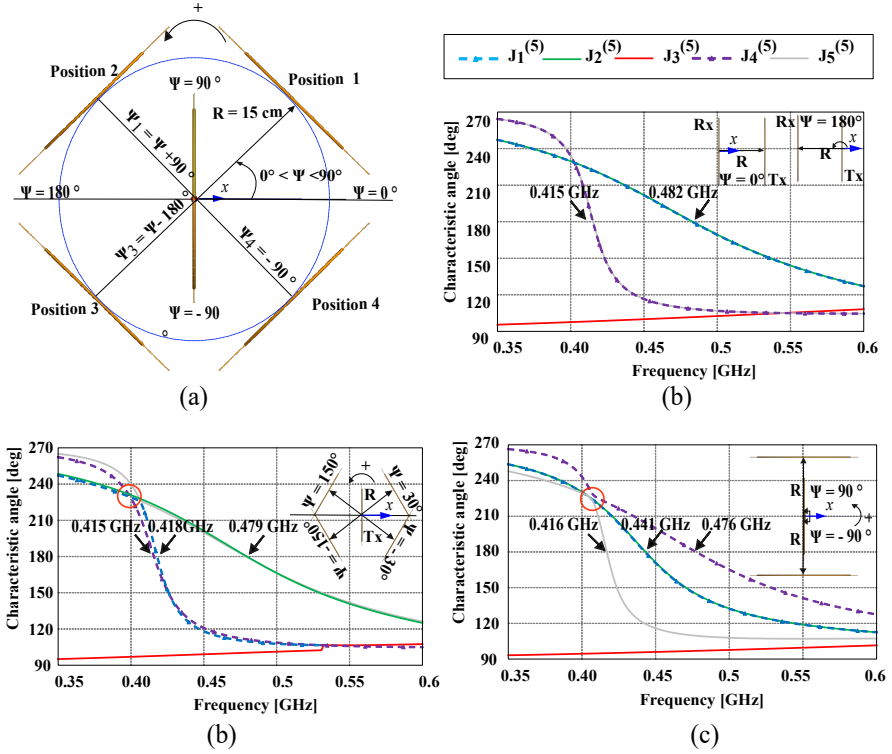


Figure 3.17: (a) Illustration of the rotational mis. of the Rx loop around the Tx loop with a radius $R = 15$ cm; (b) (CA_n) response of the antenna system at $\psi = 0^\circ$ and 180° ; (c) CA_n response at intermediate angular positions $\psi = \pm 30^\circ$ and $\pm 150^\circ$; (d) CA_n response at orthogonal orientations $\psi = \pm 90^\circ$.

tribution among the modes was analyzed to determine the mode that predominantly contributes to the received power at the Rx loop, which is referred to here as the dominant mode. The distribution of eigen currents confirms that this dominant mode corresponds to a Transmission Line Mode (TLM) characterized by horizontal nulls. Using CMT, the degree of intermodal coupling was computed based on the resonant frequencies of the TLM and its associated Antenna Mode (AM). The modal features extracted across different misalignment configurations produced consistent results. Specifically, as modal inter-coupling decreases, indicating closer frequency alignment between the dominant TLM and its corresponding AM, the system exhibits a marked drop in efficiency, as evidenced by a significant reduction in power received at the Rx coil.

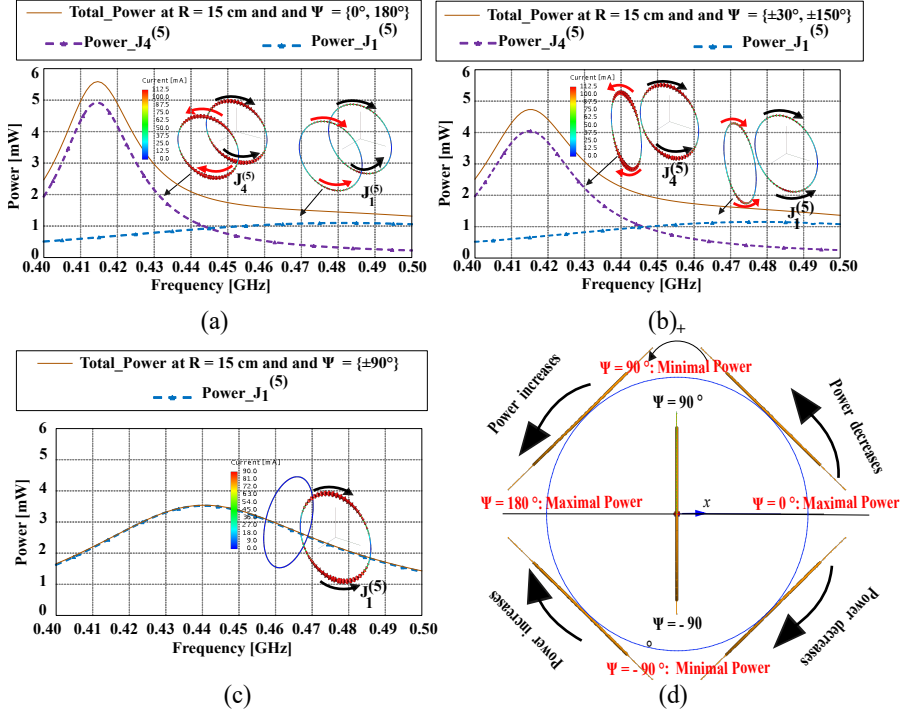


Figure 3.18: The impact of Rx loop rotational misalignment on the system's total power, including the contribution of dominant CMs and their corresponding current distributions near resonance, is analyzed at: (a) $\psi = 0^\circ$ and 180° ; (b) $\psi = \pm 30^\circ$ and $\pm 150^\circ$; (c) $\psi = \pm 90^\circ$; (d) Variation in the total received power across the full range of angular positions.

The effectiveness of this combined CMA-CMT approach, however, depends on the nature of the misalignment under investigation. For example, in cases involving lateral and azimuthal misalignments, the modal resonant frequencies remain clearly identifiable, making the application of CMT straightforward. In contrast, for rotational misalignment of the Rx coil, the CMA results exhibit dynamic tracking behavior that obscures the identification of precise resonant frequencies, thereby limiting the practical applicability of CMT in those cases.

To conclude with this chapter, the study confirms the detailed CMA to WPT in different scenarios. While prior research has examined similar analysis, those efforts were generally limited to a narrow set of misalignment conditions and often lacked experimental validation [102, 112]. In contrast, the

3.4 Main observations: CMA of the proposed WPT system

present work introduces a broader spectrum of scenarios to rigorously evaluate and validate the proposed methodology through measurement in the coming chapter.

CHAPTER 3. CMA FOR MISALIGNMENT IN WPT SYSTEM

Chapter 4

Validation of CMA for Misalignment in WPT System

To establish a comprehensive and concise reference on the applicability of Characteristic Mode Analysis (CMA) in the context of Wireless Power Transmission (WPT), the proposed analytical and simulation-based approach, presented in Chapter 3, is validated through experimental measurements. Specifically, the S-parameters are measured and the received power at the Rx coil is evaluated relative to the transmitted power. Using key modal parameters, such as resonant frequencies, magnetic field distributions, and current patterns, the dominant characteristic mode is identified. Its contribution to the overall system performance is then assessed and compared to the observed behavior of the WPT system near its resonant frequency. This comparative analysis serves as the basis for validating the effectiveness of the CMA-based proposed methodology.

4.1 Experimental Setup and Validation Methodology

To validate the proposed analysis and simulation results of the WPT system, this section presents the experimental setup used to measure the S-parameters and evaluate the received power at the Rx coil in relation to the transmitted power delivered by the Vector Network Analyzer (VNA) to the Tx coil, across the frequency range of 0.3 to 0.6 GHz. The Tx and Rx loop antennas were fab-

CHAPTER 4. VALIDATION OF CMA FOR MISALIGNMENT IN WPT SYSTEM

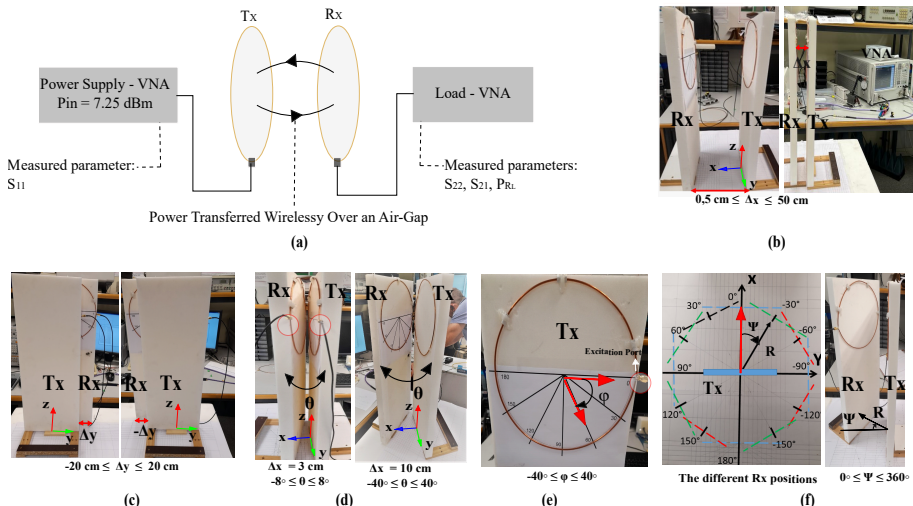


Figure 4.1: Measurement setups for the different mis. scenarios and corresponding block diagram: (a) Block diagram of the Tx and Rx loops with associated components; (b) Lateral mis. along the x-axis; (c) Lateral mis. along the y-axis at $\Delta x = 3$ cm; (d) Azimuthal mis. at two positions: $\Delta x = 3$ cm and $\Delta x = 10$ cm; (e) Rotational mis. of the excitation port; (f) Rotational mis. of the Rx.

ricated using copper wire, each with a diameter (D) of 23.18 cm (approximately 0.3λ) and a thickness (w) of 0.14 cm. The measurement setups corresponding to the various misalignment scenarios are illustrated in Fig. 4.1.

In this study, two expressions of Power Transfer Efficiency (PTE) are considered, denoted as $\text{PTE}_{\text{measured}}^1$ and $\text{PTE}_{\text{measured}}^2$, which are derived from Equations 4.1 and 4.2, respectively. Additionally, the analytical PTE, referred to as $\text{PTE}_{\text{calculated}}$, is formulated using the same expression as in Equation 4.2, but is computed based on the S-parameters obtained through full-wave electromagnetic simulations performed in FEKO, as described in [102, 113]. The two expressions are defined as follows::

$$\text{PTE}_{\text{measured}}^1 = \frac{P_{R_L}}{P_{in}} = \frac{|I_2|^2 R_L}{|I_1|^2 R_{in}} \quad (4.1)$$

$$\text{PTE}_{\text{measured}}^2 = \frac{|S_{21}|^2}{(1 - |S_{11}|^2)(1 - |S_{22}|^2)} \approx |S_{21}| \quad (4.2)$$

4.2 Measurement of The Lateral Mis. Along The X-axis

Where P_{RL} denotes the power dissipated in the load resistance R_L of the Rx coil, P_{in} is the power accepted by the Tx antenna, R_{in} represents the input resistance of the Tx antenna, and I_1 and I_2 are the currents flowing through the Tx and Rx antennas, respectively, as defined in Equation 4.1.

In particular, the input power P_{in} is configured using the VNA and set to 7.25 dBm. The corresponding power received at the Rx coil is also directly measured using the same instrument, as illustrated in the block diagram in Fig. 4.1(a). The essential parameters defined in the preceding equations are thus obtained through precise VNA measurements. This experimental setup not only enables quantitative comparisons but also supports meaningful analogies with the results derived from CMA. Additionally, Table 4.1 summarizes the key parameters discussed and provides a clear visual representation of the comparisons conducted in this study. Beyond simply comparing theoretical and measured PTE values, the study offers a comprehensive evaluation of the system's behavior under various conditions, emphasizing the role of two distinct measured PTE formulations; thereby, enriching the overall analysis and interpretation.

The primary objective of this comparison is to investigate the correlation between CMA and the performance of the WPT system in the vicinity of its resonant frequency. By leveraging the techniques and methodologies discussed in this study, CMA can be effectively employed to gain deeper insights into the coupling behavior between two coils. This understanding serves as a foundation for improving the PTE in the presence of misalignment issues commonly encountered in loop-based WPT systems in biomedical applications.

4.2 Measurement of The Lateral Mis. Along The X-axis

To explore the system behavior in greater depth, the initial measurement illustrated in Fig. 4.1(b) focuses on lateral misalignment along the x-axis. This scenario involves four distinct coil positions, spanning from the near-field (NF) to the far-field (FF), with separation distances ranging from 0.5 cm ($< \lambda/2$) to 50 cm ($> \lambda/2$).

At the shortest distance, as shown in Fig.4.2(a), the corresponding results in Table4.1 reveal a peak PTE of 88.67%, representing the highest efficiency observed. As the separation increases, as illustrated in Fig.4.2(b) and Fig.4.2(c), a significant drop in coupling efficiency is observed. Ultimately, in the final configuration (Fig. 4.2(d)), the system's performance is nearly lost.

These experimental observations are in strong agreement with the CMA analysis across the different separation distances discussed in Chapter 3. The resonance frequency f_{res} of the dominant mode, $J_4^{(1)}$, closely matches the sys-

CHAPTER 4. VALIDATION OF CMA FOR MISALIGNMENT IN WPT SYSTEM

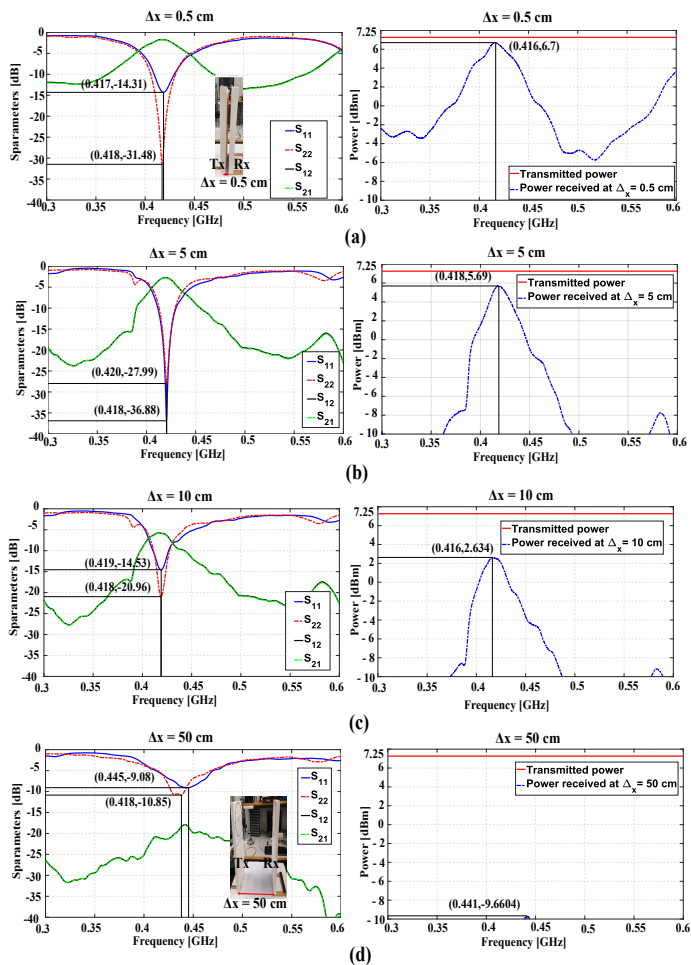


Figure 4.2: S-parameter measurements (S_{11} , S_{22} , S_{21} , and S_{12}) and PTE evaluations for various lateral mis. along the x-axis: (a) $\Delta x_1 = 0.5$ cm; (b) $\Delta x_2 = 5$ cm; (c) $\Delta x_3 = 10$ cm; and (d) $\Delta x_4 = 50$ cm.

tem's measured f_{res} . Additionally, both the measured and calculated PTEs exhibit variation trends consistent with the power peaks of the corresponding coupling mode. It is also important to highlight that $PTE_{measured}^1$, which accounts for both transmitted and received power levels, demonstrates better alignment with the theoretical PTE compared to $PTE_{measured}^2$.

4.3 Measurement of The Lateral Mis. Along The Y-axis

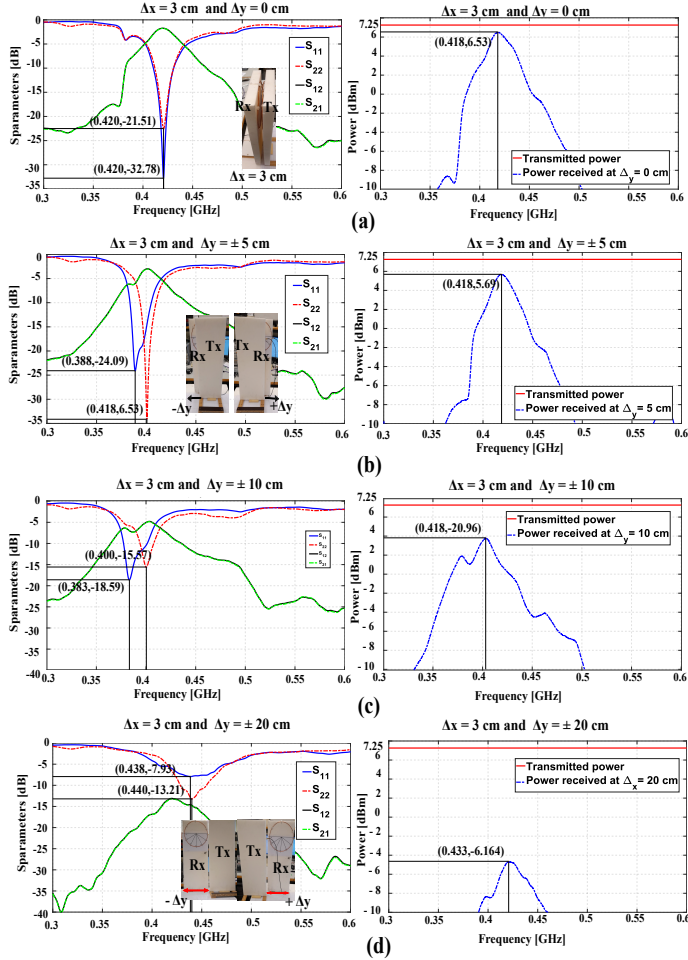


Figure 4.3: S-parameter measurements (S_{11} , S_{22} , S_{21} , and S_{12}) and PTE evaluations for various lateral mis. along the y-axis:(a) $\Delta y_1 = 0.5$ cm; (b) $\Delta y_2 = \pm 5$ cm; (c) $\Delta y_3 = \pm 10$ cm; (d) $\Delta y_4 = \pm 50$ cm.

4.3 Measurement of The Lateral Mis. Along The Y-axis

In the second scenario, illustrated in Fig. 4.1(c), a fixed lateral misalignment of 3 cm is maintained along the x-axis, while measurements are conducted at seven distinct positions along the y-axis.

CHAPTER 4. VALIDATION OF CMA FOR MISALIGNMENT IN WPT SYSTEM

These include the central position ($\Delta y = 0$) and three pairs of symmetrical offsets ranging from -20 cm to $+20$ cm. As anticipated, the coupling behavior exhibits symmetry with respect to the central position, confirming consistent performance when Δy .

Accordingly, Fig.4.3 presents the lateral misalignments along the positive y-axis. While the analytical and experimental results show strong agreement in terms of f_{res} at the initial and final positions, discrepancies arise at the intermediate offsets, where Δy is equal to ± 5 and ± 10 cm. In these cases, the theoretical predictions indicate a broader variation in f_{res} compared to the measurements. For example, at $\Delta y = \pm 10$ cm, the simulated resonance frequency associated with the dominant coupling mode $J_4^{(2)}$ is approximately 0.47 GHz. However, the corresponding measured resonance frequency shifts to a lower value of 0.403 GHz, as depicted in Fig. 4.3(c).

Similarly, as seen in the previous misalignment analysis, the PTE measured using the ratio of received to transmitted power ($\text{PTE}_{\text{measured}1}$) demonstrates closer agreement with the theoretical predictions. It is also worth noting that the theoretical values consistently exceed the measured ones, particularly at the largest misalignment distances.

4.4 Measurement of The Azimuthal Mis.

With respect to the azimuthal misalignment depicted in Fig.4.1(d), the impact of angular rotations of the Rx coil around the z-axis on system performance was evaluated at two different lateral distances along the x-axis. This approach was necessary, as rotational movement is limited at shorter separations. As shown in Fig.4.4, at a close distance of 3 cm, measurements were carried out for two angular configurations corresponding to $\theta = -8^\circ$ and $+8^\circ$. In contrast, for the larger separation distance of 10 cm, the experimental setup included wider symmetrical azimuthal rotations, reaching $\theta = -40^\circ$ and 40° .

The data presented in Table 4.1 indicate that azimuthal misalignments cause a slight reduction in all three PTE values when compared to the baseline configuration at $\theta = 0^\circ$. Notably, the PTE measured as the ratio of received to transmitted power shows the closest agreement with the values obtained from FEKO simulations. In the short range configuration, azimuthal misalignment results in a PTE decrease of approximately 4%. At a greater separation distance, the most significant angular deviation ($\theta = +40^\circ$) leads to a smaller reduction of around 2%. These findings suggest that, compared to other types of misalignment, azimuthal variations have a relatively limited effect on the system's overall PTE.

Within the context of CMA, the experimental results show strong agreement with the analysis outlined in the previous section. In particular, the modal

4.4 Measurement of The Azimuthal Mis.

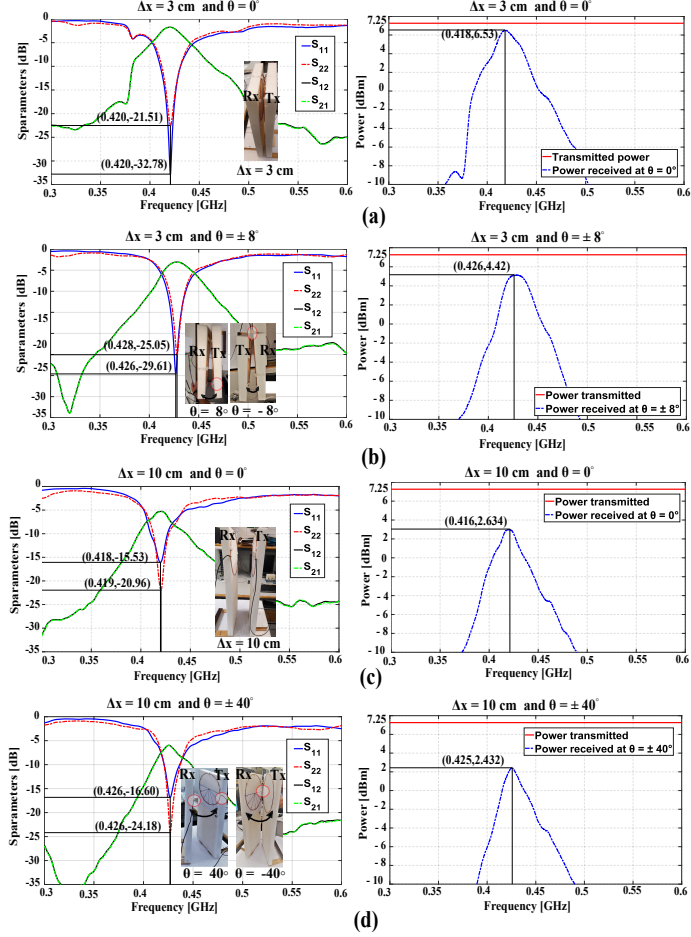


Figure 4.4: S-parameter measurements (S_{11} , S_{22} , S_{21} , and S_{12}) and PTE evaluations for the azimuthal mis. along: (a) $\Delta_x = 3$ cm and $\theta = 0^\circ$. (b) $\Delta_x = 3$ cm and $\theta = \pm 8^\circ$. (c) $\Delta_x = 10$ cm and $\theta = 0^\circ$; (d) $\Delta_x = 10$ cm and $\theta = \pm 40^\circ$.

coupling, representing the interaction between the TLM and its corresponding AM, remained unchanged, maintaining a consistent level across all identical angular misalignment values.

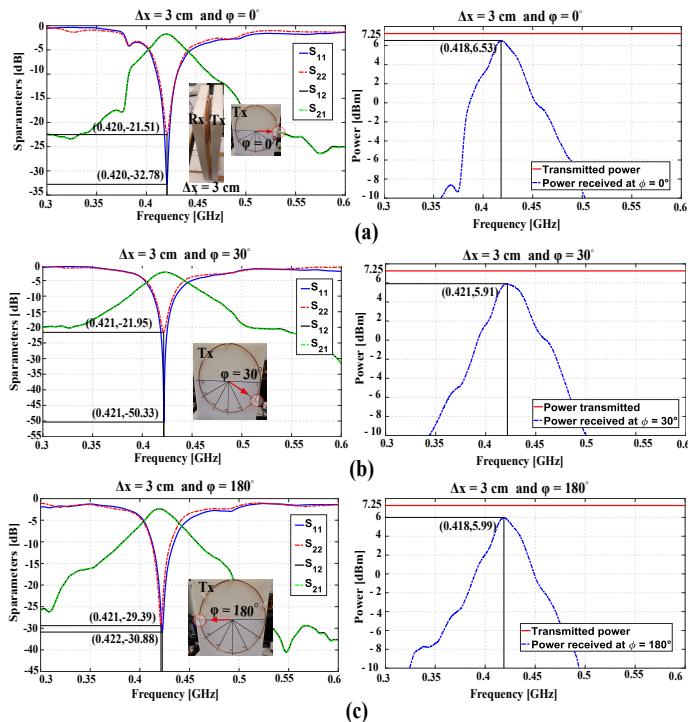


Figure 4.5: S-parameter measurements (S_{11} , S_{22} , S_{21} , and S_{12}) and PTE evaluations for Rotational mis. of the excitation port at: (a) $\Delta_x = 3$ cm and $\varphi = 0^\circ$; (b) $\Delta_x = 3$ cm and $\varphi = 30^\circ$; (c) $\Delta_x = 3$ cm and $\varphi = 180^\circ$.

4.5 Measurement of The Rotational Mis. of The Excitation Port Placed on The Tx Loop

Fig.4.5 presents the measurements related to the rotational misalignment of the excitation port on the Tx coil, as illustrated in Fig.4.1(e). The angular rotation φ varies from 0° to 180° in increments of 30° for each measurement scenario. To highlight the key findings in Table 4.1, the reference configuration, where the excitation and receiving ports are perfectly aligned, is compared with two specific cases: one with a slight rotational offset of 30° , and another with the maximum deviation of 180° . These experimental results provide valuable insights that align well with the CMA analysis. Across all configurations, the coupling axes (CAs) remained unchanged, and the eigenvalues consistently resonated at the same frequencies.

4.6 Measurement of The Rotational Mis. of The Rx Loop

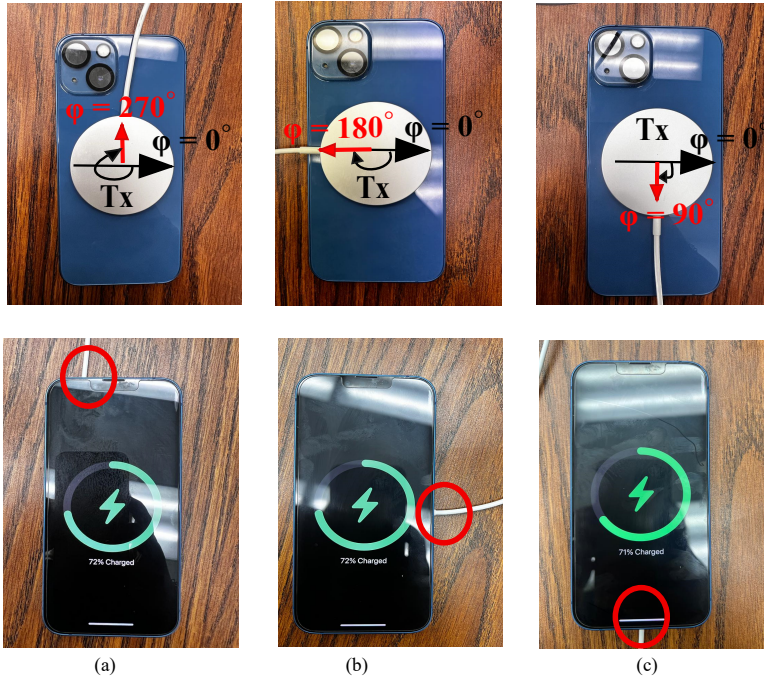


Figure 4.6: Charging iPhone13 through Qi standard based on random rotations of the Tx excitation: (a) $\varphi = 270^\circ$, (b) $\varphi = 180^\circ$, (c) $\varphi = 90^\circ$.

Notably, the rotation of the Tx excitation port does not hinder the power transfer process, which is preserved with consistently high efficiency throughout all scenarios tested. In order to establish the applicability of this configuration in practical contexts, we conducted a wireless charging experiment with an iPhone 13 using the Qi standard as shown in Fig. 4.6. This experiment involved random rotational positions for the Tx port. The results unequivocally demonstrated that, regardless of the rotational orientation, the device consistently charged without any issues.

4.6 Measurement of The Rotational Mis. of The Rx Loop

The final misalignment scenario, illustrated in Figs. 4.1(f) and 4.7, involves assessing the rotational positions of the Rx coil as it moves along a circular path with a radius of 15 cm around the Tx coil. CMA analysis of this configura-

CHAPTER 4. VALIDATION OF CMA FOR MISALIGNMENT IN WPT SYSTEM

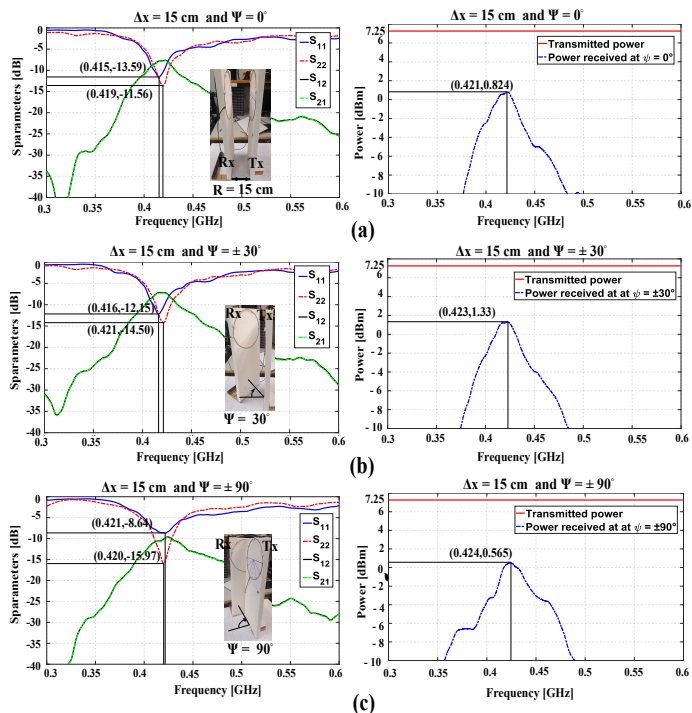


Figure 4.7: S-parameter measurements (S_{11} , S_{22} , S_{21} , and S_{12}) and PTE evaluations for the rotational mis. of the Rx loop: (a) Measurement setup; (b) $\Delta_x = 3$ cm and $\psi = 0^\circ$; (c) $\Delta_x = 3$ cm and $\psi = 30^\circ$; (d) $\Delta_x = 3$ cm and $\psi = 180^\circ$.

tion revealed that certain rotational positions exhibit similar modal behavior; however, it offered limited insight into power-related performance.

While discrepancies exist between the measured and calculated PTE values, both exhibit similar trends. For example, a 30° rotation of the Rx coil results in no noticeable power loss compared to the reference configuration, where the Tx and Rx coils are perfectly aligned. In contrast, at a 90° rotation, the calculated PTE drops to zero, and the measured PTE values reach their lowest levels. This indicates that, in this particular setup, the calculated PTE is more sensitive to rotational variation than the experimental measurements suggest.

4.7 Key Findings from Experimental Measurements

Table 4.1: Comparison between CMA and measurements under various misalignment scenarios.

Misalignment	Condition	Angle	CM	f_c (GHz)	f_m (GHz)	PTE _c	PTE _{m1}	PTE _{m2}
Lateral (x)	$\Delta x = 0.5$ cm	–	$J_4^{(1)}$	0.416	0.416	87.55%	88.67%	76.25%
	$\Delta x = 5$ cm		$J_4^{(1)}$	0.419	0.418	73.99%	69.81%	53.00%
	$\Delta x = 10$ cm		$J_4^{(1)}$	0.417	0.416	53.47%	33.96%	26.02%
	$\Delta x = 50$ cm		$J_4^{(1)}$	0.437	0.441	0.19%	0.018%	0.031%
Lateral (y)	$\Delta y = 0$ cm		$J_4^{(2)}$	0.417	0.418	82.09%	84.90%	66.56%
	$\Delta y = \pm 5$ cm		$J_4^{(2)}$	0.460	0.401	83.23%	67.92%	49.45%
	$\Delta y = \pm 10$ cm		$J_4^{(2)}$	0.469	0.403	66.77%	45.28%	33.34%
	$\Delta y = \pm 20$ cm		$J_1^{(2)}$	0.441	0.433	16.15%	5.89%	5.01%
Azimuthal	$\Delta x = 3$ cm	0°	$J_1^{(3)}$	0.417	0.418	82.09%	84.90%	66.56%
		$\pm 8^\circ$	$J_4^{(3)}$	0.412	0.426	82.06%	79.24%	48.87%
	$\Delta x = 10$ cm	0°	$J_4^{(3)}$	0.417	0.416	53.47%	33.96%	26.20%
		$\pm 40^\circ$	$J_4^{(3)}$	0.422	0.425	38.52%	31.50%	24.74%
Excitation port rot.	$\varphi = 0^\circ$		$J_1^{(4)}$	0.417	0.418	82.09%	84.90%	66.56%
	$\varphi = 30^\circ$		$J_4^{(4)}$	0.418	0.421	72.87%	73.58%	57.81%
	$\varphi = 180^\circ$		$J_4^{(4)}$	0.417	0.418	83.08%	75.47%	57.28%
Circular Rx rot.	$\psi = 0^\circ$		$J_4^{(5)}$	0.415	0.421	38.05%	22.81%	17.26%
	$\psi = \pm 30^\circ$		$J_4^{(5)}$	0.415	0.423	33.32%	26.31%	18.75%
	$\psi = \pm 90^\circ$		$J_1^{(5)}$	0.418	0.424	0%	20.67%	10.64%

4.7 Key Findings from Experimental Measurements

A review of the simulated, computed, and measured results presented in Table 4.1 reveals several important observations. One of the initial discrepancies observed between the calculated and measured PTEs can likely be attributed to differences in the excitation methods used in simulations versus experiments. Specifically, the FEKO simulations incorporate the excitation port directly into the antenna structure, whereas the experimental setup relies on a coaxial cable connected to a VNA to provide excitation. This distinction in implementation may contribute to variations in the observed performance.

It is well understood that coaxial cables possess inherent resistance, which leads to power loss in the form of heat as current flows through the conductor.

CHAPTER 4. VALIDATION OF CMA FOR MISALIGNMENT IN WPT SYSTEM

These losses tend to increase with both cable length and signal frequency. Additionally, factors such as impedance mismatches, physical bending of the cable, or discrepancies in cable length can further contribute to power loss, ultimately reducing the measured Power Transfer Efficiency (PTE). In the context of this study, any misalignment or improper handling of the coaxial cables connecting the Tx and Rx coils to the VNA may intensify power dissipation, especially under conditions of pronounced misalignment during the measurement of the WPT system.

Moreover, PTE was assessed using two distinct numerical formulations, each offering complementary insights and producing different numerical results. By definition, $\text{PTE}_{\text{measured}^2}$ and $\text{PTE}_{\text{calculated}}$ focus on the transmission characteristics of the network, while $\text{PTE}_{\text{measured}^1}$ provides a more direct evaluation of the power delivery performance of the MCR-WPT system. As shown in Table 4.1, the values of $\text{PTE}_{\text{measured}^1}$ and $\text{PTE}_{\text{measured}^2}$ differ numerically; however, the key observation is that misalignment has a consistent effect on both, resulting in similar variation trends.

Furthermore, the comparison between experimental measurements using fabricated loops and the simulation results based on CMA confirms the effectiveness of the model in accurately predicting the frequencies at which maximum power transfer occurs in the three scenarios analyzed. These frequencies closely correspond to the resonant frequencies of the dominant characteristic modes, validating the CMA approach as a reliable tool for understanding and anticipating system behavior.

In the following chapter, a novel comparison between various WPT systems will be presented. This comparison aims to address several limitations observed in previous designs, including limited transfer distance, sensitivity to misalignment, high cost, and design complexity.

Chapter 5

Comparison Between Different WPT Systems

The next generation of implantable and wearable medical devices is expected to operate within closed loop systems, incorporating sensors, actuators, and algorithms to enable dynamic and intelligent interactions between monitoring and therapeutic functions. However, the use of wires in devices, such as deep brain stimulators, pacemakers, implantable cardioverters, and defibrillators, poses several challenges. These include mechanical complications, increased risk of infection, and signal degradation due to unexpected misalignments between the transmission and receiving units.

In light of these limitations, wireless solutions are gaining increasing attention. This chapter focuses on a comparative study of various antenna systems. The objective is to identify and analyze antenna configurations that offer optimized performance, paving the way for more reliable and efficient wireless medical devices.

5.1 Description of the Proposed WPT Configurations

In WPT systems, the efficiency and robustness of the power transmission are closely related to the design of the resonators and the characteristics of the antennas used in the system [114]. As a result, a variety of architectures and hardware implementations have been proposed over the years to improve performance under various constraints [101,103,115–117]. Among these, magnetic resonance coupling between coils operating at the same resonant frequency remains the most widely used technique. However, this approach tends to

CHAPTER 5. COMPARISON BETWEEN DIFFERENT WPT SYSTEMS

show a strong sensitivity to misalignment between the transmitter and the receiver [102, 118, 119].

To address these limitations and improve PTE, several techniques have been introduced in the literature, such as the use of multiple transmitters [120], multiple receivers [121], range adaptive structures [14], and broadband designs [122]. In this chapter, a comparative study is conducted based on the Theory of Characteristic Modes (TCM), which has proven effective for offering physical insight into magnetic coupling behavior, especially when investigating misalignment effects between loop-based resonators [123].

5.1.1 Topologies Based on Loop WPT Systems

Three loop-based WPT configurations are proposed and analyzed, as illustrated in Fig. 5.1. To ensure a fair and systematic comparison, the three configurations considered in this study have identical loop dimensions and operate under the same separation distance constraints.

① Transmitter

② Receiver : Circular loop antenna

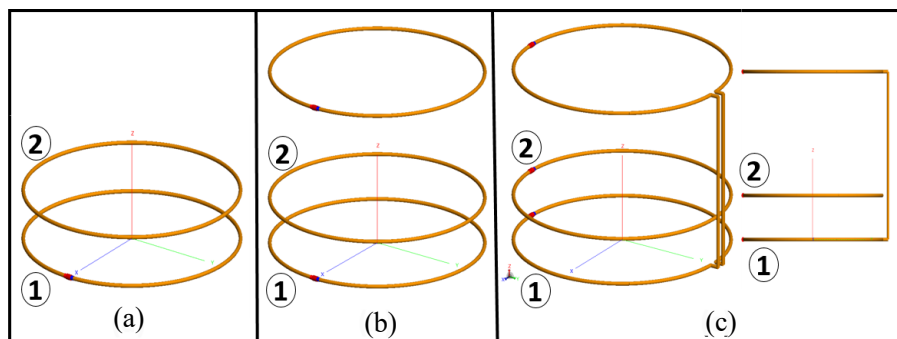


Figure 5.1: The loop-based WPT systems: (a) Single transmitter topology, (b) Dual Transmitter Topology, (c) Interconnected dual transmitter topology.

These topologies are suitable for biomedical and consumer electronics applications. The first configuration, shown in Fig. 5.1(a), consists of a single circular loop serving as the Tx, representing the simplest and most conventional design, which was already analysed in Chapter 4. The second configuration introduces a dual Tx topology, where two identical loop antennas operate in parallel as illustrated in Fig. 5.1(b), aiming to enhance power transfer efficiency. And, the third configuration, in Fig. 5.1(c), is a novel interconnected

5.1 Description of the Proposed WPT Configurations

dual Tx system, incorporates vertical interconnections between the two loops to stabilize the magnetic flux and mitigate misalignment issues between the transmitting and receiving antennas [103].

Even though the dual Tx topology has been previously introduced in the literature, a direct comparative analysis assessing its effective performance under the same conditions has never been conducted. Additionally, the interconnected dual transmitter topology represents a novel design that has not been explored in prior research. By systematically comparing these configurations, this study aims to evaluate their efficiency, misalignment resilience, and overall feasibility for WPT applications. By comparing these configurations in frequency bands spanning from 350 to 700 MHz, this study provides new insights into the impact of Tx topology on optimizing WPT system performance and addressing alignment constraints.

5.1.2 Topologies Based on Near-Field Plates WPT Systems

To further investigate performance improvements and address the directional inefficiencies often encountered in resonant WPT systems, a second group of configurations integrates Near Field Plates (NFPs) shown in Fig. 5.2.

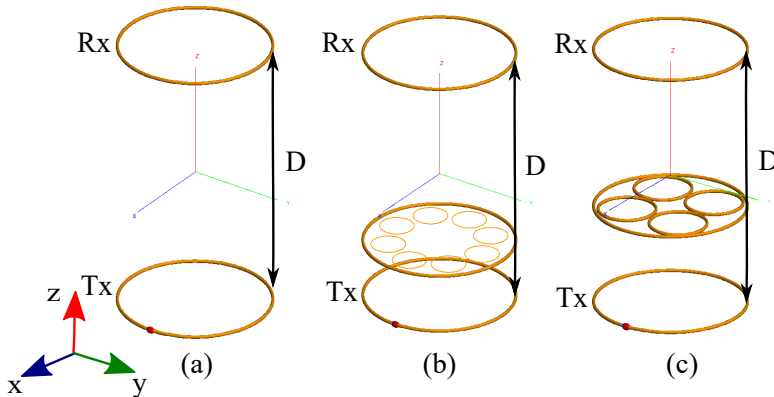


Figure 5.2: (a) Single transmitter topology, (b) WPT system using a NFP based on one set with eight peripheral loaded loops in the transmitting unit, (c) WPT system using a NFP based on one set with four peripheral loaded loops in the transmitting unit.

These structures are specifically designed to concentrate the magnetic field toward the Rx antenna while suppressing unwanted radiation, thereby enhancing both directionality and power transfer efficiency. Using NFP focus trans-

mission techniques could be applied in various areas, such as multi-user WPT systems [124], high-power charging scenarios [125], and biomedical applications to reduce health concerns [126].

This study conducts a comparison between three different configurations. The first configuration, in Fig. 5.2(a), is a single Tx system that serves as a reference point for comparison with conventional WPT structures commonly used in industrial and real-world applications. The other two configurations are enhanced WPT systems, differentiated by the number of NFPs incorporated between the Tx and Rx loops to improve NF focusing. Specifically, the second configuration (Fig. 5.2(b)) consists of a single Tx loop system integrated with eight NFPs, while the third configuration (Fig. 5.2(c)) features a similar system but with four NFPs. It is essential to note that, similar to the previously analyzed loop based configurations, the Tx and Rx loops in these configurations maintain identical dimensions. Additionally, all separation distances are kept consistent, including both the distance between the Tx and Rx loops and the distance between the Tx loop and the NFPs. These considerations are crucial to ensure a reliable basis for comparison and to derive meaningful and well-founded conclusions regarding the impact of each configuration on system performance.

5.2 Frequency Selection in the Proposed WPT Systems

The selection of the operating frequency in the proposed WPT systems is a critical factor influencing both PTE and system feasibility, particularly in biomedical applications. In particular, NF-WPT systems have been developed across a wide frequency range, from 6.765 MHz to 246 GHz, with biomedical applications often utilizing frequencies such as 0.3 MHz, 6.78 MHz, and 13.56 MHz due to their favorable inductive properties and reduced electromagnetic absorption in human tissues.

For the proposed systems analyzed in this study, a frequency within the megahertz (MHz) range was chosen to ensure a balance between PTE, system compactness, and penetration depth in real applications. Lower frequencies allow for larger inductance values, leading to higher quality factors and enabling longer transmission distances due to their extended wavelengths. However, increasing the frequency enhances the rate of change of the incident magnetic field, which is directly proportional to the received power [127].

To align with industry standards and previously validated systems, a MHz-range frequency was selected for this study, ensuring a practical trade-off between power transfer performance and biological safety considerations. This frequency range also facilitates direct comparison with existing WPT designs,

allowing for a fair evaluation of the proposed configurations in terms of misalignment sensitivity, energy efficiency, and field distribution.

5.3 Comparison Between The Loop Based WPT Systems

The loops are identical in the three different configurations. The geometric parameters of a single loop are illustrated in Fig. 5.3, with the inner radius of the loop (R) set to 120 mm and the wire width (W) measuring 5 mm. To examine the impact of separation distance on modal behavior and coupling efficiency, the spacing (d) between the two antennas is systematically varied from 5 mm to 150 mm. Before comparing the systems based on their behavior near resonance, CMA is applied to explore the various CMs and their features.

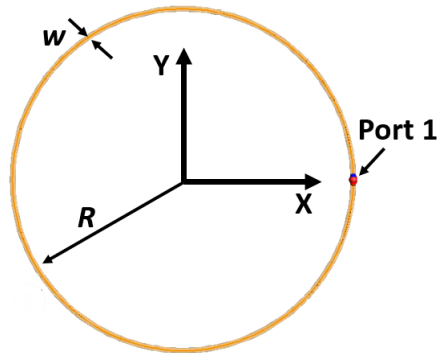


Figure 5.3: The dimensions of the loop and its characteristic parameters.

5.3.1 Comparison Based on CMA Between The Loop Based WPT Systems

The Loop based WPT systems present a relatively simple and well defined structures, making them highly suitable for CMA. Since the theory provides physical insight into current distributions and resonant behaviors, a detailed analysis of CMs, focusing on the identification of CMs, their current distributions, the total radiated power of each system, and the individual contribution of each CM to the overall power is conducted.

For the CMA, the separation distance d between the Tx and Rx loops is set to $\lambda/5$ for the single Tx topology. The same separation distance is main-

CHAPTER 5. COMPARISON BETWEEN DIFFERENT WPT SYSTEMS

tained between Tx1 and the Rx loop for the dual Tx topologies as shown in Fig. 5.4 (b) and (c). This ensures a consistent comparison under identical conditions, allowing for an accurate assessment of which configuration provides the best performance. In addition, for the dual Tx topologies, Tx2 of both configurations loops are positioned at a distance $d_1 = \lambda/3$ from Tx1, ensuring a structured arrangement that influences coupling and overall system performance.

The CA_n variations of the proposed systems across different frequency bands within the 350 to 700 MHz range are depicted in Fig. 5.4.

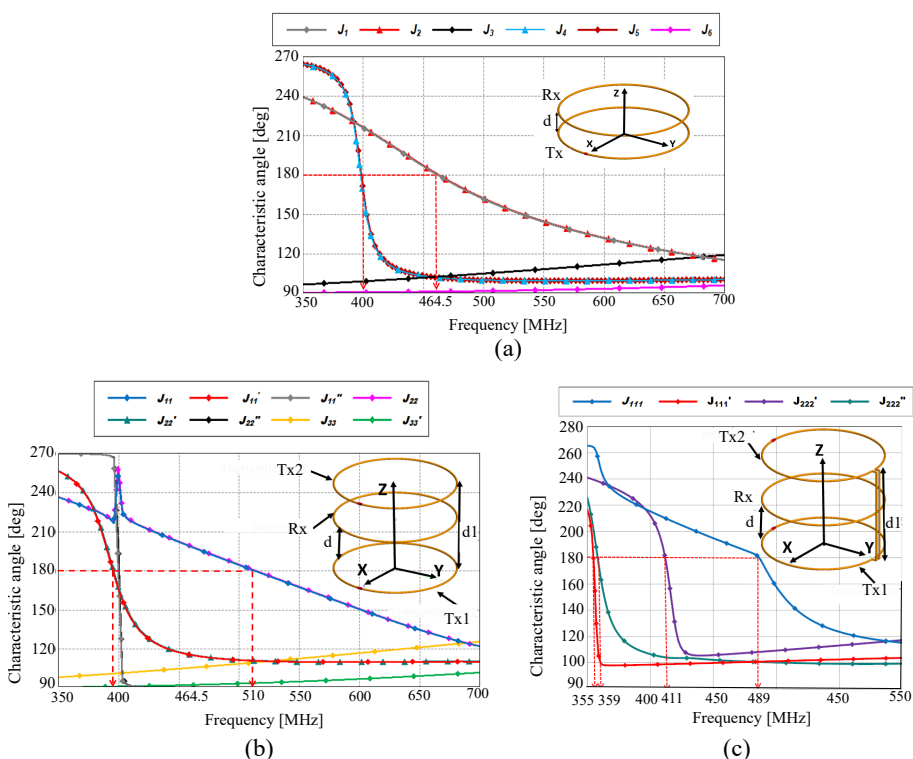


Figure 5.4: MA_n of : (a) Single Tx configuration, (b) Dual Tx configuration, (c) Dual Interconnected Tx configuration.

To better describe the CMs, the schemes of the eigen currents projection along the loops perimeters of the three configurations are shown in Fig. 5.5, Fig. 5.6, and Fig. 5.8.

5.3 Comparison Between The Loop Based WPT Systems

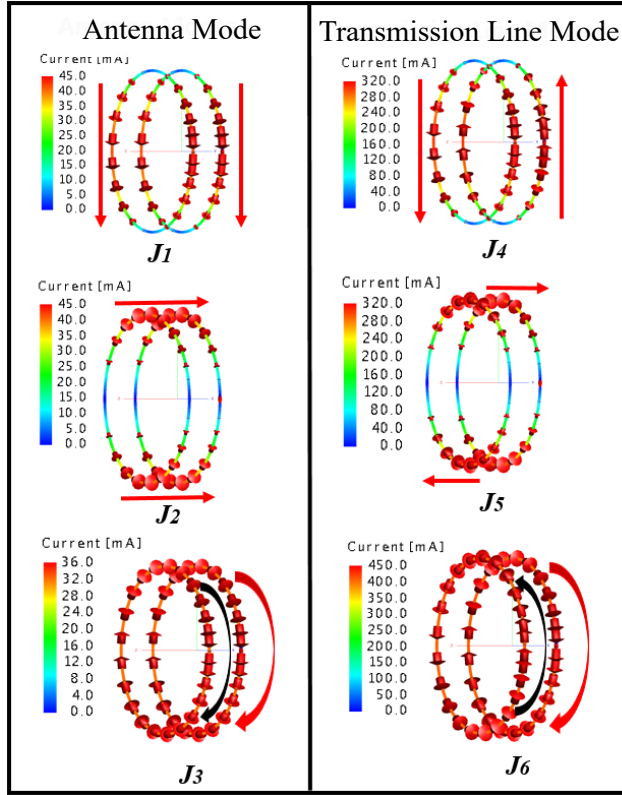


Figure 5.5: Eigen currents of the single Tx configuration.

Based on the direction of current flow and the explanations presented in previous chapters, the modes are categorized into Antenna Modes (AMs) and Transmission Line Modes (TLMs). An AM is characterized by in phase current flow in the two wires, whereas a TLM occurs when the currents flow with a 180° phase difference. For the single Tx topology, as analyzed using CMA and illustrated in Fig. 5.4(a) and Fig. 5.5, J_1 , J_2 , and J_3 are identified as AMs, while their corresponding TLMs are J_4 , J_5 , and J_6 , respectively. By drawing an analogy with the results obtained in Chapter 2, it can be observed that the current intensity of the TLMs is higher than that of the AMs, indicating a stronger influence of TLM behavior in these modes.

To conduct a comprehensive comparison, the two additional WPT configurations are analyzed following the same methodology. The second system features a dual Tx topology, as illustrated in Fig. 5.4(b), which presents the

CHAPTER 5. COMPARISON BETWEEN DIFFERENT WPT SYSTEMS

system structure along with its CMA results based on the MA_n . The Tx and RX retain the same dimensions as the loop antenna in the first topology. In this configuration, the central loop functions as the Rx, while the outer loops serve as Tx's, separated by a distance $d_1 = \lambda/3$.

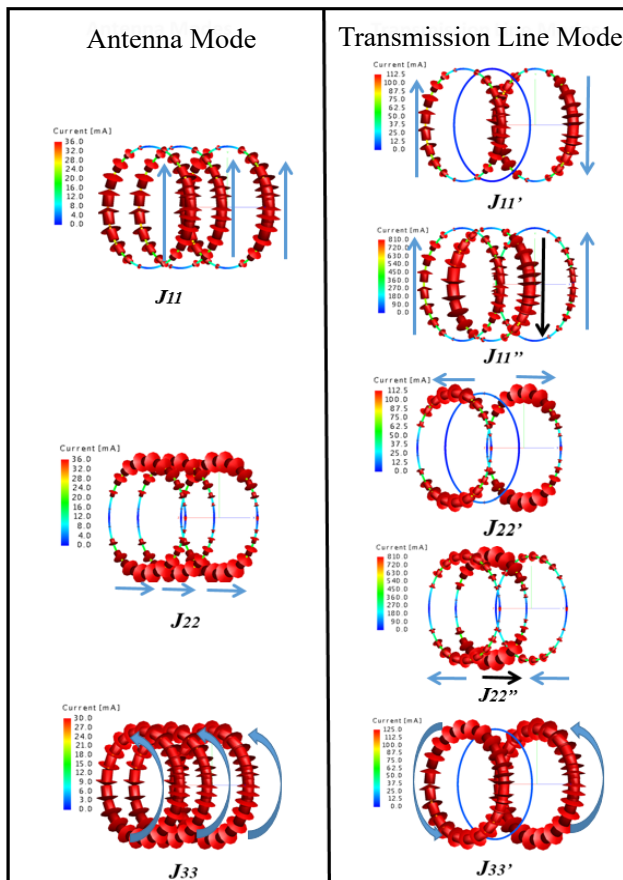


Figure 5.6: Eigen currents of the dual Tx configuration.

By drawing an analogy with the first WPT system, it is observed that the previously identified CMs remain present. However, a new pair of TLM emerges, alongside the AMs J_{11} and J_{22} , which are influenced by mode tracking. According to the current distributions shown in Fig. 5.6, the highest current intensity is associated with J_{11}' and J_{22}' , reaching 810 mA on the Rx loop, which presents a significant increase compared to the single Tx configuration.

5.3 Comparison Between The Loop Based WPT Systems

In this system, the currents in the Tx's flow in the same direction, whereas the current in the Rx flows in the opposite direction, indicating that the entire system operates as a TLM configuration. Furthermore, for the remaining CMs, the current intensity is significantly lower, reaching 0 A at the Rx when the two Tx loops exhibit TLM behavior.

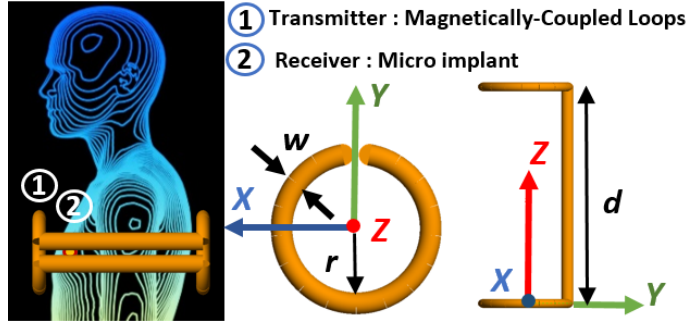


Figure 5.7: A clear visualisation of the dual interconnected Tx topology.

The simulations and results obtained for the dual Tx topology did not consider the misalignment sensitivity between the two transmitters. To overcome this limitation and ensure that both Tx's remain fixed and perfectly parallel, a dual interconnected Tx topology is introduced, offering promising potential for biomedical applications [103] as shown in Fig. 5.7(c). This configuration integrates two vertical interconnections between the transmitting loops, enhancing structural stability and reducing alignment issues.

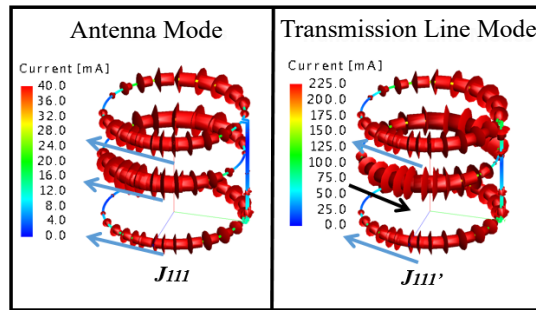


Figure 5.8: Eigen currents of the dual interconnected Tx configuration.

The separation distances in this topology remain consistent with the previous configuration of a dual Tx topology, maintaining $\lambda/5$ between the transmitting system and the receiver and $\lambda/3$ between the two transmitters for the CMA

CHAPTER 5. COMPARISON BETWEEN DIFFERENT WPT SYSTEMS

analysis. As illustrated in Fig. 5.4(c), the characteristic mode (CM) behavior exhibits noticeable differences compared to the previous two cases, leading to a concentration in the frequency band to 355–550 MHz. Additionally, the current distributions in this configuration appear less distinct than those observed in the earlier designs. However, an AM J_{111} and its corresponding TLM J_{111}^i are clearly identified in Fig. 5.8.

A key observation from the current distribution comparison is that this configuration exhibits the highest current intensity among the three proposed configurations. To gain deeper insights into the system's performance, Fig. 5.9 presents an analysis of dominant modes contribution to the total power across the different scenarios.

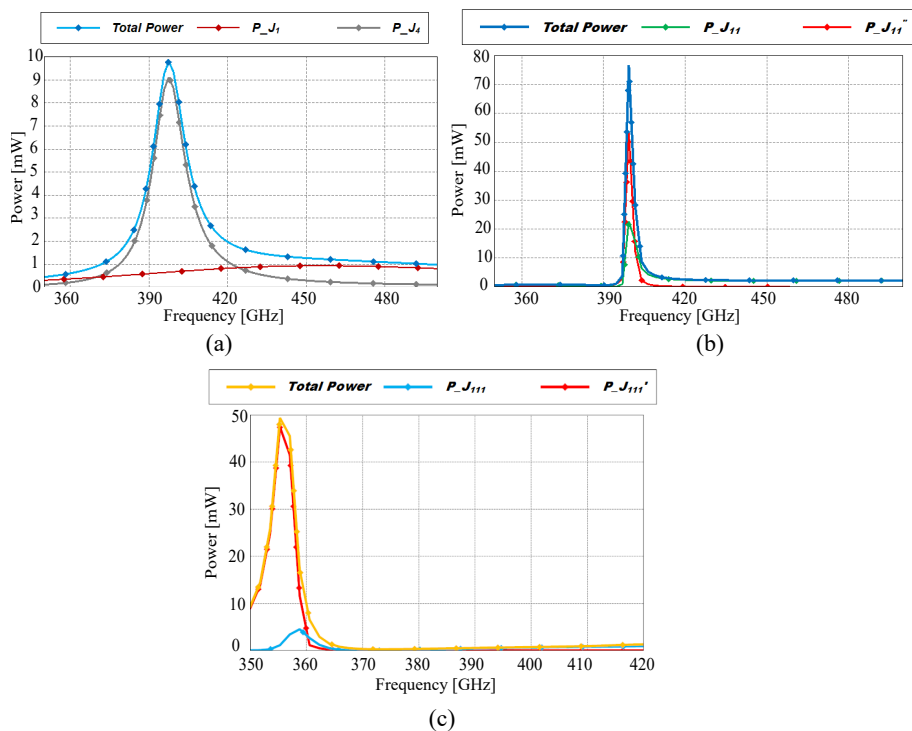


Figure 5.9: The total power of each configuration and the contribution of the dominant CM : (a) Single Tx configuration, (b) Dual Tx configuration, (c) Dual Interconnected Tx configuration.

As illustrated in Fig. 5.9(a), within the single Tx configuration, the dominant CM near the resonance frequency is TLM J_4 , which contributes the most

5.3 Comparison Between The Loop Based WPT Systems

to the system's total radiated power. In Fig. 5.9(b), the introduction of a second transmitting loop significantly enhances the coupling between the antennas, leading to a stronger TLM contribution to the total power. In this dual Tx topology, the currents in the two transmitting loops flow in phase, while the current in the receiving loop flows with a 180° phase difference, which aligns with the expected TLM behavior. This configuration improves the power transfer efficiency due to the reinforced interaction between the loops. The third configuration, shown in Fig. 5.9(c), incorporates two vertical interconnections between the transmitting loops. While this topology enhances structural stability, it results in a decrease in radiated power compared to the dual Tx configuration, suggesting that further optimization is required.

This study confirms that a dual Tx topology achieves higher radiated power compared to a single Tx system, with TLMs playing a dominant role in power transfer across all three configurations. In multi Tx topologies, TLMs are characterized by in-phase currents in the transmitting loops and a 180° phase shift in the receiving loop. However, while the interconnected dual Tx configuration successfully reduces misalignment sensitivity, it also results in lower radiated power and a shift in resonance frequency due to structural modifications.

5.3.2 A Performance Comparison Between The Loop Based WPT Systems

A comprehensive analysis of the proposed systems is carried out by examining the influence of the Tx units on power transmission within the frequency range from 350 to 550 MHz. In contrast to the initial study, where the Rx loop was fixed at a single position $\lambda/5$, the same Rx structure is retained but positioned at multiple locations to assess system performance to address a wider range of axial misalignment.

Fig. 5.10 presents the current distributions and corresponding resonant frequencies for the three proposed systems. By drawing a parallel with the Characteristic Mode Analysis (CMA), particularly the contribution of the dominant mode to the system's total power, it is evident that, in each case, the resonant frequency of the system aligns precisely with that of the dominant mode. Specifically, the single loop configuration in Fig. 5.10(a) resonates at 423 MHz, while the first dual Tx topology shown in Fig. 5.10(b) resonates at 378 MHz. The interconnected dual Tx configuration, also shown in Fig. 5.10(b), resonates at 478 MHz, making it the only case where the resonant frequency differs from the one predicted by CMA. This discrepancy can be attributed to the nature of CMA, which does not account for external excitation and is purely based on the geometry of the structure. In this particular configuration, the presence of two excitation ports placed on both transmitting loops influences the modal

CHAPTER 5. COMPARISON BETWEEN DIFFERENT WPT SYSTEMS

behavior, especially by altering the excited mode, thus leading to the observed shift in resonance.

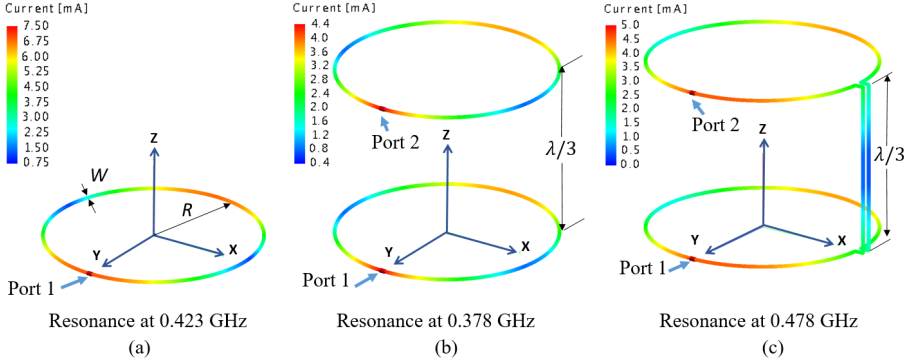


Figure 5.10: The current distribution and the corresponding resonant frequency: (a) The single Tx, (b) The dual Tx, (c) The dual interconnected Tx.

These three frequencies correspond to the point at which each system achieves its maximum radiated power. A similar trend is observed in the current intensity distributions, where the dual Tx topologies exhibit higher current magnitudes compared to the single Tx configuration.

To analyze the variation of current at the Rx antenna, its position is systematically shifted in parallel to the transmitter from 10 cm to 180 cm. This movement allows for a comprehensive evaluation of how the separation distance affects current intensity in different WPT configurations. The results reveal that the dual Tx topologies consistently generate higher current levels at the Rx antenna compared to the single Tx configuration. In the case of the single Tx system, the current I_1 gradually decreases as the separation distance increases, indicating a significant drop in coupling efficiency over longer distances.

In contrast, dual Tx systems exhibit a more stable current profile (I_2 and I_3), maintaining values above 300 mA across a wide range of distances. This behavior highlights the improved robustness of dual TX designs, making them more suitable for scenarios where the Rx position may vary or where stable performance is required over longer operating ranges. Among them, the dual Tx topology without interconnections exhibits the highest current intensity I_2 at the Rx antenna. This superior performance can be attributed to the absence of vertical structural elements, which, in the interconnected dual Tx topology I_3 , are likely to introduce additional coupling effects.

5.3 Comparison Between The Loop Based WPT Systems

These vertical interconnections may generate undesirable interactions and ohmic losses, thereby dissipating part of the transmitted energy and reducing the current level at the receiver. As a result, while the interconnected topology offers advantages in alignment stability, it also introduces structural losses that can negatively impact power transmission efficiency as shown in Fig. 5.11.

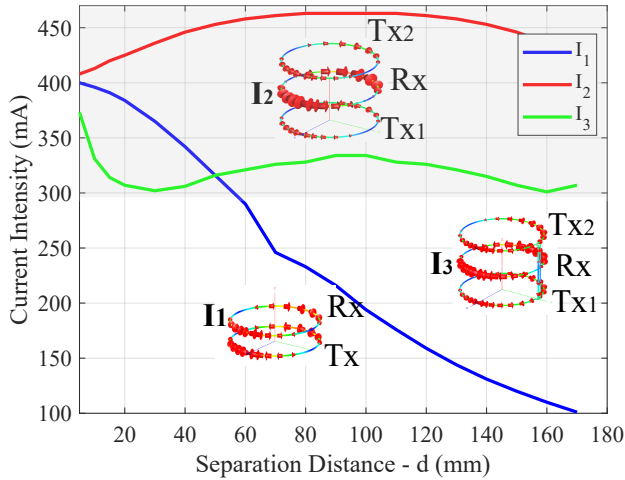


Figure 5.11: The current intensity of the Rx loop for the three systems as a function of the separation distance d .

To further highlight the comparison between the three configurations, it is essential to evaluate their PTE, which provides a direct measure of how effectively power is transferred from the transmitting unit to the receiving one. The PTE is calculated based on the ratio between the power dissipated at the load (connected to the Rx loop) and the input power accepted by the Tx system. For all three systems, the power delivered to the load is expressed as the power dissipated across the load resistance P_{RL} , which is associated with the current flowing in the Rx loop. However, the denominator varies depending on the number of transmitters supplying power.

For the single Tx configuration, shown in equation (5.1), there is only one source, and the efficiency is simply the ratio of the received power P_{RL} to the input power P_{in} :

$$\text{PTE}_1 = \frac{P_{RL}}{P_{in}} = \frac{|I_2|^2 R_L}{|I_1|^2 R_{in}} \quad (5.1)$$

CHAPTER 5. COMPARISON BETWEEN DIFFERENT WPT SYSTEMS

Where R_{in} is the input resistance, and I_1 and I_2 denote the currents in the Tx and the Rx loops.

In contrast, for the dual Tx configurations, two identical power sources feed each of the Tx loops. As a result, the total input power is effectively twice that of the single source configuration. To maintain a fair comparison and properly normalize the efficiency, the received power P_{R_L} is divided by $2P_{in}$, leading to the following expression:

$$\text{PTE}_2 = \frac{P_{R_L}}{2P_{in}} = \frac{|I_2|^2 R_L}{2|I_1|^2 R_{in}} \quad (5.2)$$

These formulations allow a consistent evaluation of efficiency across different topologies, accounting for the number of power sources involved. The resulting PTE values offer critical insights into the impact of Tx configuration on overall system performance. Using full-wave electromagnetic simulations in FEKO, the accepted power at both the transmitting and receiving antennas is accurately extracted. Based on these results, the PTE for each system is calculated around the resonant region and summarized in Fig. 5.12.

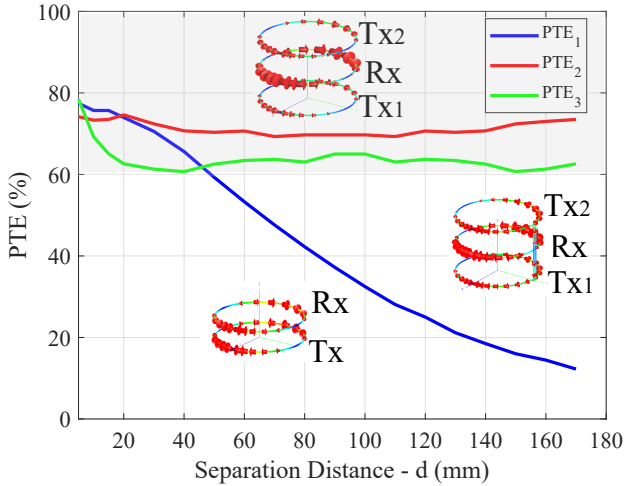


Figure 5.12: The PTE of the three systems as function of the separation distance d .

As the separation distance d increases from 5 mm to 170 mm, the single Tx configuration exhibits a significant decline in PTE from approximately 80% down to 10%, highlighting its sensitivity to misalignment. The dual Tx configuration demonstrates a much more robust performance. When the Rx is

5.4 Comparison Between The Near-Field Plates WPT Systems

optimally positioned closer to one of the Tx's, the system achieves a peak PTE of 80%. As the Rx moves toward the midpoint between the transmitters, the efficiency decreases slightly, reaching a minimum of about 70%. A similar trend is observed for the interconnected dual Tx configuration; however, its lowest PTE value is slightly lower, around 60%.

In summary, both dual Tx configurations (with and without vertical interconnections) provide higher and more stable PTE compared to the single Tx system. This stability reinforces their suitability for applications that require consistent performance under varying alignment conditions.

5.4 Comparison Between The Near-Field Plates WPT Systems

Although WPT using resonant loops is nearing commercialization, a significant challenge remains unresolved. In addition to transferring energy to the intended resonant receiving loop, the Tx loop also emits unintended radiation, which results in a power leak into the surrounding environment. The latter has been partially mitigated through the use of ferrites or metallic slabs [128]. However, these materials are lossy because of eddy current generation, and they tend to be heavy and costly. Therefore, there is a pressing need for an alternative approach to effectively control the power radiated by resonant loops.

Near Field Plates (NFPs) have been introduced as an effective method to adjust power leakage in resonant WPT systems [124]. These structures are non-periodically modulated surfaces or arrays designed to shape the electromagnetic NF. In particular, their functionality relies on constructive or destructive interference between the fields generated by the NFP and those of the primary source, enabling the formation of targeted NF distributions.

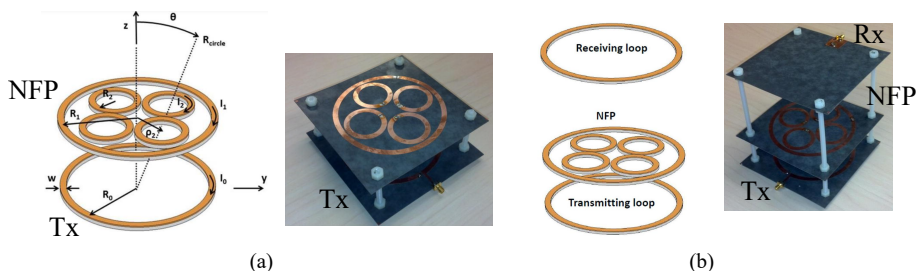


Figure 5.13: The configuration of a NFP WPT system consisting of an array of loaded loops: (a) The Tx with the NFP, (b) The full system. [124]

CHAPTER 5. COMPARISON BETWEEN DIFFERENT WPT SYSTEMS

A systematic design methodology for NFPs has been established, and experimental implementations have successfully demonstrated their ability to generate subwavelength NF patterns with high precision [124]. This study included a series of parametric investigations that evaluated the impact of dimensional variations in the WPT system that incorporates NFP with an array of four loaded loops. Specifically, the PTE using the $|S_{21}|^2$ and the magnetic field distributions were computed under different dimensional configurations, both with and without the integration of NFPs.

The novelty presented in this study lies in the comprehensive investigation of a WPT system incorporating NFPs using a multi stage approach. First, the system is analyzed through CMA to gain deeper physical insight into the existing modal behavior and their associated features prior to introducing capacitive loading into the NFP loop array. Subsequently, the influence of the NFPs' positioning between the Tx and Rx loops is evaluated to assess their impact on the PTE. Finally, a comparative study is carried out between a conventional WPT system (without NFPs) and two configurations integrating NFPs with different numbers of loaded loops. This comparison aims to evaluate how increasing the number of loops affects the magnetic field distribution and overall system performance. Such a detailed exploration of modal behavior, spatial optimization, and structural enhancement offers a novel perspective not previously addressed in the existing literature.

5.4.1 CMA of Near-Field Plates WPT System

The WPT systems analyzed incorporate NFPs positioned between two resonant coupled loops. The distance d between the TX and the NFP is fixed. CMA does not account for positional variations of the NFPs; instead, it focuses on revealing the intrinsic electromagnetic behavior of the structure prior to the inclusion of any reactive loading. By applying this method to NFP-based WPT systems, this study provides a deeper physical insight into modal behavior and introduces a novel approach to enhancing system performance through the targeted excitation of specific CMs.

The Tx and Rx loop antennas are assumed to be identical, each with a radius R equal to 53 mm and a wire width w equal to 1 mm. The fixed separation distance D between the Tx and Rx loops is set to $\lambda/2$. The CMA focuses on understanding the underlying physics through Characteristic Angles (CA_n) as depicted in Fig. 5.15, where the first nine CMs are computed in the frequency band from 0.1 to 2 GHz. The CMA results exhibit dynamic tracking behavior that obscures the identification of AM and TLM.

Accordingly, the associated eigen current distributions are illustrated in Fig. 5.15 to provide deeper insight into the CMs that exhibit the most favorable performance. This analysis helps identify how specific modes contribute to the

5.4 Comparison Between The Near-Field Plates WPT Systems

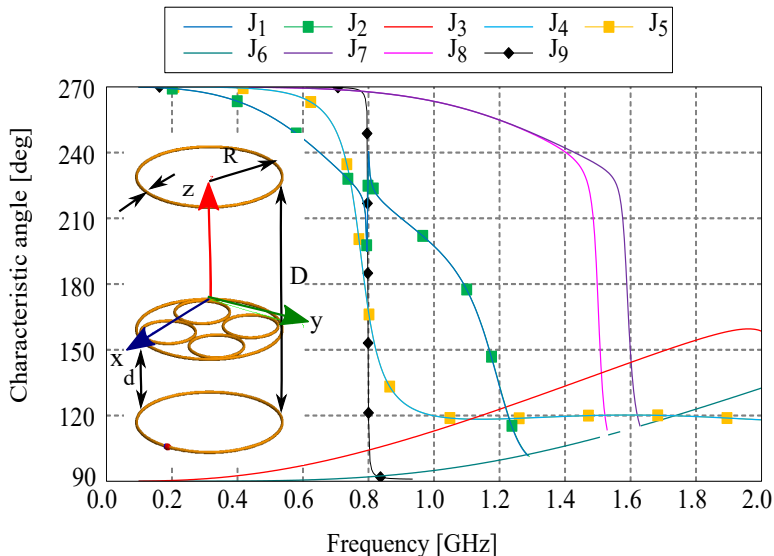


Figure 5.14: Characteristic Angle of the first nine modes of the proposed NFP WPT system.

overall field distribution. By examining the current flow patterns across the structure, the study facilitates the strategic integration of capacitive loading elements to selectively excite the most advantageous CM for improved system performance.

The primary observation is that not all CMs can be accurately visualized using the electromagnetic simulator FEKO. Nevertheless, several important insights can be drawn. Notably, higher order CMs tend to exhibit significantly weaker magnetic field intensities and unstable behavior, making them unsuitable for efficient WPT. Their corresponding current distributions often display multiple nulls along the loop perimeter, which indicates poor coupling performance. As illustrated in Fig. 5.15(f), the current magnitudes along the Tx and Rx loops are significantly lower than those observed on the NFP, where the peak current reaches 90 mA. However, for efficient PTE, it is essential that the highest current levels be concentrated at the Rx loop rather than on the NFP. This imbalance suggests suboptimal power delivery, as excessive current on the NFP indicates that a large portion of the energy is being dissipated or confined within the auxiliary structure instead of being effectively transferred to the Rx unit.

Among the examined modes, the TLMs J_1 and J_4 demonstrate favorable characteristics, particularly with respect to the current intensity observed at

CHAPTER 5. COMPARISON BETWEEN DIFFERENT WPT SYSTEMS

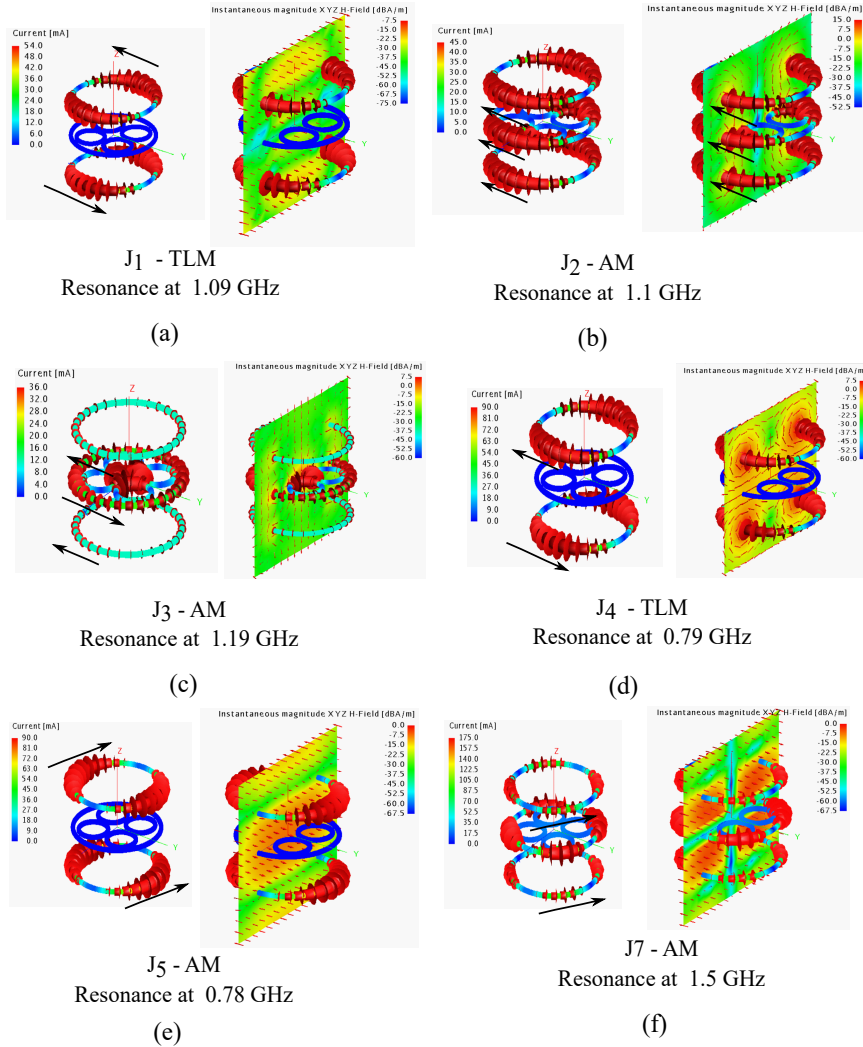


Figure 5.15: Eigen currents and their associated magnetic NF distributions in XY-plane for the visible CMs of the NFP WPT system: (a) J_1 ; (b) J_2 ; (c) J_3 ; (d) J_4 ; (e) J_5 ; (f) J_7 .

the Rx loop and the stability of the magnetic field in the region between the Tx and Rx units, where the field reaches up to 7.5 dBA/m. Additionally, TLM J_3 presents good magnetic field uniformity across the coupling region; however, the associated current magnitudes at the Tx and Rx levels are notably lower

5.4 Comparison Between The Near-Field Plates WPT Systems

than those observed on the NFP. In contrast, the AMs J_2 and J_5 exhibit comparatively weaker magnetic field intensities and current magnitudes, indicating less effective coupling performance relative to the TLMs.

The analysis confirms that the excitation of TLMs, where the Tx and Rx loops exhibit opposing current distributions, can significantly enhance the performance of NFP based WPT systems. These modes not only provide higher current intensity at the receiver loop but also contribute to a more stable and focused magnetic field in the coupling region. This behavior is essential for efficient energy transfer and can guide the strategic excitation of beneficial CMs in future WPT designs.

5.4.2 Comparison Between Conventional and NFP WPT Systems

The WPT systems analyzed incorporate NFPs positioned between two resonant coupled loops. The distance d between the transmitter and the NFP is $\lambda/8$. The Tx and Rx loop antennas are assumed to be identical, each with a radius R equal to 53 mm and a wire width w equal to 1 mm. The fixed separation distance D between the Tx and Rx loops is set to $\lambda/2$, aligning with common NF WPT operating conditions. To investigate the influence of NFP geometry on system performance shown in Fig. 5.16, two distinct configurations are proposed. The first configuration employs a set of eight peripheral loaded loops, each with a radius r_1 equal to 12.5 mm. In contrast, the second configuration incorporates four loaded loops, each with a larger radius r_2 of 20 mm. In both configurations, the loops are capacitively loaded with identical capacitors of 0.947 pF, ensuring consistent resonant behavior. This uniform loading is particularly beneficial for enhancing the excitation of TLMs as shown in Fig. 5.17, which have demonstrated superior performance in NFP based WPT systems.

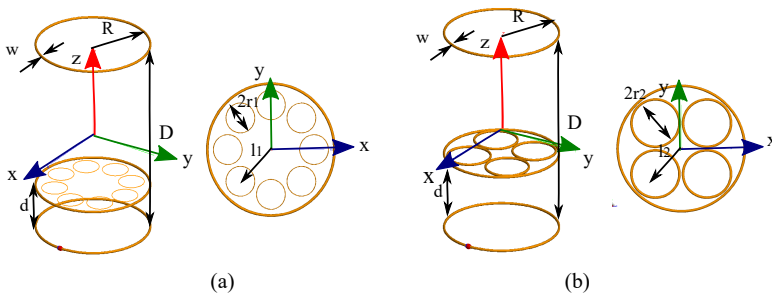


Figure 5.16: The geometry of the WPT integrating NFPs based on: (a) One set with eight peripheral loaded loops, (b) One set with four peripheral loaded loops.

CHAPTER 5. COMPARISON BETWEEN DIFFERENT WPT SYSTEMS

These two configurations are designed to explore how the number and size of the NFPs affect magnetic field shaping, power transfer efficiency, and spatial confinement in resonant WPT systems.

For optimal performance, the electromagnetic interaction between the NFPs and the Tx antenna must be constructive. This constructive interference optimizes the magnetic field strength at the location of the Rx loop, which improves the PTE. As illustrated in Fig.5.17, in comparison to the reference configuration composed solely of resonant coupled loops (i.e., without NFPs), the inclusion of NFPs leads to a significant enhancement in the performance of the system. The reference case exhibits relatively weak magnetic field intensity and reduced current at the receiver. However, when NFPs are introduced, both field strength and induced current improve considerably.

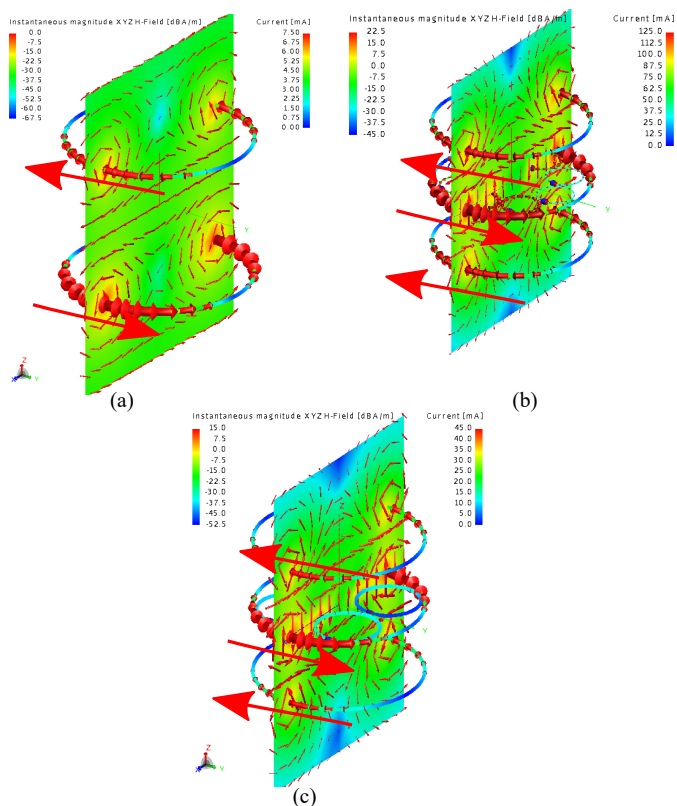


Figure 5.17: Instantaneous magnetic field and current distribution for: (a) Coupled loops at $f_{res} = 900$ MHz, (b) NFP with 8 loaded loops at $f_{res} = 938$ MHz, (c) NFP with 4 loaded loops at $f_{res} = 909$ MHz

5.4 Comparison Between The Near-Field Plates WPT Systems

Specifically, the configuration comprising eight peripheral loaded loops demonstrates the most favorable characteristics. This configuration achieves a maximum magnetic field intensity of 22.5 dBA/m at the receiver location and a peak current of 125 mA, indicating a substantial improvement in energy delivery to the load. It is important to highlight that in both NFPs based systems studied, the plates were strategically positioned at a distance of $\lambda/4$ from the Tx antenna, a location that enables efficient coupling by reinforcing the desired magnetic field pattern.

Furthermore, the PTE analysis presented in Fig. 5.18 confirms that the addition of NFPs leads to a notable improvement in efficiency. In this study, the PTE was calculated using the following expression:

$$\text{PTE} = |S_{21}|^2 \quad (5.3)$$

Among the tested configurations, the one employing a greater number of loaded loops with smaller size (eight loops in total) outperforms the configuration with fewer but larger loops. This suggests that a denser arrangement of smaller resonant elements can more effectively confine and direct the magnetic field toward the receiving unit, resulting in a higher received power and more efficient wireless energy transfer.

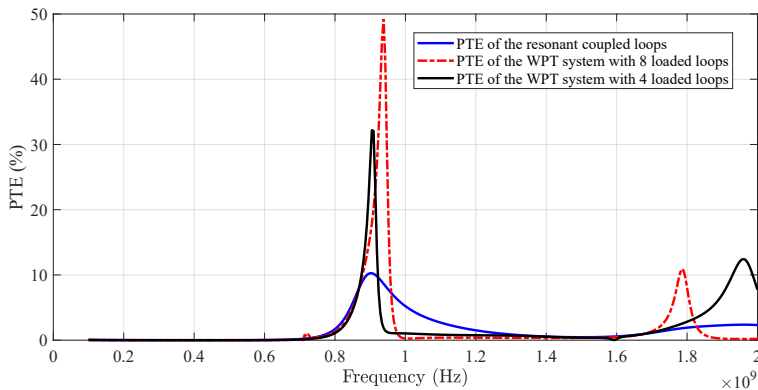


Figure 5.18: PTE of the WPT systems for $D = \lambda/4$ and $d = \lambda/2$

Overall, these results underline the crucial role of NFP geometry and placement in enhancing the electromagnetic performance of resonant WPT systems and provide a promising pathway for designing high efficiency wireless power solutions, particularly in scenarios where alignment and compactness are critical. Dual Tx topology achieves higher radiated power compared to a single

Tx system, with TLMs playing a dominant role in power transfer across all three configurations. In multi Tx topologies, TLMs are characterized by in-phase currents in the transmitting loops and a 180° phase shift in the receiving loop. However, while the interconnected dual Tx configuration successfully reduces misalignment sensitivity, it also results in lower radiated power and a shift in resonance frequency due to structural modifications. , the next step is to investigate how the positioning of the NFPs affects the PTE. Specifically, the distance between the NFP and the transmitting antenna will be varied to evaluate its impact on PTE.

5.4.3 Effect of NFPs Position Between the Tx and Rx on the PTE of the system

the same system is considered; however, in this section, the PTE is calculated for the scenario in which the NFP is placed precisely at the midpoint between the Tx and Rx antennas. This central placement corresponds to a distance $d_0 = \lambda/8$, which serves as a reference point for further evaluations.

Subsequently, the NFP was displaced from this midpoint in toward the Tx to assess the impact of its position on the overall system performance. The resulting variations in PTE are illustrated in Fig. 5.19.

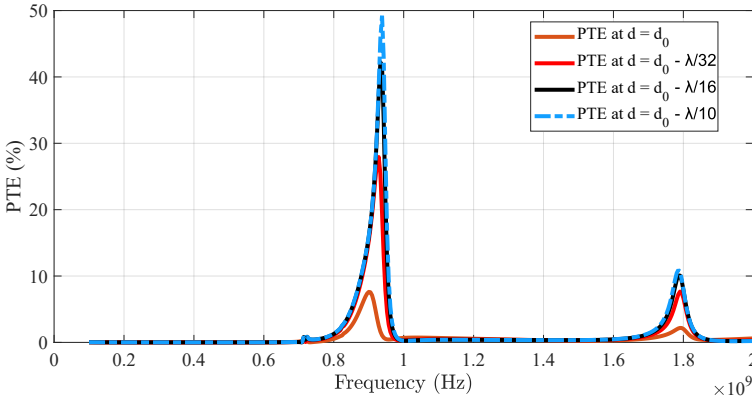


Figure 5.19: PTE in different positions of the NFP between the Tx and the Rx loops.

The simulation results reveal a clear correlation between the positioning of the NFPs and the PTE. Four distinct displacement scenarios were analyzed to assess the influence of NFP location relative to the Tx loop. The lowest PTE value, which is below 10%, was recorded when the NFPs were placed symmetrically at the midpoint between the Tx and the Rx loops, representing the

5.4 Comparison Between The Near-Field Plates WPT Systems

farthest position from the Tx. As the separation between the Tx loop and the NFPs decreased, a significant improvement in PTE was observed. In the closest tested configuration, the PTE reached approximately 50%, demonstrating that reducing the gap enhances magnetic coupling and overall system efficiency.

To explain the observed increase in PTE when the NFPs are placed closer to the Tx, we consider the role of magnetic field shaping and mutual inductance. In a WPT system based on magnetic coupling, the PTE is directly related to the square of the mutual inductance M_{eff} , which depends on the intensity and alignment of the magnetic field at the Rx. The presence of NFPs introduces additional reactive elements that enhance the magnetic field through induced currents. When these structures are properly positioned, they constructively interfere with the field generated by the Tx, thereby increasing the total magnetic field at the Rx. This phenomenon can be explained by the constructive interference between the magnetic field generated by the Tx antenna and the one induced in the NFPs. These induced fields effectively enhance the total magnetic field received at the Rx loop, thereby increasing the mutual inductance between the Tx and Rx elements.

This chapter has presented several comparative analyses between various WPT structures, using both CMA) and PTE evaluations. Among the studied configurations, the dual Tx topology without interconnections demonstrated the most stable magnetic field distribution and the highest PTE performance. The following chapter will focus on experimental validation by presenting measurements of the dual Tx topology and comparing its performance to that of the single Tx configuration while using the same power source.

CHAPTER 5. COMPARISON BETWEEN DIFFERENT WPT SYSTEMS

Chapter 6

Dual Tx WPT System for Enhanced Lateral Misalignment Tolerance

In WPT systems, lateral misalignment between Tx and Rx coils significantly reduces PTE, limiting their practical use. This chapter introduces a novel magnetically coupled resonant WPT system based on a dual-Tx configuration. Using a Wilkinson power divider, both Tx coils are excited simultaneously, forming a coherent and symmetrical magnetic field around a centrally placed Rx coil. Unlike traditional systems that rely on additional control circuits or multiple power sources, this design maintains simplicity while improving misalignment resilience.

In this chapter, simulations and experimental results are conducted to show that the proposed system sustains a wider lateral range compared to single Tx setups, demonstrating its effectiveness for biomedical applications where coil alignment cannot always be guaranteed.

6.1 Proposed Methodology

To develop effective dual Tx WPT system, a comprehensive set of analytical methods and modeling procedures was adopted. These methods aim to characterize and optimize the electromagnetic interactions within the antenna system, specifically focusing on two critical aspects, which are minimizing undesired coupling (decoupling) between the Tx loops, and enhancing the coupling between the Tx and the Rx units. Understanding and managing the electromagnetic behavior of multi Tx configurations is essential to ensure efficient and

CHAPTER 6. DUAL TX WPT SYSTEM FOR ENHANCED LATERAL MISALIGNMENT TOLERANCE

Table 6.1: Existing examples of WPT systems utilizing multi-Tx coils.

Ref.	Tx Decoupling	Axial Mis.	Freq.	Coils	Features	Mea.
[101]	Flux dist.	density ≤ 14 cm	160 kHz	Dual Tx, Dual Rx	Equivalent load resistance depends on rated load power.	✓
[104]	CMA	≤ 18 cm	350–550 MHz	Dual Tx, 1 Rx	Analytical efficiency evaluation.	×
[112]	CMA	$= 15$ cm	350–700 MHz	Dual Tx, 1 Rx	Efficiency assessed using CMA at single distance.	×
[129]	Not assessed	≤ 15 cm	85 kHz	Quad. Dual Rx	Tx, Circuit modeling and component tuning for optimal performance.	✓
[130]	Not assessed	≤ 40 cm	6.78 MHz	Up to 50 Tx, 1 Rx	Magnetic field leakage beyond targeted area.	✓
[131]	Parity Time symmetry	≤ 17 cm	120–200 kHz	Dual Tx, 1 Rx	Self-excited oscillation sensitive to stability and components.	✓
[132]	Compensating Inductor	≤ 10 cm	85 kHz	Dual Tx, 1 Rx	Reconfigurable topologies needed for misalignment tolerance.	✓

stable power delivery, particularly under misalignment or dynamic positioning scenarios. Therefore, a concise review of relevant state-of-the-art WPT systems employing multiple Tx, highlighting their design principles, limitations, and implementation challenges is conducted in Table 6.1.

The multi-Tx topology has emerged as a promising solution to enhance the efficiency of WPT systems across a broad spectrum of applications. In particular, the dual-Tx configuration presented in [101] was implemented to ensure effective energy delivery for heart pacemakers, as illustrated in Fig. 6.1(a). While the study did not propose a specific decoupling strategy between the two Tx units, it focused on analyzing the magnetic flux density distribution to evaluate performance. Furthermore, the system’s equivalent load resistance was shown to be dependent on the rated load power, emphasizing the need for careful load matching in biomedical applications. In [104, 112], CMA was employed to analyze different WPT systems for general applications. These studies demonstrated the superior efficiency of the dual Tx topology compared to other configurations, which are shown in Fig. 6.1(b). However, validation of this enhanced efficiency through experimental measurements has not yet been carried out. Other innovative solutions have been proposed in [129–132], as illustrated respectively in Fig. 6.1(c), (d), (e), and (f). Yet, these approaches encountered several limitations, including challenges in circuit modeling, complexity in component selection, and issues related to magnetic field leakage.

6.1 Proposed Methodology

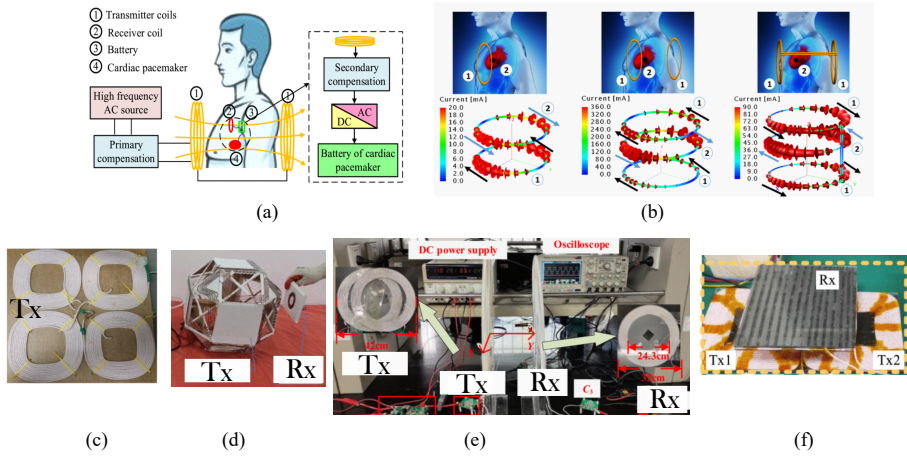


Figure 6.1: Existing examples of WPT systems utilizing multi-Tx coils: (a) Dual Tx topology [101], (b) Different dual Tx topologies [104, 112], (c) Quadruple Tx coil [129], (d) Up to 50 Tx [130], (e) Dual overlapped Tx topology [131], (f) Dual coplanar Tx topology [132].

The key distinction between the present proposed system and previous works lies in the fabrication and experimental validation of prototypes based on the proposed dual Tx solution, which employs a conventional Wilkinson Power Divider (WPD) without requiring any modifications to the input power configuration. A major advantage of the proposed approach is its compatibility with existing WPT infrastructures, as it remains independent of the shape or structural characteristics of the coils. Furthermore, the novelty of this work stems from the enhancement of the Tx unit through the addition of a second transmitter, designed to meet specific application requirements without necessitating changes to the Rx unit or the communication protocols. By generating a stable and uniform magnetic field between the two decoupled Tx coils, the proposed configuration significantly improves the tolerance to Rx positioning compared to the conventional single Tx topology.

6.1.1 The Structure of The Proposed Dual Tx MCR-WPT System

As illustrated in Fig. 6.2, the CST Computer-Aided Design (CAD) model presents a clear representation of the proposed dual Tx WPT configuration. This setup consists of two identical and uncoupled transmitting loops (Tx1 and Tx2) placed laterally, with a Rx loop strategically positioned between them.

CHAPTER 6. DUAL TX WPT SYSTEM FOR ENHANCED LATERAL MISALIGNMENT TOLERANCE

Such a topology aims to generate a stable and symmetrical magnetic field in the central region, thereby enhancing the PTE even under unexpected lateral misalignment scenarios, where precise alignment is difficult to ensure.

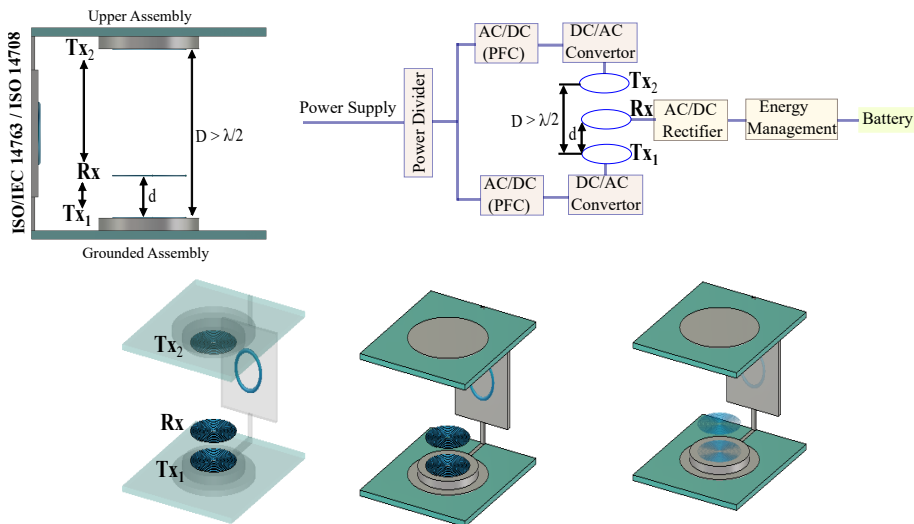


Figure 6.2: The CAD using CST and the block diagram of the proposed WPT.

To clarify the functional architecture of the system, the figure also includes a block diagram highlighting the role of key components such as the WPD used to evenly distribute power from a single source to the two Tx. The design ensures that Tx₁ and Tx₂ remain electromagnetically decoupled while operating in phase, which strengthens the magnetic flux in the Rx region without requiring any modifications to the Rx unit itself. This is particularly advantageous for biomedical applications, where the Rx is implanted and cannot be easily modified. This configuration not only simplifies circuit implementation by using a passive power splitter but also allows easy integration with existing wireless power equipment. The methodology is designed to be robust, compact, and compliant with the safety and functional requirements of implantable medical technologies.

From regulatory and technical perspectives, the proposed configuration is developed in alignment with existing biomedical standards and safety guidelines, including IEEE P2668 [133], IEEE 1708-2014 [134], and ISO 14708-1 [135], which address aspects of energy transfer, electromagnetic compatibility, and patient safety. Thus, to implement an effective dual Tx system for

WPT in biomedical applications, the experimental validation guidelines can be summarized as follows.

1. VNA loads the power to the WPD input port; hence, the power level in the output ports should be tested near the resonance of the system,
2. The output ports of the WPD should be uncoupled to maintain the decoupling between Tx1 and Tx2 loops,
3. Two uncoupled identical Tx1 and Tx2 are connected to the outputs of the WPD and positioned laterally, ensuring a separation distance greater than $\lambda/2$,
4. The Rx loop, with similar dimensions as the Tx loops, is displaced in between them and is connected to the VNA to detect the level of the Rx power.

Hence, while alterations are observed solely within the Tx antenna system, the overall design remains subject to technical constraints and regulatory compliance in practical applications with standards such as IEC 60601-1 [136], IEC 60601-1-2 [137], and IEC 62304 [138], ensuring safe and effective operation within biomedical environments.

6.2 Decoupling Techniques

In the dual Tx topology illustrated in Fig. 6.2, electrical energy from an alternating current (AC) power source is converted into high-frequency signals via a high-frequency inverter. This energy is then radiated by the Tx coils as an electromagnetic field, which is captured by the Rx coil and subsequently converted into direct current (DC) power for the target device [139].

In inductive WPT systems based on a single Tx, the electromagnetic coupling relies on longitudinally aligned dipole fields, whose strength diminishes proportionally to the cube of the distance between the Tx and Rx coils. Therefore, minimizing this separation is critical for enhancing coupling and maximizing PTE [140]. In contrast, the proposed system utilizes a dual parallel Tx configuration, where an inverse design strategy is applied. Indeed, the coupling between the Tx coils is intentionally minimized by increasing the separation between them. This design choice is validated through CMA, which provides a clear visualization of the coupling behavior between the two parallel loops in Chapter 3, Chapter 4, and Chapter 5. Notably, CMA results demonstrate that beyond specific spacing thresholds, the mutual coupling effectively vanishes. To support these findings and experimental measurements, a complementary overview of the underlying electromagnetic principles governing this decoupling behavior is also provided.

6.2.1 Decoupling Using Simulation Outcomes

In general, simulation results are critical for assessing and validating decoupling strategies in WPT systems, and they could be effective in enhancing the performance of the proposed dual Tx topology. One of the most widely used techniques in the literature involves analyzing the magnetic field distribution in the inter-Tx region to determine the optimal positioning of the Rx. The simulated magnetic field intensity confirms that the air gap between the two Tx coils establishes favorable conditions for Rx placement, enabling a NF focusing technique [140] that significantly enhances PTE when the Rx is appropriately aligned.

In general, simulation results are critical for assessing and validating decoupling strategies in WPT systems, and they could be effective in enhancing the performance of the proposed dual Tx topology. One of the most widely used techniques in the literature involves analyzing the magnetic field distribution in the inter-Tx region to determine the optimal positioning of the Rx. The simulated magnetic field intensity confirms that the air gap between the two Tx coils establishes favorable conditions for Rx placement, enabling a NF focusing technique [141] that significantly enhances PTE when the Rx is appropriately aligned.

Furthermore, S-parameters are utilized. Specifically, the S_{21} provides insight into the transmitted power between the coils, while S_{11} and S_{22} assess impedance matching. For two identical loop antennas, the PTE can be approximated as follows:

$$\text{PTE} = \frac{|S_{21}|^2}{(1 - |S_{11}|^2)(1 - |S_{22}|^2)} \approx |S_{21}| \quad (6.1)$$

In the perspective of this specific topology, to ensure minimal mutual coupling between the Tx coils, the $|S_{21}|$ should be reflecting small values.

These simulation techniques are commonly adopted across the literature as they provide early stage validation of system design and functionality. In particular, S-parameters and magnetic NF distributions are analyzed through both simulations and to support the development of a WPT system with optimized performance. However, while simulation outcomes can offer valuable insights and suggest performance optimization, their reliability is significantly improved when supported by analytical models and theoretical grounding. When simulations are reinforced by electromagnetic theory, the transition toward physical measurements and prototype fabrication becomes more secure and efficient, reducing design uncertainties and increasing the affectiveness of real-world system success.

6.2.2 Decoupling Using Electromagnetic Theory

The efficiency of inductive power transfer is highly sensitive to the spatial separation between loop antennas. In the dual Tx configuration, maintaining sufficient distance between the Tx loops is critical to minimizing mutual inductance and unintended electromagnetic coupling, both of which can lead to power leakage and degraded system efficiency. As depicted in Fig. 6.3, only one Tx loop is actively powered, while both loops are designed and modeled as perfect electric conductors (PEC). Under these conditions, the fundamental principles of electromagnetism offer a clear framework for understanding the physical mechanisms governing inductive coupling within the system.

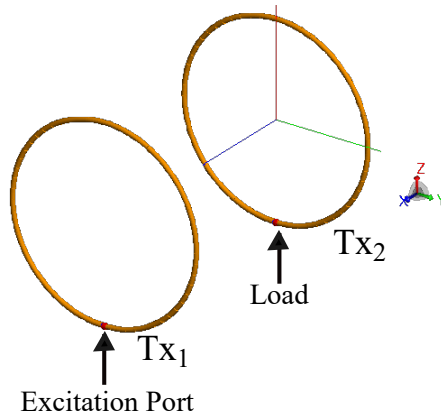


Figure 6.3: Configuration of the Two Tx Loops: Tx1 Excited and Tx2 connected to the Load.

The magnetic field B generated by Tx1 is governed by Ampere's Law, which relates it to the net current enclosed within the loop, I_{Tx1} , as expressed below [142]:

$$\oint B \, dl = \mu_0 I_{Tx1} \quad (6.2)$$

where μ_0 denotes the permeability of free space, under the assumption that both loops are modeled as perfect electric conductors (PEC). The resulting magnetic field B propagates through space and couples with Tx2, where it induces an electromotive force (EMF) in accordance with Faraday's Law:

$$\epsilon_{Tx2} = -\frac{d\Phi_B}{dt} \quad (6.3)$$

where Φ_B is the magnetic flux circulating in Tx2, and it is expressed as:

CHAPTER 6. DUAL TX WPT SYSTEM FOR ENHANCED LATERAL MISALIGNMENT TOLERANCE

$$\Phi_B = \iint_A \vec{B} \cdot d\vec{A} \quad (6.4)$$

where dA denotes the area of the Tx2 loop, and $d\vec{A}$ is the differential area element normal to the loop's surface. The term $\vec{B} \cdot d\vec{A}$ represents the component of the magnetic field perpendicular to the surface of Tx2, as illustrated in Fig. 6.4. The negative sign in Faraday's Law accounts for Lenz's Law, indicating that the induced electromotive force ϵ_{Tx2} acts in opposition to the change in magnetic flux. As a result, the magnetic field produced by the current in Tx1 extends into the surrounding space and couples with Tx2, thereby inducing an EMF through the time-varying flux linkage. In order to realize the intended decoupling between Tx1 and Tx2, the electromotive force induced in Tx2 must be minimized, ideally approaching zero.

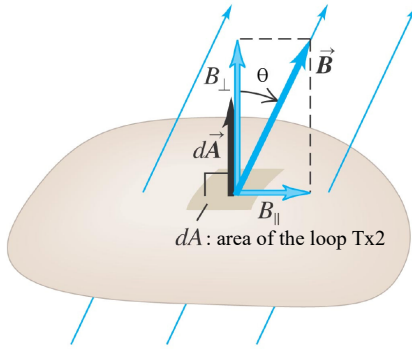


Figure 6.4: Representation of Faraday's Law: the magnetic field generated by Tx1 \vec{B} , the surface element on Tx2 $d\vec{A}$, and the angle in-between θ

In this context, θ is the angle between the magnetic field vector \vec{B} generated by Tx1 and the differential area element $d\vec{A}$ of the Tx2 coil. When the coils are perfectly aligned ($\theta = 0^\circ$), the magnetic field lines from Tx1 are fully perpendicular to the Tx2 loop surface, resulting in maximum Φ_B linkage. However, the objective of the proposed configuration is not to maximize Φ_B within Tx2, but rather to minimize it, ideally to zero, in order to suppress mutual coupling and prevent power leakage between the two Tx loops. Instead, the design aims to concentrate the magnetic flux in the space between Tx1 and Tx2, thereby enhancing the magnetic field in that region to benefit the centrally placed Rx coil. Achieving this requires careful adjustment of the spacing between Tx1 and Tx2, which plays a critical role in maximizing the field in the inter loops region while maintaining electromagnetic decoupling.

6.3 Decoupling Tx1 and Tx2: Simulations and Measurements

To better analyze and optimize the proposed configuration, the fundamental equivalent circuit model is illustrated in Fig. 6.5.

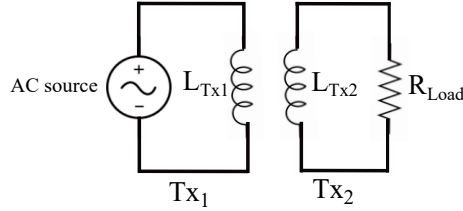


Figure 6.5: Equivalent Circuit Model of the Tx Loop System.

In this representation, Tx1 is composed of an AC voltage source (V_{Tx1}) in series with a primary loop (L_{Tx1}). Tx2, positioned nearby, consists of a secondary coil L_{Tx2} connected to a load resistance R_{Load} . The intrinsic series resistance of the Tx1 coil, denoted as R_{Tx1} , is typically not shown explicitly in simplified models, as it is commonly absorbed into the source impedance. However, this resistance plays a non-negligible role in system efficiency, as it contributes to energy dissipation in the form of heat. The total input power delivered to Tx1, denoted P_{In} , is given by the following expression:

$$PTE_2 = \frac{P_{Tx2}}{P_{Tx1}} = \frac{|I_{Tx2}|^2 R_{Load}}{|I_{Tx1}|^2 R_{Tx1}} \quad (6.5)$$

Following this comprehensive analysis of inductive coupling between two circular loops, examined through both physical intuition and mathematical formulation, magnetic field distributions will be simulated using FEKO. In parallel, PTE measurements will be conducted to validate and confirm the electromagnetic decoupling between the two Tx coils.

6.3 Decoupling Tx1 and Tx2: Simulations and Measurements

The transmitter loops (Tx1 and Tx2) and the Rx loop are each designed with a diameter D of 23.18 cm ($\simeq 0.3\lambda$) and are constructed from metal wire with a thickness (w) of 0.14 cm. The previously outlined methodologies will be employed to achieve effective decoupling between the two transmitters, while simultaneously ensuring favorable conditions for positioning the receiver between them.

6.3.1 Simulations of The Magnetic NF Plots and The Sparameters

To illustrate the impact of increasing axial separation, magnetic NF distributions simulated using FEKO, along with their corresponding S-parameters, are presented in Fig.6.6 across a frequency sweep from 0.35 to 0.6 GHz.

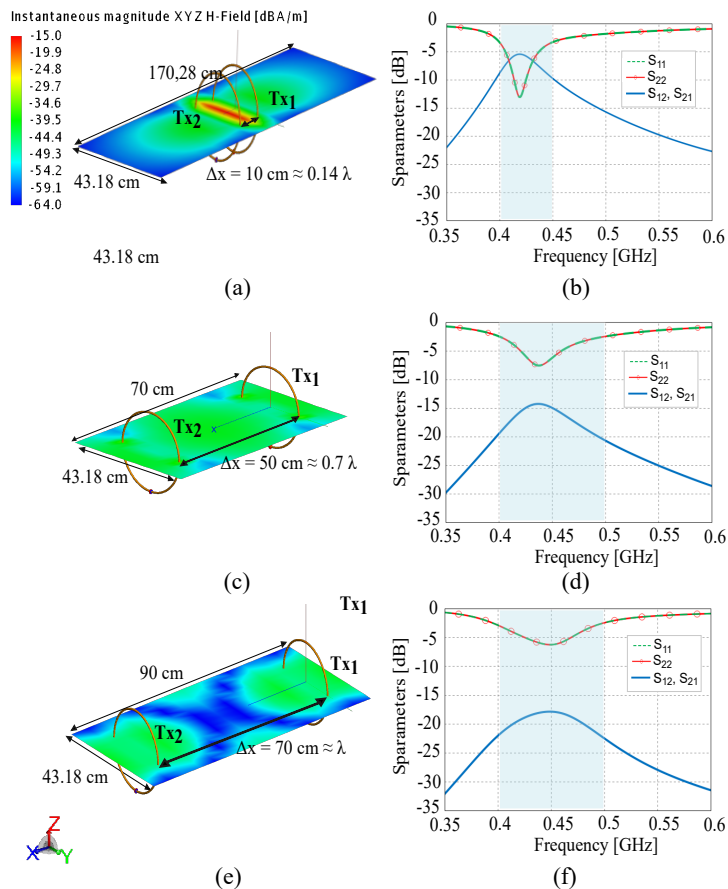


Figure 6.6: Magnetic NF distributions and corresponding S-parameters for Tx1 and Tx2 at varying separation distances: (a) and (b) $\Delta x = 10 \text{ cm}$; (c) and (d) $\Delta x = 50 \text{ cm}$, (e) and (f) $\Delta x = 70 \text{ cm}$.

For consistency and clarity, the same color scale is applied across all three cases, enabling a direct visual comparison of the magnetic field variations and effectively capturing the influence of axial misalignment on the system's elec-

6.3 Decoupling Tx1 and Tx2: Simulations and Measurements

tromagnetic behavior. The analysis begins with an evaluation of the initial configuration depicted in Fig.6.6(a), where the separation between the transmitting antennas along the x-axis is varied across three discrete values, ranging from 10 cm to 70 cm ($\simeq 0.14\lambda$ and 0.7λ , respectively). This range spans from the NF to the far-field FF region, including separations exceeding $\lambda/2$.

As the separation distance between the two transmitter loops increases, a clear decoupling effect becomes evident. In the initial configuration shown in Fig.6.6(a) and (b), where the separation is relatively small, the NF region exhibits strong electromagnetic coupling, indicated by a high magnetic field intensity reaching approximately -15 dBA/m. This high coupling efficiency is reflected in a correspondingly elevated PTE of 53.47%. However, when the separation is increased to 0.7λ , as illustrated in Fig.6.6(c) and (d), the PTE decreases and falls to just 0.19%. Yet, the magnetic field in the inter loops region is relatively uniform.

As the separation between the Tx loops is further increased, as depicted in Fig. 6.6(e) and (f), a distinct instability in the magnetic field distribution emerges. This instability is characterized by the appearance of discontinuities and fragmentation in the field lines, particularly within the central region between the coils. The field intensity in this area, predominantly represented by blue shading, indicates the weakest magnetic field strength observed across all tested configurations. This visual degradation corresponds to a complete breakdown of magnetic coupling, with the PTE dropping to nearly zero. A similar behavior confirms that beyond a certain separation distance, larger gaps between Tx1 and Tx2 not only weaken the coupling but also disrupts the spatial uniformity of the field, which renders the configuration ineffective for power transfer and unsuitable for reliable Rx placement.

6.3.2 Measurements: Optimal Configuration of The Decoupled Tx Loops

Following the simulation phase, an experimental setup was constructed to empirically evaluate the PTE under practical conditions. The system was excited using a VNA, which delivered the signal through a coaxial cable, allowing for precise control over excitation and power measurement. However, it is important to note that the measurement setup may introduce discrepancies due to the inherent resistive losses in the coaxial cables. These losses manifest as heat dissipation and tend to increase with both cable length and operating frequency, potentially leading to an underestimation of the actual system efficiency in the experimental results.

Consequently, based on the measurements illustrated in Fig. 6.7, the experimental results validate that a separation distance of 0.7λ offers an optimal balance between magnetic field stability and minimal electromagnetic coupling

CHAPTER 6. DUAL TX WPT SYSTEM FOR ENHANCED LATERAL MISALIGNMENT TOLERANCE

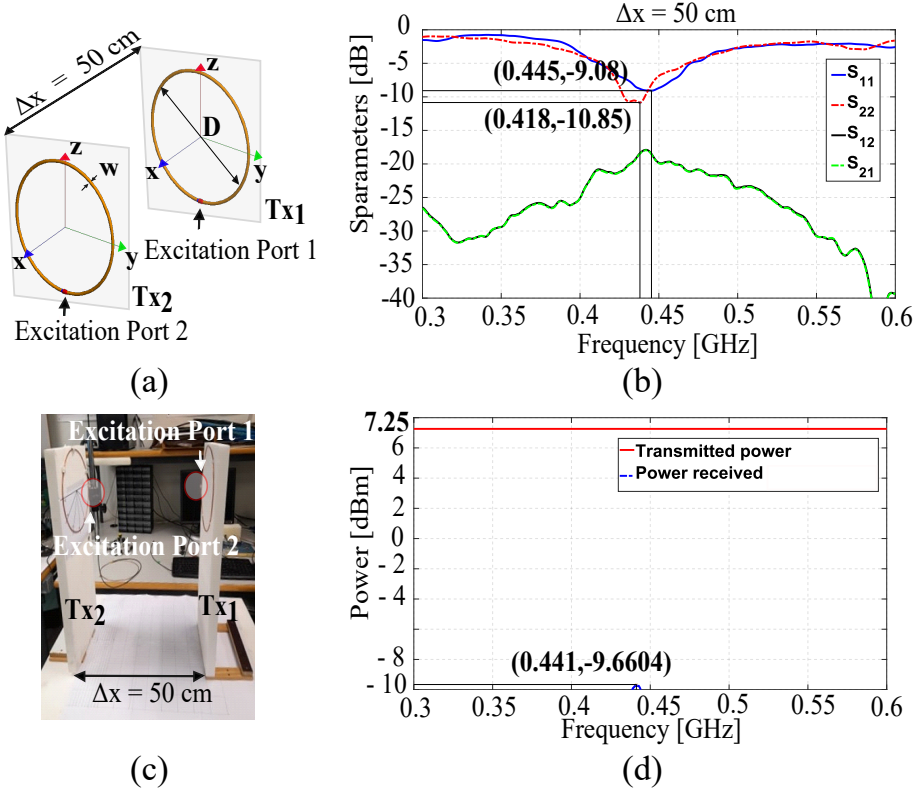


Figure 6.7: Configuration and measurements of Tx1 and Tx2 separated by a distance of $\Delta x = 50$ cm : (a) Dimensions and system layout; (b) Measurement setup; (c) Measured S-parameters (S_{11} , S_{22} , S_{21} , and S_{12}); (d) The power measurement.

between the two Tx loops. At this spacing, the measured PTE approaches 0%, indicating that unintended coupling between Tx1 and Tx2 is effectively suppressed. Specifically, Fig. 6.7(b) presents the measured S-parameters of the transmitting unit, where both S_{21} and S_{12} consistently remain below -17 dB across the frequency range of 0.3 to 0.6 GHz. These values further confirm the achievement of strong isolation between the two Tx coils. Besides, Fig. 6.7(d) illustrates the corresponding power transfer characteristics, with the peak received power at Tx2 occurring at 0.441 GHz and measuring -9.6604 dBm. It is important to note that the transmitted power (P_{Tr}) is adjusted via the VNA and was fixed at 7.25 dBm for the different measurements. This con-

6.4 Measurements and Validation of the Dual Tx WPT System

trolled excitation enables consistent and repeatable evaluation of the system's decoupling performance. Overall, the results reinforce the effectiveness of the proposed spacing strategy in maintaining field uniformity for Rx placement while ensuring minimal cross-coupling between Tx loops.

6.4 Measurements and Validation of the Dual Tx WPT System

In the previous section, the decoupling behavior between the two Tx loops was analyzed and experimentally validated. However, an additional challenge in the proposed configuration lies in the use of a single power source to drive both transmitters. To address this, the implementation of a properly designed conventional WPD becomes essential. The WPD must efficiently distribute power to both Tx coils while preserving their decoupling during operation and measurement. This power divider plays a critical role in enabling the simultaneous excitation of the dual Tx system without inducing mutual interference, thereby maintaining the system's intended electromagnetic isolation.

The final system integrates all previously analyzed components, including the dual Tx configuration, the WPD, and the Rx coil, which is positioned between the two transmitters to take advantage of the enhanced magnetic field region. To assess the effectiveness of this configuration, its performance will be compared to traditional single Tx topology. This comparative analysis is vital for quantifying improvements in PTE and evaluating the proposed system's robustness, particularly in terms of its tolerance to axial misalignment.

6.4.1 The Conventional Wilkinson Power Divider

To ensure equal-amplitude power distribution to both Tx1 and Tx2, a conventional WPD was inserted between the VNA and the dual Tx WPT system. The role of the WPD in this configuration is split the input power while simultaneously maintaining high isolation between the output ports to prevent any undesired coupling between the two Tx loops. To confirm the effectiveness of this component, its performance was evaluated through both full-wave electromagnetic simulations using AWR Microwave Office (MWO) and experimental measurements from a fabricated prototype.

The physical structure of the WPD is shown in Fig.6.8a. It consists of two quarter-wavelength ($\lambda/4$) transmission lines, each with a characteristic impedance of $\sqrt{2} Z$, connected to an isolation resistor of 100Ω placed between the two output ports (port 2 and port 3). This classical configuration is designed to ensure that when equal loads are connected, any reflected signals are dissipated in the isolation resistor rather than being coupled between outputs.

CHAPTER 6. DUAL TX WPT SYSTEM FOR ENHANCED LATERAL MISALIGNMENT TOLERANCE

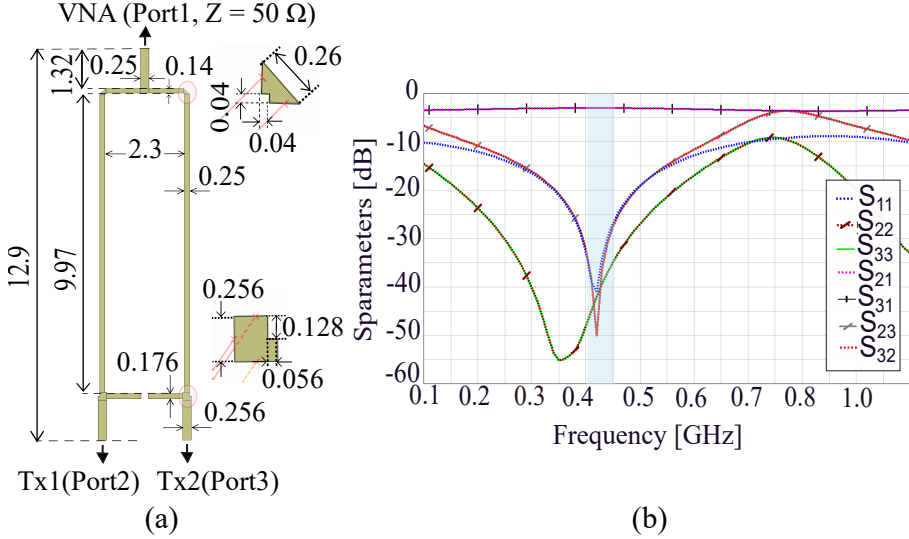


Figure 6.8: (a) The WPD layout with the specific dimensions in centimeter (cm); (b) The S-parameters associated to the WPD simulated using AWR Microwave Office (MWO).

The S-parameter results, presented in Fig. 6.8b, provide a clear validation of the WPD’s performance. The parameters S_{23} and S_{32} , which represent the transmission between the two output ports, remain below -17 dB across the frequency range of 0.1 to 1.1 GHz, demonstrating excellent isolation. Furthermore, the reflection coefficients S_{11} , S_{22} , and S_{33} , which correspond to input and output port reflections, are also low within the 0.4 to 0.45 GHz range. These results indicate good impedance matching and efficient power delivery to both Tx coils in the operating band of the system.

With the VNA supplying an input power of 7.25 dBm to the Wilkinson Power Divider (WPD), the power levels delivered to each Tx loop (P_{in}) are accurately determined by measuring the output at the WPD’s ports, as illustrated in Fig. 6.9. The measured P_{in} values remain stable across the frequency range of 0.3 to 0.6 GHz, consistently falling within the range of 3.7 to 4.2 dBm. These values closely align with the theoretical expectation of 4.47 dBm, confirming the WPD’s intended performance. As designed, the WPD equally divides the input power between the two output ports while preserving impedance matching conditions [143], thereby ensuring efficient and balanced excitation of the dual Tx system.

6.4 Measurements and Validation of the Dual Tx WPT System

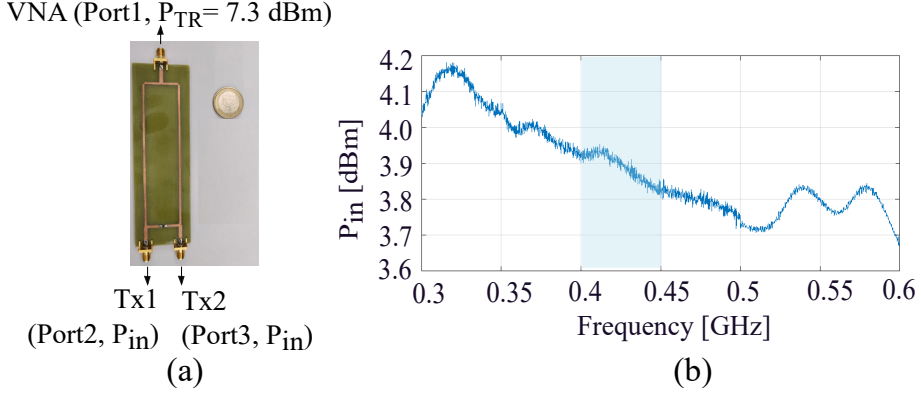


Figure 6.9: (a) The layout of the manufactured WPD; (b) The power variation at the outputs of the WPD (P_{in}) within the frequency range of 0.3 to 0.6 GHz.

6.4.2 Experimental Validation of The System

The final prototype of the WPT system incorporates the core components previously described: Tx1, Tx2, the Rx, and the WPD. To evaluate the system's performance under practical conditions, a controlled axial misalignment is introduced by shifting the Rx loop along the central axis between Tx1 and Tx2. At each position, the received power, P_{RL} , is measured to assess the spatial sensitivity of the configuration. To highlight both the novelty and the effectiveness of the proposed dual-Tx WPT system, comparisons are made across three scenarios: a basic single-Tx system without a power divide (see Fig. 6.10(a)), a single-Tx configuration with the WPD connected to only one output port (see Fig. 6.10(d)), and a full dual-Tx configuration using the WPD (see Fig. 6.10(g)). The second scenario is particularly relevant, as it emulates a real-world fault condition in which one of the Tx systems is non-functional or disconnected. Evaluating system behavior under such conditions is critical for assessing its robustness and reliability. The measured PTE values for the three configurations are calculated using the following expression:

$$\text{PTE (\%)} = \frac{P_{RL}}{P_{Tr}} \times 100 \quad (6.6)$$

where P_{Tr} represents the power denotes by the VNA, which is equal to 7.25 dBm (5.3 W), and P_{RL} denotes the measured power of the Rx unit. This ratio is calculated when both parameters are expressed in watts (W).

CHAPTER 6. DUAL TX WPT SYSTEM FOR ENHANCED LATERAL MISALIGNMENT TOLERANCE

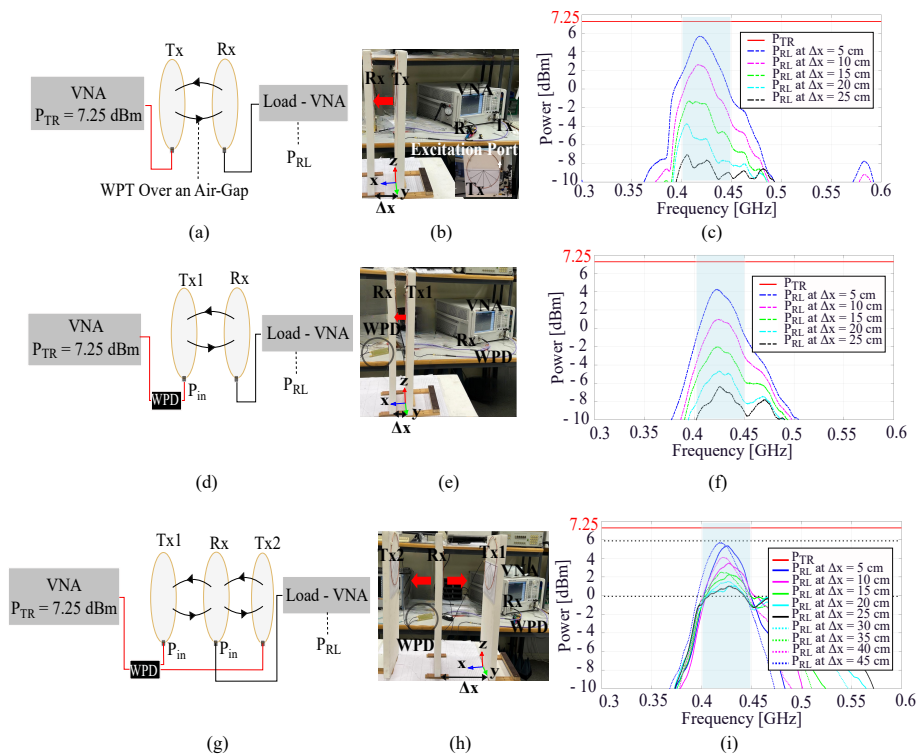


Figure 6.10: The block diagram, the measurement set-up, and the measured power of the Rx loop for Δx ranging from 5 cm (0.07λ) to 45 cm (0.7λ) of : (a)-(b)-(c) The single Tx configuration; (d)-(e)-(f) The single Tx configuration using the WPD ; (g)-(h)-(i) The dual Tx configuration using the WPD.

To enhance the clarity of the PTE comparisons across the proposed topologies, Fig.6.11 presents the PTE curves for the three configurations over the different separation distances. These results are consistent with the numerical values provided in Table6.2, which are derived from the experimental measurements shown in Figs. 6.10(c), (f), and (i). A detailed examination of the experimental results reveals that the dual-Tx configuration exhibits significantly greater robustness to lateral misalignment when compared to the single-Tx configurations. In the case of Configurations 1 and 2, which utilize a single transmitting coil, the PTE declines sharply as the Rx loop is displaced laterally. Notably, the PTE drops to near-zero values at separation distances equal

6.4 Measurements and Validation of the Dual Tx WPT System

to or exceeding 0.35λ , highlighting the limited spatial coverage and directional dependence of single Tx topologies.

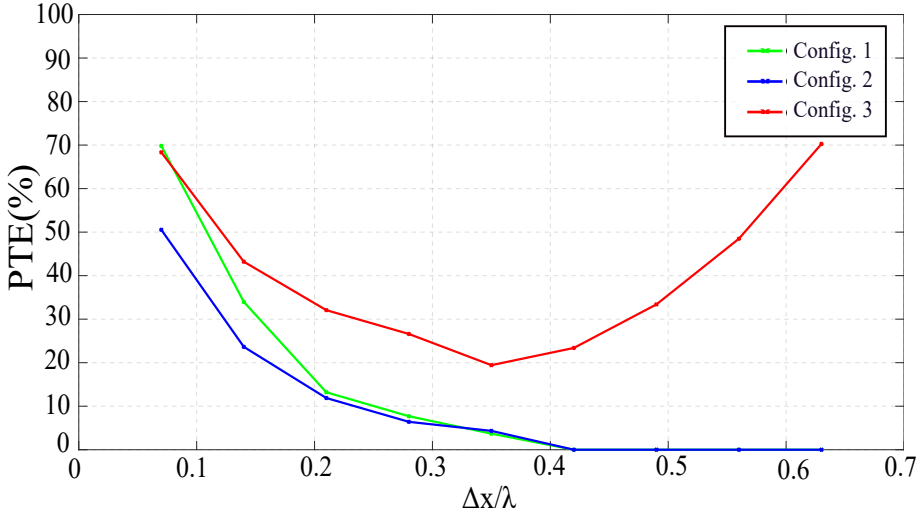


Figure 6.11: PTEs of the three configurations.

In contrast, the dual Tx configuration demonstrates a symmetrical and more spatially distributed field profile, resulting in improved tolerance to misalignment. When the Rx coil is positioned adjacent to either Tx1 or Tx2, the system achieves peak PTE values approaching 70%, confirming efficient power coupling in these regions. At the midpoint between the two Tx loops, which corresponds to a separation of 0.35λ , the PTE reaches its minimum value of 19.43%, yet still remains significantly higher than the near-zero performance observed in the single Tx cases at equivalent displacements. This symmetrical behavior suggests that the dual Tx system creates overlapping magnetic fields that maintain usable energy transfer across a broader region. Such characteristics are particularly advantageous in practical applications where the precise positioning of the Rx coil cannot be guaranteed, reinforcing the proposed configuration's suitability for misalignment-tolerant wireless power delivery.

In addition, the performance discrepancy observed between the single-Tx configurations primarily arises from Configuration 2. In this setup, only one output port of the WPD is connected to a Tx coil, while the second output port remains unterminated. The lack of a matched load at the unconnected port results in signal reflections that are not properly dissipated. These reflected signals can interfere destructively with the transmitted power, especially at

CHAPTER 6. DUAL TX WPT SYSTEM FOR ENHANCED LATERAL MISALIGNMENT TOLERANCE

Table 6.2: Comparison between the PTEs of the three configurations

Δx	Config. 1		Config. 2		Config. 3	
	PTE	$f_{(MHz)}$	PTE	$f_{(MHz)}$	PTE	$f_{(MHz)}$
0.07 λ	69.81%	417	50.54%	422	68.34%	425
0.14 λ	33.96%	418	23.64%	424	43.20%	428
0.21 λ	13.20%	418	11.88%	423	32.07%	427
0.28 λ	7.70%	411	6.41%	426	26.6%	428
0.35 λ	3.69%	419	4.33%	425	19.43%	427
0.42 λ	-	-	-	-	23.39%	427
0.49 λ	-	-	-	-	33.39%	423
0.56 λ	-	-	-	-	48.49%	422
0.63 λ	-	-	-	-	70.26%	421

close proximity, leading to noticeable power losses and a degradation in PTE. This effect is most pronounced at small separation distances, where coupling is strongest and the imbalance in the system becomes more impactful.

However, as the lateral separation Δx increases beyond 0.21 λ , the difference between Configuration 1 (single Tx without a WPD) and Configuration 2 (single Tx with one WPD port unused) diminishes. Beyond this threshold, both configurations exhibit nearly identical PTE behavior and follow a similar trend of performance degradation with increasing misalignment. This convergence suggests that, at larger distances, the adverse effects of the unterminated WPD port in Config. 2 become less significant, likely due to reduced mutual coupling and weaker field interactions.

This chapter has demonstrated that the dual Tx configuration, supported by a conventional WPD, offers a robust and effective solution for enhancing the reliability and efficiency of WPT systems. By applying fundamental electromagnetic principles, the decoupling mechanism between the two Tx coils was thoroughly analyzed and validated through both simulation and experimental results. This decoupling is critical to minimizing mutual interference, ensuring

6.4 Measurements and Validation of the Dual Tx WPT System

stable operation, and maintaining efficient power delivery to a centrally placed Rx loop.

The study also examined the behavior of the system under varying axial misalignments, with comparative analysis against single Tx topologies. The findings confirm that the dual Tx system exhibits greater tolerance to spatial misalignment and achieves higher PTE across a wider operational region. This is particularly important in real-world scenarios, such as biomedical and IoT applications, where the precise positioning of the Rx cannot always be guaranteed.

While the use of a conventional WPD allows for equal power distribution and reduced coupling, the system's performance can be further enhanced by adopting selective excitation techniques. In the following chapter, the focus will shift toward methods governed by CMA, which will be used to selectively activate specific modes within biomedical WPT systems. This approach aims to optimize field distribution, further improve PTE, and increase the robustness of WPT systems in biomedical applications, especially under dynamic or misaligned condition.

**CHAPTER 6. DUAL TX WPT SYSTEM FOR ENHANCED
LATERAL MISALIGNMENT TOLERANCE**

Chapter 7

Selective Excitation Technique for WPT in Biomedical Devices Using CMA

Building upon the insights presented in the previous chapters, where the performance of different WPT configurations was validated through simulations and experimental measurements, this chapter introduces a novel approach to further enhance system efficiency through selective excitation techniques governed by CMA. While earlier investigations highlighted the importance of decoupling and optimal loop positioning, it became evident that the dominant mode near resonance is typically the one that naturally resonates closest to the system's operating frequency. However, without control over which mode is excited, system performance remains suboptimal.

To address this, the current chapter presents a selective excitation framework based on CMA, aimed at improving PTE in Conventional Strongly Coupled Magnetic Resonance (CSCMR) systems. These systems are particularly relevant for biomedical and wearable applications. The proposed technique allows for precise control of the electromagnetic behavior of the system, leading to enhanced magnetic field strength and stability.

7.1 SCMR and CSCMR Systems

NF WPT systems utilizing Inductive Power Transfer (IPT) [48, 49, 144] have been widely implemented across a variety of applications, largely due to their structural simplicity and reliable operation when the Tx and Rx are in close proximity. While IPT proves effective at very short ranges, its transmission distance is inherently limited to just a few centimeters, and its PTE tends to drop significantly, often below 50% at mid-range separations. To address these limitations and improve both efficiency and spatial tolerance, previous chapters have explored alternative techniques and configurations based on Magnetically Coupled Resonance (MCR). Simulation and experimental results confirmed that these approaches offer notable improvements in performance, particularly in scenarios with moderate misalignment or increased separation between loops.

Among these techniques, Strongly Coupled Magnetic Resonance (SCMR) [41] and Conventional SCMR (CSCMR) [145, 146] systems have emerged as a particularly promising solution. By leveraging resonant coupling between Tx and Tx, SCMR systems extend the effective transmission range to distances comparable to the physical size of the resonators, while maintaining higher PTE than conventional IPT methods. These enhanced characteristics make SCMR a superior candidate for applications requiring greater tolerance to positioning variations and improved mid-range efficiency, particularly in the context of biomedical and IoT device integration.

7.1.1 Design Features of SCMR Systems

SCMR systems rely on the use of resonant Tx's and Rx's that are tightly coupled through their magnetic fields. These systems achieve high PTE due to the strong interaction between resonant structures, which contrasts with non-resonant systems where the coupling is inherently weak and energy exchange is minimal [147]. A conventional SCMR system typically consists of four resonant elements, commonly implemented as either four loops or a combination of loops and coils, configured to enhance magnetic coupling and minimize energy loss. An example of an SCMR system utilizing helical resonators is illustrated in Fig. 7.1.

the SCMR system is composed of four loop antennas. The source element connected directly to the power supply, which is inductively coupled to the Tx element. The Tx resonator then ensures efficient PTE and a high coupling coefficient (K_{TX-RX}) to transfer energy to the Rx resonator. Finally, the power received by the Rx resonator is delivered to the load loop through inductive coupling. To achieve high overall PTE between the source and the load over larger distances it is essential to maximize the coupling coefficients (K_s , K_d , and K_{TX-RX}).

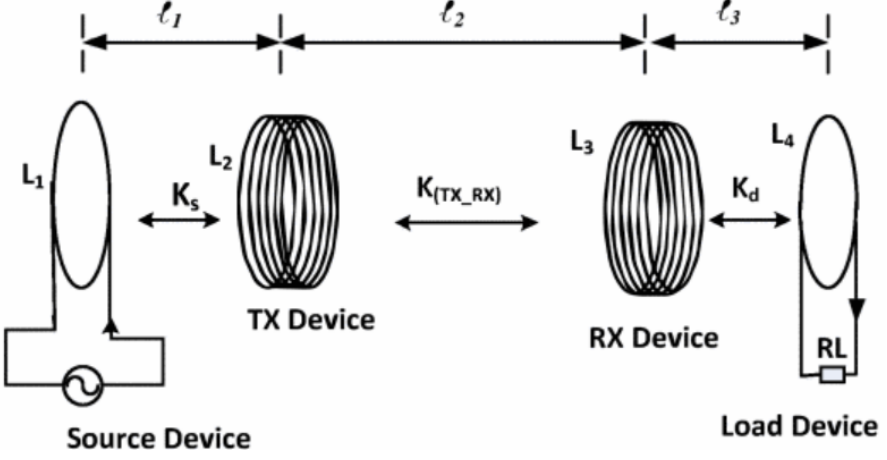


Figure 7.1: Schematic and characteristic parameters of SCMR system [148].

This requires that the SCMR design conditions be carefully considered during the system's development. Indeed, The Tx and Rx elements are both designed to operate at the same natural resonance frequency, ensuring efficient energy exchange through resonant coupling. This shared operating frequency corresponds to the point at which the quality factor of each resonator is naturally maximized, optimizing the PTE. The resonance frequency of the spiral resonator, f_r , is determined according to the expression provided in [41]:

$$f_r = \frac{1}{2\pi\sqrt{LC}} \quad (7.1)$$

The resonant frequency f_r also defines the operating frequency of the SCMR wireless power transfer system. The corresponding quality factor (Q) at this resonance can be expressed as [149] :

$$Q = \frac{2\pi f_r L}{R_{ohm} + R_{rad}} \quad (7.2)$$

where, L , R_{ohm} , and R_{rad} represent the self-inductance, ohmic resistance, and radiation resistance of the resonator, respectively. The parameter L characterizes the inductive nature of the structure.

WPT using SCMR operates within the NF inductive coupling regime. This can be achieved through two approaches: either by using a system that is naturally resonant due to its inductive properties, or by forcing resonance in a system that may not be inherently resonant. In the latter case, where the

CHAPTER 7. SELECTIVE EXCITATION TECHNIQUE FOR WPT IN BIOMEDICAL DEVICES USING CMA

system is originally inductive (magnetic), resonance can be achieved by introducing a capacitive load, as expressed in equation (5.1), to form a resonant LC circuit.

7.1.2 Limitations of SCMR Systems

One of the major limitations of conventional SCMR systems is their high sensitivity to misalignment, particularly between the Tx and Rx coils [150]. The system's efficiency tends to degrade rapidly when lateral or angular deviations occur, posing a significant challenge for practical and mobile applications. An early optimization approach for improving the performance of SCMR systems under lateral misalignment was introduced in [151], where an adaptive matching network was employed to achieve a power transfer efficiency (PTE) of 48.4%. However, this work did not address angular misalignment, which remains a critical factor in real-world scenarios. Further studies in [152] and [153] explored the effects of misalignment angles on SCMR efficiency. Nevertheless, the primary focus of these studies was on multi Tx and multi Rx WPT architectures, and their analysis of angular misalignment was limited in scope and depth. In [154], analytical models were developed to quantify PTE under both lateral and angular coil misalignments, offering valuable theoretical insights into inductive link behavior under misalignment. Later, 3D SCMR topologies were proposed in [155] shown in Fig. 7.2, their evaluation was limited to angular misalignment up to 90° , with no investigation into lateral misalignment or extended-range performance.

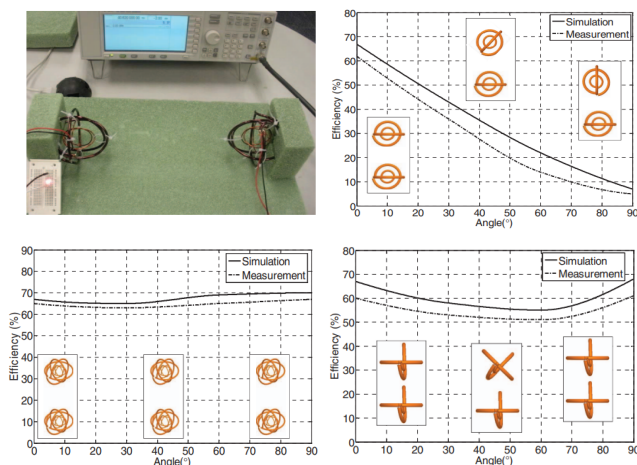


Figure 7.2: 3D SCMR systems to overcome angular misalignment [155].

In the context of biomedical applications, the feasibility of wireless electricity (witrlicity) using SCMR systems to power wireless body sensor networks (WBSNs) has been explored in [156]. A comprehensive theoretical analysis was conducted to investigate the oscillatory behavior and energy transfer dynamics within the system. A prototype system was developed and evaluated, as illustrated in Fig. 7.3. The experimental results demonstrated that the SCMR technology offers a promising and efficient solution for wirelessly powering multiple body worn sensors, highlighting its potential for seamless integration into biomedical monitoring systems.

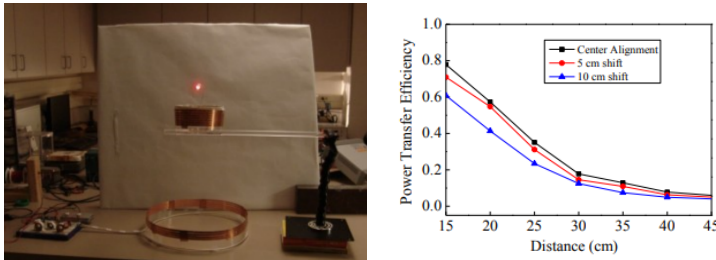


Figure 7.3: CMR systems to power wireless body sensor networks (WBSNs). [156]

A major limitation of such SCMR WPT systems is their reliance on two or more physically separate coils, which significantly increases the overall volume and spatial footprint of the setup. Additionally, these systems typically require multiple independent power sources with carefully controlled phase shifts to maintain optimal performance.

7.1.3 CSCMR Systems

In this context, Conventional Strongly CSCMR WPT systems, illustrated in Fig. 7.4 and initially introduced in [157], represent an evolution of traditional SCMR architectures. These systems are characterized by the use of concentric and coplanar configurations within both the Tx and Rx units.

Specifically, the design involves reducing the physical dimensions of the source and load loops to allow their integration within the Tx and Rx resonators, respectively. This compact arrangement not only facilitates miniaturization but has also demonstrated improved performance metrics, including enhanced PTE, when compared to conventional SCMR systems [62, 150, 158]. Therefore, CSCMR represents a highly promising WPT method, as it achieves power transfer efficiencies comparable to those of conventional SCMR systems while offering the additional advantage of a conformal structure that requires minimal volume for implementation.

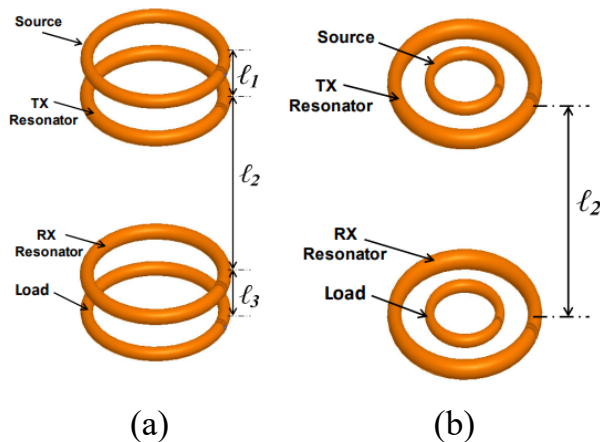


Figure 7.4: (a) SCMR system, (b) CSCMR system. [157]

In the context of biomedical applications, the power requirements of Implantable Medical Devices (IMDs) and Wearable Medical Devices (WMDs) vary depending on the specific functionality and operational demands of each device. Critically, the more efficient a wireless power transfer method is, the lower the power that needs to be supplied at the Tx side. This reduction not only decreases the intensity of the generated electromagnetic fields but also minimizes the Specific Absorption Rate (SAR), thereby enhancing patient safety. Given these considerations, CSCMR systems are expected to outperform traditional resonant inductive coupling techniques, particularly in terms of safety and integration potential. Their combination of high efficiency and compact, conformal design makes them well-suited for biomedical environments where minimizing device size, reducing exposure to electromagnetic fields, and ensuring reliable power delivery are critical design priorities. As a result, CSCMR emerges as a highly attractive solution for the next generation of wireless powering systems in medical applications.

7.1.4 CSCMR Systems For Biomedical Application

Numerous studies have demonstrated the adverse impact of the human body on the performance of WPT systems, particularly regarding the degradation of PTE [159–161]. Although these effects have been investigated for a variety of implantable systems across different implantation sites [162–164], there remains a significant gap in the literature concerning wearable WPT systems. The few available studies addressing wearable configurations have typically considered

only a limited number of body locations and often lacked comprehensive experimental validation. For example, [165] examined merely two body locations through simulations without reporting any measured data and focused on a physically large WPT system unsuitable for wearable applications.

Consequently, the key factor of CSCMR systems lies in the rigorous and systematic evaluation of wearable and implementable WPT system performance across multiple locations on the human body. In particular, safety considerations have been integral to the development of CSCMR systems from their inception, with complete SAR analyses conducted to assess their biological compatibility and ensure safe integration with the human body. In [153], the CSCMR system, simulated with 1 W input power, demonstrates significantly reduced SAR levels, which is approximately 35 times lower than conventional resonant inductive coupling, as shown in Fig. 7.5. This confirms CSCMR’s superior safety and compactness for biomedical wireless power transfer applications.

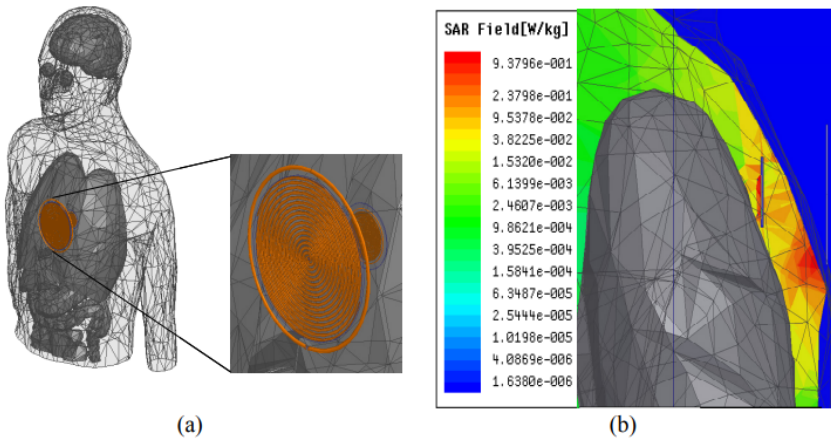


Figure 7.5: (a) CSCMR WPT for IMDs; (b) Related SAR distribution. [153]

More recently [62], the performance of the proposed CSCMR system for wearable applications was comprehensively evaluated at 26 distinct locations on the human body, as illustrated in Fig. 7.6.

These anatomical sites were systematically grouped into five regions: head (1–5), neck/bicep (6–10), arm (11–15), torso (16–21), and leg (22–26). The results demonstrated that CSCMR systems are particularly well-suited for wearable technologies, owing to their significantly lower SAR compared to conventional WPT systems. Importantly, the SAR values remained within ICNIRP

CHAPTER 7. SELECTIVE EXCITATION TECHNIQUE FOR WPT IN BIOMEDICAL DEVICES USING CMA

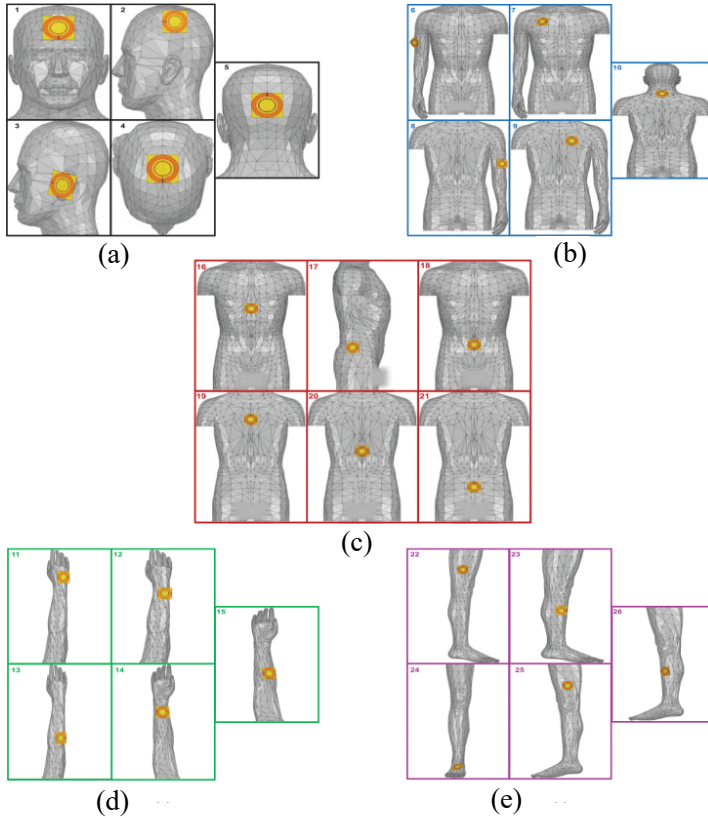


Figure 7.6: Examples of different placements and orientations of the CSCMR system for wearable devices on 26 different locations [62]: (a) head (1-5); (b) neck/bicep (6-10); (c) torso (16-21); (d) arm (11-15); and (e) leg (22-26).

and IEEE safety guidelines, even when the system operated at input power levels exceeding 1 W. These findings confirm that the CSCMR approach is biologically safe, making it a compelling candidate for reliable wireless powering in biomedical devices.

However, the results confirm that CSCMR systems suffer from efficiency loss near the human body due to tissue absorption. Efficiency can be improved by using ferromagnetic substrates and maintaining a 10 mm separation from the body to comply with ICNIRP RF exposure limits [166]. While CSCMR remains a promising platform for biomedical WPT devices, further optimization is needed, especially for implantable applications.

7.1.5 Limitations of the Existing Analysis of CSCMR Systems

As illustrated in Fig.7.7, various CSCMR systems have been proposed in the literature to improve PTE and enhance the practicality of biomedical applications [62,150,152,158]. Among them, the CSCMR system demonstrates superior performance, attributed to its concentric loop design, and is particularly suitable for wearable devices owing to the planar configuration of its Tx and Rx units. Consequently, recent studies have further developed and investigated the CSCMR system to assess its efficiency when positioned in close proximity to the human body, as depicted in Fig.7.7.

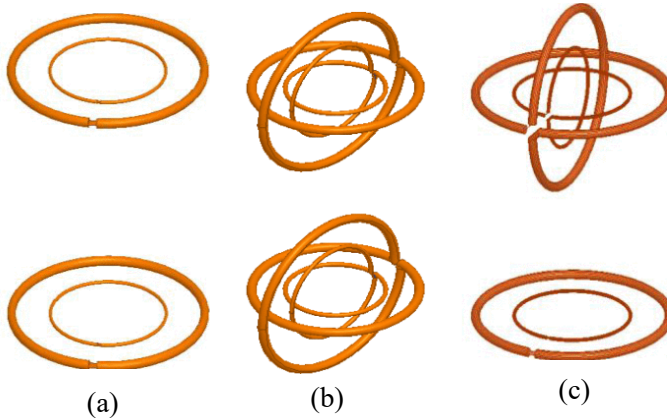


Figure 7.7: Examples of different configurations proposed in the literature of SCMR systems: (a) CSCMR; (b) 3-D SCMR; (d) Hybrid- SCMR. [150]

Key findings from previous studies reveal that early optimization efforts predominantly targeted specific strategies, such as modifying the size and geometry of the system and employing different substrate materials. Moreover, performance evaluations of both simulated and fabricated prototypes were primarily based on PTE calculations derived from S-parameters. However, the underlying physical mechanisms of the system were largely neglected, leaving its optimization incomplete and highlighting the need for further investigation and alternative approaches. Notably, when the CSCMR-WPT system is positioned on the human body. This reduction is highly dependent on the specific placement site, as adjacent biological tissues absorb a portion of the generated electromagnetic fields.

To address the gap in understanding the physical performance of CSCMR systems, this research introduces, for the first time, a selective excitation technique based on modal analysis. This innovative approach provides a detailed

exploration of the system's behavior, offering a clearer understanding of the electromagnetic interactions within the WPT system. By focusing on specific modes of excitation, this study establishes a foundation for optimizing CSCMR systems in wearable and IoT applications, where efficiency and performance are critical. The insights gained from this analysis serve as a valuable reference for future research, paving the way for improvements in design and providing a deeper understanding of the underlying physical phenomena in WPT systems.

7.2 CMA Analysis of the Tx Unit and the CSCMR System Before Adding Capacitive Loading

While specific coupling mechanisms are essential for achieving high PTE and generating a strong magnetic field, previous research has not conclusively demonstrated the physical performance of CSCMR systems from a detailed electromagnetic perspective. In this study, CMA is employed to analyze the CSCMR structure prior to the introduction of any capacitive loading. This investigation aims to reveal how capacitive elements influence the excitation of different modes and affect the system's behavior at resonance. The principal parameters of the CSCMR system used in this study are summarized in Table 7.1, corresponding to the geometry illustrated in Fig. 7.8(a).

Table 7.1: Characteristic parameters of The analysed CSCMR system

r_1	30 mm
$w1$	0.8 mm
r_2	50 mm
$w2$	2.2 mm

7.2.1 CMA of The Tx

Using FEKO and following the procedure outlined Chapter 3, a CMA of the Tx unit was performed across the frequency range of 0.5 to 2 GHz, as illustrated in Fig. 7.9. The primary objective of this analysis is to evaluate the CMs to identify those capable of producing the most stable and intense magnetic NF distribution.

The results reveal the presence of two sets of degenerate modes, with each set comprising two modes resonating at identical frequencies. Specifically, the first pair (J_{Tx1} and J_{Tx2}) resonates at 1.02 GHz, while the second pair resonates at 1.73 GHz. In addition to these, another mode, J_{Tx3} , was identified. This

7.2 CMA Analysis of the Tx Unit and the CSCMR System Before Adding Capacitive Loading

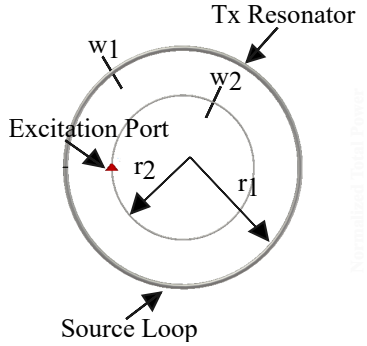


Figure 7.8: Schematic of the analysed Tx of CSCMR system and its key parameters.

mode is characterized as non-resonant, exhibiting predominantly positive frequency variation and primarily storing magnetic energy rather than radiating it. For clarity, the eigen-currents and their corresponding magnetic near-field distributions in the XY-plane for the various characteristic modes of the Tx loop are presented in Fig. 7.10, where degenerate modes have been grouped and displayed together in a consolidated manner within a single row.

The eigenc current distributions along the wire structures, presented in Fig.7.10 and corresponding to the modal behavior illustrated in Fig.7.9, demonstrate that the third characteristic mode (J_{Tx3}) exhibits the most favorable properties. This later is characterized by a complete, uninterrupted current loop on the Tx resonator. It generates a highly dense and uniform magnetic NF distribution, outperforming the other identified modes. In contrast, the other modes (J_{Tx1} , J_{Tx2} , J_{Tx4} , and J_{Tx5}) are associated with weaker and less uniform magnetic fields. Consequently, the selective excitation of J_{Tx3} is particularly beneficial for achieving a strong and stable magnetic field around the Tx loop. Therefore, it significantly enhances magnetic coupling and contributes to the optimization of the PTE of the CSCMR system.

7.2.2 CMA of The CSCMR System

To evaluate the performance of the CSCMR-WPT system, the Rx unit was positioned at a distance of 120 mm from the Tx unit. The key characteristics of the system at its resonant frequency of 1.69 MHz are illustrated in Fig.7.11.

The analysis clearly reveals that the magnetic coupling between the Tx and Rx units is notably weak under these conditions. As shown in Fig.7.11(b), the magnetic NF intensity does not exceed -7.5 dBA/m, indicating insufficient field strength for effective energy transfer. Consequently, this weak coupling results

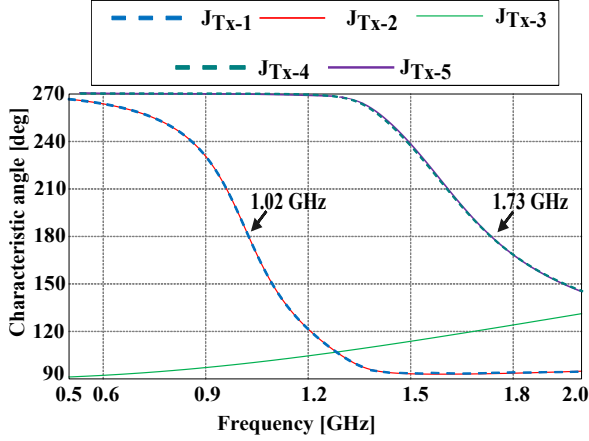


Figure 7.9: CA_n of the Tx unit of the CSCMR system within the frequency range from 0.05 to 2 GHz.

in a very low PTE, highlighting the need for further system optimization to enhance field concentration and coupling strength at the desired operating frequency. Furthermore, the values of the S parameters around the resonance of the system reinforce this observation. Notably, the reflection coefficient S_{11} remains around -7 dB, suggesting that a significant portion of the input power is reflected back toward the source rather than being radiated or transferred effectively. Ideally, it should be below -10 dB to ensure good impedance matching and efficient power injection into the system. Similarly, the transmission coefficient S_{21} , which reflects the strength of coupling between the Tx and Rx, is below -10 dB, indicating poor energy transfer between the two units.

These results demonstrate that the system exhibits poor matching, weak magnetic coupling, and low PTE at the evaluated setup. This initial assessment highlights the need for targeted improvements, such as enhancing mode excitation, modifying the resonator structure, or introducing capacitive loading to achieve a functional and efficient WPT system for wearable applications. To achieve optimized system performance, CMA was conducted, treating the Tx and Rx sides collectively as a single antenna unit. Functional and non-functional modes were identified by comparing the corresponding magnetic NF distributions. In this context, a functional mode is defined by the presence of a highly stable and dense magnetic field between the Tx and Rx units, while non-functional modes are characterized by weak and unstable magnetic field distributions. The various NF distributions and associated current patterns of the CMs associated to the structure are illustrated in Fig. 7.12.

7.2 CMA Analysis of the Tx Unit and the CSCMR System Before Adding Capacitive Loading

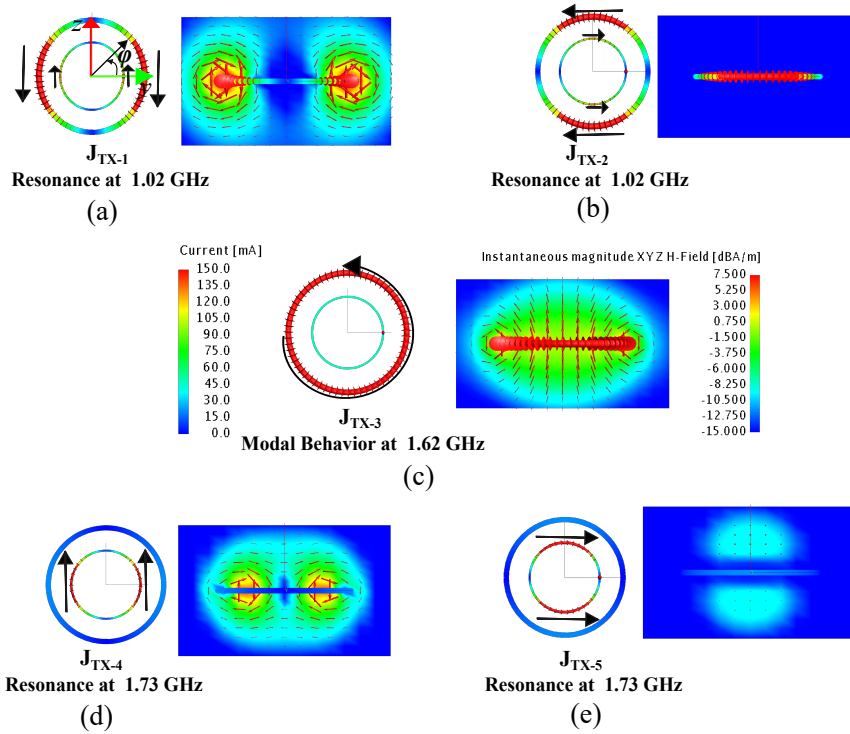


Figure 7.10: Eigen-current distributions, their intensities, and the corresponding magnetic NF distributions in the XZ-plane of the Tx unit in the CSCMR system: (a) J_{Tx1} ; (b) J_{Tx2} ; (c) J_{Tx3} ; (d) J_{Tx4} ; (e) J_{Tx5} .

By correlating the CMA results with the measured system performance shown in Fig.7.11, it becomes evident that the system's poor performance near resonance is directly linked to the dominance of the characteristic mode $J_{CSCMR-5}$, as depicted in Fig.7.12(d). Specifically, this CM does not generate a sufficiently strong or uniform magnetic NF between the Tx and Rx units, leading to weak coupling and thus low PTE. The predominance of this non-functional mode at resonance explains the observed inefficiencies and highlights the necessity of exciting more favorable modes to enhance system performance.

In contrast, exciting the mode $J_{CSCMR-3}$, as illustrated in Fig. 7.12(d), offers a highly promising pathway for improving the overall performance of the CSCMR system. The associated magnetic near-field (NF) distribution exhibits a high field density, reaching up to 45 dBV/m, which is the highest among all analyzed modes. Furthermore, the current distribution of $J_{CSCMR-3}$ is characterized by a uniform and extensive flow along the resonators of the CSCMR

CHAPTER 7. SELECTIVE EXCITATION TECHNIQUE FOR WPT IN BIOMEDICAL DEVICES USING CMA

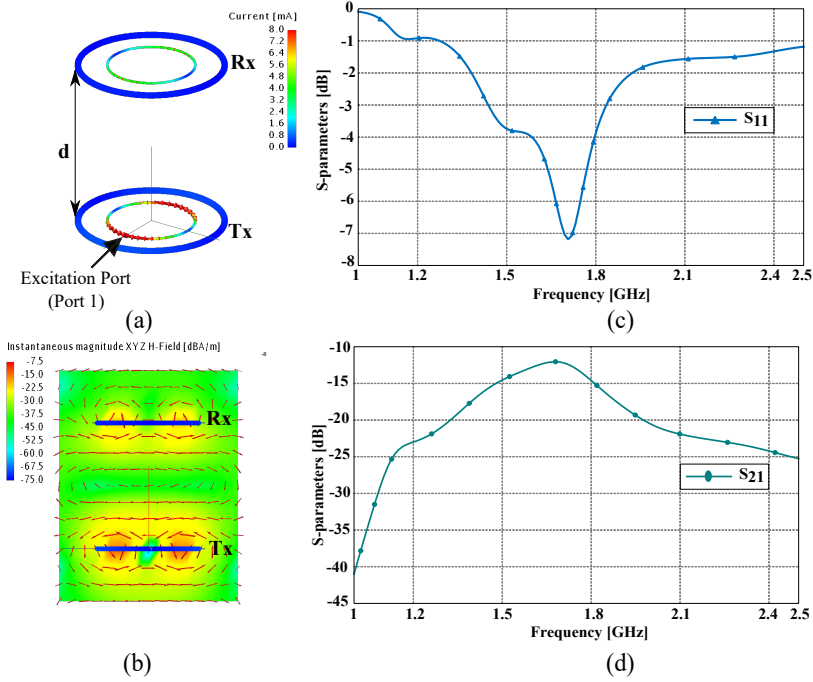


Figure 7.11: (a) The current distribution of the system near its resonance ($f_{res} = 1.69$ MHz); (b) The magnetic NF distribution of the system in XZ-plane; (c) S_{11} : Sparameter of the Tx port ; (d) S_{21} .

structure, notably without the presence of current nulls. This mode represents a loop-type mode that primarily generates strong inductive energy, enhancing magnetic coupling between the Tx and Rx units. Importantly, $J_{CSCMR-3}$ is not associated with a sharp resonant frequency, but rather exists continuously across a broad frequency range. Modal analysis conducted between 50 MHz and 2 GHz indicates that this mode exhibits its optimal behavior in terms of both maximum magnetic field intensity and favorable current distribution around the frequency f_r , which is equal to 76 MHz.

The strong and stable magnetic NF generated by this CM, coupled with its wide spatial current distribution, makes it an ideal candidate for significantly enhancing the PTE of the CSCMR WPT system.

7.3 Discrimination of The Unfunctionnal Modes Using Selective Excitation Technique

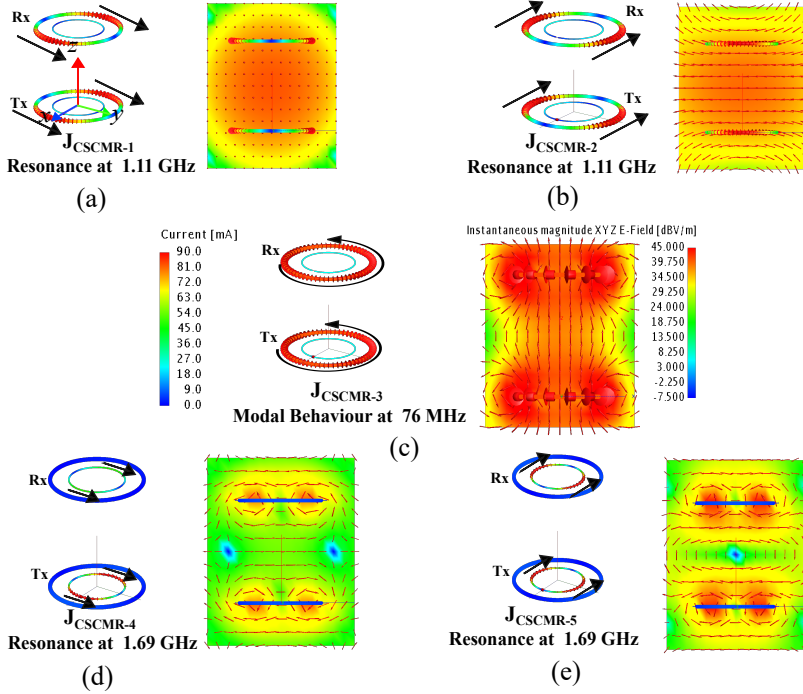


Figure 7.12: Eigen currents and their associated magnetic NF distributions in XZ-plane of the CSCMR system before introducing the capacitive loads: (a) $J_{CSCMR-1}$; (b) $J_{CSCMR-2}$; (c) $J_{CSCMR-3}$; (d) $J_{CSCMR-4}$; (e) $J_{CSCMR-5}$.

7.3 Discrimination of The Unfunctionnal Modes Using Selective Excitation Technique

CMA has been traditionally applied in antenna design, particularly for optimizing radiation characteristics and mitigating mutual coupling between closely spaced elements. In these contexts, selective excitation techniques are often utilized to achieve desired radiation properties, such as enforcing a specific polarization of the feeding source or selectively exciting a particular characteristic mode (CM) [79, 167–169].

In contrast to these conventional applications, the present work extends the concept of selective excitation into the domain of WPT. In particular, discrete reactive loading is strategically introduced to deliberately excite a specific mode within the CSCMR-WPT system. This approach is aimed at enhancing the magnetic coupling between the transmitter and receiver, thereby significantly

CHAPTER 7. SELECTIVE EXCITATION TECHNIQUE FOR WPT IN BIOMEDICAL DEVICES USING CMA

improving the system's PTE. Rather than focusing on radiated FF properties, the objective shifts towards optimizing NF magnetic interactions, offering a novel adaptation of CMA principles for efficient wireless powering in biomedical and wearable applications.

7.3.1 Selective Excitation Technique Using CMA

In earlier approaches, the design methodology is based on satisfying the SCMR condition. This condition requires that both the Tx and Rx resonators are tuned to resonate at the same frequency. When this synchronization is achieved, the system naturally operates at the maximum Q-factor for both the Tx and Rx loops, maximizing energy transfer efficiency [150]. The specific frequency at which the quality factor of an individual loop is maximized, denoted as f_r , can be derived based on the physical properties and dimensions of the system. It is given by:

$$f_r = \frac{c^{8/7} \mu_0^{1/7} \rho^{1/7}}{4 \cdot 15^{2/7} \pi^{11/7} r_{c1}^{2/7} r_1^{6/7}} \quad (7.3)$$

where c is the speed of light in a vacuum, μ_0 is the permeability of free space, ρ is the material resistivity, r_1 is the radius of the loop, r_{c1} is the radius of the conductor (wire) of the loop.

To ensure that both the Tx and Rx loops resonate precisely at f_r , lumped capacitors are introduced in parallel with each resonator. The inclusion of these capacitive elements is critical, as they enable precise tuning of the system's resonant frequency to the optimal operating point where the maximum Q factor is achieved. In the absence of lumped capacitors, the loops would naturally resonate at significantly higher frequencies due to their intrinsic inductance and minimal parasitic capacitance, leading to a diminished and poorly confined magnetic NF.

By integrating appropriately selected lumped capacitors into the system, f_r is effectively shifted to a lower value. This adjustment not only maximizes energy storage within the resonant loops but also significantly increases the circulating current, thereby reinforcing the excitation of the desired CM, $J_{CSCMR-3}$. The value of the lumped capacitance C required to achieve resonance at f is given by the following expression:

$$C = \frac{1}{(2\pi f_{max})^2 L} \quad (7.4)$$

where L is the inductance of the Tx and Rx loops:

$$L = \mu_0 r_1 \left[\ln \left(\frac{8r_1}{r_{c1}} \right) - 2 \right] \quad (7.5)$$

7.4 Comparison between SCMR and CSCMR Systems based on CMA

Following the SCMR condition equations and based on the predetermined dimensions of the proposed system, the lumped capacitors are calculated to be 22 pF. The same embedded capacitor will also be incorporated into a conventional SCMR system. The primary objective of this comparison is to validate that CMA provides consistent and correlating insights with previous studies, specifically confirming that the CSCMR configuration exhibits higher efficiency from a modal perspective. This approach not only strengthens the physical interpretation provided by CMA but also reinforces the superiority of CSCMR systems relative to traditional SCMR designs in terms of mode excitation and coupling performance. In this context and based on previous comparison in [150], Fig. 7.13 shows the schematic the final schematic of the both systems with respect to the demensions in Table 7.1 and as mentioned both loaded capacitors are equal to 22pF.

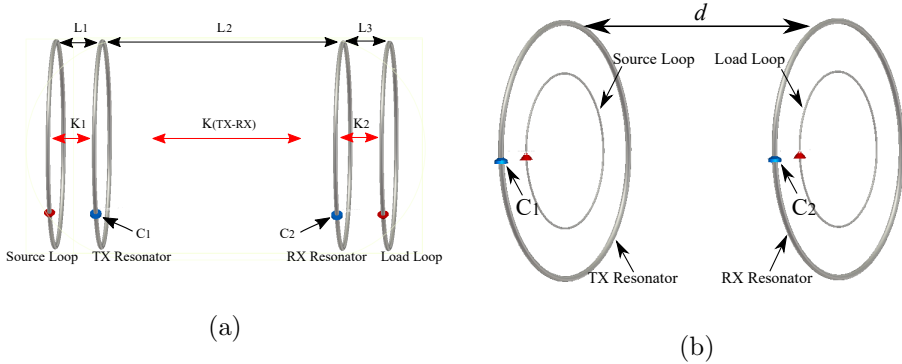


Figure 7.13: Schematic and dimensions of : (a) The traditional SCMR system; (b) The CSCMR system.

7.4 Comparison between SCMR and CSCMR Systems based on CMA

Following the addition of the loading capacitors, designed based on the modal behavior of the CSCMR system, key parameters such as the resonant frequencies of the dominant and higher-order modes, the modal field distributions, and the modal current patterns on the antenna surfaces become the primary focus for a detailed comparison of the physical behavior exhibited by the two systems as shown in Fig. 7.14 and 7.15.

The modal analysis of the SCMR system was conducted over the frequency range of 60 to 100 MHz. Beginning with the identification of the dominant CM,

CHAPTER 7. SELECTIVE EXCITATION TECHNIQUE FOR WPT IN BIOMEDICAL DEVICES USING CMA

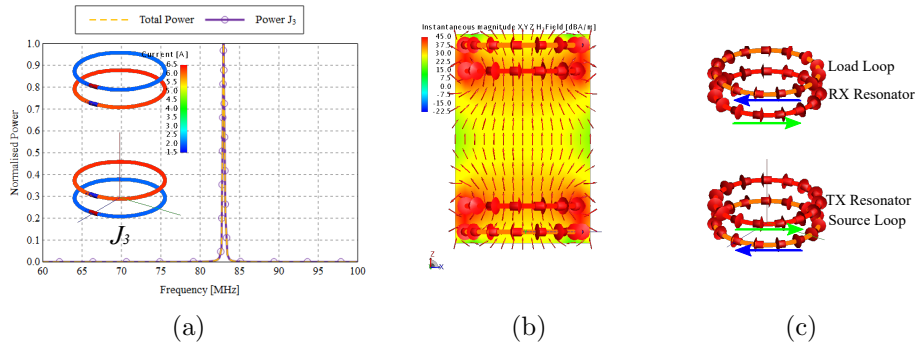


Figure 7.14: The CMA of the CSCMR system

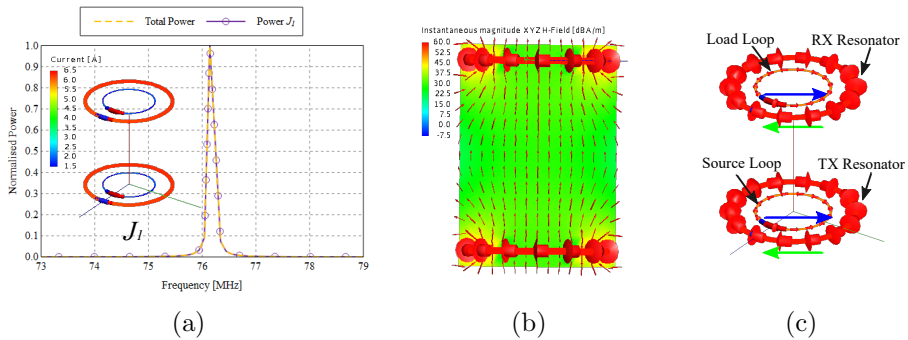


Figure 7.15: The CMA of the CSCMR system:

7.4 Comparison between SCMR and CSCMR Systems based on CMA

Fig. 7.14(a) illustrates that the incorporation of loading capacitors significantly enhances the excitation of the eigen-current J_3 near the system's resonant frequency, identified at 83 MHz. As a result, J_3 becomes the principal contributor to the total radiated and stored power in the vicinity of resonance, playing a dominant role in facilitating the coupling phenomenon between the Tx and Rx units. Furthermore, Fig. 7.14(b) reveals that the maximum current intensity associated with J_3 reaches 6.5 A, with the current distribution highly concentrated along the surfaces of the Tx and Rx resonators. Moreover, the inductive nature of the coupling mechanism is clearly demonstrated by the closed-loop current paths formed on the four antennas of the SCMR system. Specifically, the currents on the source loop and the Tx resonator flow in opposite directions, and a similar behavior is observed between the load loop and the Rx resonator. According to CMA, this configuration corresponds to a TLM. Correspondingly, the magnetic NF distribution, shown in Fig. 7.14(c), exhibits a maximum magnetic field density of 45 dBA/m, characterized by a stable and dense field bridging the Tx and Rx units. These results confirm that the optimized excitation of J_3 substantially strengthens the magnetic coupling, thereby improving the overall efficiency of the SCMR-WPT system.

The CMA of the CSCMR system was performed over the frequency range of 73 to 79 MHz. As illustrated in Fig. 7.15, similar observations to those made for the SCMR system were recorded, particularly regarding the dominant mode and the current intensity distribution. The mode J_1 , which corresponds to the previously identified $J_{CSCMR-3}$ mode before the introduction of loading capacitors, emerges as the main contributor to the system's total power near resonance. As shown in Fig. 7.15(a), this dominant behavior occurs around the resonant frequency of 76.2 MHz. The maximum current intensity, reaching 6.5 A, is concentrated along the surfaces of the Tx and Rx resonators. Examining the current distribution of J_1 , illustrated in Fig. 7ch13(a), it is evident that the Tx and Rx antennas exhibit identical structural characteristics. All four loops form closed current paths over their surfaces, and the current flows in the same direction across the Tx and Rx resonators, while flowing in the opposite direction across the source and load loops. This configuration effectively establishes two coplanar TLMs, where one represents the Tx antenna and the other the Rx antenna.

When compared to the SCMR system, the CSCMR system exhibits a more convergent and uniform magnetic field, with a slight improvement in field intensity. Specifically, the maximum magnetic field density reaches 60 dBA/m in the CSCMR system, compared to 45 dBA/m observed for the SCMR configuration. This enhanced NF density demonstrates the superior magnetic coupling achievable with CSCMR. Furthermore, the planar and compact architecture of the CSCMR design makes it more suitable for biomedical applications, especially in scenarios where minimal volume and efficient coupling are critical.

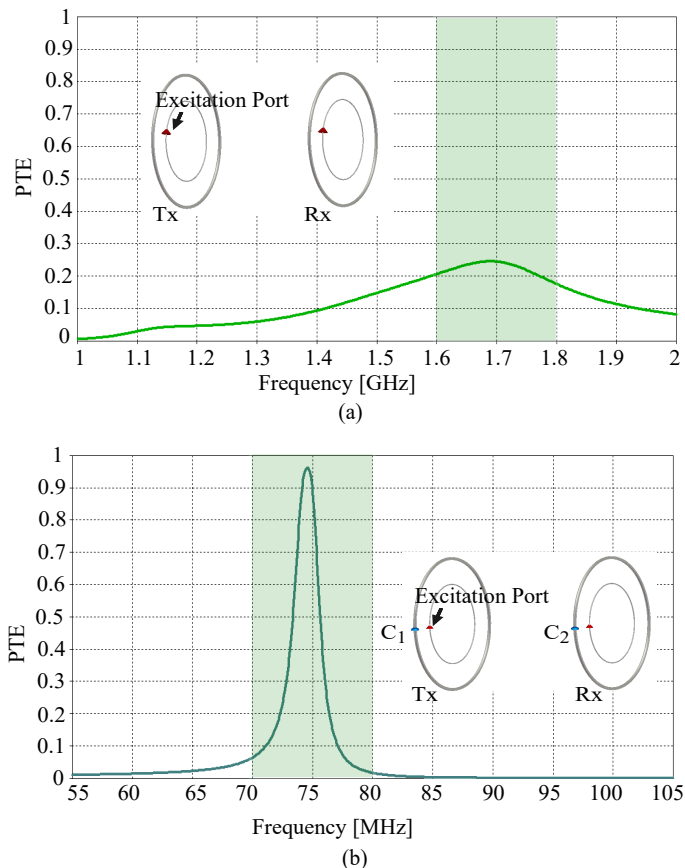


Figure 7.16: The PTE of the CSCMR system: (a) Without lumped capacitors on the Tx and Rx resonators; (b) With lumped capacitors on the Tx and Rx resonators.

7.5 The Final Performance of the CSCMR system

Following the outlined design methodology, the integration of lumped capacitive loads into the Tx and Rx resonators, combined with insights obtained from CMA, has led to a significant improvement in the PTE of the CSCMR system, particularly under conditions of lateral misalignment, as illustrated in Fig. 7.16. The PTE of the system was initially below 25% prior to the addition of the loading capacitors, and improved to approximately 95% following their

7.5 The Final Performance of the CSCMR system

incorporation. The results clearly demonstrate that this optimization strategy not only enhanced the magnetic coupling strength but also impacted the electrical characteristics of the system. Notably, while the physical dimensions of the CSCMR structure remained unchanged, the electrical length of the system was substantially increased, resulting in a pronounced shift in the resonant frequency from 1.69 MHz to 74.9 MHz.

It is also important to address the slight discrepancy observed between the resonant frequency of the dominant characteristic mode, $J_{CSCMR-3}$ (76 MHz), and the measured system resonant frequency (74.9 MHz). This minor variation can be attributed to the influence of secondary modes. Although the dominant mode primarily governs the behavior of the system near resonance, the presence of adjacent modes can subtly modify the overall electromagnetic response, slightly shifting the resonance point. Such observations are consistent with the underlying principles of CMA, where even weak modal interactions can influence the system's performance.

Overall, although CSCMR systems have already demonstrated significant potential in addressing misalignment challenges in WPT for biomedical applications with respect to regulatory and safety standards, they still present limitations when operating in close proximity to the human body. In such cases, the PTE tends to drop significantly due to the lossy nature of biological tissues. To address these limitations, the present study offers a new perspective by applying CMA to CSCMR systems for the first time. The findings of this work establish a clear and systematic methodology for optimizing CSCMR configurations, even under misalignment conditions. Based on these results, future research can further explore the use of CMA as a tool to enhance the performance and robustness of CSCMR systems across various misalignment scenarios, offering new avenues for improving WPT reliability in biomedical environments.

**CHAPTER 7. SELECTIVE EXCITATION TECHNIQUE FOR
WPT IN BIOMEDICAL DEVICES USING CMA**

Chapter 8

Conclusion

In this section, the main conclusions obtained throughout the course of the thesis are synthesized. All the objectives established at the outset of the research have been successfully achieved. Accordingly, it is pertinent to summarize the key findings, highlight the contributions made, and suggest directions for future research.

In **Chapter 1**, the state of the art relevant to the primary applications addressed in this thesis was introduced:

- There is an increasing demand for highly efficient Wireless Power Transfer (WPT) systems in the field of biomedical applications, aimed at enabling multiple functionalities for monitoring and interfacing with the human body. While most existing solutions rely on inductive and magnetic coupling techniques, they often lack a comprehensive physical understanding of the underlying antenna system behavior.
- Loop based systems, utilizing Inductive Power Transfer (IPT) and Magnetic Resonant Coupling (MRC), have become the leading candidates for efficient wireless power transfer to biomedical devices. However, these systems remain highly sensitive to misalignment, and existing research has mainly offered general simulation and measurement guidelines without proposing a comprehensive or systematic methodology.

Chapter 2 This chapter addresses the Theory of Characteristic Modes and introduces the main parameters utilized in modal analysis. In addition, a comprehensive review of the state of the art on characteristic modes is presented, leading to the following key findings:

- CMA has proven to be a powerful tool for mitigating coupling between antennas, whether integrated within the same device or across different

CHAPTER 8. CONCLUSION

devices such as smartphones, tablets, or CubeSats. Numerous solutions leverage CMA by strategically positioning antennas to excite distinct platform modes, thereby enhancing isolation.

- CMA has been increasingly utilized to understand and enhance the performance of WPT systems. CMA offers the advantage of enabling system optimization independently of the feeding mechanism, providing a deeper understanding of the modal behavior, which is crucial for accurately characterizing and improving system performance.
- Most existing applications of CMA to WPT systems have not incorporated validation through experimental measurements, nor have they accounted for the effects of various potential misalignment scenarios.

In **Chapter 3**, the impact of misalignment in Magnetically Coupled Resonant Wireless Power Transfer (MCR-WPT) systems has been evaluated. A configuration based on two identical loops was selected, targeting applications such as biomedical implants, Qi wireless charging, and wearable technologies. Typical misalignments between transmitting (Tx) and receiving (Rx) loops, caused by user or device movement, were studied through simulation and post-processing analyses. The following conclusions are extracted:

- For first time, a CMA based methodology, governed by Coupled Mode Theory, has been established for coupling analysis, providing a solid reference for researchers aiming to integrate CMA into WPT system design more systematically and effectively.
- Simulation results and post-processing analyses were carried out to investigate the relationship between intermodal behavior and coupling mechanisms governing the overall performance of the system.
- The study focuses on understanding modal variations under misalignment conditions, identifying which characteristic modes exhibit superior energetic properties and contribute most effectively to sustaining efficient WPT.

In **Chapter 4**, the validation of CMA for WPT systems operating under misalignment conditions has been carried out through experimental measurements. The key conclusions drawn from this validation are summarized below:

- The comparison between fabricated prototypes and CMA based simulations demonstrated that the resonant frequencies associated with maximum power transfer correspond closely to the resonant frequencies of the dominant characteristic modes, thus validating CMA as a reliable predictive tool for WPT system behavior.

-
- The Power Transfer Efficiency (PTE) is less sensitive to rotational misalignment and is predominantly affected by lateral misalignment.
 - An analogy was drawn between the modal behavior and Coupled Mode Theory, confirming that the transmission line (odd) mode dominates in strong coupling regions, while the antenna (even) mode emerges when coupling diminishes.

In **Chapter 5**, a comparative study of different WPT systems for biomedical applications has been presented, focusing on enhancing the robustness and efficiency of the power link under misalignment conditions using CMA. Both loop based WPT configurations and near-field plate (NFP) assisted systems were analyzed using CMA and PTE evaluations. The following conclusions have been obtained:

- The importance of frequency selection in the proposed WPT systems has been emphasized. A frequency within the megahertz (MHz) range was deliberately chosen to balance PTE, system compactness, and biological safety, aligning with industry standards and facilitating meaningful comparisons with existing designs.
- Dual Tx topology achieves higher radiated power compared to a single Tx system, with Transmission Line Modes (TLMs) playing a dominant role in power transfer across all three configurations. In multi Tx topologies, TLMs are characterized by in-phase currents in the transmitting loops and a 180° phase shift in the receiving loop. However, while the interconnected dual Tx configuration successfully reduces misalignment sensitivity, it also results in lower radiated power and a shift in resonance frequency due to structural modifications.
- NFPs were introduced between the Tx and Rx to enhance magnetic coupling. It was demonstrated that by appropriately positioning the NFPs and increasing the number of loaded loops, the magnetic field distribution at the receiver can be effectively shaped and reinforced, resulting in a significant improvement in the Power Transfer Efficiency (PTE).
- Overall, the dual Tx configuration without interconnections emerged as the most robust topology, offering the highest PTE and the most stable magnetic field distribution among the studied structures, making it the best candidate for experimental validation in the next chapter.

Chapter 6 conducts the development and experimental validation of a dual Tx configuration supported by a conventional Wilkinson Power Divider (WPD) for WPT systems. Unlike traditional systems that rely on additional control

CHAPTER 8. CONCLUSION

circuits or multiple power sources, this design maintains simplicity while improving misalignment resilience. The following conclusions have been obtained:

- Fundamental electromagnetic principles were applied to thoroughly analyze the decoupling mechanism between the two Tx coils. This decoupling, confirmed through both detailed simulations and experimental measurements, was shown to be critical for minimizing mutual interference, ensuring stable system operation, and maintaining efficient power delivery to a centrally positioned Rx loop.
- A key distinction of the proposed system lies in the use of a conventional Wilkinson Power Divider (WPD), which enables the experimental validation of a dual Tx configuration without requiring any modifications to the input power network. The choice of a WPD ensures compatibility with existing WPT infrastructures, offering a flexible and scalable solution that remains independent of the specific coil geometry while enhancing the system's tolerance to Rx misalignment through the generation of a stable and uniform magnetic field.
- A complete 3D CAD design of the proposed system was developed to illustrate the structural configuration for real-world applications and to emphasize its practical feasibility for fabrication and deployment.
- The behavior of the dual Tx system under varying axial misalignment conditions was examined and compared against single Tx topologies. Experimental results demonstrated that the dual Tx configuration exhibits greater tolerance to spatial misalignments and achieves higher PTE across a broader operational region, thereby reinforcing its potential for biomedical and IoT applications where precise alignment cannot be guaranteed.

Lastly, in **Chapter 7**, Conformal Strongly Coupled Magnetic Resonance (CSCMR) systems were introduced and analyzed, emphasizing their improved performance and suitability for biomedical applications due to their compact, planar configurations. Existing limitations in the physical analysis of CSCMR systems were also identified.

- A complete CMA based technique of the Tx unit and the entire CSCMR system was conducted prior to the introduction of capacitive loading. Modal analysis provided insights into the dominant modes governing the system's behavior and magnetic field distribution.
- A selective excitation technique, based on CMA, was developed for the first time to discriminate between functional and non-functional modes, ensuring that only the modes contributing to efficient energy transfer were excited.

- A detailed comparison between SCMR and CSCMR systems was performed using CMA results, demonstrating that CSCMR configurations achieve superior modal performance, particularly in maintaining a strong and uniform magnetic field.
- Finally, the optimized CSCMR system's performance was validated, showing significant improvements in PTE, stability under misalignment, and overall system compactness, confirming the effectiveness of the CMA guided selective excitation approach.

8.1 Further work

The research conducted in this thesis opens several promising avenues for further investigation. While this work has successfully applied the Theory of Characteristic Modes (TCM) to analyze and optimize antenna designs in free space, its extension to more complex, realistic environments remains largely unexplored.

One significant limitation lies in the absence of TCM analysis through the human body. The classical theory is primarily formulated for Perfect Electric Conductors (PEC), making it less applicable in lossy and inhomogeneous biological environments. Future work could focus on developing a generalized or adapted version of the TCM that accounts for the electromagnetic properties of human tissues. This transformation would pave the way for a more accurate and application, specific modal analysis of implantable or wearable biomedical antennas, potentially enhancing both safety and efficiency.

Furthermore, the current study exclusively considers antennas built from PEC materials. Expanding this framework to include antennas designed from biocompatible and flexible materials, such as conductive polymers, hydrogels, or textile-based conductors, could bridge the gap between theoretical models and real-world biomedical applications. Such materials are more compatible with human tissue and could lead to more practical and clinically viable WPT systems.

Another compelling direction involves exploring dual-transmitter (dual-Tx) topologies with bi-modal operation. In this approach, each transmitter would operate at a distinct frequency, corresponding to a specific characteristic mode, thereby covering both near-field and far-field regions. Coupled with a dual-band receiver, this configuration could significantly enhance system adaptability and power transfer efficiency across varying implantation depths and orientations. This hybrid near/far-field strategy could broaden the scope of wireless energy delivery in biomedical contexts, offering better performance under diverse and dynamic physiological conditions.

CHAPTER 8. CONCLUSION

Collectively, these research directions aim to bring the theoretical foundations of this thesis closer to tangible medical innovations, fostering safer, more robust, and more efficient wireless power transfer systems for next-generation biomedical devices.

Appendix A

Technical Results

A.1 JCR Indexed journals

- **F.Abderrazak**, E.Antonino-Daviu, Larbi Talbi and M.Ferrando-Bataller. “Characteristic Modes Analyses for Misalignment in Wireless Power Transfer System.” *IEEE Access*, 12, 65007-65023, 2024.
- **F.Abderrazak**, E.Antonino-Daviu, Huifang Wu, and M.Ferrando-Bataller. “Enhancing Resilience to Axial Misalignment in Wireless Power Transfer Systems for Internet of Things Devices.” *IEEE Internet of Things Journal*, under submission, 2025.

A.2 International Conferences

- H.Wu, H. Naseri, P. PourMohammadi, **F.Abderrazak** and T. A., “Reconfigurable Dual-band OAM Antenna for Microwave and Millimeter-Wave Applications.” *2025 IEEE International Symposium on Antennas and Propagation and USNC-URSI Radio Science Meeting (AP-S/URSI)*. Ottawa, Ontario, Canada, July 2025.
- **F. Abderrazak**, P. PourMohammadi, L. Talbi, E. Antonino-Daviu, T. A. Denidni and M. Ferrando-Bataller, “Selective Excitation Technique for Wireless Power Transfer in Wearable Devices Using CMA.” *2024 7th Conference on Cloud and Internet of Things (CIoT) (pp.1-6)*. Montreal, QC, Canada, 29-31 October 2024.
- **F. Abderrazak**, E. Antonino-Daviu, L. Talbi and M. Ferrando-Bataller, “Analysis on Power Transfer Efficiency Using Near Field Plates.” *2022*

CHAPTER A. TECHNICAL RESULTS

IEEE International Symposium on Antennas and Propagation and USNC-URSI Radio Science Meeting (AP-S/URSI) (pp. 1738-1739). Denver, CO, USA, 10-15 July 2022.

- **F. Abderrazak**, E. Antonino-Daviu, L. Talbi and M. Ferrando-Bataller, “Characteristic Mode Analysis of SCMR and CSCMR Systems.” *2022 16th European Conference on Antennas and Propagation (EuCAP) (pp. 1-5). Madrid, Spain, 27 March–1 April 2022.*
- E. Antonino-Daviu, C. A. Chuquitarco-Jiménez, **F. Abderrazak** and M. Ferrando-Bataller, “Dual-Band Planar Antenna with AMC Screen for On-Body Applications.” *2021 IEEE International Symposium on Antennas and Propagation and USNC-URSI Radio Science Meeting (APS/URSI) (pp. 1623-1624). Singapore, Singapore, 4-10 December 2021.*
- **F. Abderrazak**, E. Antonino-Daviu, L. Talbi and M. Ferrando-Bataller, “A Performance Comparison of Three Topologies of Circular Loop Antennas Transmitting Systems.” *2021 IEEE 19th International Symposium on Antenna Technology and Applied Electromagnetics (ANTEM) (pp. 1-2). Winnipeg, MB, Canada, 8-11 August 2021.*
- **F. Abderrazak**, E. Antonino-Daviu, M. Ferrando-Bataller, L. Talbi and A. Al Qaraghuli, “A Comparative Study between Different Loop Antennas Topologies for Wireless Power Transmission Based on Modal Analysis.” *2021 15th European Conference on Antennas and Propagation (EuCAP) (pp. 1-5). Düsseldorf, Germany, 22-26 March 2021.*
- **F. Abderrazak**, E. Antonino-Daviu, M. Ferrando-Bataller and L. Talbi, “Analysis of Magnetically-Coupled Loops Based on Characteristic Modes.” *2020 IEEE International Symposium on Antennas and Propagation and North American Radio Science Meeting (pp. 121-122). Montreal, QC, Canada, 5-10 July 2020.*
- **F. Abderrazak**, E. Antonino-Daviu and M. Ferrando-Bataller, “Power Transfer Efficiency Analyzed Using Characteristic Mode Coupling Between Two Parallel Loops.” *2020 14th European Conference on Antennas and Propagation (EuCAP) (pp. 1-5). Copenhagen, Denmark, 15-20 March 2020.*
- D. Santillán-Haro, **F. Abderrazak**, E. Antonino-Daviu and M. Ferrando-Bataller, “On the Bandwidth of Loop Antennas Using Characteristic Mode Analysis.” *2019 IEEE International Symposium on Antennas and Propagation and USNC-URSI Radio Science Meeting (pp. 851-852). Atlanta, GA, USA, 7-12 July 2019.*

A.3 National Conferences

- **F. Abderrazak**, E. Antonino-Daviu, M. Hayouni, M. Ferrando-Bataller and F. Choubani, “XXXIV Simposium Nacional de la Unión Científica Internacional de Radio (URSI 2019): Libro de Resúmenes.” *Seville, Spain, 4-6 September 2019 (pp. 1-4)*.

A.4 Stays In Other Institutions

- **Research stay at the Radio Frequency Laboratory.**
INRS, January 2024 - August 2024
Montreal, QC, Canada.

A.5 Fellowships

- **Mobility grants for students with FPI UPV or CoTutela.**
2021-2024
Universitat Politècnica de València.
- **Bourses de persévérance scolaire.**
2022-2025
UQO — Université du Québec en Outaouais.

A.6 Awards

- **Assemblée annuelle 2023 STARaCom (Third Prize)**
Contribution: “Analyse des modes caractéristiques des systèmes SCMR et CSCMR fabriqués .”

A.7 International Seminars

- **Title : University degree VS Professional training courses.**
Midocean University, Saudi Arabia
2025
- **Title : The application of Theory of Characteristic Modes**
Midocean University, Saudi Arabia
2024
- **Title : Iot Implementation In Civil Engineering**
Universidad Nacional Intercultural Fabiola Salazar Leguía de Bagua, Peru
2020

A.8 Professional Achievements

- **Member of the STARaCom Student Engagement committee**
2024-2025
McGill University.

- **University Lecturer and Assistant**
2022-2025
Université du Québec en Outaouais.
Algonquin College.

References

- [1] R. Malviya, S. Karakuş, and M. Roy, *Embedded Systems for Biomedical Applications*. CRC Press, 2025.
- [2] M. Jasim, A. J. A. Al-Gburi, M. Hanif, Z. A. Dayo, M. M. Ismail, and Z. Zakaria, “An extensive review on implantable antennas for biomedical applications: Health considerations, geometries, fabrication techniques, and challenges,” *Alexandria Engineering Journal*, vol. 112, pp. 110–139, 2025.
- [3] H.-J. Meisel and N. Agarwal, “Commentary on “biomaterials in spinal implants: a review”,” *Neurospine*, vol. 17, no. 1, p. 111, 2020.
- [4] N. Filip, I. Radu, B. Veliceasa, C. Filip, M. Pertea, A. Clim, A. C. Pinzariu, I. C. Drochioi, R. L. Hilitanu, and I. L. Serban, “Biomaterials in orthopedic devices: current issues and future perspectives,” *Coatings*, vol. 12, no. 10, p. 1544, 2022.
- [5] M. P. Powell, N. Verma, E. Sorensen, E. Carranza, A. Boos, D. P. Fields, S. Roy, S. Ensel, B. Barra, J. Balzer *et al.*, “Epidural stimulation of the cervical spinal cord for post-stroke upper-limb paresis,” *Nature medicine*, vol. 29, no. 3, pp. 689–699, 2023.
- [6] S. J. Edwards, V. Wakefield, T. Jhita, K. Kew, P. Cain, and G. Marce-niuk, “Implantable cardiac monitors to detect atrial fibrillation after cryptogenic stroke: a systematic review and economic evaluation,” *Health Technology Assessment (Winchester, England)*, vol. 24, no. 5, p. 1, 2020.
- [7] K. Y. Wu, J. K. Fujioka, P. Daigle, and S. D. Tran, “The use of functional biomaterials in aesthetic and functional restoration in orbital surgery,” *Journal of Functional Biomaterials*, vol. 15, no. 2, p. 33, 2024.
- [8] Y. Zhou, C. Liu, and Y. Huang, “Wireless power transfer for implanted medical application: A review,” *Energies*, vol. 13, no. 11, p. 2837, 2020.

REFERENCES

- [9] A. Ben Amar, A. B. Kouki, and H. Cao, "Power approaches for implantable medical devices," *sensors*, vol. 15, no. 11, pp. 28 889–28 914, 2015.
- [10] A. Basir and H. Yoo, "Efficient wireless power transfer system with a miniaturized quad-band implantable antenna for deep-body multitasking implants," *IEEE Transactions on Microwave Theory and Techniques*, vol. 68, no. 5, pp. 1943–1953, 2020.
- [11] A. Aldaoud, J.-M. Redoute, K. Ganesan, G. S. Rind, S. E. John, S. M. Ronayne, N. L. Opie, D. J. Garrett, and S. Prawer, "Near-field wireless power transfer to stent-based biomedical implants," *IEEE Journal of Electromagnetics, RF and Microwaves in Medicine and Biology*, vol. 2, no. 3, pp. 193–200, 2018.
- [12] D. Khan, A. Ahmad, and D.-y. Choi, "Design and optimization of a mid-field wireless power transfer system for enhanced energy transfer efficiency," *Symmetry*, vol. 16, no. 6, p. 753, 2024.
- [13] D. Sharma, S. Kumar, N. Singh, B. K. Kanaujia, S. P. Singh, and A. Lay-Ekuakille, "Far-field wireless power transmission and measurement for a leadless transcatheter pacing system," *IEEE Transactions on Instrumentation and Measurement*, vol. 72, pp. 1–12, 2023.
- [14] W. Zhong, C. Zhang, X. Liu, and S. R. Hui, "A methodology for making a three-coil wireless power transfer system more energy efficient than a two-coil counterpart for extended transfer distance," *IEEE Transactions on Power Electronics*, vol. 30, no. 2, pp. 933–942, 2014.
- [15] C. Xiao, D. Cheng, and K. Wei, "An lcc-c compensated wireless charging system for implantable cardiac pacemakers: Theory, experiment, and safety evaluation," *IEEE Transactions on Power Electronics*, vol. 33, no. 6, pp. 4894–4905, 2018.
- [16] Y.-D. Lee, K.-W. Kim, and G.-W. Moon, "A self-compensated planar coil with integrated single-switch regulator for wireless power transfer (wpt) systems," *IEEE Transactions on Power Electronics*, vol. 36, no. 10, pp. 10 954–10 958, 2021.
- [17] P. Chen, H. Yang, R. Luo, and B. Zhao, "A tissue-channel transcutaneous power transfer technique for implantable devices," *IEEE Transactions on Power Electronics*, vol. 33, no. 11, pp. 9753–9761, 2018.
- [18] R. Sedehi, D. Budgett, J. Jiang, X. Ziyi, X. Dai, A. P. Hu, and D. McCormick, "A wireless power method for deeply implanted biomedical de-

- vices via capacitively coupled conductive power transfer,” *IEEE Transactions on Power Electronics*, vol. 36, no. 2, pp. 1870–1882, 2021.
- [19] J. S. Ho, A. J. Yeh, E. Neofytou, S. Kim, Y. Tanabe, B. Patlolla, R. E. Beygui, and A. S. Poon, “Wireless power transfer to deep-tissue microimplants,” *Proceedings of the National Academy of Sciences*, vol. 111, no. 22, pp. 7974–7979, 2014.
- [20] C. Liu, Y. Zhang, and X. Liu, “Circularly polarized implantable antenna for 915 mhz ism-band far-field wireless power transmission,” *IEEE Antennas and Wireless Propagation Letters*, vol. 17, no. 3, pp. 373–376, 2018.
- [21] N. Nguyen, N. Ha-Van, and C. Seo, “Midfield wireless power transfer for deep-tissue biomedical implants,” *IEEE Antennas and Wireless Propagation Letters*, vol. 19, no. 12, pp. 2270–2274, 2020.
- [22] M. Li, A. Khaleghi, A. Hasanvand, R. P. Narayanan, and I. Balasingham, “A new design and analysis for metasurface-based near-field magnetic wireless power transfer for deep implants,” *IEEE Transactions on Power Electronics*, vol. 39, no. 5, pp. 6442–6454, 2024.
- [23] A. Singer and J. T. Robinson, “Wireless power delivery techniques for miniature implantable bioelectronics,” *Advanced Healthcare Materials*, vol. 10, no. 17, p. 2100664, 2021.
- [24] C. M. Collins and M. B. Smith, “Calculations of b1 distribution, snr, and sar for a surface coil adjacent to an anatomically-accurate human body model,” *Magnetic Resonance in Medicine: An Official Journal of the International Society for Magnetic Resonance in Medicine*, vol. 45, no. 4, pp. 692–699, 2001.
- [25] R. Wu, W. Li, H. Luo, J. K. Sin, and C. P. Yue, “Design and characterization of wireless power links for brain–machine interface applications,” *IEEE Transactions on Power Electronics*, vol. 29, no. 10, pp. 5462–5471, 2014.
- [26] T. Sun, X. Xie, G. Li, Y. Gu, Y. Deng, and Z. Wang, “A two-hop wireless power transfer system with an efficiency-enhanced power receiver for motion-free capsule endoscopy inspection,” *IEEE transactions on Biomedical Engineering*, vol. 59, no. 11, pp. 3247–3254, 2012.
- [27] G. Sun, B. Muneer, Y. Li, and Q. Zhu, “Ultracompact implantable design with integrated wireless power transfer and rf transmission capabilities,” *IEEE Transactions on Biomedical Circuits and Systems*, vol. 12, no. 2, pp. 281–291, 2018.

REFERENCES

- [28] G. Monti, P. Arcuti, and L. Tarricone, “Resonant inductive link for remote powering of pacemakers,” *IEEE Transactions on Microwave Theory and Techniques*, vol. 63, no. 11, pp. 3814–3822, 2015.
- [29] L. Li, H. Liu, H. Zhang, and W. Xue, “Efficient wireless power transfer system integrating with metasurface for biological applications,” *IEEE Transactions on Industrial Electronics*, vol. 65, no. 4, pp. 3230–3239, 2017.
- [30] H. Rahmani and A. Babakhani, “A dual-mode rf power harvesting system with an on-chip coil in 180-nm soi cmos for millimeter-sized biomedical implants,” *IEEE Transactions on Microwave Theory and Techniques*, vol. 67, no. 1, pp. 414–428, 2018.
- [31] Z. Zhang, H. Pang, A. Georgiadis, and C. Cecati, “Wireless power transfer—an overview,” *IEEE transactions on industrial electronics*, vol. 66, no. 2, pp. 1044–1058, 2018.
- [32] E. Falkenstein, M. Roberg, and Z. Popovic, “Low-power wireless power delivery,” *IEEE Transactions on microwave theory and techniques*, vol. 60, no. 7, pp. 2277–2286, 2012.
- [33] C. Liu, Y.-X. Guo, H. Sun, and S. Xiao, “Design and safety considerations of an implantable rectenna for far-field wireless power transfer,” *IEEE Transactions on antennas and Propagation*, vol. 62, no. 11, pp. 5798–5806, 2014.
- [34] E. Y. Chow, A. L. Chlebowski, S. Chakraborty, W. J. Chappell, and P. P. Irazoqui, “Fully wireless implantable cardiovascular pressure monitor integrated with a medical stent,” *IEEE Transactions on Biomedical Engineering*, vol. 57, no. 6, pp. 1487–1496, 2010.
- [35] R. A. Bercich, D. R. Duffy, and P. P. Irazoqui, “Far-field rf powering of implantable devices: Safety considerations,” *IEEE Transactions on Biomedical Engineering*, vol. 60, no. 8, pp. 2107–2112, 2013.
- [36] S. A. A. Shah and H. Yoo, “Radiative near-field wireless power transfer to scalp-implantable biotelemetric device,” *IEEE Transactions on Microwave Theory and Techniques*, vol. 68, no. 7, pp. 2944–2953, 2020.
- [37] N. Tesla, “Apparatus for transmitting electrical energy.” Dec. 1 1914, uS Patent 1,119,732.
- [38] J. M. Fernandez and J. A. Borrás, “Contactless battery charger with wireless control link,” Feb. 6 2001, uS Patent 6,184,651.

-
- [39] J. Hirai, T.-W. Kim, and A. Kawamura, "Wireless transmission of power and information and information for cableless linear motor drive," *IEEE transactions on Power Electronics*, vol. 15, no. 1, pp. 21–27, 2000.
- [40] A. Atiyha, M. Zeer, and A. A. A. Samhan, "Investigation of the parameters influencing the efficiency of wireless transmission of electrical power," in *From Machine Learning to Artificial Intelligence: The Modern Machine Intelligence Approach for Financial and Economic Inclusion*. Springer, 2025, pp. 653–668.
- [41] A. Kurs, A. Karalis, R. Moffatt, J. D. Joannopoulos, P. Fisher, and M. Soljacic, "Wireless power transfer via strongly coupled magnetic resonances," *science*, vol. 317, no. 5834, pp. 83–86, 2007.
- [42] X.-C. Wei, E.-P. Li, Y. L. Guan, and Y. Chong, "Simulation and experimental comparison of different coupling mechanisms for the wireless electricity transfer," *Journal of Electromagnetic Waves and Applications*, vol. 23, no. 7, pp. 925–934, 2009.
- [43] M. A. Siddiqui *et al.*, "Smart approach of power transfer," *Int. J. Res. Stud. Sci., Eng. Technol*, vol. 2, no. 4, pp. 32–37, 2015.
- [44] S. Veismoradi and A. S. Kia, "Investigation on various types of wireless power transmission systems," in *International Conference on Science and Engineering*, 2015.
- [45] O. Akpeghagha, C. M. Iwunna, M. M. Igwele, and H. Okoro, "Witricity: design and implementation of a wireless power transfer system via inductive coupling," *International Journal of Innovative Research and Advanced Studies (IJIRAS)*, vol. 6, no. 4, pp. 16–19, 2019.
- [46] Z. Yan, B. Yang, H. Liu, C. Chen, M. Waqas, R. Mai, and Z. He, "Efficiency improvement of wireless power transfer based on multitransmitter system," *IEEE Transactions on Power Electronics*, vol. 35, no. 9, pp. 9011–9023, 2020.
- [47] N. Ha-Van, S. Tretyakov, and C. Simovski, "Optimal frequencies for wireless power transfer through biological tissues," *IEEE Open Journal of Antennas and Propagation*, 2025.
- [48] M. Parise and G. Antonini, "On the inductive coupling between two parallel thin-wire circular loop antennas," *IEEE Transactions on Electromagnetic Compatibility*, vol. 60, no. 6, pp. 1865–1872, 2018.

REFERENCES

- [49] Z. Yao, S. Luo, Z. Zhang, G. Li, X. Wei, X. Shen, N. Zhang, P. T. Krein, and H. Ma, "Analysis and design of multifrequency compensation strategy for wide misalignment tolerance in inductive power transfer systems," *IEEE Transactions on Power Electronics*, vol. 38, no. 9, pp. 11 705–11 718, 2023.
- [50] Y.-D. Tai, B. Widdicombe, R. R. Unnithan, D. B. Grayden, and S. E. John, "Design and optimization of inductive wireless power transfer to endovascular devices," *TechRxiv*, 2025.
- [51] H. K. Abduljaleel, S. Mutashar, and S. K. Gharghan, "Survey of near-field wireless communication and power transfer for biomedical implants," *Engineering and Technology Journal*, vol. 42, no. 08, pp. 1080–1103, 2024.
- [52] C. Zheng, H. Ma, J.-S. Lai, and L. Zhang, "Design considerations to reduce gap variation and misalignment effects for the inductive power transfer system," *IEEE Transactions on Power Electronics*, vol. 30, no. 11, pp. 6108–6119, 2015.
- [53] B. M. Mosammam and M. Mirsalim, "New integrated tripolar pad using double-sided lcc compensation for wireless power transfer," *IEEE Transactions on Vehicular Technology*, vol. 69, no. 12, pp. 15 633–15 643, 2020.
- [54] K. Lee and W. Lee, "Effect of misaligned relay on output power and efficiency in wireless power transfer," *IEEE Access*, vol. 9, pp. 49 448–49 456, 2021.
- [55] V. Prasanth and P. Bauer, "Distributed ipt systems for dynamic powering: Misalignment analysis," *IEEE Transactions on Industrial Electronics*, vol. 61, no. 11, pp. 6013–6021, 2014.
- [56] S. Jain, A. Bharadwaj, and A. Sharma, "Spatially arranged relay coils to improve the misalignment tolerance at an enhanced transfer distance," *IEEE Transactions on Antennas and Propagation*, vol. 72, no. 3, pp. 2171–2180, 2024.
- [57] D. Brizi, M. Conte, and A. Monorchio, "A performance-enhanced antenna for microwave biomedical applications by using metasurfaces," *IEEE Transactions on Antennas and Propagation*, vol. 71, no. 4, pp. 3314–3323, 2023.
- [58] H. Banerjee and H. Ren, "Electromagnetically responsive soft-flexible robots and sensors for biomedical applications and impending challenges," *Electromagnetic Actuation and Sensing in Medical Robotics*, pp. 43–72, 2018.

-
- [59] S. Roy, A. W. Azad, S. Baidya, M. K. Alam, and F. Khan, “Powering solutions for biomedical sensors and implants inside the human body: A comprehensive review on energy harvesting units, energy storage, and wireless power transfer techniques,” *IEEE Transactions on Power Electronics*, vol. 37, no. 10, pp. 12 237–12 263, 2022.
- [60] V. Lazzoni, D. Brizi, and A. Monorchio, “Spatial filtering magnetic metasurface for misalignment robustness enhancement in wireless power transfer applications,” *Scientific Reports*, vol. 13, no. 1, p. 560, 2023.
- [61] R. Saha, Z. Kaffash, and S. A. Mirbozorgi, “Multi-resonator wireless inductive power link for wearables on the 2d surface and implants in 3d space of the human body,” *IEEE Transactions on Biomedical Circuits and Systems*, vol. 18, no. 5, pp. 1024–1036, 2024.
- [62] J. Barreto, G. Perez, A.-S. Kaddour, and S. V. Georgakopoulos, “A study of wearable wireless power transfer systems on the human body,” *IEEE Open Journal of Antennas and Propagation*, vol. 2, pp. 86–94, 2021.
- [63] J. Gao, S. Tian, C. Yuan, Z. Ma, C. Gao, G. Yan, R. Li, Q. Tan, and L. Zhang, “Design and optimization of a novel double-layer helmholtz coil for wirelessly powering a capsule robot,” *IEEE Transactions on Power Electronics*, 2023.
- [64] R. Garbacz and R. Turpin, “A generalized expansion for radiated and scattered fields,” *IEEE transactions on Antennas and Propagation*, vol. 19, no. 3, pp. 348–358, 1971.
- [65] R. Harrington and J. Mautz, “Theory of characteristic modes for conducting bodies,” *IEEE transactions on antennas and propagation*, vol. 19, no. 5, pp. 622–628, 1971.
- [66] —, “Computation of characteristic modes for conducting bodies,” *IEEE Transactions on Antennas and Propagation*, vol. 19, no. 5, pp. 629–639, 1971.
- [67] M. Cabedo-Fabres, E. Antonino-Daviu, A. Valero-Nogueira, and M. F. Bataller, “The theory of characteristic modes revisited: A contribution to the design of antennas for modern applications,” *IEEE Antennas and Propagation Magazine*, vol. 49, no. 5, pp. 52–68, 2007.
- [68] J. Molins-Benlliure, E. Antonino-Daviu, M. Cabedo-Fabrés, and M. Ferrando-Bataller, “On-ground small ltcc chip antenna and its placement on iot devices,” *IEEE Antennas and Wireless Propagation Letters*, vol. 22, no. 9, pp. 2065–2069, 2023.

REFERENCES

- [69] B. Feng, B. Yang, L. Deng, Z. Zhou, X. Ding *et al.*, “A compact vehicle-mounted garden-themed artistic antenna with isolation improvement for 2g/3g/lte/5g sub-6-ghz/wifi/bluetooth communications,” *IEEE Transactions on Vehicular Technology*, vol. 72, no. 4, pp. 4851–4862, 2022.
- [70] J. Molins-Benlliure, E. Antonino-Daviu, M. Cabedo-Fabrés, and M. Ferrando-Bataller, “Four-port wide-band cavity-backed antenna with isolating x-shaped block for sub-6 ghz 5g indoor base stations,” *IEEE Access*, vol. 9, pp. 80 535–80 545, 2021.
- [71] W. Ren, Z. Wang, W. Nie, W. Mu, C. Li, and M. Wang, “A transparent ultra-wideband antenna fed by cpw based on characteristic mode theory,” *Applied Computational Electromagnetics Society Journal (ACES)*, pp. 987–998, 2024.
- [72] M. Veletic, E. H. Apu, M. Simic, J. Bergsland, I. Balasingham, C. H. Contag, and N. Ashammakhi, “Implants with sensing capabilities,” *Chemical Reviews*, vol. 122, no. 21, pp. 16 329–16 363, 2022.
- [73] R. H. Turpin, *Basis transformation, least square, and characteristic mode techniques for thin-wire scattering analysis*. The Ohio State University, 1969.
- [74] R. Harrington, J. Mautz, and Y. Chang, “Characteristic modes for dielectric and magnetic bodies,” *IEEE Transactions on Antennas and Propagation*, vol. 20, no. 2, pp. 194–198, 1972.
- [75] Y. Chang and R. Harrington, “A surface formulation for characteristic modes of material bodies,” *IEEE transactions on antennas and propagation*, vol. 25, no. 6, pp. 789–795, 1977.
- [76] A. Yee and R. Garbacz, “Self- and mutual-admittances of wire antennas in terms of characteristic modes,” *IEEE Transactions on Antennas and Propagation*, vol. 21, no. 6, pp. 868–871, 1973.
- [77] Q. Wu, W. Su, Z. Li, and D. Su, “Reduction in out-of-band antenna coupling using characteristic mode analysis,” *IEEE Transactions on Antennas and Propagation*, vol. 64, no. 7, pp. 2732–2742, 2016.
- [78] S. Rao, D. Wilton, and A. Glisson, “Electromagnetic scattering by surfaces of arbitrary shape,” *IEEE Transactions on antennas and propagation*, vol. 30, no. 3, pp. 409–418, 1982.
- [79] P. Liang and Q. Wu, “Characteristic mode analysis of antenna mutual coupling in the near field,” *IEEE Transactions on Antennas and Propagation*, vol. 66, no. 7, pp. 3757–3762, 2018.

-
- [80] Y. Chen and C.-F. Wang, "Characteristic-mode-based improvement of circularly polarized u-slot and e-shaped patch antennas," *IEEE Antennas and Wireless Propagation Letters*, vol. 11, pp. 1474–1477, 2012.
- [81] M. Capek, P. Hazdra, P. Hamouz, and J. Eichler, "A method for tracking characteristic numbers and vectors," *Progress In Electromagnetics Research B*, vol. 33, pp. 115–134, 2011.
- [82] N. M. Mohamed-Hicho, E. Antonino-Daviu, M. Cabedo-Fabrés, J. P. Ciardini, and M. Ferrando-Bataller, "On the interaction of characteristic modes in slot antennas etched on finite ground planes," in *2016 10th European Conference on Antennas and Propagation (EuCAP)*. IEEE, 2016, pp. 1–5.
- [83] Z. Yang, D. Su, Y. Li, and Y. Liu, "An improved method for tracking of characteristic modes," in *2016 IEEE International Conference on Computational Electromagnetics (ICCEM)*. IEEE, 2016, pp. 103–105.
- [84] M. M. Elsewe and D. Chatterjee, "Modal analysis of patch slot designs in microstrip patch antennas," in *2016 IEEE/ACES International Conference on Wireless Information Technology and Systems (ICWITS) and Applied Computational Electromagnetics (ACES)*. IEEE, 2016, pp. 1–2.
- [85] M. Khan and D. Chatterjee, "Characteristic mode analysis of a class of empirical design techniques for probe-fed, u-slot microstrip patch antennas," *IEEE Transactions on Antennas and Propagation*, vol. 64, no. 7, pp. 2758–2770, 2016.
- [86] —, "Characteristic modes for u-slot's feed placement," in *2017 IEEE International Symposium on Antennas and Propagation & USNC/URSI National Radio Science Meeting*. IEEE, 2017, pp. 743–744.
- [87] —, "Analysis of reactive loading in a u-slot microstrip patch using the theory of characteristic modes [antenna applications corner]," *IEEE Antennas and Propagation Magazine*, vol. 60, no. 6, pp. 88–97, 2018.
- [88] J. J. Borchardt and T. C. Lapointe, "U-slot patch antenna principle and design methodology using characteristic mode analysis and coupled mode theory," *IEEE Access*, vol. 7, pp. 109 375–109 385, 2019.
- [89] T. LaPointe, "Characterization of wideband u-slot patch antennas through characteristic modal analysis and coupled mode theory," 2018.
- [90] J. J. Borchardt and T. C. LaPointe, "Analysis of a u-slot patch using characteristic mode analysis and coupled mode theory," in *2019 IEEE International Symposium on Antennas and Propagation and USNC-URSI Radio Science Meeting*. IEEE, 2019, pp. 1515–1516.

REFERENCES

- [91] R.-Z. Lian and X.-Y. Guo, “Work-energy principle (wep)-based characteristic mode theory for wireless power transfer systems,” in *2023 8th International Conference on Computer and Communication Systems (ICCCS)*, 2023, pp. 623–632.
- [92] A. A. Eteng, “Characteristic-mode analysis of coupled split-ring resonators,” *Journal of Electrical Engineering*, vol. 73, no. 6, pp. 413–418, 2022.
- [93] R. Lian, “Research on the work-energy principle based characteristic mode theory for scattering systems,” *arXiv preprint arXiv:1907.11787*, 2019.
- [94] A. Karalis, J. D. Joannopoulos, and M. Soljačić, “Efficient wireless non-radiative mid-range energy transfer,” *Annals of physics*, vol. 323, no. 1, pp. 34–48, 2008.
- [95] H. A. Haus, “Waves and fields in optoelectronics,” (*No Title*), 1984.
- [96] C.-J. Chen, T.-H. Chu, C.-L. Lin, and Z.-C. Jou, “A study of loosely coupled coils for wireless power transfer,” *IEEE Transactions on Circuits and Systems II: Express Briefs*, vol. 57, no. 7, pp. 536–540, 2010.
- [97] D. Lin, C. Zhang, and S. R. Hui, “Mathematical analysis of omnidirectional wireless power transfer—part-i: Two-dimensional systems,” *IEEE Transactions on Power Electronics*, vol. 32, no. 1, pp. 625–633, 2016.
- [98] M. Wang, J. Feng, Y. Shi, and M. Shen, “Demagnetization weakening and magnetic field concentration with ferrite core characterization for efficient wireless power transfer,” *IEEE Transactions on Industrial Electronics*, vol. 66, no. 3, pp. 1842–1851, 2019.
- [99] Z. Luo and X. Wei, “Analysis of square and circular planar spiral coils in wireless power transfer system for electric vehicles,” *IEEE Transactions on Industrial Electronics*, vol. 65, no. 1, pp. 331–341, 2018.
- [100] D. H. Nguyen, “Dynamic optical wireless power transfer for electric vehicles,” *IEEE Access*, vol. 11, pp. 2787–2795, 2023.
- [101] C. Liu, C. Jiang, J. Song, and K. Chau, “An effective sandwiched wireless power transfer system for charging implantable cardiac pacemaker,” *IEEE Transactions on Industrial Electronics*, vol. 66, no. 5, pp. 4108–4117, 2018.
- [102] F. Abderrazak, E. Antonino-Daviu, and M. Ferrando-Bataller, “Power transfer efficiency analyzed using characteristic mode coupling between

- two parallel loops,” in *2020 14th European Conference on Antennas and Propagation (EuCAP)*. IEEE, 2020, pp. 1–5.
- [103] F. Abderrazak, E. Antonino-Daviu, M. Ferrando-Bataller, and L. Talbi, “Analysis of magnetically-coupled loops based on characteristic modes,” in *2020 IEEE International Symposium on Antennas and Propagation and North American Radio Science Meeting*. IEEE, 2020, pp. 121–122.
- [104] F. Abderrazak, E. Antonino-Daviu, L. Talbi, and M. Ferrando-Bataller, “A performance comparison of three topologies of circular loop antennas transmitting systems,” in *2021 IEEE 19th International Symposium on Antenna Technology and Applied Electromagnetics (ANTEM)*, 2021, pp. 1–2.
- [105] —, “Characteristic mode analysis of scmr and cscmr systems,” in *2022 16th European Conference on Antennas and Propagation (EuCAP)*, 2022, pp. 1–5.
- [106] —, “Analysis on power transfer efficiency using near field plates,” in *2022 IEEE International Symposium on Antennas and Propagation and USNC-URSI Radio Science Meeting (AP-S/URSI)*, 2022, pp. 1738–1739.
- [107] D. Kong, J. Zhao, L. Mao, Y. Yin, and J. Zhang, “High-quality factor coil winding method accounting for proximity effect resistance and turn-to-turn mutual inductance,” *Journal of Power Electronics*, pp. 1–12, 2025.
- [108] T. Arakawa, S. Goguri, J. V. Krogmeier, A. Kruger, D. J. Love, R. Mudumbai, and M. A. Swabey, “Optimizing wireless power transfer from multiple transmit coils,” *IEEE Access*, vol. 6, pp. 23 828–23 838, 2018.
- [109] J.-S. Hong, “Couplings of asynchronously tuned coupled microwave resonators,” *IEE Proceedings-Microwaves, Antennas and Propagation*, vol. 147, no. 5, pp. 354–358, 2000.
- [110] J. J. Borchardt, “Coupled and characteristic modes of a wideband slot antenna using feko,” in *2021 International Applied Computational Electromagnetics Society Symposium (ACES)*. IEEE, 2021, pp. 1–4.
- [111] F. Abderrazak, E. Antonino-Daviu, L. Talbi, and M. Ferrando-Bataller, “Characteristic modes analyses for misalignment in wireless power transfer system,” *IEEE Access*, vol. 12, pp. 65 007–65 023, 2024.
- [112] F. Abderrazak, E. Antonino-Daviu, M. Ferrando-Bataller, L. Talbi, and A. Al Qaraghuli, “A comparative study between different loop antennas topologies for wireless power transmission based on modal analysis,” in

REFERENCES

- 2021 15th European Conference on Antennas and Propagation (EuCAP)*, 2021, pp. 1–5.
- [113] D. Vital and S. Bhardwaj, “Misalignment resilient anchor-shaped antennas in near-field wireless power transfer using electric and magnetic coupling modes,” *IEEE Transactions on Antennas and Propagation*, vol. 69, no. 5, pp. 2513–2521, 2021.
- [114] H. Xueliang, C. Weijie, Z. Yalong, W. Wei, and T. Linlin, “Comparative study on the two kinds of models in the technology of magnetic coupling resonance system,” *Transactions of China Electrotechnical Society*, vol. 28, no. S2, pp. 13–17, 2013.
- [115] H. W. R. Liang, H. Wang, C.-K. Lee, and S. R. Hui, “Analysis and performance enhancement of wireless power transfer systems with intended metallic objects,” *IEEE Transactions on Power Electronics*, vol. 36, no. 2, pp. 1388–1398, 2020.
- [116] C. Liu, C. Jiang, J. Song, and K. Chau, “An effective sandwiched wireless power transfer system for charging implantable cardiac pacemaker,” *IEEE Transactions on Industrial Electronics*, vol. 66, no. 5, pp. 4108–4117, 2018.
- [117] X. Li, J. Hu, H. Wang, X. Dai, and Y. Sun, “A new coupling structure and position detection method for segmented control dynamic wireless power transfer systems,” *IEEE Transactions on Power Electronics*, vol. 35, no. 7, pp. 6741–6745, 2020.
- [118] A. Reatti, L. Pugi, F. Corti, and F. Grasso, “Effect of misalignment in a four plates capacitive wireless power transfer system,” in *2020 IEEE International Conference on Environment and Electrical Engineering and 2020 IEEE Industrial and Commercial Power Systems Europe (EEEIC/I&CPS Europe)*. IEEE, 2020, pp. 1–4.
- [119] M. Haerinia and S. Noghianian, “Analysis of misalignment effects on link budget of an implantable antenna,” in *2019 URSI International Symposium on Electromagnetic Theory (EMTS)*. IEEE, 2019, pp. 1–4.
- [120] R. Johari, J. V. Krogmeier, and D. J. Love, “Analysis and practical considerations in implementing multiple transmitters for wireless power transfer via coupled magnetic resonance,” *IEEE Transactions on Industrial Electronics*, vol. 61, no. 4, pp. 1774–1783, 2013.
- [121] Z. Liu, Z. D. Chen, and H. Zhao, “A simple structure of planar transmitting array for multi-receiver wireless power reception,” in *2017 IEEE Wireless Power Transfer Conference (WPTC)*. IEEE, 2017, pp. 1–2.

-
- [122] S. Jeong, T.-H. Lin, and M. M. Tentzeris, "A real-time range-adaptive impedance matching utilizing a machine learning strategy based on neural networks for wireless power transfer systems," *IEEE Transactions on Microwave Theory and Techniques*, vol. 67, no. 12, pp. 5340–5347, 2019.
- [123] C. Song, Y. Huang, J. Zhou, P. Carter, S. Yuan, Q. Xu, and Z. Fei, "Matching network elimination in broadband rectennas for high-efficiency wireless power transfer and energy harvesting," *IEEE Transactions on Industrial Electronics*, vol. 64, no. 5, pp. 3950–3961, 2016.
- [124] M. F. Imani and A. Grbic, "Unidirectional wireless power transfer using near-field plates," *Journal of Applied Physics*, vol. 117, no. 18, 2015.
- [125] A. Markvart, M. Song, S. Glybovski, P. Belov, C. Simovski, and P. Kapitnova, "Metasurface for near-field wireless power transfer with reduced electric field leakage," *IEEE Access*, vol. 8, pp. 40 224–40 231, 2020.
- [126] M. F. Imani and A. Grbic, "Unidirectional wireless power transfer using near-field plates," *Journal of Applied Physics*, vol. 117, no. 18, 2015.
- [127] J. Wang, M. P. Leach, E. G. Lim, Z. Wang, Z. Jiang, R. Pei, and Y. Huang, "A conformal split-ring loop as a self-resonator for wireless power transfer," *IEEE Access*, vol. 8, pp. 911–919, 2019.
- [128] G. Zhu and D. Gao, "Highly effective leakage magnetic field suppression by using a reactive coil in perfectly aligned ev wireless charging systems," *Journal of Power Electronics*, vol. 20, pp. 11–21, 2020.
- [129] P. Darvish, A. Hossain, S. Mekhilef, K. S. Tey, M. B. Mubin, J. Yin, M. M. Akhtar, A. Mustafa, H. Khalid, T. Imtiaz *et al.*, "Dual-receiver based naturally decoupled coil structure with improved rotational misalignment tolerance for wpt systems," *IEEE Transactions on Transportation Electrification*, vol. 10, no. 3, pp. 5412–5423, 2023.
- [130] Y. Li, B. Zhang, Y. Zhai, H. Wang, B. Yuan, and Z. Lou, "A novel type of 3-d transmitter for omnidirectional wireless power transfer," *IEEE Transactions on Power Electronics*, vol. 39, no. 5, pp. 6537–6548, 2024.
- [131] H. Chen, D. Qiu, C. Rong, and B. Zhang, "A double-transmitting coil wireless power transfer system based on parity time symmetry principle," *IEEE Transactions on Power Electronics*, vol. 38, no. 11, pp. 13 396–13 404, 2023.
- [132] Y. Zhang, W. Pan, H. Wang, Z. Shen, Y. Wu, J. Dong, and X. Mao, "Misalignment-tolerant dual-transmitter electric vehicle wireless charging system with reconfigurable topologies," *IEEE Transactions on Power Electronics*, vol. 37, no. 8, pp. 8816–8819, 2022.

REFERENCES

- [133] Q. H. Lai and C. S. Lai, "Healthcare with wireless communication and smart meters," *IEEE Consumer Electronics Magazine*, vol. 12, no. 4, pp. 53–62, 2023.
- [134] X. Zhou, W. Wu, and S. Bao, "Mobile health: Ieee standard for wearable cuffless blood pressure measuring devices," *Zhongguo yi Liao qi xie za zhi= Chinese Journal of Medical Instrumentation*, vol. 39, no. 4, pp. 285–287, 2015.
- [135] J. G. Delfino and T. O. Woods, "New developments in standards for mri safety testing of medical devices," *Current Radiology Reports*, vol. 4, pp. 1–9, 2016.
- [136] A. Walker, "Functional safety certification from automotive to medical," *Software Quality Professional Magazine*, vol. 18, no. 4, 2016.
- [137] K. Armstrong, "Why few (if any) medical devices comply with their emc standard, and what can be done about it," in *2014 IEEE International Symposium on Electromagnetic Compatibility (EMC)*. IEEE, 2014, pp. 929–934.
- [138] A. Walker, "Improving medical risk management using automotive standards," in *dHealth 2020–Biomedical Informatics for Health and Care*. IOS Press, 2020, pp. 263–270.
- [139] A. AHMAD, "Analysis of wireless charging schemes for electric vehicles," Ph.D. dissertation, ALIGARH MUSLIM UNIVERSITY ALIGARH, 2019.
- [140] K. Van Schuylenbergh and R. Puers, *Inductive powering: basic theory and application to biomedical systems*. Springer, 2009.
- [141] H. Jung and B. Lee, "Optimization of magnetic field focusing and null steering for selective wireless power transfer," *IEEE Transactions on Power Electronics*, vol. 35, no. 5, pp. 4622–4633, 2019.
- [142] Adeniran and A. Olusakin, "Modelling and comparative analysis of inductively coupled circular and square loop wireless power transfer at uhf band for automobile charging," *Acta Electronica Malaysia*, vol. 7, no. 1, pp. 8–14, 2023.
- [143] X. Cao, H. Sato, K.-D. Xu, W. Jiang, S. Gong, and Q. Chen, "A systematic method for efficient wireless powering to implantable biomedical devices," *IEEE Transactions on Antennas and Propagation*, vol. 71, no. 3, pp. 2745–2757, 2023.

-
- [144] G. A. Covic and J. T. Boys, "Inductive power transfer," *Proceedings of the IEEE*, vol. 101, no. 6, pp. 1276–1289, 2013.
- [145] H. Hu and S. V. Georgakopoulos, "Multiband and broadband wireless power transfer systems using the conformal strongly coupled magnetic resonance method," *IEEE Transactions on Industrial Electronics*, vol. 64, no. 5, pp. 3595–3607, 2016.
- [146] K. Bao, C. L. Zekios, and S. V. Georgakopoulos, "Miniaturization of scmr systems using multilayer resonators," *IEEE Access*, vol. 7, pp. 143 445–143 453, 2019.
- [147] C. A. Balanis, *Antenna theory: analysis and design*. John wiley & sons, 2016.
- [148] O. Jonah, S. V. Georgakopoulos, and H. Hu, "Antenna structures for wireless power transfer via resonance magnetic," in *WAMICON 2013*, 2013, pp. 1–4.
- [149] O. Jonah and S. V. Georgakopoulos, "Wireless power transmission to sensors embedded in concrete via magnetic resonance," in *WAMICON 2011 Conference Proceedings*. IEEE, 2011, pp. 1–6.
- [150] D. Liu, H. Hu, and S. V. Georgakopoulos, "Misalignment sensitivity of strongly coupled wireless power transfer systems," *IEEE Transactions on Power Electronics*, vol. 32, no. 7, pp. 5509–5519, 2017.
- [151] S. Lee, H. Hoang, Y. Choi, and F. Bien, "Efficiency improvement for magnetic resonance based wireless power transfer with axial-misalignment," *Electronics letters*, vol. 48, no. 6, pp. 339–340, 2012.
- [152] W. Zhong and S. Hui, "Auxiliary circuits for power flow control in multi-frequency wireless power transfer systems with multiple receivers," *IEEE Transactions on Power Electronics*, vol. 30, no. 10, pp. 5902–5910, 2014.
- [153] D. Ahn and S. Hong, "Effect of coupling between multiple transmitters or multiple receivers on wireless power transfer," *IEEE Transactions on Industrial Electronics*, vol. 60, no. 7, pp. 2602–2613, 2012.
- [154] K. Fotopoulou and B. W. Flynn, "Wireless power transfer in loosely coupled links: Coil misalignment model," *IEEE Transactions on magnetics*, vol. 47, no. 2, pp. 416–430, 2010.
- [155] O. Jonah, S. V. Georgakopoulos, and M. M. Tentzeris, "Orientation insensitive power transfer by magnetic resonance for mobile devices," in *2013 IEEE Wireless Power Transfer (WPT)*, 2013, pp. 5–8.

REFERENCES

- [156] F. Zhang, S. A. Hackwoth, X. Liu, C. Li, and M. Sun, "Wireless power delivery for wearable sensors and implants in body sensor networks," in *2010 Annual International Conference of the IEEE Engineering in Medicine and Biology*, 2010, pp. 692–695.
- [157] O. Jonah, "Optimization of wireless power transfer via magnetic resonance in different media," 2013.
- [158] O. Jonah, S. Geogakopoulos, and M. Tentzeris, "Strongly coupled wireless power transfer with conformal structures," in *IEEE Antennas Propagat. Society Internat. Symp*, 2013.
- [159] F. Wen and X. Huang, "Human exposure to electromagnetic fields from parallel wireless power transfer systems," *International journal of environmental research and public health*, vol. 14, no. 2, p. 157, 2017.
- [160] Q. Yuan, Q. Chen, and K. Sawaya, "Effect of nearby human body on wpt system," in *Proceedings of the 5th European Conference on Antennas and Propagation (EUCAP)*. IEEE, 2011, pp. 3983–3986.
- [161] I. Laakso, S. Tsuchida, A. Hirata, and Y. Kamimura, "Evaluation of sar in a human body model due to wireless power transmission in the 10 mhz band," *Physics in Medicine & Biology*, vol. 57, no. 15, p. 4991, 2012.
- [162] A. K. RamRakhyani, S. Mirabbasi, and M. Chiao, "Design and optimization of resonance-based efficient wireless power delivery systems for biomedical implants," *IEEE transactions on biomedical circuits and systems*, vol. 5, no. 1, pp. 48–63, 2010.
- [163] T. Campi, S. Cruciani, M. Feliziani, and A. Hirata, "Wireless power transfer system applied to an active implantable medical device," in *2014 IEEE wireless power transfer conference*. IEEE, 2014, pp. 134–137.
- [164] R.-F. Xue, K.-W. Cheng, and M. Je, "High-efficiency wireless power transfer for biomedical implants by optimal resonant load transformation," *IEEE Transactions on Circuits and Systems I: Regular Papers*, vol. 60, no. 4, pp. 867–874, 2012.
- [165] O. Jonah, S. V. Georgakopoulos, and M. M. Tentzeris, "Wireless power transfer to mobile wearable device via resonance magnetic," in *WAMI-CON 2013*. IEEE, 2013, pp. 1–3.
- [166] C. Goiceanu, R. Danulescu, and E. Danulescu, "Some considerations on the challenges related to the use of the new icnirp restrictions for human exposure to radiofrequency fields," *Radiation Protection Dosimetry*, vol. 199, no. 8-9, pp. 818–825, 2023.

- [167] R. Martens and D. Manteuffel, "A feed network for the selective excitation of specific characteristic modes on small terminals," in *2012 6th European Conference on Antennas and Propagation (EUCAP)*, 2012, pp. 1842–1846.
- [168] E. Antonino-Daviu, M. Cabedo-Fabrés, M. Sonkki, N. Mohamed Mohamed-Hicho, and M. Ferrando-Bataller, "Design guidelines for the excitation of characteristic modes in slotted planar structures," *IEEE Transactions on Antennas and Propagation*, vol. 64, no. 12, pp. 5020–5029, 2016.
- [169] W. Su, Q. Zhang, S. Alkaraki, Y. Zhang, X.-Y. Zhang, and Y. Gao, "Radiation energy and mutual coupling evaluation for multimode mimo antenna based on the theory of characteristic mode," *IEEE Transactions on Antennas and Propagation*, vol. 67, no. 1, pp. 74–84, 2018.